1-1-2010

The Synthesis, Structure, And Properties Of Group 2 Poly(pyrazolyl)borates And Their Use For The Atomic Layer Deposition Of Group 2 Borates

Mark J. Saly
Wayne State University

Recommended Citation

Saly, Mark J., "The Synthesis, Structure, And Properties Of Group 2 Poly(pyrazolyl)borates And Their Use For The Atomic Layer Deposition Of Group 2 Borates" (2010). *Wayne State University Dissertations.* Paper 184.

THE SYNTHESIS, STRUCTURE, AND PROPERTIES OF GROUP 2 POLY(PYRAZOLYL)BORATES AND THEIR USE FOR THE ATOMIC LAYER DEPOSITION OF GROUP 2 BORATES

by

MARK JOSEPH SALY

DISSERTATION

Submitted to the Graduate School

of Wayne State University,

Detroit, Michigan

in partial fulfillment of the requirements

for the degree of

DOCTOR OF PHILOSOPHY

2010

MAJOR: CHEMISTRY (Inorganic)

Approved by:

____

Advisor Date

____

____

____

____

DEDICATION

To my mother, Dorothy P. Hull

The person who has always supported me and has shown me that
there are no bounds to what one can accomplish.

ACKNOWLEDGMENTS

I would like to express my thanks to Professor Charles H. Winter for his guidance and support as my advisor at Wayne State University. I am grateful to my committee members, Professor Stephanie L. Brock, Professor Jin K. Cha, and Professor Mark Cheng, for their comments and suggestions on my thesis.

I would like to thank Dr. Mary Jane Heeg and Dr. Bashar Ksebati for their support in the characterization of new compounds. I would also like to thank the past and present group members for their support and friendship. In particular I would like to thank Dr. Monika Weidman and Dr. Mahesh Karunarathne for the helpful advice and useful ALD discussions. I would like to thank Chris Snyder, Tom Knisley, Ben Swarts, and Tomacz Respondek for the enjoyable conversations and social life outside the lab. I want to give special thanks to Dr. Charles Dezelah for helpful discussions and suggestions regarding ALD film growth.

I would like to thank Sheryl McCann who was by my side in the beginning of my graduate school career and who gave me infinite amounts of support, encouragement, and love. I would like to thank my mother, Dorothy Hull, for all of her support and encouragement. Finally, I would like to thank my mother’s husband, Dean Hull, and my two brothers, Jon and Eric, for their love and support.

TABLE OF CONTENTS

LIST OF TABLES

LIST OF FIGURES

LIST OF CHARTS

LIST OF ABBREVIATIONS

ABBREVIATION	LONG FORM
AFM	Atomic Force Microscopy
ALD	Atomic Layer Deposition
amak	$[OC(CF_3)CH_2N(CH_2CH_2OMe)_2]^-$
Bp^{R2}	bis(3,5-dialkylpyrazolyl)borate
Bp	bis(pyrazolyl)borate
Bp^{iPr2}	bis(3,5-diisopropylpyrzolyl)borate
Bp^{tBu2}	bis(3,5-di-*tert*-butylpyrazolyl)borate
CMOS	Complimentary Metal-Oxide Semiconductor
CVD	Chemical Vapor Deposition
dfhd	decafluoroheptanedionate
DMAC	dimethylacetamide
DRAM	Dynamic Random Access Memory
ERDA	Elastic Recoil Detection Analysis
FED	Field Emission Display
fod	heptafluorodimethyloctanedionate
hfac	hexafluoroacetylacetonate
hmtt	hexamethyltriethylenetetramine
iPr_2PzH	3,5-diisopropylpyrazole
LED	Light Emitting Diode
L^{iPr}	$[iPrNC(CH_3)CHC(CH_3)NiPr]^-$
L^{NMe2}	$[Me_2NC(CH_3)CHC(CH_3)NMe_2]^-$
L^{tBu}	$[tBuNC(CH_3)CHC(CH_3)NtBu]^-$
pmdt	pentamethyldiethylenetriamine

PVD	Physical Vapor Deposition
SEM	Scanning Electron Microscopy
tetraen	tetramethylethylenediamine
TFEL	Thin Film Electroluminescence
thd	2,2,6,6-tetramethylheptanedionate
TGA	Thermogravimetric Analysis
Tp	tris(pyrazolyl)borate
Tp^{Et2}	tris(3,5-diethylpyrazolyl)borate
Tp^{Me2}	tris(3,5-dimethylpyrazolyl)borate
Tp^{iPr2}	tris(3,5-diisopropylpyrazolyl)borate
Tp^{nPr2}	tris(3,5-di-n-propylpyrazolyl)borate
Tp^{R2}	tris(3,5-dialkylpyrazolyl)borate
XPS	X-Ray Photoelectron Spectroscopy
XRD	X-Ray Diffraction
1	$[BaTp_2]_2$
2	$SrTp_2$
3	$SrTp^{Me2}{}_2$
4	$BaTp^{Me2}{}_2$
5	$CaTp^{Et2}{}_2$
6	$SrTp^{Et2}{}_2$
7	$BaTp^{Et2}{}_2$
8	$CaTp^{nPr2}{}_2$
9	$SrTp^{nPr2}{}_2$
10	$BaTp^{nPr2}{}_2$
11	$LiBp^{tBu2}$

12.. $CaBp^{tBu2}{}_2$

13.. $SrBp^{tBu2}{}_2$

14.. $BaBp^{tBu2}{}_2(THF)$

15.. $BaTp^{tBu2}{}_2$

16.. HBp^{tBu2}

17.. KBp^{iPr2}

18.. $KTp^{iPr2}(iPr_2PzH)_3$

19.. $CaBp_2(THF)_2$

20.. $SrBp_2(THF)_2$

21.. $BaBp_2(THF)_4$

22.. $CaBp^{iPr2}(THF)_2$

23.. $SrBp^{iPr2}(THF)_2$

24.. $BaBp^{iPr2}(THF)_2$

25.. $TpCaBH_4$

26.. $[TpCaBH_4(THF)]_4$

27.. $TpCaBH_4(THF)_2$

28.. $[TpCa(\mu\text{-}B(OMe)_4)CaTp][B(OMe)_4]$

29.. $[(TpCaB(OEt)_3O)_3B]\cdot EtOH$

CHAPTER 1

Introduction

1.1 Important Materials Containing Calcium, Strontium, and Barium Ions

The heavy alkaline earth ions are important constituents in many technologically important materials.[1] Perovskite materials such as $SrTiO_3$,[2] $BaTiO_3$,[3] $(Ba,Sr)TiO_3$ (BST),[4] and $CaZrO_3$[5] are useful ferroelectric materials with high dielectric constants.[6] Other materials containing group 2 ions with high dielectric constants include $CaCu_3Ti_4O_{12}$ (CCTO)[7] and $SrBi_2Ta_2O_9$ (SBTO)[8] with ε values of ~10^4-10^5 and 300, respectively. These materials have practical application as capacitors in dynamic random access memories (DRAMs) and metal gates for high-performance logic Complementary Metal-Oxide-Semiconductor (CMOS) applications.[1-8] $TlBa_2Ca_{n-1}Cu_nO_{2n+3}$, $Tl_2Ba_2Ca_{n-1}Cu_nO_{2n+3}$, $(Tl,Pb)Sr_2Ca_{n-1}Cu_nO_{2n+3}$, $Sr_2CuO_2(CO_3)$ and $YBa_2Cu_3O_{7-x}$ are high-T_c superconductors with transition temperatures up to 124 K.[9] The fluorides of the alkaline-earth metals (CaF_2 and SrF_2) have high dielectric constants, a wide transmission range, and low refractive indices.[10] These characteristics make the group 2 fluorides useful for optical components (UV laser systems, lenses, prisms, windows), optical coatings, optical filters, and waveguides.[10] SrS and BaS are promising matrix materials for phosphors in thin film electroluminescent (TFEL) devices when doped with di- or trivalent lanthanide ions.[11,12] The group 2 metal borates are structurally diverse and have many important applications. Since the discovery of β-BaB_2O_4, a nonlinear optical crystal primarily used in laser frequency conversion,[13,14] there has been research centered towards the synthetic development of calcium and strontium borate-based materials. Calcium rare earth oxyborates ($LnCa_4O(BO_3)_3$, Ln = La, Nd, Sm, Gd, Er, Y),[15] lanthanide doped $Ca_3(BO_3)_2$,[16] and lanthanide doped $Ca_5(BO_3)_3F$[17] have practical application in laser technology due to their non-linear optical properties. Calcium and strontium borate-based materials containing lanthanide ions are strong phosphors, and thus have potential use in the development of light-emitting diodes (LEDs) and field-emission displays (FEDs).[18,19]

1.2 Thin Film Deposition Methods

Often it is necessary to obtain these materials as thin films for implementation into technological devices. Vapor phase thin film depositions, which include physical vapor deposition (PVD),[20] chemical vapor deposition (CVD),[21] and atomic layer deposition (ALD),[22] are the most widely employed deposition techniques in the microelectronics industry because of the conformal films obtained. Conformality is the ability of a film to coat a topographically complex surface uniformly.[20-22] In order for a device to function properly, it is crucial for all holes and trenches to be coated uniformly. PVD, CVD, and ALD are able to coat features uniformly to varying degrees, which will be discussed in detail below.

1.2.1 Physical Vapor Deposition (PVD)

In a typical PVD film growth process, individual atoms are removed from a liquid or solid source and travel through an evacuated chamber until the atoms impinge on a solid surface and condense to form a film (Figure 1).[20] The removal of the atoms from the source can be done thermodynamically by thermal heating or laser ablation, or by kinetically sputtering the surface with electrons, atoms, ions, or photons.[20] A typical evaporative PVD experiment is shown in Figure 1a. There are two types of source evaporation techniques which involve quasi-equilibrium and non-equilibrium processes.[20] In the quasi-equilibrium case, the source is in a near steady state equilibrium between the liquid and gas phase. An example of this kind of evaporator is called a Knudsen cell, which consists of a heated container with a small hole. The source vapor slowly permeates through the hole and travels towards a substrate and condenses. In non-equilibrium evaporative methods the source is volatized in an open container, such as a boat or crucible, and the source vapor diffuses through the chamber towards the substrate.[20] Another non-equilibrium evaporation process used in PVD involves the use of an electron beam. The electron beam is directed towards the source to cause localized heating at the surface. The surface heats up enough to vaporize the source, which then is directed towards the substrate

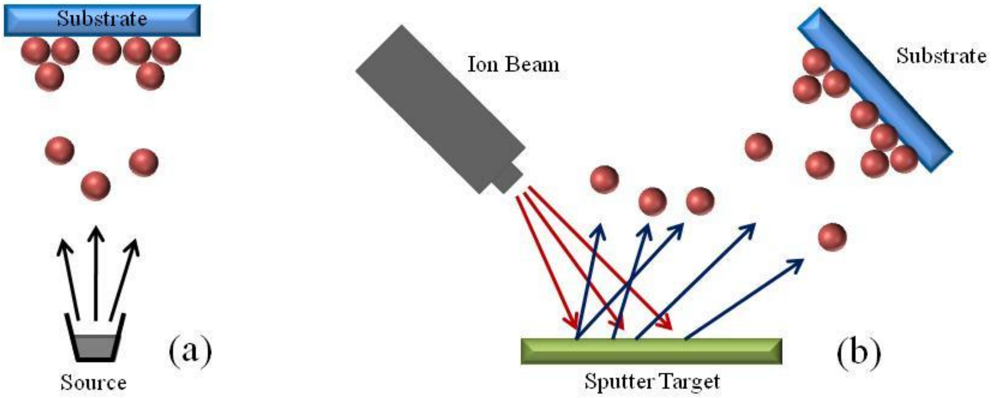

Figure 1. (a) Evaporative PVD and (b) Sputter PVD.[20]

Sputter-based PVD film growth is carried out by bombarding the surface of the source, often called the target, with high energy particles (Figure 1b). The incident particles are usually inert gas ions, however, any ion, neutral atom, or molecule can be used.[20] The impact of the energetic particles on the target causes surface atoms to be kinetically dislodged. The ejected atoms or sputtered atoms are then directed towards a substrate resulting in the formation of a thin film.

Evaporative and sputtered PVD have the ability to grow thin films at high growth rates. However, in the case of evaporative sputtering, the growth is highly directional affording films with exaggerated columnar microstructure.[20] Directionality in evaporative PVD is a result of the source atoms traveling to the substrate with a low probability of in flight collisions with background gas atoms.[20] In sputtered PVD, the film growth occurs in a relatively non-directional way. This is because the increased gas pressure in the chamber leads to gas-phase scattering of the sputtered atoms. This multidirectional film growth leads to a wide distribution of atoms on the film and better step-coverage.[20] Unfortunately, many PVD processes result in film growth with poor step coverage over features with high aspect ratios, which is related to the low surface mobility of the source atoms, as well as the inherent directionality of PVD film growth.[20] Additionally, PVD is regarded as a line-of-sight film growth method, meaning that the source species sticks to whatever surface it hits, thus the adsorbing species never makes it all the way down to the bottom of the high-aspect-ratio feature.

1.2.2 Thin Film Growth by CVD

In CVD film growth, one or more precursors are introduced to a heated substrate.[21] Once the precursors come close or in contact with the heated substrate, a series of complex reactions ensue, affording a thin film.[21] CVD is widely used in the semiconductor industry because of the conformal films obtained at high throughput.[21] Figure 2 illustrates common processes that occur in the CVD growth of a metal oxide. First the precursors are introduced to the heated substrate, usually through an inert gas stream. Once the precursors come close enough to the substrate within the heated zone (blue square), many processes can occur. The precursor can immediately react with the secondary precursor in the gas phase (b and d) which can result in gas phase precipitation of the metal oxide. Gas phase precipitation can lead to the formation of fine particles which can incorporate into the film, affording non-conformal film growth.[21b] The precursors can also adsorb to the surface and undergo oxidation and reduction reactions (c and e). Adsorption can be divided into physisorption (where van der Waals interactions keep the adsorbing molecule on the surface) or chemisorption (where the adsorbing molecule forms a chemical bond with the surface). All unreacted species and elimination products eventually make it to the inert gas stream and are purged out of the reactor.

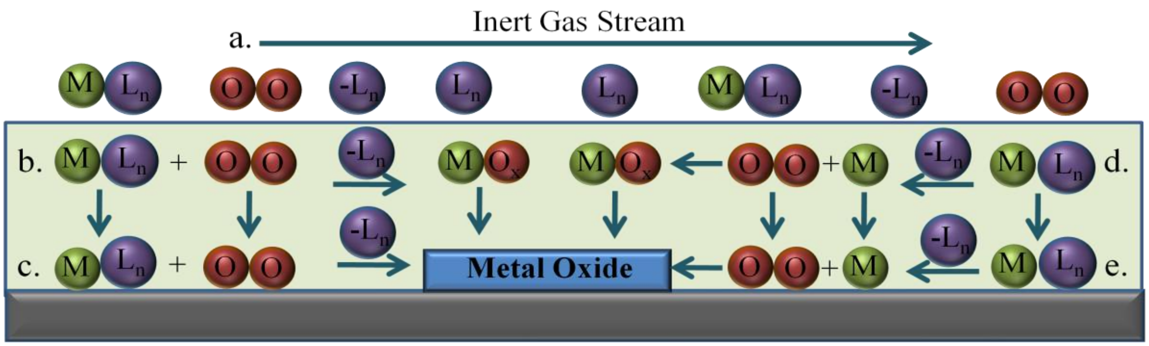

Figure 2. Selected steps in the CVD film growth of a metal oxide.[21]

Since film growth proceeds by complex surface and gas phase reactions in CVD, precursor selection is very important. The precursors need to be volatile, thermally stable enough to make it to the reactor, and reactive at substrate temperatures.[21] The nature of the precursor can have large effects on the uniformity, conformality, and coverage of the deposited thin film. The ability of a precursor to react with or stick to a surface is called the relative sticking coefficient (RSC).[21b] The RSC of a molecule should depend on the surface conditions as well as the characteristics of the molecule at the deposition temperature. If a precursor forms an unstable radical at the substrate it would likely react with anything it strikes, and thus have a high RSC. In contrast, precursors with low RSCs would be relatively stable at the deposition temperature. Precursors with low RSCs usually have high surface mobility and therefore afford conformal thin films.[21b]

Currently, CVD is the primary thin film growth method for the semiconductor industry. However, sometimes it can be difficult to obtain conformal films on high-aspect-ratio features with CVD. With the rapid decrease of feature sizes in microelectronics devices, a new deposition technique is needed for the deposition of thin films for the manufacture of these devices. There has been recent interest in atomic layer deposition (ALD) because of its ability to deposit conformal films with excellent thickness control.[22]

1.2.3 Atomic Layer Deposition

ALD film growth, originally called atomic layer epitaxy (ALE), was developed in the 1970s by Suntola for the manufacture of flat panel displays based on TFEL.[22] Miniaturization of devices in the semiconductor industry has developed a need to produce conformal thin films with excellent thickness control at the atomic layer.[22] ALD is able to coat high-aspect-ratio features with unprecedented conformality and excellent thickness control.[22] In ALD, two or more precursors are introduced to the substrate in a stepwise manner and are separated by an inert purge.[22] Keeping the reactants separated by an inert purge results in film growth occurring exclusively by surface reactions.[22] This type of film growth is referred to as self-limited and as long as the precursor concentrations are high enough to saturate the reactive sites on the film, a constant growth rate is achieved throughout the deposition. Recently, ALD has been used in the deposition of three dimensional substrates such as nanoparticles, viruses, and nanotubes.[22f]

A typical ALD process is shown in Figure 3, which involves the ALD growth of Al_2O_3 using trimethylaluminum (TMA) and water.[23d] In this case, a silicon substrate is terminated with hydroxyl groups. First, TMA is introduced to the substrate and undergoes protonylsis reactions with the available hydroxyl groups on the surface. Once all the surface sites have reacted, the reaction chamber is purged of all excess TMA and methane using an inert gas. Next, water vapor is added to the reaction chamber and all of the available surface methyl groups react to eliminate methane gas. The excess water vapor and methane gas are purged out of the chamber with an inert gas. At the end of the cycle the surface is terminated with hydroxyl groups, with some of the surface species condensing to form aluminum oxide bridging units. Repetition of ALD cycles affords smooth thin films of Al_2O_3 with excellent thickness control.

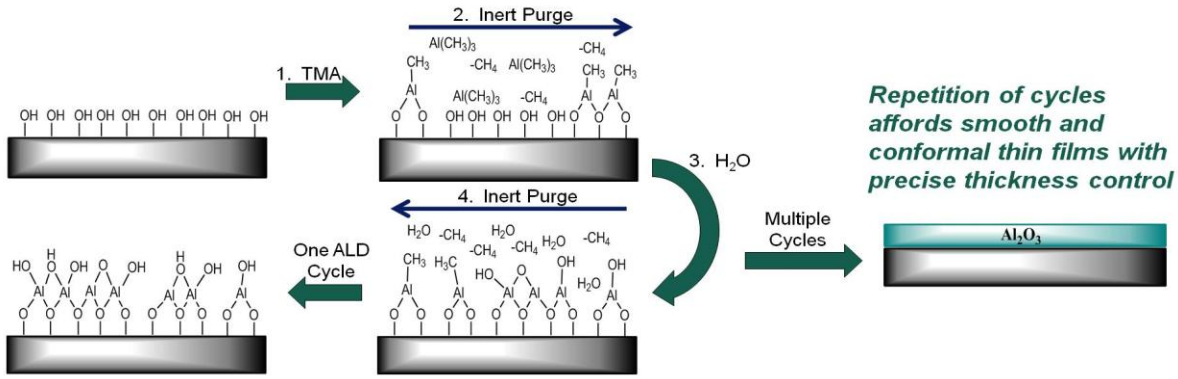

Figure 3. Steps in the ALD cycle of Al_2O_3 using TMA and water: 1) Introduction of TMA to the hydroxylated substrate 2) Inert gas purge of excess TMA and reaction byproducts 3) Introduction of water to the methylated substrate 4) Inert gas purge of excess water and reaction byproducts.

In ALD, a precursor adsorbs to the available surface sites on the substrate. Once all of the adsorption sites are consumed, there is no place for excess precursor to adsorb and only a theoretical monolayer can form.[22] In a plot of precursor pulse length versus growth rate (Figure 4), the minimal amount of precursor required for self-limited film growth occurs where the red region (A) meets the green region (B). Precursor pulse lengths beyond this point result in self-limited film growth.

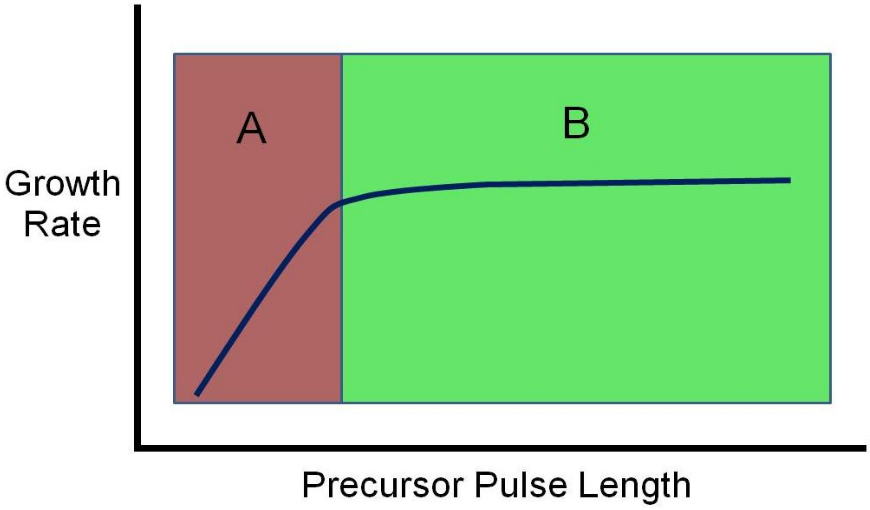

Figure 4. Plot of precursor pulse length versus growth rate. Region A (Red): Sub-saturative film growth. Region B (green): Surface sites are saturated.

In many ALD processes there exists a region of constant growth rate independent of temperature (Figure 5).[22a-c] This region is referred to as the "ALD Window". At lower temperatures, an increase in growth rate can be observed which is indicative of precursor condensation (dashed line, region I). Insufficient reactivity at lower temperatures can also lead to a decrease in growth rate, as demonstrated by the solid line in region I (blue). At the upper end of the ALD curve, a decrease in growth rate can occur as a result of precursor desorption from too much thermal energy. The dashed line in region III (red) shows the growth rate increasing exponentially, a common feature observed for ALD processes in which the precursor is self decomposing at higher temperatures. Although there are some advantages to having an ALD window, such as precise thickness control irrespective of slight temperature fluctuations, it is not completely necessary. However, saturation of the reactive surface sites is necessary to demonstrate an ALD growth mechanism.[22]

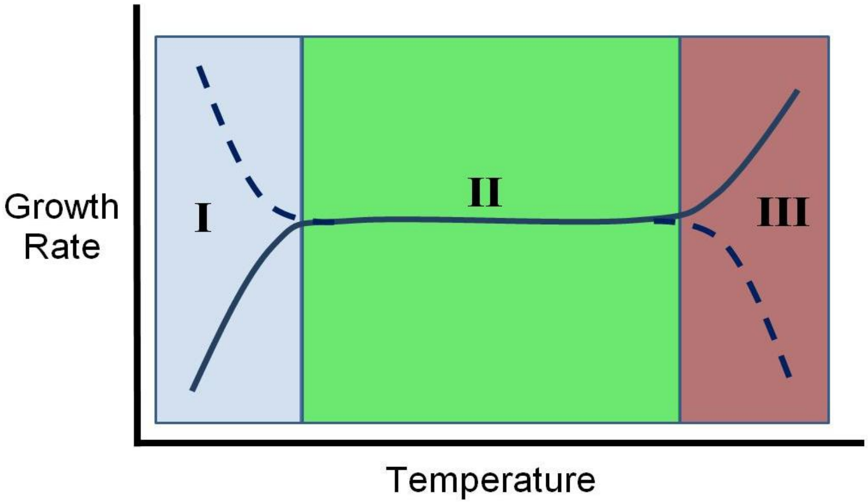

Figure 5. A plot of temperature versus growth rate. Region I (blue): Insufficient reactivity (solid line), Precursor condensation (dashed line). Region II (green): ALD window. Region III (red): Precursor desorption (dashed line), Precursor self-decomposition (solid line).

ALD film growth has several advantages over other vapor phase methods. The thickness of the film is only dependent on the number of reaction cycles, affording thin films with excellent thickness control. Since ALD growth occurs only by surface reactions, the precursor fluxes and gas flows are not crucial to the formation of uniform and conformal films over large areas.[22a] Keeping the precursors separated allows for the use of highly reactive compounds which can afford thin films at low temperatures. Furthermore, the presence of an ALD window for a particular ALD process allows the growth rate to remain constant even in the event of temperature fluctuations.[22a]

There are several requirements for suitable ALD precursors. The precursors need to have exceptional thermal stability.[22] If the precursor decomposes at the substrate, the self-limited film growth mechanism is lost affording non-conformal films with poor thickness control.[22] Additionally, the precursor needs to possess high volatility.[22] If the vapor pressure is too low in the reaction chamber, efficient saturation of the surface will not occur. Finally, the precursor needs to be reactive toward a secondary source. Low reactivity will either lead to low growth rates or no film growth at all. Some metal precursors that have been extensively employed for ALD include metal halides, metal alkyls and alkoxides, cyclopentadienyl complexes, and silyl-based compounds.[22a] Commonly used nonmetal precursors include water, ozone, hydrogen peroxide, hydrogen gas for sulfides, and ammonia for nitrides.[22a] A more detailed description of ALD precursors will be discussed below.

1.3 Group 2 CVD Precursors

Despite large research efforts, calcium, strontium, and barium precursors for CVD remain scarce.[1] Heavier alkaline earth precursors are plagued by low volatility, poor thermal stability, and low reactivity. These issues can be attributed to the small charge-to-size ratios and inherently low Lewis acidities of the metal ions.[1] Saturation of the metal ion coordination sphere is necessary to overcome these issues, since group 2 ions typically form oligomeric complexes with low volatility and poor thermal stability.[1] One strategy in obtaining group 2 monomeric complexes is to employ bulky ligands or neutral donor ligands to saturate the coordination sphere.[1] Unfortunately, neutral donor basic ligands tend to dissociate from the metal during volatilization, reforming oligomeric group 2 complexes.[1] Many different ligand systems have been used in an effort to synthesize volatile and thermally stable group 2 CVD precursors. These include complexes containing β-diketonate, β-ketoiminate, alkoxide, and pyrazolate ligands.[1]

1.3.1 Group 2 CVD Precursors Containing thd Ligands

Group 2 complexes containing *β*-diketonate-based ligands have had the most utility in CVD applications.[1b,23] Thd (thd = 2,2,6,6-tetramethylheptanedionate) complexes of calcium, strontium, and barium (Chart 1a) were previously synthesized by treating the appropriate metal ethoxide with Hthd in hexane.[24-26] An alternative approach for the synthesis of $[Ba(thd)_2]_4$ was reported by Drozdov and Trojanov which involved the direct reaction of barium metal with Hthd in hexane.[27] Unfortunately, these complexes suffer from low volatility (volatilization temperatures of ~ 200-230 °C/0.05 Torr) and low thermal stability owing to their oligomeric structures.[24-26] Neutral ligands containing basic heteroatoms such as oxygen and nitrogen are often employed to prevent oligomerizaton. A 5:1 N_2/NH_3 gas mixture was bubbled into a hexane solution of $[Ba(thd)_2]_4$ which resulted in the formation of $[Ba(thd)_2(NH_3)_2]_2$.[28] In TGA experiments, the final residue of $[Ba(thd)_2(NH_3)_2]_2$ was about 8 % compared to about 16 % observed in the TGA trace for $[Ba(thd)_2]_4$.[28] Paw and co-workers[29] were able to isolate the monomeric complexes $M(thd)_2(THF)_4$ (THF = tetrahydrofuran) by crystallization of the strontium and barium thd oligomers from tetrahydrofuran (Chart 1b).[29] $Ba(thd)_2(THF)_4$ and $Sr(thd)_2(THF)_4$ displayed unusually low melting points of 25 and 30 °C, respectively. However, THF ligand loss occurred at low temperatures (< 40 °C°) and by 150 °C, all of the THF ligands were liberated affording the unsolvated barium and strontium thd oligomers.[29] Drake and Williams[30] employed triglyme to stabilize monomeric structures of calcium and barium thd complexes (Chart 1c). Mass spectrometry displayed large mass-to-charge peaks corresponding to disassociated triglyme and $[M(thd)_2]_n$ oligomers. Attempted sublimation of $M(thd)_2(triglyme)$ at 100 °C/10^{-3} Torr resulted in triglyme loss with the formation of $[Ca(thd)_2]_3$ and $[Ba(thd)_2]_4$.[30] The treatment of

$[Ba(thd)_2]_4$ with various polyamines afforded the stable monomeric complexes of $Ba(thd)_2(pmdt)$ (pmdt = pentamethyldiethylenetriamine) and Ba(thd)(hmtt) (hmtt = hexamethyltriethylenetetramine), (Chart 1c and 1d, respectively).[31] The greater basicity of the polyamines relative to the glymes enhanced the vapor transport of $Ba(thd)_2$. However, $Ba(thd)_2(pmdt)$ and $Ba(thd)_2(hmtt)$ still exhibited dissociation of the polyamine ligand during sublimation at about 110 and 130 °C/0.05 Torr, respectively.[31]

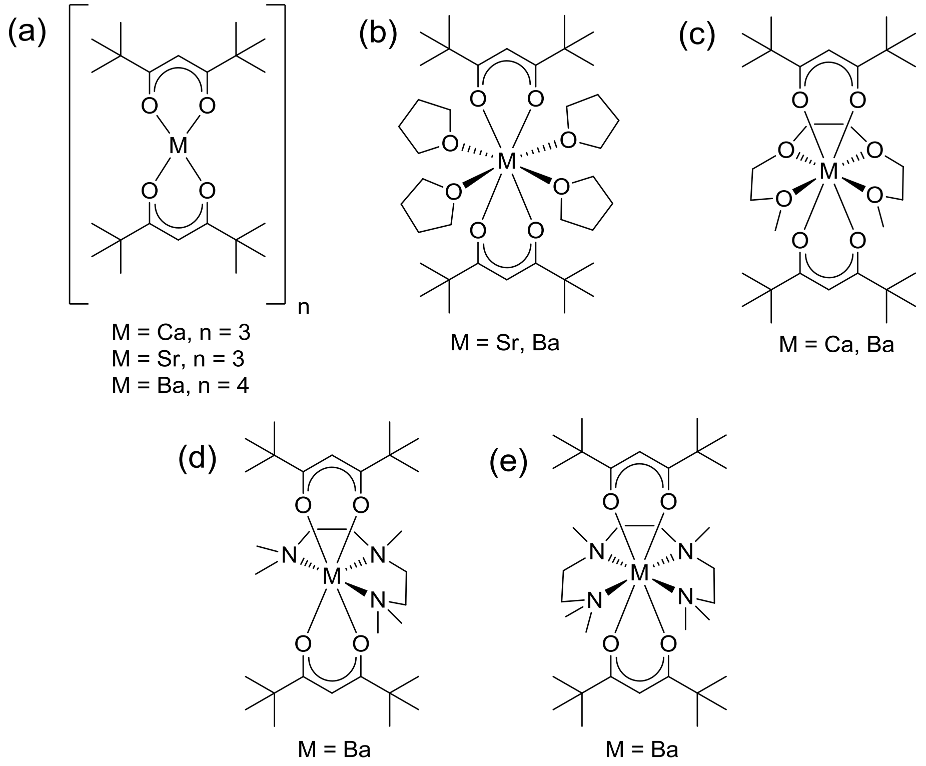

M = Ca, n = 3
M = Sr, n = 3
M = Ba, n = 4

M = Sr, Ba

M = Ca, Ba

M = Ba

M = Ba

Chart 1. $M(thd)_2$ complexes containing various neutral donating ligands

1.3.2 Group 2 CVD Precursors Containing Fluorinated β-Diketonate Ligands

While neutral donors are able saturate the coordination spheres of thd-based group 2 complexes and form monomers, the complexes still possess low thermal stability with minimal increase in volatility.[28-31] Fluorinated β-diketonate ligands can decrease the lattice energies from the presence of lone pair/lone pair electron repulsions and therefore increase the volatility and decrease the melting points of the complexes.[23a] The electron withdrawing fluorine groups on the ligands can also increase the Lewis acidity of the metal ions, resulting in more thermally stable complexes.[23a] Calcium, strontium, and barium complexes containing the hfac ligand (hfac = hexafluoroacetylacetonate) are oligomeric and decompose between 170 and 260 °C.[32] Similarly, "$Ba(fod)_2$" (fod = heptafluorodimethyloctanedionate) has poor qualities for use as a CVD precursor because the complex decomposes at vapor transport temperatures of 200-250 °C.[33] Incorporation of neutral macrocyclic ligands afforded monomeric complexes with better volatility than group 2 hfac-based complexes (Chart 2).[34,35] Using 18-crown-6 to saturate the coordination sphere of the $M(hfac)_2$ core (Chart 2a), resulted in the formation of volatile molecules that sublime from 80-150 °C at 10^{-2} Torr.[34] Watson and coworkers[35] isolated $Ba(thd)_2$(1-aza-18-crown-6) , shown in Chart 2b, and found that the complex volatilizes at ~135 °C/0.05 Torr, but decomposes at around 220 °C. Group 2 hfac-based complexes with neutral macrocyclic ligands decompose in the temperature range of 220-261 °C, and thus are not significantly more thermally stable than the oligomeric thd, hfac, and fod barium complexes. Coordination sphere saturation can also be accomplished by employing various glymes as shown in Chart 3(a and b).[36] $Ca(hfac)_2$(triglyme), $Sr(hfac)_2$(tetraglyme), and $Ba(hfac)_2$(tetraglyme) sublime at 100, 115, and 150 °C/0.3 Torr with decomposition occurring in the range of 247-256 °C.[36a] Marks and coworkers were able to increase the volatility (120-160 °C/10^{-2} Torr) and decrease the melting points substantially (as low as 34 °C) by coordinating various unsymmetrical glymes to the $Ba(hfac)_2$ cores (Chart 3b).[36b,c] Liquid precursors, under film growth conditions, are attractive because the surface area of solid precursors can change during cycling leading to unstable vapor pressures and irreproducible film stoichiometry. Stable complexes of M(dfhd)$_2$(H$_2$O) (Chart 3c) (dfhd = decafluoroheptanedionate) were previously synthesized[37] and undergo a slow structural rearrangement that substantially decreases the volatility. All of the fluorinated CVD complexes presented self-decompose at temperatures of > 240 °C to form the metal fluoride slowly.[35,36]

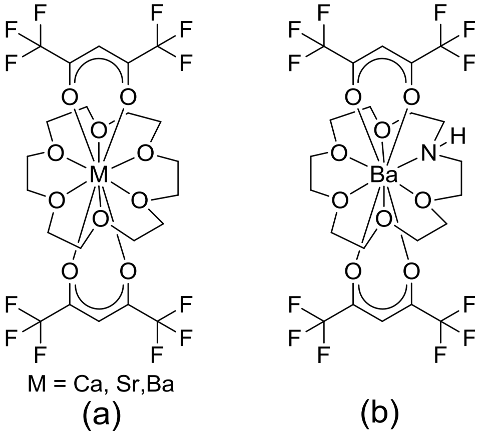

Chart 2. Selected group 2 hfac-based complexes containing (a) 18-crown-6 and (b) 1-aza-18-crown-6.

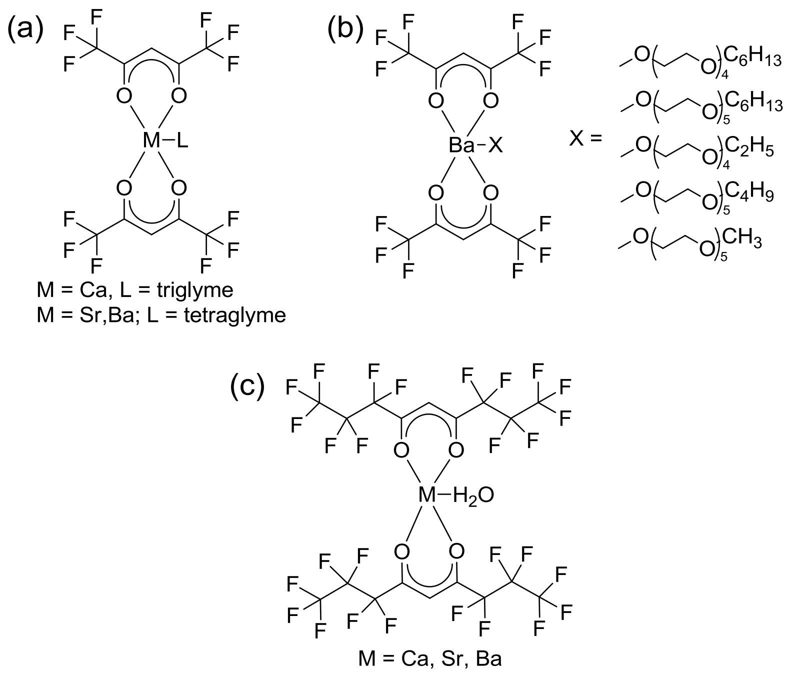

Chart 3. (a and b) Group 2 hfac-based complexes with various glymes. (c) Group 2 complexes containing the (dfhd) ligand.

1.3.3 Group 2 CVD Precursors Containing β-Diketoiminate-Based or Related Ligands

One issue with highly fluorinated group 2 CVD precursors is the facile incorporation of fluoride ion into the material, which can be detrimental to the materials properties. In an effort to avoid fluoride contamination, Marks and coworkers developed a series of barium complexes containing β-diketoiminate ligands with appended polyether lariats (Chart 4a) and encapsulating polyether tethers (Chart 5).[38] The function of the appended ether groups is to saturate the coordination sphere of the metal ion and also introduce asymmetry to the complex.[38] Asymmetric ligands are expected to help reduce the lattice energies in molecular solids, decrease the melting points, and increase the volatilities. These β-diketoiminate complexes sublime between 150 and 200 °C/10^{-3} Torr, and some have low enough melting points to volatilize as liquids.[38b,c] Although these complexes exhibit good volatility, all of them decompose during sublimation with subsequent loss of the protonated ligand.[38] Trifluoromethyl groups on the backbone of the β-ketoiminate ligand were able to increase the thermal stability enough to prevent free ligand loss during sublimation, however, the final residues in the TGA traces were high.[39] Recently, Hubert-Pfalzgraf and coworkers[40] structurally characterized a series of calcium, strontium, and barium compounds that contain a β-diketoiminate ligand with methyl groups in the 3- and 5-positions of the carbon backbone and a bis(diisopropyl)amine appendage off the nitrogen atoms (Chart 4b). These complexes had very poor characteristics for CVD because of their low volatility, but could find use in liquid injection CVD, since they have high solubility in hydrocarbon solvents.[40]

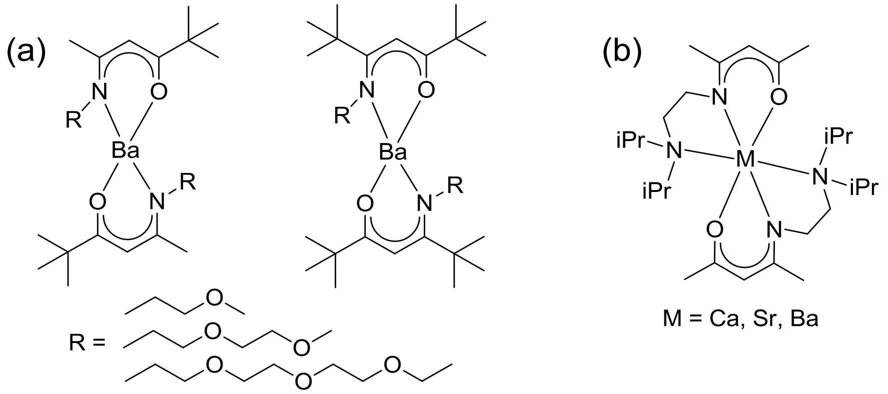

Chart 4. Barium complexes containing *β*-diketoiminate ligands with appended polyether lariats.

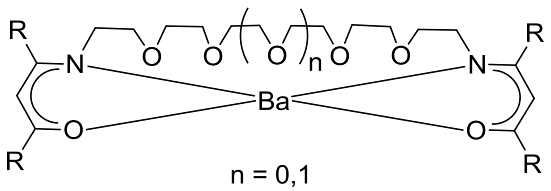

Chart 5. Barium complexes composed of β-diketoiminate ligands with encapsulating polyether tethers

Previously our group has developed a series of group 2 complexes that contain β-diketiminate ligands with isopropyl (L^{iPr}), *tert*-butyl (L^{tBu}), and dimethylamido (L^{NMe2}) groups on the nitrogen core atoms.[41] Calcium and strontium complexes containing L^{iPr} and L^{tBu} and $Ba(L^{tBu})_2$ all existed as monomers in the solid state and sublimed at temperatures of 100-135 °C/0.05 Torr with > 60% recoveries.[41a] In contrast, $[Ba(L^{iPr})_2]_2$ exists as a dimer in the solid state and accordingly has a higher sublimation temperature (~170 °C/0.05 Torr).[41a] Replacing the ligand to L^{NMe2} afforded the calcium complex as a monomer and the strontium and barium analogues as dimers.[41b] Careful comparison of the sublimation temperatures of $Ca(L^{NMe2})_2$, $[Sr(L^{NMe2})_2]_2$, and $[Ba(L^{NMe2})_2]_2$ with the L^{iPr} analogues revealed that the complexes containing the L^{iPr} ligand had lower volatility.[41b] The higher volatility was determined to be a result of the lone pair/lone pair repulsions from the dimethylamido groups, analogous to the phenomena observed in fluorinated complexes.[41b]

1.3.4 Group 2 CVD Precursors Containing Various Ligands

Although the β-diketonate complexes have been the most widely used, there has also been the development of other group 2 complexes for potential CVD applications. Group 2 complexes containing alkoxide-based ligands ($M(OR)_2$) are usually non-volatile and suffer from low thermal stability, which is related to the small steric profile of the ligands.[42] The use of bulkier alkoxides (OR, R = CEt_3, CMeEtiPr, CMe_3, $CH(CMe_3)_2$, $C(CF_3)_3$, and $CH(CF_3)_2$) afforded several calcium, strontium, and barium complexes with sufficient volatility.[42c] The decomposition temperatures of these complexes ranged from 260-350 °C, with a decomposition temperature of 350 °C for $Ba(OCEt_3)_2$.[42c] There are no structural data reported for these complexes and most likely they exist as oligomeric complexes since volatilization of the strontium and barium complexes did not occur until high temperatures (>

230 °C).[42c] Another approach is the use of chelating alkoxide-based ligands which can attach to the metal center and sufficiently saturate the coordination sphere of the metal and possibly lead to volatile complexes. Chisholm and coworkers synthesized $H_4Ba_6(\mu_6\text{-}O)(OCH_2CH_2OCH_3)_{14}$ by treating barium granules with 2-methoxyethanol in toluene followed by sublimation of the crude at 160°C/10^{-1} Torr.[42a] The bulkier alkoxide-based ligands, $[OC(OiPr)_2tBu]^-$ and $[OC(OEt)_2tBu]^-$, coordinated to the metal center in a κ^3-fashion through the oxygen atoms.[42d] The group 2 metal alkoxides were synthesized by the treatment of $M[N(SiMe_3)_2]_2$ with $HOC(OiPr)_2tBu$ in hexane to afford the appropriate calcium, strontium, and barium complexes (eq 1).[42d] Alternatively, $Ba[OC(OEt)_2tBu]_2$ can be synthesized by transmetalation of BaI_2 with the potassium salt, $K[OCtBu(CH_2OEt)_2]$ (eq 2).[42d] All of these complexes sublimed between 150 and 185 °C at 10^{-2} mbar and did not leave any significant residue.[42d] Employment of the higher denticity alkoxide ligand, amak (amak = $OC(CF_3)_2CH_2N(CH_2CH_2OMe)_2$), afforded monomeric complexes of strontium and barium that underwent sublimation at 150 °C/0.2 Torr overnight with no appreciable decomposition (Chart 6).[42e] TGA on these samples under oxygen indicated that decomposition started to occur at 220 °C with the final residue at 500 °C being mainly composed of polycrystalline metal fluoride.[42e]

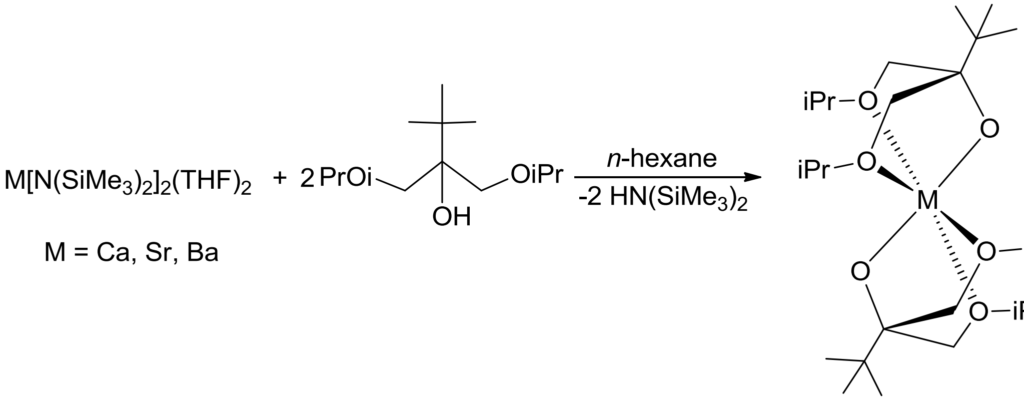

(1)

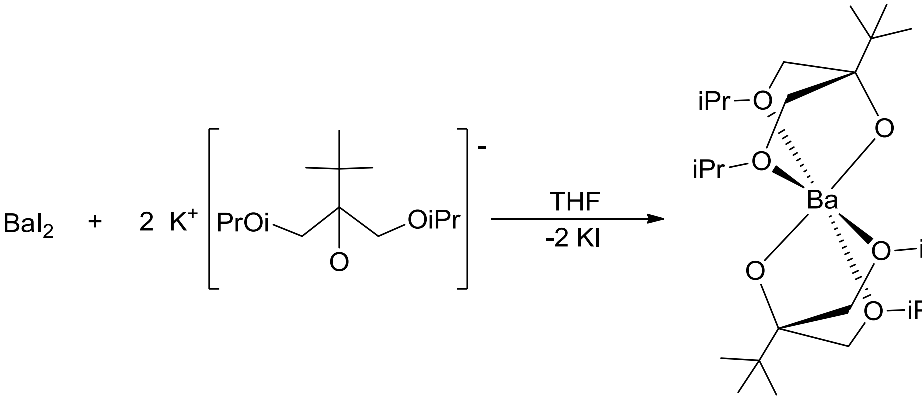

(2)

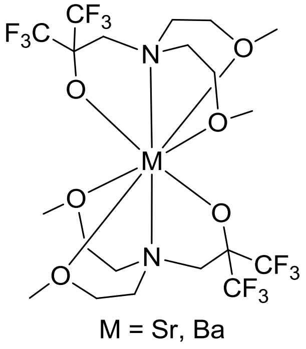

Chart 6. M(amak)$_2$ complexes.

Ligands such as pyrazolates,[43] thioacetates,[44] pyrrolates,[45] and tris(pyrazolyl)borates[46] (Tp^{R2}) have been used in attempts at the synthesis of group 2 complexes suitable for use in CVD. Calcium, strontium, and barium pyrazolates exist as oligomers in the solid state and decompose before volatilization.[43] Our group previously synthesized monomeric strontium and barium complexes containing 3,5-di-*tert*-butylpyrazolate ligands with various glymes added to saturate the coordination sphere of the metal ion.[43b,c] However, during preparative sublimation experiments the neutral ligands would dissociate, followed by the formation of metal pyrazolate oligomers.[43b,c] Hampden-Smith and coworkers[44] developed a series of group 2 metal thioacetates (M(SOCME)$_2$, M = Ca, Sr) containing various polydentate neutral donors for application as single-source precursors for the deposition of metal sulfide thin films.[44] Precursor self-decomposition to the metal sulfide began at 300 °C and due to the lack of volatility, the precursors could only be employed in aerosol-assisted CVD.[44] Bis[(2-dimethylaminomethyl)pyrrolyl]calcium complexes that contain neutral nitrogen donor ligands (trimethylethylenediamine (trien), pyridine) show one step sublimation weight loss between 70-140 °C and final residues of ~23 % in the TGA trace, and thus could find potential use as CVD precursors.[45] Malandrino and coworkers demonstrated the CVD film growth of $Mg_2B_2O_5$ and BaB_2O_4 using $MgTp_2$ and "$BaTp_2$", respectively, with O_2 as the oxygen source at temperatures between 700-900 °C.[46]

1.4 Group 2 ALD Precursors

As previously mentioned above, ALD precursors need to have exceptional volatility and thermal stability. Unfortunately, the majority of group 2 CVD precursors do not possess the required thermal stability to function as useful ALD precursors. The only group 2 CVD precursors that have been widely employed in ALD film growth contain thd ligands. However, their volatility is quite low (> 200 °C at reduced pressures)[23] with low reactivity.[48,49] Cyclopentadienyl precursors of calcium, strontium, and barium are much more reactive toward water and are the only other class of group 2 precursors for which ALD growth studies have been reported.

1.4.1 ALD Film Growth using Group 2 thd-Based Precursors

Group 2 ALD precursors containing thd ligands have been almost exclusively $[Ca(thd)_2]_3$, $[Sr(thd)_2]_3$, and $[Ba(thd)_2]_4$, presumably because neutral ligand loss during vapor transport could result in inclusion of unwanted impurities in the thin film. The one exception involved the ALD film growth of CaS using the monomeric complex $[Ca(thd)_2(tetraen)]$ (tetraen = tetraethylenepentamine) and H_2S.[50] Surprisingly, the complex sublimed intact at a temperature of 95 °C/0.06 Torr[50] compared to ~200 °C/0.06 Torr for $[Ca(thd)_2]_3$.[23] TGA experiments and isothermal mass-change determinations indicate that at higher temperatures (> 200°C) partial decomposition of the precursor occurs, most likely related to amine loss.[50] Calcium, barium, and strontium sulfides have been previously deposited by ALD using the corresponding thd complexes and H_2S.[12] Optimized film growth conditions for the deposition of CaS resulted in an observed ALD window from 325-400 °C.[12c] One issue with $[Sr(thd)_2]_3$ and $[Ba(thd)_2]_4$ is that they readily absorb impurities or solvent molecules which can affect the evaporation behavior, thereby causing irreproducibility problems in between ALD runs. Soininen and Ritala developed a method to synthesize the strontium and barium thd compounds in situ during the ALD growth of the relevant metal sulfide by vaporizing the Hthd and leading the vapor over the solid strontium or barium source, which was either Sr, $Sr(OH)_2$, SrO, $SrCO_3$, or $Ba(OH)_2$.[12e,f] In all cases, the precursors saturated the surface to afford high quality polycrystalline SrS and BaS thin films.[12e,f] The ALD growth of SrF_2 and CaF_2 was done using $[Ca(thd)_2]_2$ and $[Sr(thd)_2]_2$ as respective metal sources and the fluoride source was obtained by in situ production of HF from the thermal decomposition of ammonium fluoride.[10a] Uniform films were obtained for CaF_2 from 320 to 400 °C with a constant growth rate, whereas the growth rate for SrF_2 decreased with an increase in temperature.[10a] HF is an aggressive chemical that can etch silicates and therefore is not desirable for ALD. Accordingly, Leskelä and coworkers[10b,c] demonstrated the ALD growth of CaF_2 using $[Ca(thd)_2]_3$ as the calcium source and TiF_4 as the fluorine source. The authors suggest that the reaction occurring during the ALD growth involves transmetalation between "$Ca(thd)_2$" and TiF_4 to afford CaF_2 and $Ti(thd)_4$.[10b] The observed growth rate within the ALD window (300-350 °C) was four times higher than that obtained in the HF-based process.[10b]

$$2Ca(thd)_2\,(g) + TiF_4\,(g) \longrightarrow 2CaF_2\,(s) + Ti(thd)_4\,(g) \qquad (3)$$

The most common material deposited by ALD using $[Sr(thd)_2]_3$ as the strontium source is $SrTiO_3$ because of its favorable dielectric properties.[48] A major drawback of the group 2 thd complexes is their low reactivity towards common oxygen source reagents such as O_2, water, and hydrogen peroxide.[48] Attempted ALD depositions of $SrTiO_3$ with $Sr[(thd)_3]_3/O_3$ cycles and subsequent $Ti(OiPr)_4/H_2O$ cycles afforded thin films containing significant amounts of $SrCO_3$.[51] Post annealing treatments of amorphous Sr-Ti-O-CO_3 films at 650-900 °C resulted in single crystalline $SrTiO_3$ (tausonite), along with reduction in carbonate content.[51] Similar results were obtained when $[Ca(thd)_2]_3$ and O_3 were used in the attempted preparation of CaO by ALD.[52] Instead, the formation of $CaCO_3$ occurred and only could be converted to CaO by annealing under O_2 at 670 °C.[52] Formation of carbonate occurs from the O_3 reacting with the $[Ca(thd)_2]_3$ at the substrate surface, which forms an atmosphere of H_2O and CO_2. The CO_2 then chemisorbs onto the metal oxide affording thin films rich in carbonate.[51] To avoid the formation of carbonates, plasma activated O_2 was used as the oxygen source.[48b] X-ray photoelectron spectroscopy (XPS) depth profiling experiments on films deposited at 250 °C indicated that the carbon concentration was near the detection limit, and thus virtually free of carbonate.[48b] Kwon and coworkers demonstrated the ALD growth of $SrTiO_3$ using $[Sr(thd)_2]_3$, $Ti(OiPr)_4$, and plasma activated water.[48d] At deposition temperatures of 250 °C and strontium source temperatures of < 200 °C, the depositions proceeded by ALD growth and stoichiometric $SrTiO_3$ amorphous thin films were obtained.[48d] $Ti(OiPr)_4$ has a low decomposition temperature of ~280 °C and thus only permits ALD growth up to 270 °C.[48e] Depositions done at 370 °C with the use of a crystalline $SrTiO_3$ seed layer led to the ALD growth of crystalline $SrTiO_3$.[49] $SrTiO_3$ displays the best dielectric properties in the crystalline phase, and post annealing treatments can result in thin films with low densities and micro-cracks, thus it is advantageous to obtain crystalline $SrTiO_3$ thin films during depositions.[49] Other examples of employing group 2 thd-based complexes for the ALD of multilayer films include the deposition of $La_{1-x}Ca_xMnO_3$[53] and $La_{1-x}Sr_xFeO_3$.[54]

1.4.2 ALD Film Growth using Group 2 Cyclopentadienyl-Based Precursors

The chemistry of group 2 metallocenes has been extensively developed,[55] however, only group 2 complexes containing bulky metallocenes have found practical use in ALD (Chart 7). There has only been a few ALD studies using $[Ba(C_5Me_5)_2]_n$ and its THF adduct (Chart 7a), which included the deposition of BaS and $BaTiO_3$.[56,57] In the deposition of $BaTiO_3$ using $[Ba(C_5Me_5)_2]_n$, $Ti(OiPr)_4$, and water, the deposition temperature had to be kept at 275 °C due to the thermal decomposition of the barium source.[56a] $[Ba(C_5Me_5)_2]_n$ is polymeric in the solid state, which is likely why the compound has poor thermal stability.[55] When $Ba(C_5Me_5)_2(THF)_n$ and H_2S were used in the ALD growth of BaS, self-limited film growth was observed from 240-300 °C.[56b] The ALD growth up to higher temperatures in the deposition of BaS versus the deposition of $BaTiO_3$ is probably not related to the additional THF ligand, since upon volatilization the THF ligand is lost.[57] Neutral ligands such as THF, diethylamine, triethylamine, diglyme, and triglyme have been previously used to obtain monomeric $Ba(C_5Me_5)_2$ complexes, however, these complexes decomposed as indicated by high residues in the TGA traces (35-50%) and low recoveries in preparative sublimations (32-63 %).[57] $Sr(C_5Me_5)_2(THF)$ has only been used for the ALD growth of SrS thin films (Chart 7a), and an ALD window was observed from 280 to 350 °C.[56b] Using $Sr(C_5H_2iPr_3)_2(THF)$ as the strontium source showed a wider ALD window at temperatures between 260 and 400 °C (Chart 7b).[56b] The increase in the temperature range and of the upper limit of the ALD window suggests that the bulkier 1,3,5-triisopropylcyclopentadienyl ligand is able to confer higher thermal stability to the strontium metal ion than the pentamethyl analogue. In the ALD growth of calcium oxide using water as the oxygen source, plots of calcium precursor pulse length versus growth rate at various temperatures showed that the surface never saturated as a result of precursor self-decomposition.[52] Strontium and barium complexes containing the 1,2,4-tri-*tert*-butylcyclopentadienyl ligands have the highest thermal stability out of all the other group 2 cyclopentadienyl-based complexes (Chart 7c).[57,58] TGA under an N_2 atmosphere showed that $Sr(C_5H_2tBu_3)_2$ and $Ba(C_5H_2tBu_3)_2$ evaporated in a single step with low residues (< 10 %) within the same temperature range.[57,58] Sublimations of $Sr(C_5H_2tBu_3)_2$ and $Ba(C_5H_2tBu_3)_2$ under reduced pressure took place at temperatures as low as 120 and 160 °C, respectively, with recoveries of > 90 %.[57,58] In preliminary deposition experiments, the ALD growth of $BaTiO_3$ was carried out using $Ba(C_5H_2tBu_3)_2$, $Ti(OiPr)_4$, and water. Self-limited film growth was observed up to 350 °C, which is the highest temperature for ALD growth out of all the other barium cyclopentadienyl complexes.[57,58]

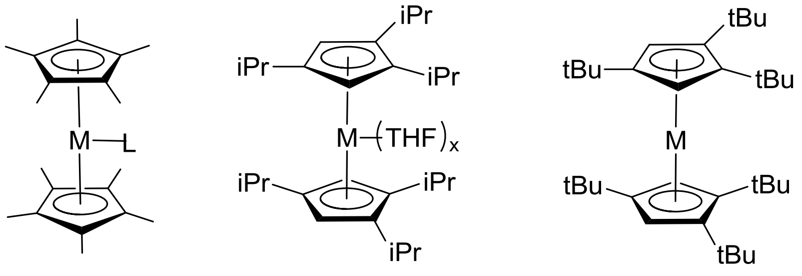

M = Sr, Ba
L = (THF)$_n$ dien, trien,
diglyme, triglyme
(a)

M = Ca, x = 0
M = Sr, x = ~1.4
M = Ba, x = 2
(b)

M = Sr,Ba
(c)

Chart 7. Selected Group 2 cyclopentadienyl-based ALD Precursors

1.5 Group 2 Poly(pyrazolyl)borate Complexes

The major problem of group 2 ALD precursors is their lack of thermal stability. Neutral ligands tend to dissociate at volatilization temperatures and most anionic ligands are not sterically demanding enough to saturate the coordination sphere of the group 2 ion. Polypyrazolylborate ligands, also referred to as scorpionates, could be useful in the synthesis of volatile and thermally stable group 2 ALD precursors. Polypyrazolylborate ligands have been known for over 32 years, with more than 170 different polypyrazolylborate ligands available and over 1400 publications related to this ligand.[59] The two main classes of polypyrazolylborate ligands are the tris(pyrazolyl)borates (Tp^{R2}) and the bis(pyrazolyl)borates (Bp^{R2}), shown in Chart 8.[59] Tp^{R2}-based ligands are frequently compared to cyclopentadienide ions because they are both monoanionic, occupy three coordination sites (κ^3-N,N,N), and donate six electrons. The Bp^{R2}-based systems are similar to the β-diketonate system because they both can chelate in a κ^2-fashion, (κ^2-N,N for Bp^{R2}; κ^2-O,O for β-diketonate).[59] However, unlike the β-diketonate ligand, an additional third coordination site is available through the electron rich boron-hydrogen bond and therefore Bp^{R2} ligands are better suited to saturate the coordination sphere of the metal ion.[59] In Bp^{R2} and Tp^{R2}-based ligands, additional stability can be obtained through introduction of alkyl substituents in the 3- and 5-positions of the pyrazolyl rings.[59] The most common way to transfer these ligands to metals is to prepare the potassium salts of the ligands and then transfer them to other metals by salt metathesis reactions.[59] The potassium salts can easily be synthesized by preparing a melt of free pyrazole and potassium borohydride at high temperatures (eq. 3 and 4).[59] After the appropriate amount of hydrogen gas has evolved, a typical workup procedure would include precipitation of the white solid from common nonpolar solvents such as toluene or hexane.[59] Once pure potassium salts are obtained, treatment of metal halides with the potassium Tp^{R2} or Bp^{R2}-based salts usually afford metal poly(pyrazolyl)borate complexes.

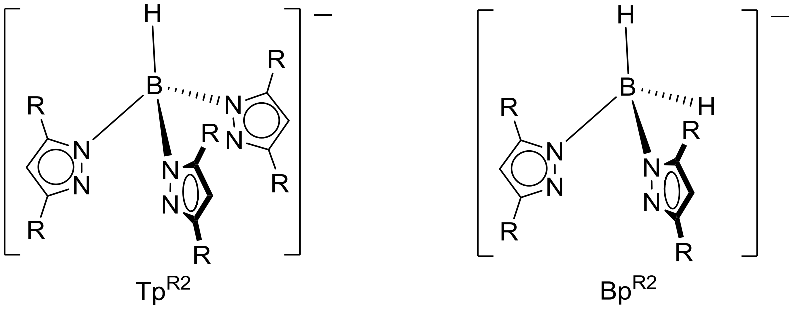

Chart 8. Tris and bis(pyrazolyl)borate-based ligand systems.

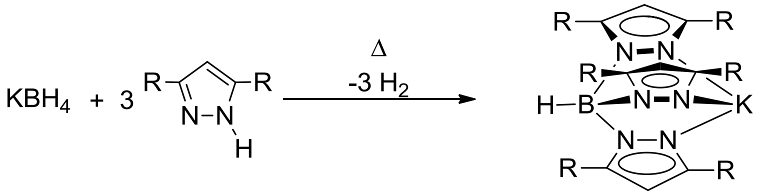

(4)

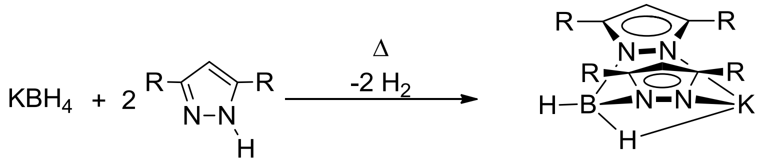

(5)

1.6 Thesis Problem

As previously mentioned, there are many important materials which contain group 2 ions and often it is desirable to have them as thin films.[1] CVD and ALD are two vapor phase film deposition methods which afford conformal thin films.[21,22] Unfortunately, there are problems with existing group 2 ALD and CVD precursors which can be related to the high size-to-charge ratios of the metal ions. The two major classes of useful group 2 CVD and ALD precursors are the β-diketonate and cyclopentadienyl-based complexes. Group 2 precursors containing thd ligands have low volatility and are not reactive for use in the ALD of metal oxides using common oxygen sources.[48] The use of fluorinated thd ligands to form volatile group 2 complexes may incorporate fluorine, which can be detrimental to the films properties.[32-36] Group 2 complexes containing bulky cyclopendienyl ligands have had the most success in ALD, however, they are air sensitive and may be pyrophoric in some instances.[50-58] The need for thermally stable and volatile precursors for ALD is apparent. An increase in thermal stability relative to existing ALD precursors can decrease impurity content and also lead to the deposition of crystalline material.

This thesis focuses on the synthetic development of group 2 precursors containing poly(pyrazolyl)borate ligands for use in ALD or CVD. The goal is to synthesize and structurally characterize $\mathrm{Tp}^{\mathrm{R2}}$ and $\mathrm{Bp}^{\mathrm{R2}}$-based group 2 complexes that have various alkyl substituents in the 3- and 5- positions of the pyrazolyl moieties. The thermal stability and volatility of the complexes will be assessed by TGA, solid state decomposition determinations, and preparative sublimations. ALD growth studies of calcium, strontium, and barium will be performed using optimum precursors and studied by varying film growth parameters. The composition and surface morphology of the films will be assessed using XPS, X-ray diffraction (XRD), elastic recoil detection analysis (ERDA), atomic force microscopy (AFM) and scanning electron microscopy (SEM).

CHAPTER 2

Volatility, High Thermal Stability, and Low Melting Points In Heavier Alkaline Earth Metal Complexes

2.1 Introduction

As described in Chapter 1, group 2 complexes containing thd-[48,49] and cyclopentaldienyl-based[50-58] ligands are the only compounds that are thermally stable and volatile enough for ALD. Our group has recently reported the ALD growth of Ta_2O_5 films from $Ta(NtBu)(tBu_2pz)_3$ (tBu_2pz = 3,5-di-*tert*-butylpyrazolate) and ozone.[60] Significantly, an ALD window was observed between 300 and 450 °C, implying that $Ta(NtBu)(tBu_2pz)_3$ is stable in this temperature range. The only possible source of this exceptional thermal stability was the tBu_2pz ligands. The use of pyrazolate ligands to prepare thermally stable group 2 complexes may lead to useful ALD film growth. The complexes $Ca_3(tBu_2pz)_6$, $Sr_4(tBu_2pz)_8$, and $Ba_6(tBu_2pz)_{12}$ have been reported, but have very low vapor pressures due to their oligomeric structures.[43e] Monomeric group 2 bis(pyrazolate) complexes containing neutral donor ligands decompose extensively upon heating, and do not possess sufficient thermal stability for use in ALD due to neutral ligand loss.[43a-d] Tris(pyrazolyl)borate-based ligand systems are stericially demanding enough to afford monomeric complexes. Previously it was shown that calcium, strontium, and barium complexes containing tris(3,5-dimethylpyrazolyl)borate (Tp^{Me2}) ligands form volatile complexes (sublime ~200 °C/10^{-3} Torr), however, investigation into their thermal stability and volatility was minimal.[61a-d] Recently, the deposition of β-BaB_2O_4 thin films by CVD was reported using barium tris(pyrazolyl)borate (“$BaTp_2$”) as the source compound, and thermogravimetric analyses suggested that “$BaTp_2$” exhibits good thermal stability.[46a]

In this chapter, the synthesis, structure, and properties of a series of homoleptic calcium, strontium, and barium complexes containing various substituted tris(pyrazolyl)borate ligands is described. With the exception of $[BaTp_2]_2$, the compounds documented herein exhibit good volatility and exceptional thermal stability, and many melt at temperatures below those required for vapor transport. These new complexes thus represent a breakthrough in precursor design for CVD and especially ALD growth of thin films containing the heavier group 2 elements.

2.2 Results and Discussion

Synthetic Aspects. The complexes $SrTp_2$ (**1**),[62] “$BaTp_2$” ($[BaTp_2]_2$), (**2**),[62] $SrTp^{Me2}{}_2$ (**3**),[61d] and $BaTp^{Me2}{}_2$ (**4**)[61d] were prepared according to literature procedures. Access to analogs containing other 3,5-dialkyl-substituted Tp ligands required synthesis of the corresponding potassium salts, which have not been previously reported. These salts were prepared by heating a solid mixture of potassium borohydride with a slight excess of either 3,5-diethylpyrazole or 3,5-di-n-propylpyrazole at temperatures between 180-190 °C, followed by precipitation with hexane, to afford white powders of potassium tris(3,5-diethylpyrazolyl)borate (KTp^{Et2}, 61%) and potassium tris(3,5-di-n-propylpyrazolyl)borate (KTp^{nPr2}, 31%) after workup (eq 6). KTp^{Et2} and KTp^{nPr2} are very soluble in tetrahydrofuran and toluene. KTp^{nPr2} is also slightly soluble in hexane, which led to the low isolated yield. The compositions were verified by spectroscopic and analytical methods. Characteristic bands for the boron-hydrogen stretch at 2444 cm^{-1} and for the carbon-nitrogen stretch at 1533

cm^{-1} were found in the infrared spectra of both compounds. The ^1H NMR spectra for KTp^{Et2} showed a resonance for the 4-hydrogen atom of the pyrazolyl group at δ 5.82, as well as resonances belonging to two magnetically inequivalent ethyl groups. Similarly, the ^1H NMR spectra for KTp^{nPr2} contained a resonance at δ 5.77 belonging to the 4-hydrogen atom of the pyrazolyl group, and resonances corresponding to two magnetically inequivalent n-propyl groups.

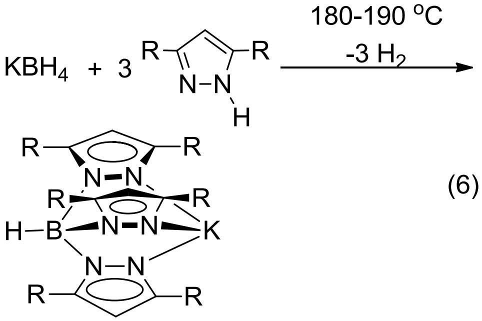

KTp^{Et2}, R = Et, 61%
KTp^{nPr2}, R = nPr, 31%

(6)

Treatment of MI_2 (M = Ca, Sr) or $BaI_2(THF)_3$ with two equivalents of KTp^{Et2} or KTp^{nPr2} yielded **5-10** in good to moderate yields (eq 7). Complexes **5-7** are soluble in hexane, from which colorless crystals suitable for X-ray crystallography were grown at -23 °C. Complexes **8-10** are very soluble in hexane and increase in solubility in going from the calcium derivative **8** to the barium complex **10**. Complexes **8** and **9** exist as colorless crystalline solids, whereas **10** is a colorless, greasy solid. Samples of **1-10** for microanalyses were obtained by preparative sublimations at 0.05 Torr.

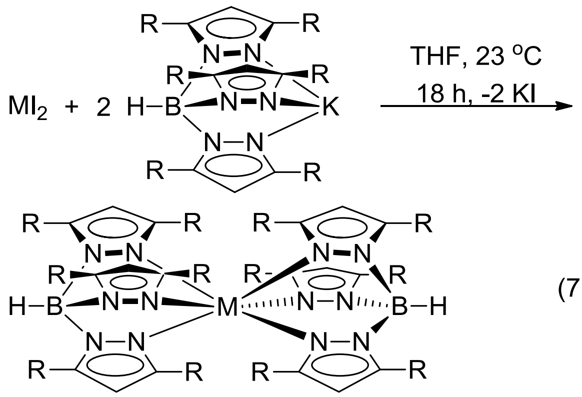

(7)

5, M = Ca, R = Et, 64%
6, M = Sr, R = Et, 64%
7, M = Ba, R = Et, 67%
8, M = Ca, R = nPr, 51%
9, M = Sr, R = nPr, 75%
10, M = Ba, R = nPr, 39%

The compositions of **1**, **2**, and **5**-**10** were assessed by ^{1}H NMR and ^{13}C{^{1}H} NMR spectroscopy, infrared spectroscopy, and C, H, N microanalyses. As detailed below, **1** and **5**-**10** exist as six-coordinate mononuclear complexes containing two tridentate tris(pyrazolyl)borate ligands, whereas **2** exists as an eight-coordinate dinuclear complex composed of two terminal and two bridging Tp ligands. Complexes **1** and **2** were originally reported by Trofimenko,[62] but X-ray crystallographic analyses have not been previously reported for either complex. Malandrino suggested that **2** possessed a monomeric structure, based upon observation of monomeric molecular ion in the fast atom bombardment mass spectrum and lack of higher mass peaks.[46a] The present work clearly demonstrates a dimeric solid state structure for **2**. Malandrino also reported a melting point of 300 °C for **2** from differential scanning calorimetry.[46a] In the present work, multiple determinations on sublimed samples of **2** revealed a consistent melting point of 250-252 °C. Complexes **1** and **2** both have a boron-hydrogen infrared stretching frequency of 2529 cm^{-1}. The boron-hydrogen infrared stretches in **5-7** and **8-10** fall in the range of 2526-2532 cm^{-1} and 2470-2517 cm^{-1}, respectively, with no notable trend upon increasing ionic size from calcium, strontium, to barium. The ^{1}H NMR and ^{13}C{^{1}H} NMR spectra of **1** and **2** at 23 °C are similar to each other, with resonances belonging to three different protons and carbon atoms from the pyrazolyl rings. The ^{1}H NMR and ^{13}C{^{1}H} NMR spectra for **5-7** and **8-10** are similar to the spectra for KTp^{Et2} and KTp^{nPr2}, respectively. In the ^{1}H NMR spectra of **1-10**, the boron-bound hydrogen atoms resonated as a very broad singlet between δ 4.7 and 5.0.

To gain insight into the solution structure of **2**, ^{1}H NMR spectra were recorded in toluene-d_8 at room temperature and -80 °C. The ^{1}H NMR spectrum at room temperature showed a triplet at δ 5.97, corresponding to the hydrogen atom at the 4-position of the pyrazolyl groups, and two doublets at δ 7.57 and 7.03 belonging to the hydrogen atoms at the 3- and 5-positions of the pyrazolyl groups. The ^{1}H NMR spectrum at -80 °C had a total of six equal intensity resonances corresponding to two inequivalent Tp ligands (δ 7.76, 7.40, 7.29, 6.61, 6.07, 5.81). These resonances are consistent with the terminal and bridging Tp ligands in the dimeric structure of **2** (see below) and further suggest that the bridging pyrazolyl groups are undergoing site exchange rapidly at -80 °C.

Volatility and Thermodynamic Stability Study. Compounds **1-10** were studied by melting point and decomposition determinations, preparative sublimations, and thermogravimetric analysis (TGA) to assess their initial suitability as ALD and CVD precursors. The data for **1-10** are summarized in Table 1. Careful decomposition temperatures were determined using a melting point apparatus with sealed capillary tubes containing a few milligrams of **1-10**, as described in the experimental section. The calcium complexes **5** and **8** do not decompose below 400 °C. Strontium complexes **1** and **3**

decompose at 363 and 380 °C, respectively, whereas the higher alkyl-substituted derivatives **6** and **9** show no evidence for decomposition up to 400 °C. The barium complexes **2**, **4**, **7**, and **10** decompose between 330 and 380 °C, and the thermal stability increases with increasing size of the groups at the 3- and 5-positions of the tris(pyrazolyl)borate ligands. The decomposition temperature of **2** (330 °C) was the lowest among **1-10**, probably due to its dimeric structure. Purified solids of **1-10** were carefully sublimed at 0.05 Torr on a preparative scale (0.5-1.0 g), as described in the experimental section, to assess volatility and thermal stability during vapor transport. Complex **1** is the most volatile among **1-10** and sublimes at 200 °C with a sublimed recovery of 99.3% and a residue of 0.1%. Complexes **3** and **8-10** are the least volatile of the series, with sublimation temperatures of 240 °C. Significantly, **8-10** melt before sublimation (mp **8** = 169-172 °C, mp **9** = 164-168 °C, mp **10** = 141-144 °C), and are therefore sublime from liquids. Complexes **4** and **5-7** sublime between 210 and 220 °C, and **6** and **7** volatilize as liquids (mp **6** = 188-190 °C, mp **7** = 129-131 °C). The sublimed recoveries for **5-9** are ≥99.0%, with corresponding nonvolatile residues of <1%. Complexes **4** and **10** have sublimed recoveries of 91.4 and 97.7%, with nonvolatile residues of 0.4 and 2.1%, respectively. Complexes **2** and **3** have low sublimed recoveries of 78.4 and 85.5%, with nonvolatile residues of 17.3 and 7.3%, respectively.

Table 1. Preparative sublimation data and decomposition temperatures for **1-10**. All sublimations were carried out on a 0.5-1.0 g scale, and were complete within 3-5 hours.

Compound	Sublimation Temperature (°C/0.05 Torr)	% Recovery	% Residue	Decomposition Temperature (°C)
1	200	99.3	0.1	~363
2	220	78.4	17.3	~330
3	240	85.5	7.3	~380
4	220	91.4	0.4	~350
5	210	99.3	0.2	>400
6	210	99.0	0.1	>400
7	215	99.0	0.8	~380
8	240	99.3	0.2	>400
9	240	99.1	0.6	>400
10	240	97.7	2.1	~380

The TGA traces for **1-4** are shown in Figure 6. Complexes **1** and **2** show a single sublimation step from 248-354 °C and 301-420 °C with residues of 9.5 and 46.5%, respectively. The TGA traces for **3** and **4** exhibit a single sublimation step from 325-409 °C and 287-394 °C, respectively, and both show residues of 3.6%. Figure 7 contains the TGA traces for **5-10**. Weight loss for **5** occurs between 277-387 °C, with a residue of 0.1%. The TGA traces for **6** and **7** are similar and reveal a single sublimation step from 299-398 °C, with residues of 2.4 and 1.1%, respectively. Complexes **8-10** have very similar TGA traces composed of single sublimation steps from 298-420 °C, with residues of 2.2, 1.5, and 5.5%, respectively.

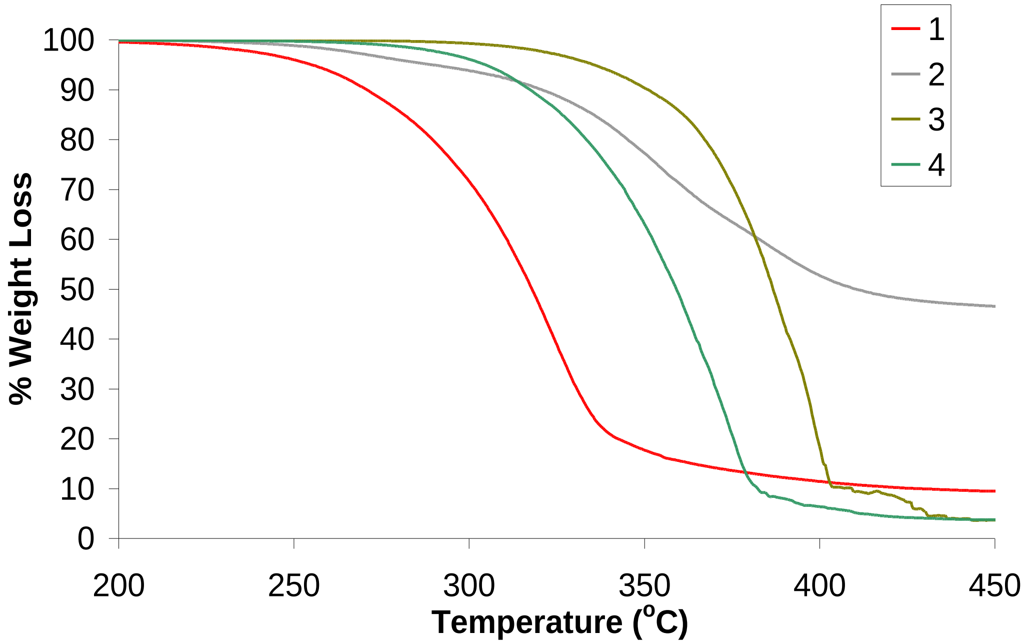

Figure 6. TGA traces for **1-4** from 200 to 450 °C at 10 °C/min.

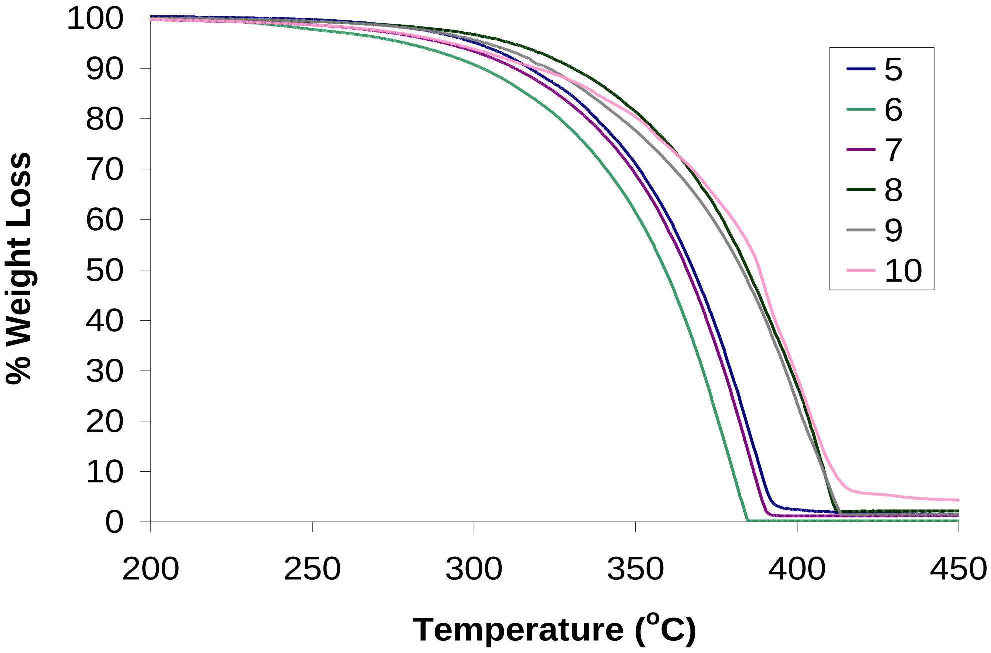

Figure 7. TGA traces for **5-10** from 200 to 450 °C at 10 °C/min.

This work documents the combination of exceptional thermal stability and reasonable volatility in **1-10**. The barium precursors **7** and **10** decompose in the solid state at about 375 °C, whereas the calcium and strontium complexes **5**, **6**, **8**, and **9** decompose at >400 °C. The high thermal stability of **5-10** is further supported by the excellent recoveries in the preparative sublimation studies and low residues observed in the TGA traces. The higher thermal stability of **5-10**, compared to analogs **1-4**, is probably related to kinetic protection of the electron-rich B-H moieties and metal centers by the ethyl and n-propyl groups. A pervasive problem in the CVD growth of films containing the heavier group 2 elements is premature or concurrent precursor thermal decomposition during vapor transport.[1] The exceptional thermal stability of **5-10**, as described herein, eliminates the issue of solid state decomposition during vapor transport. In addition, ALD growth requires that a precursor be thermally stable at the film growth temperature, to avoid loss of the self-limited growth mechanism and emergence of CVD-like growth.[22] Previous work in our lab suggested that the upper temperature range of self-limited growth corresponds closely to the solid state decomposition temperatures of several metalorganic ALD precursors.[63] As such, use of **7** and **10** in ALD growth may allow self-limited ALD growth up to about 375 °C, and to >400 °C for **5**, **6**, **8**, and **9**. To our knowledge, **5-10** are the most stable thermally stable heavier group 2 metalorganic precursors available to date. Among **1-10**, **5-7** sublime with <1% nonvolatile residues between 210-215 °C/0.05 Torr and have the highest thermal stabilities for each metal. In addition, **6-8** melt prior to vaporization, and thus undergo vapor transport from liquids. Precursors that undergo vapor transport from liquids are highly desirable, since they avoid particles from solid precursors and facilitate steady vapor transport due to the relatively constant surface area of a liquid, compared to irregular vapor transport from solid precursors with changing surface areas. As such, **6-8** have the best film growth precursor properties in the series. In addition, **6-8** are solids at ambient temperature and are air and water stable, which allows convenient laboratory manipulation.

Malandrino has reported the use of "$BaTp_2$" (**2**) as a CVD precursor for the growth of BaB_2O_4 films, and also showed that this compound exhibited a single weight loss event in the TGA trace with a nonvolatile residue of 9% at 340 °C.[46a] As documented herein, **2** possesses the poorest precursor properties among **1-10**: it sublimes slowly at 220 °C/0.05 Torr, leaves a 17.3% nonvolatile residue after sublimation, decomposes at about 330 °C in the solid state, and afforded a 45.6% nonvolatile residue in the TGA trace after heating to 450 °C. The poor precursor characteristics of **2** are clearly related to its dimeric solid state structure.

Structural Aspects. The X-ray crystal structures of **1**, **2**, and **5-7** were determined to establish the geometries about the metal centers and the bonding modes of the Tp and Tp^{Et2} ligands. Experimental crystallographic data are summarized in Table 2, selected bond lengths and angles are given in Tables 3-6, and perspective views are presented in Figures 8-12. The X-ray crystal structures of **3** and **4** have been previously reported.[61a-d] A low precision X-ray crystal structure determination of **9** revealed a monomeric formulation with a molecular structure similar to that of **6**. Single crystals of **8** and **10** with sufficient quality for X-ray crystal structure determinations could not be grown, despite many attempts. The molecular structures of **8** and **10** are presumably comparable to those of **5**, **7**, and **9**.

The molecular structures of **1**, **5**, and **6** are similar and their perspective views are shown in Figures 8, 10, and 11. The unit cell of **1** contains two crystallographically independent molecules that exhibit identical metrical parameters within experimental uncertainty. As such, only data for the molecule containing Sr(1) will be discussed herein. Molecules of **1**, **5**, and **6** exist as mononuclear complexes with two Tp or $\mathrm{Tp^{Et2}}$ ligands coordinated to the metal center in a tridentate fashion through the nitrogen atoms. The three pyrazolyl moieties on the two Tp and $\mathrm{Tp^{Et2}}$ ligands are arrayed in a staggered conformation, affording distorted octahedral geometry. The average strontium-nitrogen bond lengths for **1** and **6** are 2.593(15) and 2.606(9) Å, respectively, which are within experimental error of each other as well as with the strontium-nitrogen bond lengths in **3** (avg = 2.597(6) Å).[61b] The average calcium-nitrogen bond length in **5** is 2.459(6) Å and is similar to those of $\mathrm{CaTp_2}$ (avg = 2.44(2) Å)[61e] and $\mathrm{CaTp^{Me2}{}_2}$ (2.454(2) Å).[61b] The boron-metal-boron' bond angles are 180° for **1**, **5**, and **6**.

A perspective view of **7** is shown in Figure 12. Overall, the structure of **7** is similar to those of **5** and **6** in that it has two $\mathrm{Tp^{Et2}}$ ligands with distorted octahedral geometry. The barium-nitrogen bond distances in **7** range between 2.751(2) and 2.816(2) Å (avg = 2.78(2) Å), which are similar to the values previously reported for **4** (avg = 2.760(1),[61a] 2.754(3) Å[61d]). Unlike **1**, **5**, and **6**, the boron-barium-boron' angle in **7** is bent (165.1(1)°). Interestingly, the boron-nitrogen-nitrogen and nitrogen-boron-nitrogen bond angles are virtually identical for **5-7**, even though the ionic size of the metal increases through the series and **7** additionally adopts a bent conformation.

A perspective view of **2** is shown in Figure 9. The molecular structure of **2** consists of a dinuclear complex with two $\mathrm{BaTp_2}$ units related by a center of inversion. Each barium ion contains a terminally-bound Tp ligand coordinated in a tridentate fashion. The metal ions are held together by two symmetrical Tp ligands, which involve one pyrazolyl moiety bonding in an η^5-fashion to one barium ion, and the same pyrazolyl ring bonding κ^1 to the other barium ion. The other two pyrazolyl moieties bridge the metal centers, with each one binding in an κ^1-fashion through the lone pairs on the nitrogen atoms. The barium-nitrogen distances in the terminal Tp ligands range from 2.760(4)-2.880(3) Å (avg. = 2.81(5) Å), which are longer than the barium-nitrogen distances in **4** and **7**. This elongation is likely related to a higher coordination number of eight for **2**, versus only six for **4** and **7**. The Ba-N(7) and Ba-N(12)' bond lengths are 2.820(1) Å and 2.821(1) Å, respectively. The Ba-N(9)' bond length is 2.941(1) Å, which is quite long compared to the σ-interactions in the terminal and bridging Tp ligands. The boron-nitrogen-nitrogen and nitrogen-boron-nitrogen bond angles range from 120.71(11)-125.06(17) and 105.0(2)-122.9(3)°, respectively. These large ranges illustrate the flexibility of the Tp ligand. The average carbon-nitrogen, carbon-carbon, and nitrogen-nitrogen bond lengths in the κ^1-pyrazolyl rings are 1.346(5) Å, 1.383(5) Å, and 1.364(5) Å, respectively. These values are consistent with delocalized bonding and compare well with those of **1** (C-N_{avg} = 1.346(10), C-C_{avg} = 1.381(15), N-N = 1.364(9) Å). The bond distances inside the η^5-pyrazolyl ring (N(9)-C(13) = 1.344(2) Å, C(13)-C(14) = 1.400(2) Å, C(14)-C(15) = 1.384(2) Å, C(15)-N(10) = 1.356(2) Å, N(10)-N(9) = 1.369(1) Å) are within experimental error of the values in the κ^1-pyrazolyl moieties in **2** and the pyrazolyl rings in **1**. Therefore, the η^5-pyrazolyl group π-cloud is not significantly perturbed by coordination to the barium ion.

The molecular structure of **2** contains an η^5-pyrazolyl-barium interaction and is the first example of such a bonding mode in a group 2 tris(pyrazolyl)borate complex. Examples of η^5-pyrazolyl interactions with group 1 metal ions have been documented in $\text{KTp}^{\text{CF3,CH3}}$ ($\text{KTp}^{\text{CF3,CH3}}$ = hydrotris(3-trifluoromethyl-5-methylpyrazolyl)borate) and $\text{KLL}_2{}'$ (L = tris[3-(2-methoxy-1,1-dimethylethyl)pyrazolyl]borate, L' = 3-(2-methoxy-1,1-

dimethylethyl)pyrazole).[64,65] Stalke and coworkers[66] reported X-ray crystal structure of $Ba[(Pz^*)_3Ge]_2{\cdot}(dioxane)_{0.5}$ (Pz* = 3,5-dimethylpyrazolyl), in which two of the six Pz* moieties are coordinated to the barium ions in an η^4-fashion. The remaining Pz* ligands bond to the barium ions with conventional σ-bonds through the 2-nitrogen atoms. The Ba-N(9) and Ba-N(10) distances within the η^5-pyrazolyl-barium interaction in **2** are 3.087(1) Å and 3.211(1) Å, respectively, which are longer than the average σ-bonded barium-nitrogen distances in $Ba[(Pz^*)_3Ge]_2{\cdot}(dioxane)_{0.5}$ (2.947 Å). The average barium-carbon contacts in $Ba[(Pz^*)_3Ge]_2{\cdot}(dioxane)_{0.5}$ are 3.334 Å and compare well with the related values in **2** (3.173(1)-3.400(1), avg = 3.318(5) Å). Metallocenes such as $Ba(C_5Me_5)_2$,[67] $Ba(C_5H(C_3H_7)_4)_2$,[68] and $Ba(C_5H_3(SiMe_3)_2)_2$[69] have average barium-carbon bond distances of 2.98(1), 2.94(1), and 3.01(2) Å, respectively, which are shorter than the barium-carbon distances in **2**. These differences reflect the anionic nature of the cyclopentadienyl ligands, the more neutral ligand character of the pyrazolyl groups in **2**, as well as the higher coordination number in **2** compared to the barocenes.

A summary of important structural parameters for **5-7** is shown in Table 7. As the metal ion radius increases, the average cis nitrogen-metal-nitrogen intraligand bond angle decreases and the average nitrogen-metal-nitrogen' interligand bond angle increases. In addition, the average boron-nitrogen-nitrogen and nitrogen-boron-nitrogen angles are the same within experimental uncertainty in **5-7**, which suggests that the cavity size of the Tp^{Et2} ligand does not change even though the size of the metal ion increases. The constant cavity size is attributed to the 5-ethyl groups of the pyrazolyl moieties, which interact sterically with the boron-hydrogen fragment and prevent the boron-nitrogen-nitrogen angle from expanding. Since the metal-nitrogen distances increase while the cavity size remains the same, the average nitrogen-metal-nitrogen intraligand bond angle decreases and the average nitrogen-metal-nitrogen' interligand angle increases. Belderraín and coworkers[61d] made a similar correlation by comparing the nitrogen-metal-nitrogen intraligand bond angle and nitrogen-metal-nitrogen' interligand angle for MTp^{Me2}_2 (M = Mg, Ca, Sr, Ba). It is not surprising that the Tp^{Me2} and Tp^{Et2} ligands have very similar structural parameters with respect to the nitrogen-metal-nitrogen intraligand and nitrogen-metal-nitrogen' interligand angles, since the steric profiles of methyl and ethyl groups are similar. As previously noted, the boron-barium-boron' bond angle in **7** is 165.1(1)°, whereas **5** and **6** have linear boron-metal-boron' angles. The smaller ionic radii of the metal ions in **5** and **6** probably force linear boron-metal-boron' angles due to interligand steric interactions, while the larger ionic radius of the barium ion in **7** allows some bending.

Table 2. Crystal data and data collection parameters for **1**, **2**, and **5-7**.

	1	**2**	**5**	**6**	**7**
Formula	$C_{18}H_{20}B_2N_{12}Sr$	$C_{36}H_{40}B_4Ba_2N_{24}$	$C_{42}H_{68}B_2CaN_{12}$	$C_{42}H_{68}B_2SrN_{12}$	$C_{42}H_{68}B_2BaN_{12}$
FW	513.70	1126.84	802.78	850.32	900.04
space group	P2(1)/c	C2/c	P2(1)/n	P2(1)/n	P2(1)/n
a (Å)	13.4182(4)	19.8850(11)	11.0949(4)	11.3183(2)	17.2512(5)
b (Å)	14.8732(4)	15.9199(11)	12.5709(4)	12.5687(3)	12.9047(4)
c (Å)	11.7611(3)	16.6548(13)	16.6206(6)	16.4972(4)	21.9773(6)
β	94.8380(10)	119.481(4)	106.084(2)	106.2430(10)	111.670(2)
V (Å^3)	2338.82(11)	4589.7(5)	2227.38(13)	2253.15(9)	4546.8(2)
Z	4	4	2	2	4
T (K)	100(2)	100(2)	100(2)	100(2)	100(2)
λ(Å)	0.71073	0.71073	0.71073	0.71073	0.71073
ρ_{calcd} (g, cm^{-3})	1.459	1.631	1.197	1.253	1.315
μ (mm^{-1})	2.338	1.764	0.185	1.240	0.917
R(F)(%)	5.74	2.48	7.67	5.07	3.54
Rw(F)(%)	13.33	5.82	20.24	13.23	8.32

$R(F) = \Sigma||Fo|-|Fc||/ \Sigma|Fo|$, $R_w(F)^2 = [\Sigma w(Fo^2-Fc^2)^2/ \Sigma w(Fo^2)^2]^{1/2}$ for $I > 2\sigma(I)$

Table 3. Selected bond lengths (Å) and angles (deg) for **1**.

Sr(1)-N(1)	2.585(4)	N(1)-Sr(1)-N(5)	78.42(13)
Sr(1)-N(3)	2.610(4)	N(1)-Sr(1)-N(5)’	101.58(13)
Sr(1)-N(5)	2.584(4)	N(3)-Sr(1)-N(3)’	180
N(1)-Sr(1)-N(1)’	180	N(3)-Sr(1)-N(5)	71.23(13)
N(1)-Sr(1)-N(3)	77.16(12)	N(3)-Sr(1)-N(5)’	108.77(13)
N(1)-Sr(1)-N(3)’	102.84(12)	N(5)-Sr(1)-N(5)’	180

Table 4. Selected bond lengths (Å) and angles (deg) for **2**.[a]

Ba(1)-N(1)	2.829(1)	Ba(1)-C(13)	3.173(3)
Ba(1)-N(3)	2.785(1)	Ba(1)-C(14)	3.379(2)
Ba(1)-N(5)	2.880(3)	Ba(1)-C(15)	3.400(1)
Ba(1)-N(5)’	2.760(4)	N(1)-Ba(1)-N(3)	68.42(4)
Ba(1)-N(7)	2.820(1)	N(1)-Ba(1)-N(5)’	70.67(8)
Ba(1)-N(9)	3.087(1)	N(1)-Ba(1)-N(5)	67.40(7)
Ba(1)-N(9)’	2.941(1)	N(3)-Ba(1)-N(5)’	73.10(8)
Ba(1)-N(10)	3.211(1)	N(3)-Ba(1)-N(5)	66.93(7)
Ba(1)-N(12)’	2.821(1)		

[a] The atoms N(5)’, N(6)’, C(7)’, C(8)’, C(9)’, and B(1)’ are part of an alternate set of positions describing a 50/50 disorder. Other primed designations (N(5)’, N(9)’ and N(12)’) reflect symmetry related positions.

Figure 8. Perspective view of **1** with thermal ellipsoids at the 50% probability level.

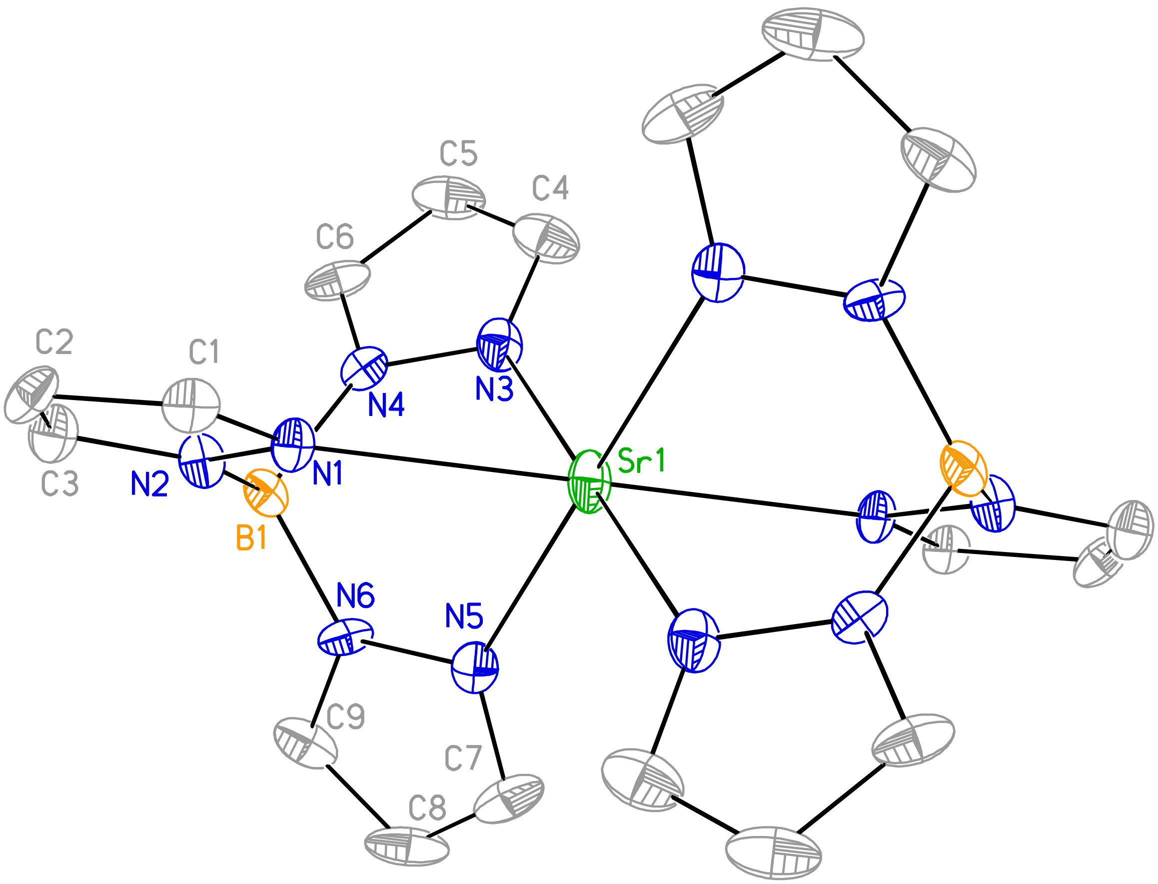

Figure 9. Perspective view of **2** with thermal ellipsoids at the 50% probability level.

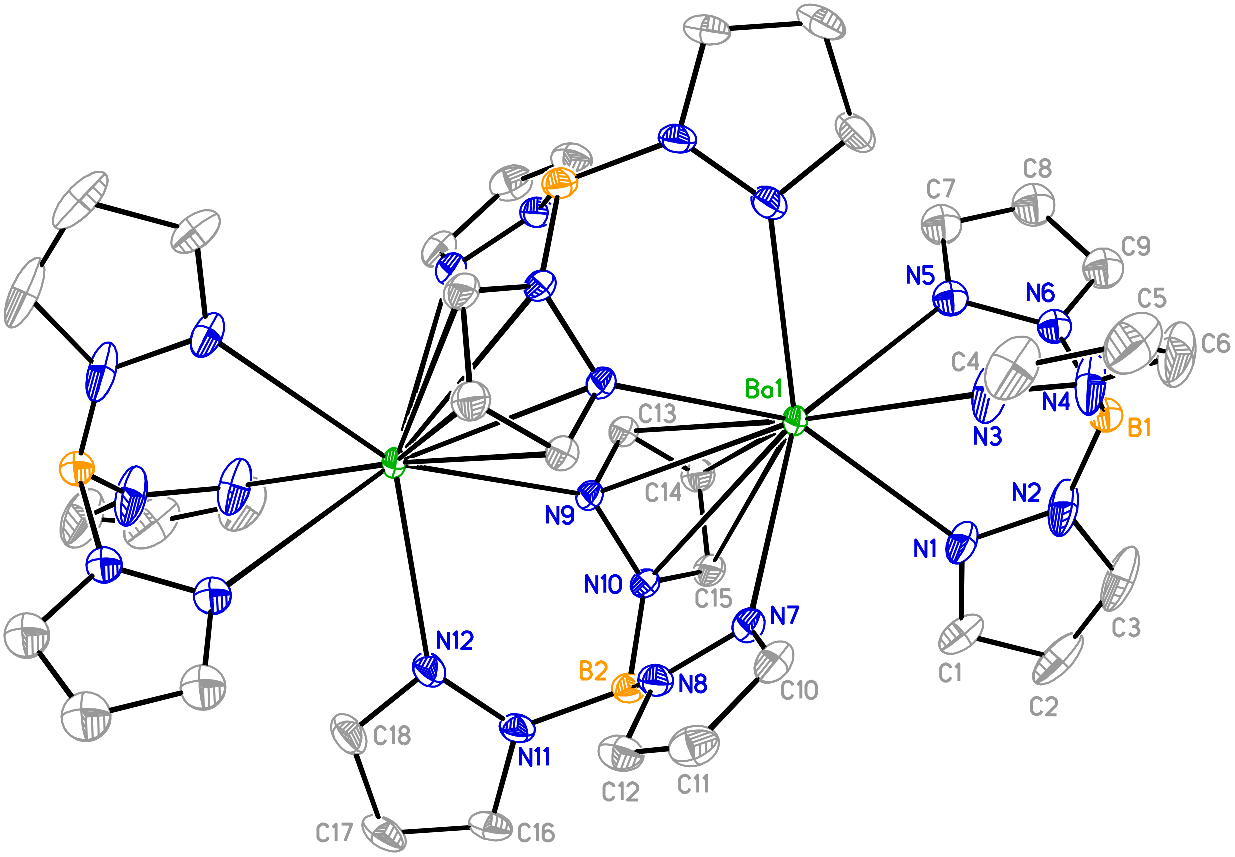

Table 5. Selected bond lengths (Å) and angles (deg) for **5** and **6**.

	5	**6**
M-N(1)	2.465(2)	2.615(2)
M-N(3)	2.460(2)	2.606(2)
M-N(5)	2.453(2)	2.598(2)
N(1)-M-N(1)’	180	180
N(1)-M-N(3)	79.17(7)	75.34(6)
N(1)-M-N(3)’	100.83(7)	104.66(6)
N(1)-M-N(5)	79.49(7)	74.67(6)
N(1)-M-N(5)’	100.51(7)	105.33(6)
N(3)-M-N(3)’	180	180
N(3)-M(1)-N(5)	78.07(8)	73.43(6)
N(3)-M(1)-N(5)’	101.93(8)	106.57(6)
N(5)-M(1)-N(5)’	180	180

Figure 10. Perspective view of **5** with thermal ellipsoids at the 50% probability level.

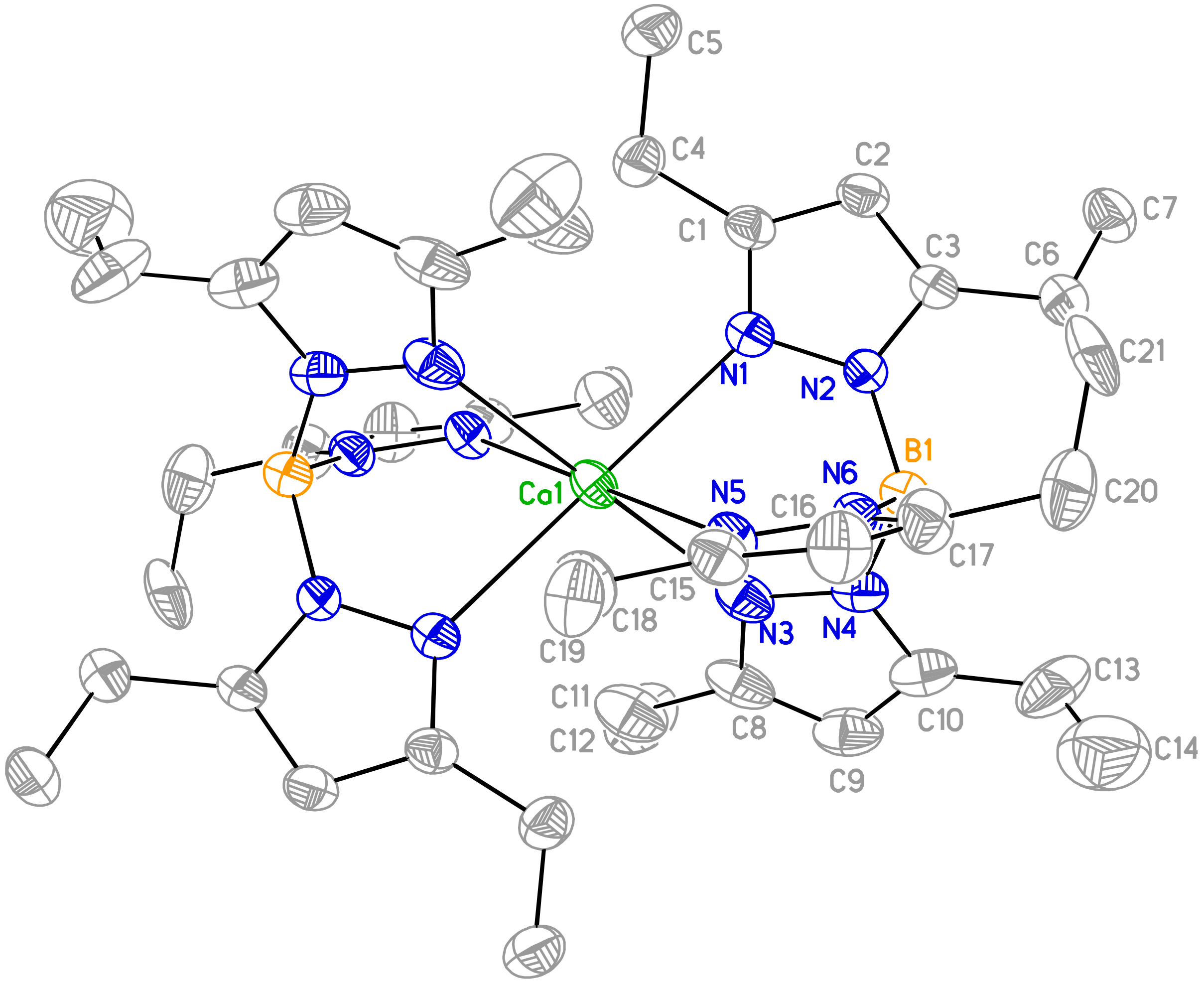

Figure 11. Perspective view of **6** with thermal ellipsoids at the 50% probability level.

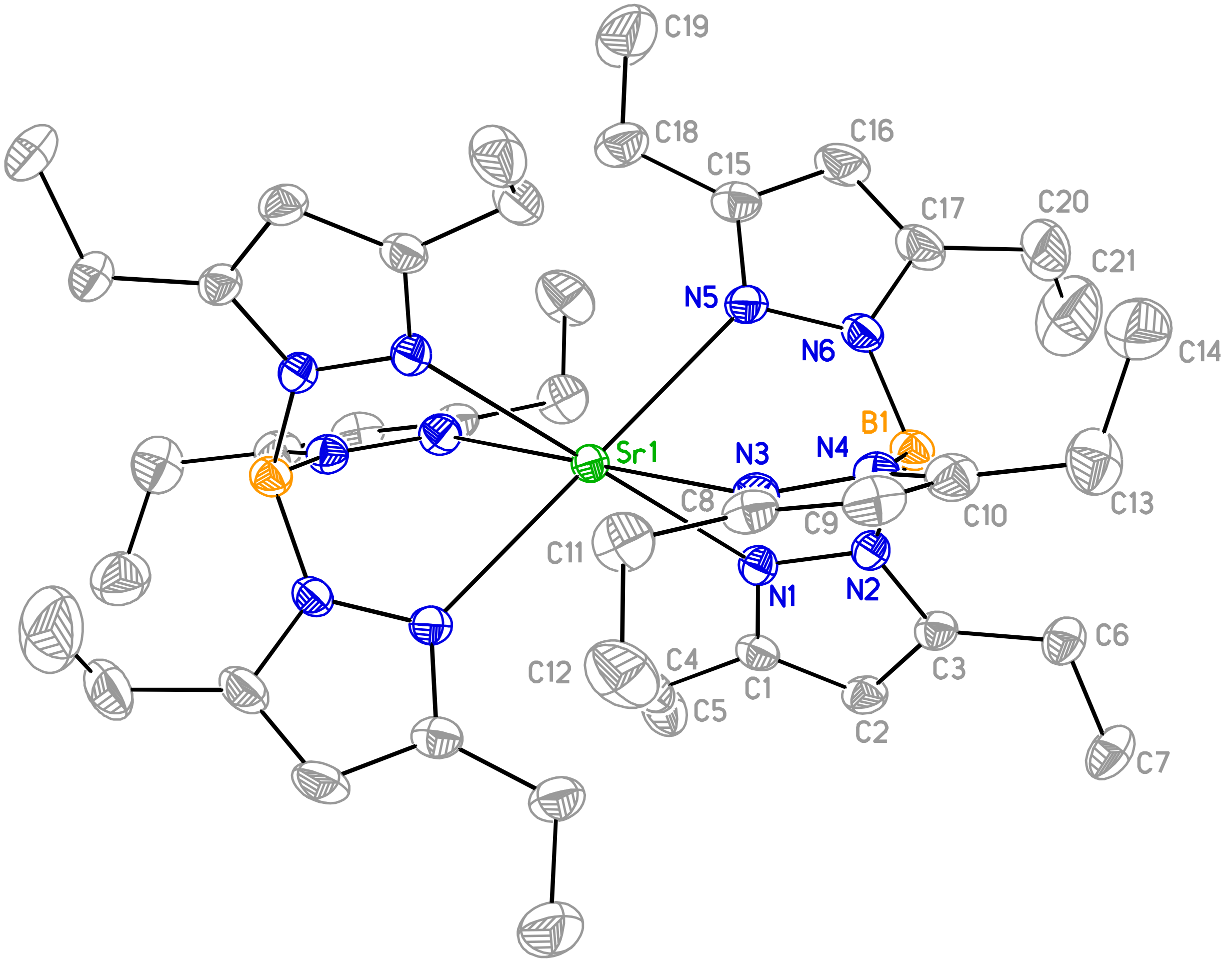

Table 6. Selected bond lengths (Å) and angles (deg) for **7**.

Ba-N(1)	2.769(2)	N(3)-Ba-N(5)	68.47(6)
Ba-N(3)	2.781(2)	N(3)-Ba-N(7)	95.35(6)
Ba-N(5)	2.789(2)	N(3)-Ba-N(9)	164.22(6)
Ba-N(7)	2.759(2)	N(3)-Ba-N(11)	102.23(6)
Ba-N(9)	2.816(2)	N(5)-Ba-N(7)	163.75(6)
Ba-N(11)	2.751(2)	N(5)-Ba-N(9)	127.32(6)
N(1)-Ba-N(3)	70.24(5)	N(5)-Ba-N(11)	112.96(5)
N(1)-Ba-N(5)	72.98(5)	N(7)-Ba-N(9)	68.87(6)
N(1)-Ba-N(7)	100.85(5)	N(7)-Ba-N(11)	70.71(6)
N(1)-Ba-N(9)	111.77(5)	N(9)-Ba-N(11)	73.05(6)
N(1)-Ba-N(11)	168.54(6)		

Table 7. Comparison of the average metal-nitrogen bond lengths (Å), average cis nitrogen-metal-nitrogen' (deg) intraligand bond angles, average cis nitrogen-metal-nitrogen interligand bond angles (deg), average boron-nitrogen-nitrogen angles (deg), and average nitrogen-boron-nitrogen angles (deg) for **5**-**7**.

Complex	M-N	N-M-N$_{\text{intraligand}}$	N-M-N'$_{\text{interligand}}$	B-N-N	N-B-N
5	2.459(6)	78.9(8)	101.1(7)	121.9(4)	110.6(6)
6	2.606(9)	74.5(1)	105.5(1)	122.1(6)	110.8(5)
7	2.78(2)	71(2)	108(11)	122.2(5)	111.3(6)

Figure 12. Perspective view of **7** with thermal ellipsoids at the 50% probability level.

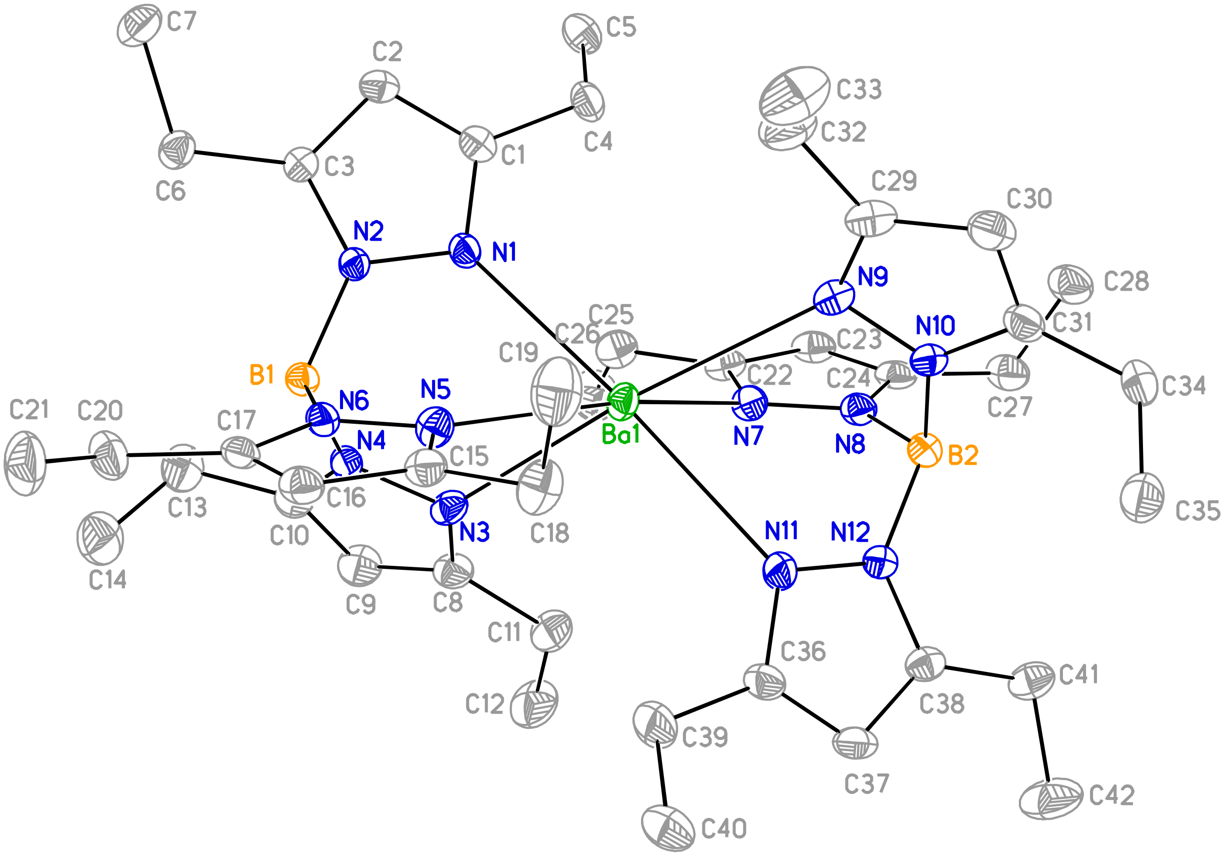

2.3 Conclusions

Calcium, strontium, and barium complexes containing various tris(pyrazolyl)borate ligands have been synthesized and structurally characterized, and their volatilities and thermal stabilities were assessed. Complex **2** was structurally characterized, and exists with an unusual dimeric solid state structure. The remaining complexes adopt monomeric solid state structures with distorted octahedral geometries. The low thermal stability and volatility of **2** is likely related to its dimeric structure. Complexes **1** and **3**-**10** exhibit high thermal stabilities and volatilities, as demonstrated by the TGA traces, preparative sublimations, and melting point/decomposition determinations. Furthermore, **6-10** sublime as liquids, and are thus promising candidates for CVD and ALD film growth precursors. ALD growth studies employing the complexes described herein will be reported separately from our laboratory.

2.4 Experimental Section

General Considerations. All reactions were performed under argon using standard glovebox or Schlenk line techniques. Tetrahydrofuran was distilled from sodium benzophenone ketyl. Hexane was distilled from P_2O_5. KTp,[62] KTp^{Me2},[70] MTp_2 (M = Sr, **1**; Ba, **2**),[62] MTp^{Me2}_2 (M = Sr, **3**; Ba, **4**),[61d] 3,5-diethylpyrazole,[71] 3,5-di-n-propylpyrazole,[71] and the β-diketones[72] used for the pyrazole syntheses were prepared according to literature procedures. $BaI_2(THF)_3$ was prepared by treating a slight excess of barium (1.1 equivalents) with iodine (1.0 equivalent) in refluxing tetrahydrofuran. The number of THF ligands was estimated by the weight loss observed in the TGA trace. All other chemicals and solvents were purchased from Acros.

^{1}H and ^{13}C{^{1}H} NMR spectra were obtained at 400, 300, 125, or 75 MHz in dichloromethane-d_2 or benzene-d_6, as indicated. Infrared spectra were obtained using Nujol as the medium. Elemental analyses were performed by Midwest Microlab, Indianapolis, IN. It was necessary to add V_2O_5 as a combustion enhancing agent for **10** to obtain acceptable carbon values. Melting points were obtained on a Haake-Buchler HBI digital melting point apparatus or an Electrothermal Model 9200 melting point apparatus and are uncorrected. TGA was conducted on a Perkin Elmer Pyris 1 TGA system between 25 and 450 °C, using nitrogen as the flow gas with a heating rate of 10 °C/min.

$SrTp_2$ (1). The analytical sample was obtained by sublimation at 200 °C/0.05 Torr: mp 273-275 °C; IR (Nujol, cm^{-1}) $\nu_{B\text{-}H}$ = 2529, $\nu_{C\text{-}N}$ = 1533; ^{1}H NMR (CD_2Cl_2, 23 °C, δ) 7.82 (d, J = 1.8 Hz, 6H, C*H*), 7.62 (d, J = 1.8 Hz, 6H, C*H*), 6.24 (t, J = 2.0 Hz, 6H, 4-C*H*), 4.8 (broad s, 2H, B-H); ^{13}C{^{1}H} NMR (CD_2Cl_2, 23 °C, ppm) 140.97 (s, *C*-H), 136.76 (s, *C*-H), 104.45 (s, 4-*C*H).

Anal. Calcd for $C_{18}H_{20}B_2N_{12}Sr$: C, 42.09; H, 3.92; N, 32.72. Found: C, 42.24; H, 4.01; N, 32.78.

$[BaTp_2]_2$ (2). The analytical sample was obtained by sublimation at 220 °C/0.05 Torr: mp 250-252 °C; IR (Nujol, cm^{-1}) $\nu_{B\text{-}H}$ = 2529, $\nu_{C\text{-}N}$ = 1533; ^{1}H NMR (toluene-d_8, 23 °C, δ) 7.57 (d, J = 1.8 Hz, 12H, C*H*), 7.03 (d, J = 1.8 Hz, 12H, C*H*), 5.97 (t, J = 1.8 Hz, 12H, 4-C*H*), 5.0 (broad s, 4H, B-H); ^{1}H NMR (toluene-d_8, -80 °C, δ) 7.76 (s, C*H*), 7.40 (s, C*H*), 7.29 (s, C*H*), 6.61 (s, C*H*), 6.07 (s, C*H*), 5.81 (s, C*H*); ^{13}C{^{1}H} NMR (CD_2Cl_2, 23 °C, ppm) 140.60 (s, *C*-H), 136.63 (s, *C*-H), 104.55 (s, 4-*C*H).

Anal. Calcd for $C_{36}H_{40}B_4Ba_2N_{24}$: C, 38.37; H, 3.58; N, 29.83. Found: C, 38.25; H, 3.38; N, 29.68.

Preparation of KTp^{Et2}. A 50-mL round-bottomed flask was charged with potassium borohydride (1.711 g, 0.0317mol), 3,5-diethylpyrazole (13.400 g, 0.108 mol), and a stir bar. The mixture was slowly heated in an oil bath to 190 °C, while carefully monitoring hydrogen evolution. Once the gas evolution ceased (~2.3 L of H_2 collected), the hot oil bath was removed and the reaction mixture was cooled to ~140 °C, at which point hexane (15 mL) was added. The reaction mixture was placed in a freezer at -23 °C for 2 hours, resulting in the formation of a white precipitate. The white solid was collected by vacuum filtration on a medium glass frit and was washed with cold hexane (40 mL) to afford KTp^{Et2} as a white powder (8.102 g, 61%): mp 189-191 °C; IR (Nujol, cm^{-1}) $\nu_{B\text{-}H}$ = 2444, $\nu_{C\text{-}N}$ = 1534; ^{1}H NMR (CD_2Cl_2, 23 °C, δ) 5.82 (s, 3H, 4-C*H*), 4.7 (broad s, 1H, B-H), 2.65 (q, J = 7.6 Hz, 6H, $CH_3C\mathit{H}_2$), 2.54 (q, J = 7.5 Hz, 6H, $CH_3C\mathit{H}_2$), 1.20 (t, J = 7.4 Hz, 9H, $C\mathit{H}_3CH_2$), 1.08 (t, J = 7.6 Hz, 9H, $C\mathit{H}_3CH_2$); $^{13}C\{^1H\}$ NMR (CD_2Cl_2, 23 °C, ppm) 153.70 (s, C_q), 151.23 (s, C_q), 100.48 (s, 4-*C*H), 22.20 (s, $CH_3\mathit{C}H_2$), 20.67 (s, $CH_3\mathit{C}H_2$), 14.30 (s, $\mathit{C}H_3CH_2$) 13.71 (s, $\mathit{C}H_3CH_2$).

Anal. Calcd for $C_{21}H_{34}BKN_6$: C, 59.99; H, 8.15; N, 19.99. Found: C, 60.36; H, 8.13; N, 20.26.

Preparation of KTp^{nPr2}. In a similar fashion to the preparation of KTp^{Et2}, treatment of potassium borohydride (2.117 g, 0.0392 mol) with 3,5-di-n-propylpyrazole (20.000 g, 0.131 mol) afforded KTp^{nPr2} as a white powder (6.148 g, 31%): mp 109-110 °C; IR (Nujol, cm^{-1}) $\nu_{B\text{-}H}$ = 2444, $\nu_{C\text{-}N}$ = 1533; ^{1}H NMR (CD_2Cl_2, 23 °C, δ) 5.77 (s, 3H, 4-C*H*), 4.7 (broad s, 1H, B-H), 2.58 (t, J = 7.5 Hz, 6H, C*H*$_2$CH$_2$CH$_3$), 2.46 (t, J = 7.8 Hz, 6H, C*H*$_2$CH$_2$CH$_3$), 1.59 (sextet, J = 7.7 Hz, 6H, CH$_2$C*H*$_2$CH$_3$), 1.44 (sextet, J = 7.5 Hz, 6H, CH$_2$C*H*$_2$CH$_3$) 0.95 (t, J = 7.4 Hz, 9H, CH$_2$CH$_2$C*H*$_3$), 0.89 (t, J = 7.4 Hz, 9H, CH$_2$CH$_2$C*H*$_3$); ^{13}C{^{1}H} NMR (CD$_2$Cl$_2$, 23 °C, ppm) 152.13 (s, *C*$_q$), 149.63 (s, *C*$_q$), 101.70 (s, 4-*C*H), 31.35 (s, *C*H$_2$CH$_2$CH$_3$), 29.56 (s, *C*H$_2$CH$_2$CH$_3$), 23.62 (s, CH$_2$*C*H$_2$CH$_3$), 22.91 (s, CH$_2$*C*H$_2$CH$_3$), 14.41 (s, CH$_2$CH$_2$*C*H$_3$), 14.30 (s, CH$_2$CH$_2$*C*H$_3$).

Anal. Calcd for $C_{27}H_{46}BKN_6$: C, 64.27; H, 9.19; N, 16.65. Found: C, 64.46; H, 9.02; N, 16.73.

Preparation of CaTp^{Et2}$_2$ (5). A 250-mL Schlenk flask was charged with CaI$_2$ (0.372 g, 1.27 mmol), KTp^{Et2} (1.047 g, 2.49 mmol), and a stir bar. Tetrahydrofuran (100 mL) was added, resulting in the immediate formation of a white precipitate. The reaction mixture was stirred for 18 h, at which time the volatile components were removed under reduced pressure to afford a white residue. Hexane (50 mL) was added to the residue, and the resulting mixture was filtered through a 3-cm pad of Celite on a medium glass frit to yield a clear filtrate. Removal of the volatile components under reduced pressure afforded **5** as a white powder (0.804 g, 64%). The analytical sample and single crystals for the X-ray crystallographic analysis were obtained by crystallization from hexane at -23 °C: mp 225-226 °C; IR (Nujol, cm^{-1}) $\nu_{B\text{-}H}$ = 2529, $\nu_{C\text{-}N}$ = 1533; ^{1}H NMR (CD$_2$Cl$_2$, 23 °C, δ) 5.80 (s, 6H, 4-C*H*), 4.8 (broad s, 2H, B-H), 2.90 (q, J = 7.5 Hz, 12H, C*H*$_2$CH$_3$), 2.08 (q, J = 7.5 Hz, 12H, C*H*$_2$CH$_3$), 1.25 (t, J = 7.7 Hz, 18H, CH$_2$C*H*$_3$), 0.95 (t, J = 7.7 Hz, 18H, CH$_2$C*H*$_3$); ^{13}C{^{1}H} NMR (CD$_2$Cl$_2$, 23 °C, ppm) 155.35 (s, *C*$_q$), 151.44 (s, *C*$_q$), 100.43 (s, 4-*C*H), 21.14 (s, *C*H$_2$CH$_3$), 20.78 (s, *C*H$_2$CH$_3$), 13.57 (s, CH$_2$*C*H$_3$), 13.30 (s, CH$_2$*C*H$_3$).

Anal. Calcd for $C_{42}H_{68}B_2CaN_{12}$: C, 62.83; H, 8.54; N, 20.94. Found: C, 62.89; H, 8.45; N, 21.01.

Preparation of $SrTp^{Et2}{}_2$ (6). In a fashion similar to the preparation of **5**, treatment of SrI_2 (0.817 g, 2.39 mmol) with KTp^{Et2} (1.978 g, 4.70 mmol) afforded **6** as a white solid (1.274 g, 64%). The analytical sample and single crystals for the X-ray crystallographic analysis were obtained by crystallization from hexane at -23 °C: mp 188-190 °C; IR (Nujol, cm^{-1}) ν_{B-H} = 2532, ν_{C-N} = 1533; ^1H NMR (CD_2Cl_2, 23 °C, δ) 5.82 (s, 6H, 4-C*H*), 4.8 (broad s, 2H, B-H), 2.87 (q, J = 7.5 Hz, 12H, CH_2CH_3), 2.22 (q, J = 7.5 Hz, 12H, CH_2CH_3), 1.25 (t, J = 7.4 Hz, 18H, CH_2CH_3), 1.01 (t, J = 7.7 Hz, 18H, CH_2CH_3); $^{13}C\{^1H\}$ NMR (CD_2Cl_2, 23 °C, ppm) 154.96 (s, C_q), 151.81 (s, C_q), 100.58 (s, 4-*C*H), 21.38 (s, CH_2CH_3), 21.18 (s, CH_2CH_3), 13.69 (s, CH_2CH_3), 13.57 (s, CH_2CH_3).

Anal. Calcd for $C_{42}H_{68}B_2N_{12}Sr$: C, 59.32; H, 8.06; N, 19.77. Found: C, 59.04; H, 7.79; N, 19.82.

Preparation of $BaTp^{Et2}{}_2$ (7). A 250-mL Schlenk flask was charged with $BaI_2(THF)_3$ (0.689 g, 1.134 mmol), KTp^{Et2} (0.934 g, 2.221 mmol), and a stir bar. Tetrahydrofuran (80 mL) was added, resulting in the immediate formation of a white precipitate. The reaction mixture was stirred for 18 h, at which point the volatile components were removed under reduced pressure to afford a white residue. Hexane (60 mL) was added and the resulting mixture was filtered through a 3-cm pad of Celite on a medium glass frit to yield a clear, colorless filtrate. The filtrate was reduced in volume under reduced pressure to about 20 mL and the flask was placed in the freezer at -23 °C for 18 h. Removal of the solvent by cannula, followed by vacuum drying, afforded colorless crystals of **7** (0.686 g, 67%): mp 129-131 °C;

IR (Nujol, cm^{-1}) $\nu_{B\text{-}H}$ = 2526, $\nu_{C\text{-}N}$ = 1532; ^1H NMR (CD_2Cl_2, 23 °C, δ) 5.82 (s, 6H, 4-C*H*), 4.8 (broad s, 2H, B-H), 2.79 (q, J = 7.3 Hz, 12H, CH_2CH_3), 2.28 (q, J = 7.5 Hz, 12H, CH_2CH_3), 1.17 (t, J = 7.4 Hz, 18H, CH_2CH_3), 1.04 (t, J = 7.8 Hz, 18H, CH_2CH_3); $^{13}C\{^1H\}$ NMR (CD_2Cl_2, 23 °C, ppm) 154.31 (s, C_q), 151.68 (s, C_q), 100.85 (s, 4-*C*H), 21.49 (s, CH_2CH_3), 21.00 (s, CH_2CH_3), 13.99 (s, CH_2CH_3), 13.64 (s, CH_2CH_3).

Anal. Calcd for $C_{42}H_{68}B_2N_{12}Ba$: C, 56.04; H, 7.62; N, 18.80. Found: C, 55.96; H, 7.76; N, 18.80.

Preparation of $CaTp^{nPr2}{}_2$ (8). In a fashion similar to the preparation of **5**, treatment of CaI_2 (0.150 g, 0.510 mmol) with KTp^{nPr2} (0.515 g, 1.02 mmol) afforded **8** as a white solid (0.250 g, 51%). The analytical sample and single crystals for the X-ray crystallographic analysis were obtained by crystallization from hexane at -23 °C: mp 169-172 °C; IR (Nujol, cm^{-1}) $\nu_{B\text{-}H}$ = 2517, $\nu_{C\text{-}N}$ = 1532; ^1H NMR (CD_2Cl_2, 23 °C, δ) 5.76 (s, 6H, 4-C*H*), 4.8 (broad s, 2H, B-H), 2.82 (t, J = 7.5 Hz, 12H, $CH_2CH_2CH_3$), 1.59 (t, J = 8.1 Hz, 12H, $CH_2CH_2CH_3$), 1.59 (sextet, J = 7.4 Hz, 12H, $CH_2CH_2CH_3$), 1.38 (sextet, J = 7.7 Hz, 12H, $CH_2CH_2CH_3$), 0.96 (t, J = 7.4 Hz, 18H, $CH_2CH_2CH_3$), 0.66 (t, J = 7.4 Hz, 18H, $CH_2CH_2CH_3$); $^{13}C\{^1H\}$ NMR (CD_2Cl_2, 23 °C, ppm) 154.08 (s, C_q), 149.79 (s, C_q), 101.68 (s, 4-*C*H), 29.89 (s, $CH_2CH_2CH_3$), 29.76 (s, $CH_2CH_2CH_3$), 23.20 (s, $CH_2CH_2CH_3$), 22.59 (s, $CH_2CH_2CH_3$), 14.35 (s, $CH_2CH_2CH_3$), 14.18 (s, $CH_2CH_2CH_3$).

Anal. Calcd for $C_{54}H_{92}B_2CaN_{12}$: C, 66.78; H, 9.55; N, 17.31. Found: C, 67.02; H, 9.27; N, 17.56.

Preparation of $SrTp^{nPr2}{}_2$ (9). In a fashion similar to the preparation of **5**, treatment of SrI_2 (0.340 g, 0.996 mmol) with KTp^{nPr2} (0.991 g, 1.96 mmol) afforded **9** as a white solid

(0.750 g, 75%). The analytical sample and single crystals for the X-ray crystallographic analysis were obtained by crystallization from hexane at -23 °C: mp 164-168 °C; IR (Nujol, cm^{-1}) $\nu_{B\text{-}H}$ = 2511, $\nu_{C\text{-}N}$ = 1532; ^{1}H NMR (CD_2Cl_2, 23 °C, δ) 5.76 (s, 6H, 4-C*H*), 4.8 (broad s, 2H, B-H), 2.78 (t, J = 7.7 Hz, 12H, $CH_2CH_2CH_3$), 2.11 (t, J = 8.1 Hz, 12H, $CH_2CH_2CH_3$), 1.57 (sextet, J = 7.5 Hz, 12H, $CH_2CH_2CH_3$), 1.41 (sextet, J = 7.9 Hz, 12H, $CH_2CH_2CH_3$), 0.95 (t, J = 7.4 Hz, 18H, $CH_2CH_2CH_3$), 0.70 (t, J = 7.7 Hz, 18H, $CH_2CH_2CH_3$); $^{13}C\{^{1}H\}$ NMR (CD_2Cl_2, 23 °C, ppm) 153.56 (s, C_q), 150.07 (s, C_q), 101.88 (s, 4-*C*H), 30.43 (s, $CH_2CH_2CH_3$), 29.80 (s, $CH_2CH_2CH_3$), 23.02 (s, $CH_2CH_2CH_3$), 22.96 (s, $CH_2CH_2CH_3$), 14.26 (s, $CH_2CH_2CH_3$), 14.21 (s, $CH_2CH_2CH_3$).

Anal. Calcd for $C_{54}H_{92}B_2N_{12}Sr$: C, 63.67; H, 9.10; N, 16.57. Found: C, 63.48; H, 8.97; N, 16.57.

Preparation of $BaTp^{nPr2}_2$ (10). In a fashion similar to the preparation of **5**, treatment of $BaI_2(THF)_3$ (1.65 g, 2.74 mmol) with KTp^{nPr2} (1.00 g, 5.49 mmol) afforded **10** as a colorless, waxy solid (0.54 g, 39%). The analytical sample was obtained by sublimation at 240 °C/0.05 Torr: mp 141-144 °C; IR (Nujol, cm^{-1}) $\nu_{B\text{-}H}$ = 2470, $\nu_{C\text{-}N}$ = 1532; ^{1}H NMR (CD_2Cl_2, 23 °C, δ) 5.77 (s, 6H, 4-C*H*), 4.8 (broad s, 2H, B-H), 2.71 (t, J = 7.6 Hz, 12H, $CH_2CH_2CH_3$), 2.21 (t, J = 8.2 Hz, 12H, $CH_2CH_2CH_3$), 1.51 (sextet, J = 7.6 Hz, 12H, $CH_2CH_2CH_3$), 1.46 (sextet, J = 7.5 Hz, 12H, $CH_2CH_2CH_3$), 0.93 (t, J = 7.2 Hz, 18H, $CH_2CH_2CH_3$), 0.74 (t, J = 7.4 Hz, 18H, $CH_2CH_2CH_3$); $^{13}C\{^{1}H\}$ NMR (C_6D_6, 23 °C, ppm) 152.47 (s, C_q), 149.96 (s, C_q), 102.78 (s, 4-*C*H), 30.82 (s, $CH_2CH_2CH_3$), 29.59 (s, $CH_2CH_2CH_3$), 23.65 (s, $CH_2CH_2CH_3$), 22.80 (s, $CH_2CH_2CH_3$), 14.32 (s, $CH_2CH_2CH_3$), 14.07 (s, $CH_2CH_2CH_3$).

Anal. Calcd for $C_{54}H_{92}B_2BaN_{12}$: C, 60.70; H, 8.68; N, 15.74. Found: C, 60.97; H, 8.77; N, 15.79.

Preparative Sublimation Studies. For the sublimation experiments, 2.5 cm diameter, 30 cm long glass tubes were employed. One end of the tube was sealed and the other end was equipped with a 24/40 male glass joint. In an argon-filled glove box, the compound to be sublimed (0.5-1.0 g) was loaded into a 1.0 x 4.0 cm glass tube and this tube was placed at the sealed end of the glass sublimation tube. The sublimation tube was fitted with a 24/40 vacuum adapter, and then was inserted into a horizontal Buchi Kugelrohr oven such that about 15 cm of the tube was situated in the oven. A vacuum of 0.05 Torr was established, and the oven was heated to the indicated temperature. The compounds sublimed to the cool zone just outside of the oven. The percent recovery was obtained by weighing the sublimed product. The percent nonvolatile residue was calculated by weighing the 1.0 x 4.0 cm glass tube at the end of the sublimation. Data are given in the text and in Table 7.

Thermal Decomposition Studies. In an argon-filled dry box, a melting point capillary tube was charged with 1-2 mg of a sample of **1-10** and the end of the tube was sealed with a small amount of stopcock grease. The capillary tube was then removed from the dry box, and the end was flame sealed. The capillary tube was transferred to an Electrothermal Model 9200 melting point apparatus, and was then heated at 5 °C/min from 25 to 400 °C. In this fashion, samples of **1-10** were visually observed for discoloration or other evidence of decomposition over the 75 minute experiments. This procedure allowed qualitative assessment of thermal stability up to 400 °C. Data are given in the text and in Table 7.

X-Ray Crystallographic Structure Determinations for 1, 2, and 5-7. Diffraction data were measured on a Bruker *X8 APEX-II* kappa geometry diffractometer with Mo radiation and a graphite monochromator. Frames were collected at 100 K with the detector at 40 mm, 0.3° between each frame, and were recorded for 5-10 s. *APEX-II*[73] and *SHELX*[74] software were used in the collection and refinement of the models. Crystals of **1** grew as colorless rods upon sublimation. These crystals were all twinned; more than 6 specimens were assayed. A twinned sample was selected and the structure was satisfactorily extracted using software *Cell_Now* and *TwinAbs*, which found a 180° twin rotation about the 13 Å axis. 62310 reflections were measured, yielding 6845 unique data. Hydrogen atoms were placed in calculated and observed positions. The asymmetric unit contains two half-molecules with Sr(1) and Sr(2) each occupying a crystallographic inversion center. Crystals of **2** were colorless and irregular. 87104 reflections were counted, which averaged to 9769 independent data. Hydrogen atoms were placed at calculated or observed positions. All atoms occupy general positions in the cell, but the molecule itself occupies a crystallographic inversion center. Disorder was observed for one portion of the ligand, consequently B(1), N(5), N(6), C(7), C(8) and C(9) were assigned 50/50 partial positions and kept isotropic. Complex **5** crystallized as colorless parallelepipeds. 65160 hkl data points were harvested, which averaged to 5821 data. Hydrogen atoms were calculated, except that the H atom on B(1) was observed. The asymmetric unit contains one half molecule with the Ca ion occupying a crystallographic inversion center. The two atoms C(19) and C(20) were assigned two half-positions each. Crystals of **6** were colorless rhomboids. 65719 reflections were counted, which averaged to 7210 independent data. Hydrogen atoms were calculated, except that the H atom on B(1) was observed. The asymmetric unit contains one half molecule, with the Sr ion occupying a crystallographic inversion center. Crystals of **7** were colorless rods. 146747 data were integrated, which averaged into 12342 independent data. Hydrogen atoms were placed in observed or calculated positions. Two partial sites were assigned for the terminal atom C(33). All atoms occupy general positions in the cell.

CHAPTER 3

Highly Distorted κ^3-N,N,H Bonding of Bis(3,5-di-*tert*-butyl(pyrazolyl)borate Ligands to the Heavier Group 2 Elements

3.1 Introduction

In chapter 2, the synthesis and properties of a series of group 2 tris(pyrazolyl)borate (Tp) complexes and 3,5-disubstituted (Tp^{R2}) derivatives were described and they exhibited excellent thermal stability and sufficient volatility, with the best strontium and barium precursors having solid state decomposition temperatures of > 400 and 380 °C, respectively. A drawback of $BaTp^{Et2}_2$ and other group 2 precursors containing Tp-based ligands is their low vapor pressures; temperatures of $\geq$ 200 °C at 0.05 Torr are required to effect sublimation. To reduce molecular weight, increase volatility, and maintain good thermal stability, the Bp^{tBu2} ligand was employed. Bp ligands typically bond to metal ions in a κ^3-N,N,H-fashion, through the two 2-nitrogen atoms of the pyrazolyl groups and to one of the two electron rich boron-bound hydrogen atoms.[59] Bp ligands can be tuned sterically and electronically by adjusting the substituents in the 3- and 5-positions of the pyrazolyl moeities.[59] Also Bp ligands can have lower molecular weights than Tp ligands, since they contain only two pyrazolyl groups, and may be more reactive toward hydrolysis in ALD film growth due to the more open boron-hydrogen bonds. Accordingly, complexes containing Bp-based ligands may be useful as ALD precursors. A key consideration in obtaining high thermal stability in Tp-based complexes is to employ alkyl substituents in the 3- and 5-positions of the pyrazolyl groups, which encapsulate the metal center and the boron-hydrogen moieties and reduce decomposition pathways and rates. Parkin and coworkers reported synthetic routes to

$LiBp^{tBu2}$ and $TlBp^{tBu2}$.[75] However, no additional complexes containing the Bp^{tBu2} ligand have been described since this disclosure. Thallium, zinc, and cadmium complexes containing the related asymmetric $Bp^{R,R'}$ (R = tBu, R' = H, Me, iPr) ligands have been reported.[75,76] There are few examples of group 2 complexes containing Bp ligands. Synthetic routes to $MBp^{Me2}{}_2(THF)$ (M = Ca, Sr, Ba; Bp^{Me2} = bis(3,5-dimethylpyrazolyl)borate), $MBp^{tBu}{}_2(THF)$ (M = Ca, Sr, Ba; Bp^{tBu} = bis(3-*tert*-butylpyrazolyl)borate), and $BaTp^{Me2}Bp^{Me2}$ (Tp^{Me2} = tris(3,5-dimethylpyrazolyl)borate) have been described, however, none of these complexes was structurally characterized.[61d] Sohrin and coworkers performed group 2 ion extraction studies with the Bp ligand, and found that significant extraction did not occur for Ca^{2+}, Sr^{2+}, or Ba^{2+}.[77,61e] The crystal structures $MgBp(THF)(\mu\text{-}Cl)_2MgBp(THF)_2$, $MgBp_2(THF)$, and $MgBp_2(THF)_2$ have been reported, and among the three complexes, only $MgBp_2(THF)$ contains a κ^3-N,N,H-Bp ligand.[78]

Herein, the synthesis, structure, and properties of a series of calcium, strontium, and barium complexes containing the Bp^{tBu2} ligand are described. These complexes exist as monomers, contain κ^3-N,N,H-Bp^{tBu2} ligands as determined by X-ray crystallography, are volatile, and possess high thermal stabilities. These are the first structurally characterized Bp-based complexes of the heavier group 2 elements. Accommodation of the bulky *tert*-butyl groups within the coordination spheres of the group 2 metal ions affords large distortions of the Bp^{tBu2} ligands.

3.2 Results and Discussion

Preparation of New Complexes. Attempts to prepare KBp^{tBu2} by treatment of KBH_4 with two equivalents of 3,5-di-*tert*-butylpyrazole (tBu_2pzH) under a variety of conditions (heating solid mixtures between 130-150 °C, refluxing in toluene) failed, and only complex mixtures of starting materials and products resulted. LiBp^{tBu2} was described in a communication,[19] however, neither a detailed procedure nor characterization data were reported. In this chapter, LiBp^{tBu2}(THF) (**11**) was obtained as colorless crystals in 49% yield upon treatment of $LiBH_4$ with two equivalents of tBu_2pzH in refluxing toluene for 18 h, followed by crystallization from tetrahydrofuran at -23 °C (eq 8).

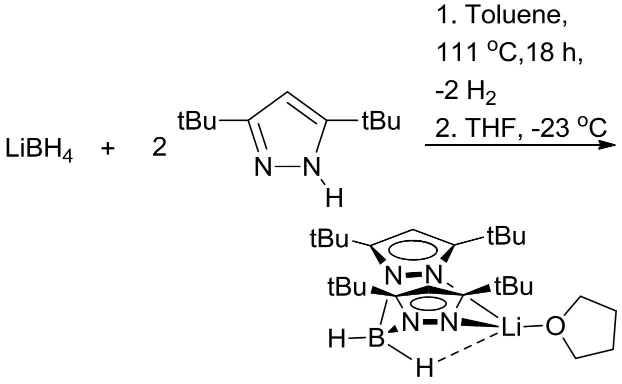

(8)

11, 49%

The thallium complex TlBp^{tBu2} was prepared by adaption of a literature method involving the salt metathesis of **11** with thallous acetate.[75] Further treatment of two equivalents of TlBp^{tBu2} with one equivalent of a group 2 metal iodide in tetrahydrofuran afforded complexes **12-14** in 63-79% yields (eq 9). Sublimation of **14** at 205 °C/0.05 Torr led to loss of the tetrahydrofuran ligand, and afforded **5** in 37% yield (eq 10). Complexes **12-15** are soluble in hexane, and the solubility increases with the metal size in the order **12** <**13** < **14** ≈ **15**.

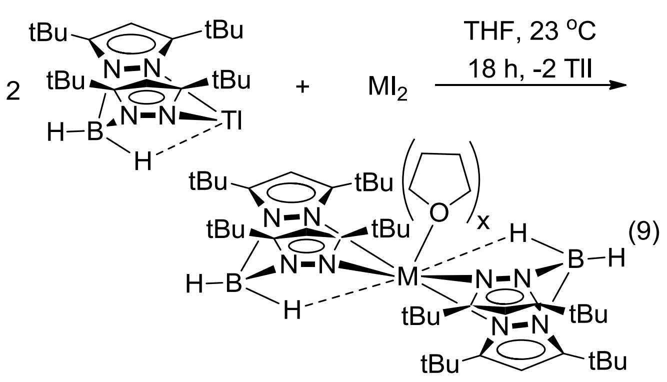

12, M = Ca, x = 0, 67%
13, M = Sr, x = 0, 79%
14, M = Ba, x = 1, 63%

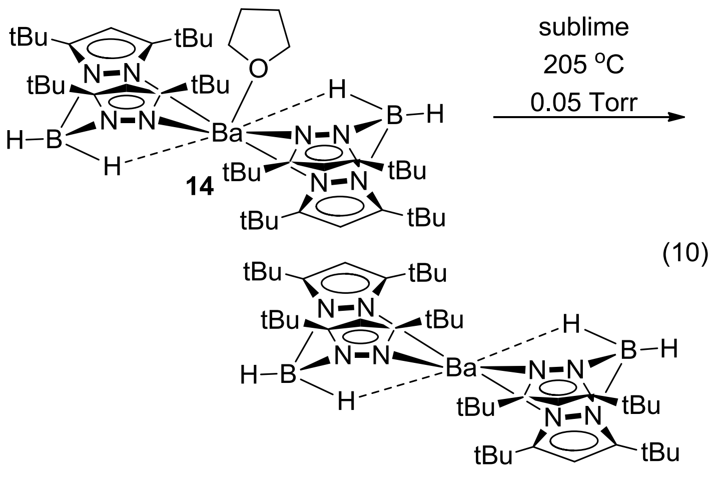

15, 37%

In several preparations of **12-14**, small and varying amounts of a side product were observed. An X-ray crystal structure determination showed this side product to be the protonated species $BH_2(tBu_2pz)(tBu_2pzH)$ (**16**), as described in detail below. It is likely, that **16** originated from traces of acetic acid in our thallous acetate reagent. Accordingly, an independent synthesis of **16** was developed. Treatment of **11** with one equivalent of pivalic acid in tetrahydrofuran for 3 h afforded **16** in 78% yield after workup (eq 11). Reaction times longer than 3 h led to the appearance of free tBu_2pzH in ^1H NMR spectrum of the crude product mixture. Under these conditions, the boron-nitrogen bond of the pyrazolyl group in **16** is likely being protonated by the pivalic acid, leading to tBu$_2$pzH and decomposition.

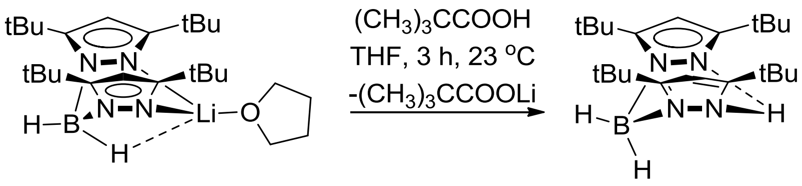

11

16, 78%

(11)

The compositions of **11-16** were established by a combination of spectroscopic and analytical techniques, and by X-ray crystal structure determinations of **13-16**. In the ^{1}H NMR spectra of **11-16**, the 4-hydrogen atom resonances of the tBu$_2$Pz moieties were observed between δ 6.11 and 5.96. The two magnetically inequivalent *tert*-butyl methyl resonances in **11-16** were observed between δ 1.62 and 1.45 and δ 1.36 and 1.16, respectively. The ^{1}H NMR spectra for **11** and **14** additionally contain resonances belonging to the 2- and 3-hydrogen atoms of the tetrahydrofuran ligands at δ 3.5 and 1.3, respectively. The boron-bound hydrogen atoms in **11-16** appeared as broad resonances and ranged from δ 4.58 to 4.50. The ^{13}C{^{1}H} NMR spectra for **11-16** contained all of the expected resonances. Interestingly, only one set of pyrazolyl resonances was observed in the ^{1}H and ^{13}C{^{1}H} NMR spectra of **16** at ambient temperature, implying that proton transfer between the pyrazolyl and pyrazole moieties is rapid at this temperature. In the infrared spectra of **11-16**, the stretching frequencies associated with the boron-bound hydrogen atoms ranged from 2564 to 2066 cm^{-}

^{1}, which are similar to related values in complexes containing Bp-based ligands.[59] The carbon-nitrogen stretching frequencies for **11-15** were observed over a narrow range of 1523 to 1519 cm^{-1}, whereas the related value in **16** appeared at 1562 cm^{-1}. The shift to higher wave numbers in **16** is likely related to coordination of Bp^{tBu2} ligands to metals in **11-15**, compared to the protonated form of **16**.

Structural Aspects. The X-ray crystal structures of **13-16** were determined to establish the geometries about the metal centers and the bonding modes of the Bp^{tBu2} ligands. Experimental crystallographic data are summarized in Table 8, selected bond lengths and angles are given in Tables 9-12, and perspective views are presented in Figures 13-16. It was not possible to grow single crystals of **12** that were of sufficient quality for an X-ray structural determination. The molecular structure of **11** was established through a low resolution X-ray crystal structure, but a higher quality data set could not be obtained in spite of many attempts.

The molecular structure of **16** (Figure 16) serves as a reference for **13-15**. Compound **16** exists with two hydrogen atoms, one tBu_2pz group, and one tBu_2pzH group arranged about a boron atom. The nitrogen-boron-nitrogen angle is 109.20(9)°, consistent with tetrahedral geometry at boron. The tBu_2pzH proton resides on N(3), with a nitrogen-hydrogen distance of 0.97(2) Å. This proton is further engaged in an intramolecular hydrogen bond to N(1), with a distance of 1.78(2) Å and an N(3)-H-N(1) angle of 143(1)°. The X-ray crystal structure of $BH_2(pz)(pzH)$ has been determined,[79] and displays a nitrogen-hydrogen σ-bond distance of 0.98 Å, which is similar to that of **16**. Unlike **16**, however, the intramolecular H•••N distance is 3.80 Å, which rules out an intramolecular hydrogen bond. The molecular structures of TlBp^{tBu2},[75] TlTp^{tBu2},[80] and U(Bp^{tBu,Me})$_2$I[81] serve as highly relevant comparisons to **16**. Table 13 lists selected metrical parameters for **13-16**, $TlBp^{tBu2}$, and $U(Bp^{tBu,Me})_2I$. Parkin and Chisholm have demonstrated that the Tl-N-N-B torsional angles (τ) can afford a quantitative measure of the steric congestion about the metal center caused by the *tert*-butyl substituents.[80] For $TlBp^{tBu2}$ and $TlTp^{tBu2}$, the τ values average 22.2(13) and 22.8°, respectively.[75,80] The related values in $U(Bp^{tBu,Me})_2I$ range between 17.6 and 21.3°, and average 19.4(10)°.[81] Another measure of steric congestion created by the *tert*-butyl groups is the torsion angle between the four pyrazolyl group nitrogen atoms. For **16**, this torsion angle is 8.36(8)°, compared to values of 0.3(15)° for $TlBp^{tBu2}$ and 20.8(12)° for $U(Bp^{tBu,Me})_2I$.[75,81] There are no intramolecular *tert*-butyl methyl hydrogen-hydrogen contacts in **16** that are less than 2.40 Å. Since the van der Waals radius of a hydrogen atom is 1.20 Å,[82] the *tert*-butyl groups in **16** are able to minimize steric interactions efficiently.

The molecular structures of **13-15** possess similar ligand arrangements (Figures 13-15), and will be discussed together. The asymmetric unit of **15** contains two independent half-molecules, with the barium ions occupying inversion centers. Complexes **13** and **15** have coordination spheres composed of two κ^3-Bp^{tBu2} ligands, whereas **14** contains two κ^3-Bp^{tBu2} ligands and a tetrahydrofuran ligand. The metal-nitrogen distances in **13-15** range from 2.561(1)-2.644(1), 2.746(2)-2.840(2), and 2.742(1)-2.793(1) Å, respectively. In spite of the different coordination numbers, the average barium-nitrogen distances in **14** (2.790 Å) and **15** (2.774 Å) are similar. The strontium-nitrogen bond distances in **13** are similar to those in $SrTp_2$ (**1**) ($Sr\text{-}N_{avg}$ = 2.593(12) Å) and $SrTp^{Et2}{}_2$ (**6**) ($Sr\text{-}N_{avg}$ = 2.606(7) Å). The barium-nitrogen distances in **14** and **15** are comparable to those in $[BaTp_2]_2$ (**2**) ($Ba\text{-}N_{avg}$ = 2.82(4) Å) and $BaTp^{Et2}{}_2$ (**7**) ($Ba\text{-}N_{avg}$ = 2.78(2) Å). The metal-nitrogen bond distances in **13-15** are slightly longer than the related values in the structurally similar η^5-β-diketiminate complexes $Sr(tBuNC(CH_3)CHC(CH_3)NtBu)_2$ (2.473-2.517 Å) and $Ba(tBuNC(CH_3)CH\text{-}C(CH_3)NtBu)_2$ (2.617-2.680 Å).[41a] The longer bond distances in **13-15** likely result from the more congested coordination spheres, compared to $M(tBuNC(CH_3)CHC(CH_3)NtBu)_2$. Complexes **13-15** also feature short intramolecular metal-hydrogen distances to one of the two boron-bound hydrogen atoms within each ligand, affording overall κ^3-N,N,H-Bp^{tBu2} ligand coordination modes. The metal-hydrogen distances in **13-15** are 2.56(1) and 2.59(1) Å, 2.83(2) and 2.89(2) Å, and 2.66(2) and 2.71(2) Å, respectively. These values are similar to those observed in $M(BH_4)_2(THF)_2$, $M(BH_4)_2(diglyme)_2$, and $M(BH_4)_2$(18-crown-6) (M = Sr, 2.60-2.91 Å; M = Ba, 2.66-2.98 Å).[83] The sum of the van der Waals radii for hydrogen and strontium ions is 3.60-3.70 Å, while the similar sum for hydrogen and barium ions is 3.80-3.90 Å.[82] Accordingly, strong metal-hydrogen interactions are present in **13-15**. The barium-oxygen distance in **14** is 2.701(2) Å.

Significant distortions are present in the ligand coordination modes of **13-15**. For comparison, the average M-N-N-B torsion (τ) angles in $TlBp^{tBu2}$ and $U(Bp^{tBu,Me})_2I$ are 22.2(13) and 19.4(10)°, respectively.[75,80] In **13**, the ligand containing N(5)-N(8) has τ values of 20.00(8) and 22.28(8)°, which are similar to those in $TlBp^{tBu2}$ and $U(Bp^{tBu,Me})_2I$. Furthermore, this ligand has a nitrogen-nitrogen-nitrogen-nitrogen torsion angle of 1.64(7)°, which is similar to the values in **16** and $TlBp^{tBu2}$. Thus, the ligand containing N(5)-N(8) adopts a typical Bp^{tBu2} coordination mode to the strontium ion. By contrast, the ligand in **13** containing N(1)-N(4) has τ values of 31.82(7) and 40.73(7)°, and has a nitrogen-nitrogen-nitrogen-nitrogen torsion angle of 45.68(7)°. The bending of the ligand containing N(1)-N(4) appears to arise through avoidance of steric interactions between the *tert*-butyl methyl groups on C(18), C(37), and C(41). There are no hydrogen-hydrogen interactions with these methyl groups that are shorter than 2.40 Å, but only because the ligand distorts to avoid such crowding. There are close hydrogen-hydrogen contacts in **13** (1.92(2) Å, hydrogen atoms on C(31) and C(42); 2.26(2) Å, hydrogen atoms on C(11) and C(20)) that are associated with *tert*-butyl groups on the 5-positions of the pyrazolyl moieties. Such crowding is consistent with the observation by Chisholm and Parkin that the 5-*tert*-butyl substituents lead to τ values of up to 24.4° in complexes containing the Tp^{tBu2} ligand.[80] Complex **14** has the most distorted metal-ligand bonding among **13**-**15**. The ligand in **14** containing N(1)-N(4) has τ values of 31.87(23) and 53.65(20)°, while the values in the ligand containing N(5)-N(8) are 27.55(24) and 60.90(19)°. The nitrogen-nitrogen-nitrogen-nitrogen torsion angles in **14** are 59.6(2) (N(1)-N(4)) and 64.6(2)° (N(5)-N(8)). The extreme distortions in **14** appear to arise from the crowded coordination sphere resulting from the tetrahydrofuran ligand and avoidance of *tert*-butyl/*tert*-butyl steric interactions. There are close 5-*tert*-butyl/5'-*tert*-butyl methyl group hydrogen-hydrogen contacts in **14** of 2.22(2) (hydrogen atoms on C(10) and C(21)) and 2.32(2) Å (hydrogen atoms on C(31) and C(43)). Most of the *tert*-butyl groups in **14** are situated over adjacent pyrazolyl group C_3N_2 cores, in between the *tert*-butyl groups attached to the cores. In **15**, the ligand containing N(1)-N(4) has τ values of 44.45(13) and 24.14(14)°, while the analogous values for the ligand containing N(5)-N(8) are 47.83(14) and 25.53(16)°. The nitrogen-nitrogen-nitrogen-nitrogen torsion angles in **15** are 40.5(1) (N(1)-N(4)) and 44.5(1)° (N(5)-N(8)). These torsion angles are smaller than the related values in **14**, perhaps because **15** has a lower coordination number. As in **14**, the ligands in **15** distort to find positions where *tert*-butyl methyl group steric interactions are minimized. The 5-*tert*-butyl groups within each ligand in **15** are forced to reside close to each other, which leads to a short hydrogen-hydrogen contact of 2.35(2) Å between the methyl groups containing C(10) and C(20).

Important structural aspects of **13-15** include the κ^3-N,N,H-Bp^{tBu2} ligands and the highly distorted ligand bonding modes that are imparted by accommodation of the bulky *tert*-butyl groups within the coordination sphere. κ^3-N,N,H-coordination of Bp-based ligands is common.[59,75] However, few group 2 Bp complexes have been structurally characterized. The molecular structure of $MgBp_2(THF)$ was recently reported, and features one κ^3-N,N,H-Bp ligand with a long magnesium-hydrogen distance of 2.69 Å.[78] The complex $CaTp^{tBu}{}_2$ exists as Ca(κ^3-N,N,N-Tp^{tBu})(κ^3-N,N,H-Tp^{tBu}), due to the steric bulk of the 3-*tert*-butyl substituents on the pyrazolyl groups.[84] The calcium-hydrogen distance in the κ^3-N,N,H-Tp^{tBu} ligand is 2.47(2) Å. A strontium complex containing a Bp-like κ^3-C,C,H-bis(imidazolin-2-ylidene-1-yl)borate ligand, $Sr(BH_2Im^{tBu}{}_2)(N(SiMe_3)_2)(THF)_2$, has a strontium-hydrogen distance of 2.87(3) Å to one of the boron-bound hydrogen atoms, compared to related values of 2.56(1) and 2.59(1) Å in **13**.[85] In view of the low coordination number obtained by coordination of four nitrogen atoms of the two Bp^{tBu2} ligands in **13-15** and the ionic bonding in these complexes, the presence of strong metal-hydrogen interactions to one boron-bound hydrogen atom in each ligand is not surprising. Chisholm and Parkin have demonstrated that steric repulsion between the pyrazolyl 5-*tert*-butyl substituents in metal complexes containing Bp^{tBu2} and Tp^{tBu2} ligands lead to τ values of 17.3-24.4°.[75,76,80] Complexes **13-15** contain similar 5-*tert*-butyl crowding, as described above, and such interactions certainly contribute to the observed ligand distortions. However, the τ values in **16**, $TlBp^{tBu2}$,[75] and other complexes containing $Tp^{tBu}{}_2$ ligands[80] do not exceed 25°, whereas the τ values in **13-15** span 20 to 61°. The large τ values in **13-15** are accompanied by large nitrogen-nitrogen-

nitrogen-nitrogen torsion angles (40-65°), compared to nitrogen-nitrogen-nitrogen-nitrogen torsion angles of 0.3(15) to 20.8(12)° in **16**, $TlBp^{tBu2}$,[75] and $U(Bp^{tBu,Me})_2I$.[81] As documented herein, these additional ligand distortions in **13-15** arise from accommodation of two bulky Bp^{tBu2} ligands about the group 2 metal ions. Specifically, this work suggests that the large distortions in metal-ligand bonding arise from interligand 3-*tert*-butyl steric interactions within the coordination spheres of **13-15**.

Table 8. Crystal data and data collection parameters for **13-16**.

	13	**14**	**15**	**16**
Formula	$C_{44}H_{80}B_2N_8Sr$	$C_{48}H_{88}B_2BaN_8O$	$C_{44}H_{80}B_2Ba$	$C_{22}H_{41}BN_4$
FW	830.40	952.22	880.12	372.40
Space group	P1bar	P1bar	P1bar	$P2_1/c$
a (Å)	9.9420(3)	11.9236(4)	10.4116(3)	12.1330(3)
b (Å)	12.0663(4)	14.9379(5)	13.6556(4)	10.5005(3)
c (Å)	20.9332(6)	17.8692(5)	19.4015(6)	19.2542(4)
α (°)	74.0190(10)	95.582(2)	107.4940(10)	
β (°)	87.174(2)	109.115(2)	94.077(2)	107.9330(10)
γ (°)	89.441(2)	112.563(2)	105.4050(10)	
V ($Å^3$)	2411.21(13)	2684.92(15)	2501.92(13)	2333.86(10)
Z	2	2	2	4
T (K)	100(2)	100(2)	100(2)	100(2)
λ (Å)	0.71073	0.71073	0.71073	0.71073
ρ_{calc} g cm^{-3}	1.144	1.178	1.168	1.060
μ mm^{-1}	1.155	0.779	0.829	0.062
R(F) (%)	3.15	4.42	3.56	4.38
Rw(F) (%)	7.34	7.43	8.39	11.15

$R(F) = \sum \| Fo | - | Fc \| / \sum | Fo |$; $Rw(F) = [\sum w(Fo^2 - Fc^2)^2 / \sum w(Fo^2)^2]^{1/2}$ for $I > 2\sigma(I)$.

Table 9. Selected bond lengths (Å) and angles (deg) for **13**.

Sr-N(1)	2.5636(7)	Sr-N(2)	3.2067(7)
Sr-N(3)	2.6444(7)	Sr-N(4)	3.2021(7)
Sr-N(5)	2.5677(7)	Sr-N(6)	3.2950(7)
Sr-N(7)	2.5606(8)	Sr-N(8)	3.3091(7)
Sr-H(B(1))	2.56(1)	Sr-H(B(2))	2.59(1)
N(1)-Sr-N(2)	24.70(2)	N(1)-Sr-N(3)	78.84(2)
N(1)-Sr-N(4)	72.10(2)	N(2)-Sr-N(3)	57.99(2)
N(2)-Sr-N(4)	47.54(2)	N(3)-Sr-N(4)	25.02(2)
N(5)-Sr-N(6)	23.25(2)	N(5)-Sr-N(7)	69.99(2)
N(5)-Sr-N(8)	62.42(2)	N(6)-Sr-N(7)	62.67(2)
N(6)-Sr-N(8)	47.16(2)	N(7)-Sr-N(8)	22.92(2)
N(2)-B(1)-N(4)	110.81(7)	N(6)-B(2)-N(8)	113.76(7)
N(1)-N(2)-B(1)	116.31(7)	N(3)-N(4)-B(1)	115.30(7)
N(5)-N(6)-B(2)	116.18(7)	N(7)-N(8)-B(2)	115.39(7)

Figure 13. Perspective view of **13** with thermal ellipsoids at the 50% probability level.

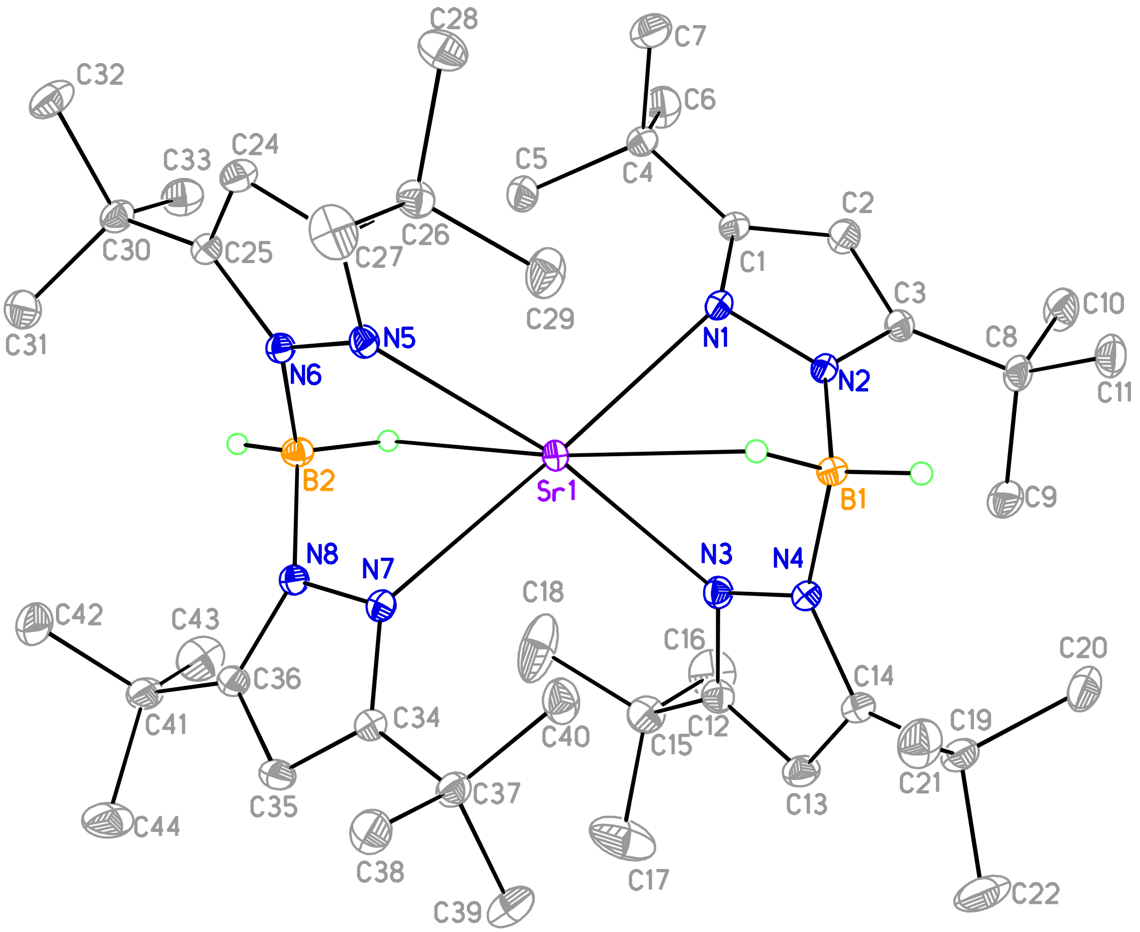

Table 10. Selected bond lengths (Å) and angles (deg) for **14**.

Ba-N(1)	2.840(2)	Ba-N(2)	3.491(2)
Ba-N(3)	2.746(2)	Ba-N(4)	3.301(2)
Ba-N(5)	2.807(2)	Ba-N(6)	3.485(2)
Ba-N(7)	2.765(2)	Ba-N(8)	3.233(2)
Ba-O	2.701(2)	Ba-H(B(1))	2.83(2)
Ba-H(B(2))	2.89(2)	N(1)-Ba-N(3)	82.24(6)
N(1)-Ba-N(2)	22.38(5)	N(2)-Ba-N(3)	69.32(6)
N(1)-Ba-N(4)	58.15(5)	N(3)-Ba-N(4)	24.32(5)
N(2)-Ba-N(4)	114.1(2)	N(5)-Ba-N(7)	85.51(6)
N(5)-Ba-N(6)	22.22(5)	N(6)-Ba-N(7)	70.45(5)
N(5)-Ba-N(8)	60.11(5)	N(7)-Ba-N(8)	25.40(5)
N(6)-Ba-N(8)	46.43(5)	N(3)-N(4)-B(1)	114.6(2)
N(1)-N(2)-B(1)	117.2(2)	N(7)-N(8)-B(2)	113.90(19)
N(5)-N(6)-B(2)	117.9(2)	N(6)-B(2)-N(8)	114.9(2)
N(2)-B(1)-N(4)	114.1(2)		

Figure 14. Perspective view of **14** with thermal ellipsoids at the 50% probability level.

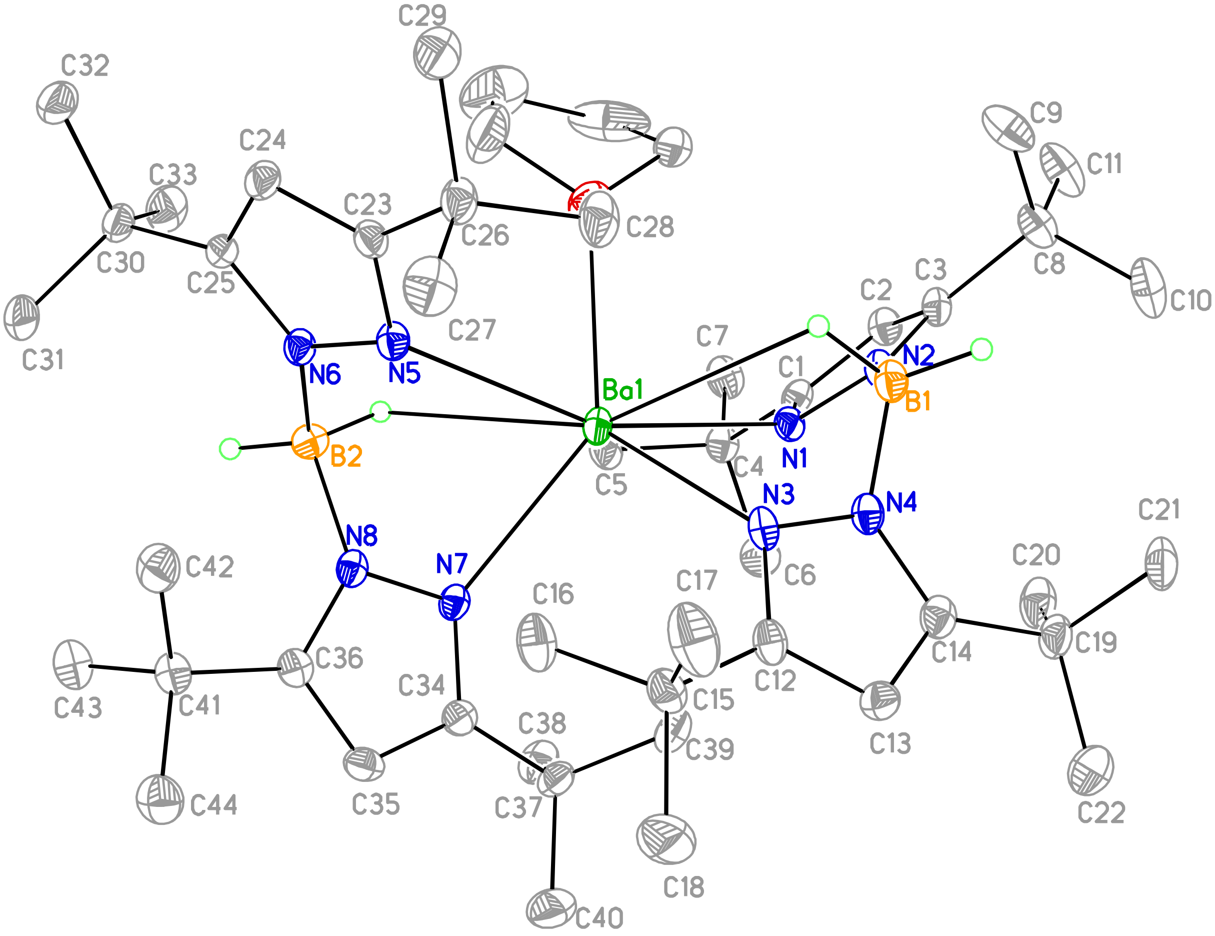

Table 11. Selected bond lengths (Å) and angles (deg) for **15**.

Ba(1)-N(1)	2.7933(1)	Ba(1)-N(2)	3.373(1)
Ba(1)-N(3)	2.7417(1)	Ba(1)-N(4)	3.459(1)
Ba(2)-N(5)	2.7803(1)	Ba(2)-N(6)	3.2878(1)
Ba(2)-N(7)	2.7797(1)	Ba(2)-N(8)	3.458(2)
Ba(1)-H(B(1))	2.71(2)	Ba(2)-H(B(2))	2.66(2)
N(1)-Ba(1)-N(2)	23.51(4)	N(1)-Ba(1)-N(3)	70.69(4)
N(1)-Ba(1)-N(4)	53.43(4)	N(2)-Ba(1)-N(3)	65.95(4)
N(2)-Ba(1)-N(4)	44.25(3)	N(3)-Ba(1)-N(4)	22.21(3)
N(5)-Ba(2)-N(6)	24.63(4)	N(5)-Ba(2)-N(7)	72.09(4)
N(5)-Ba(2)-N(8)	54.44(4)	N(6)-Ba(2)-N(7)	67.16(4)
N(6)-Ba(2)-N(8)	45.01(4)	N(7)-Ba(2)-N(8)	22.55(3)
N(1)-N(2)-B(1)	115.34(12)	N(3)-N(4)-B(1)	116.35(13)
N(5)-N(6)-B(2)	117.34(12)	N(7)-N(8)-B(2)	116.10(13)
N(2)-B(1)-N(4)	110.41(13)	N(6)-B(2)-N(8)	111.61(14)

Figure 15. Perspective view of **15** with thermal ellipsoids at the 50% probability level.

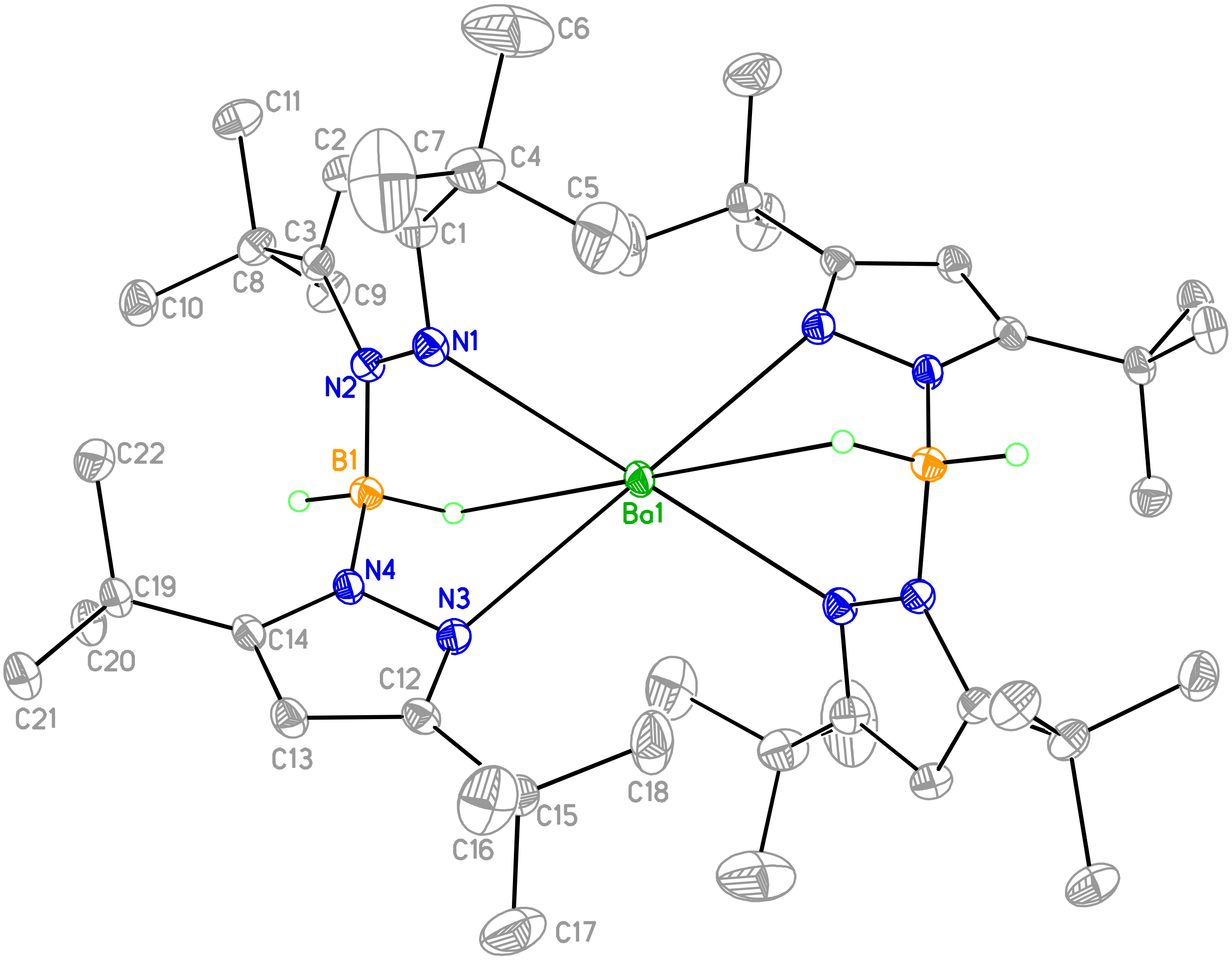

Table 12. Selected bond lengths (Å) and angles (deg) for **16**.

B-N(2)	1.558(2)	B-N(4)	1.596(2)
N(1)-N(2)	1.379(1)	N(3)-N(4)	1.363(1)
N(1)-C(1)	1.336(1)	C(1)-C(2)	1.401(2)
C(2)-C(3)	1.391(2)	C(3)-N(2)	1.361(1)
N(3)-C(12)	1.341(1)	C(12)-C(13)	1.389(2)
C(13)-C(14)	1.399(2)	C(14)-N(4)	1.350(1)
B-N(2)-N(1)	117.85(8)	B-N(4)-N(3)	118.46(8)
N(2)-B-N(4)	109.20(9)		

Figure 16. Perspective view of **16** with thermal ellipsoids at the 50% probability level.

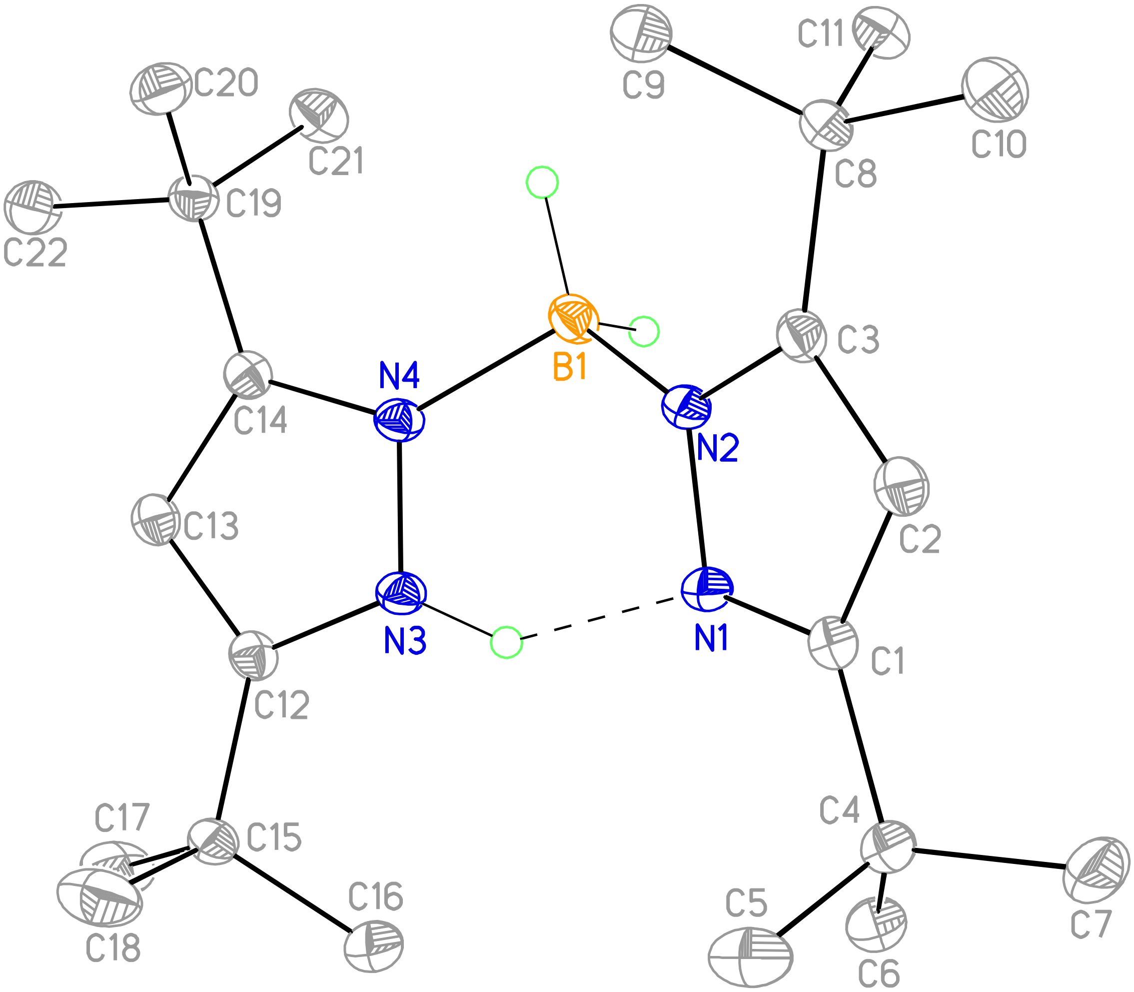

Table 13. Selected metrical parameters for **13-16** and related complexes.

Complex	N-N-N-N torsion angle (°)	M-N-N-B torsion angle (°)
13	N(1)-N(2)-N(4)-N(3) 45.68(7)	Sr-N(1)-N(2)-B(1) 31.82(7)
	N(5)-N(6)-N(8)-N(7) 1.64(7)	Sr-N(3)-N(4)-B(1) 40.73(7)
		Sr-N(5)-N(6)-B(2) 22.28(8)
		Sr-N(7)-N(8)-B(2) 20.00(8)
14	N(1)-N(2)-N(4)-N(3) 59.6(2)	Ba-N(1)-N(2)-B(1) 31.87(23)
	N(5)-N(6)-N(8)-N(7) 64.6(2)	Ba-N(3)-N(4)-B(1) 53.65(20)
		Ba-N(5)-N(6)-B(2) 27.55(24)
		Ba-N(7)-N(8)-B(2) 60.90(19)
15	N(1)-N(2)-N(4)-N(3) 40.5(1)	Ba(1)-N(1)-N(2)-B(1) 44.45(13)
	N(5)-N(6)-N(8)-N(7) 44.5(1)	Ba(1)-N(3)-N(4)-B(1) 24.14(14)
		Ba(2)-N(5)-N(6)-B(2) 47.83(14)
		Ba(2)-N(7)-N(8)-B(2) 25.53(16)
16	N(1)-N(2)-N(4)-N(3) 8.36(8)	
Tl(Bp^{tBu2})[19]	N(1)-N(2)-N(4)-N(3) 0.3(15)	Tl-N(2)-N(1)-B -20.8(13)
		Tl-N(4)-N(3)-B -23.7(13)
U(Bp^{tBu,Me})$_2$I[26]	N(1)-N(5)-N(6)-N(2) 20.8(12)	U-N(1)-N(5)-B(1) 19.3(10)
	N(3)-N(7)-N(8)-N(4) 20.8(12)	U-N(2)-N(6)-B(1) 21.3(10)
		U-N(3)-N(7)-B(2) 17.6(10)
		U-N(4)-N(8)-B(2) 19.4(11)

Volatility and Thermal Decomposition. To assess thermal stability and volatility of **12-15,** thermogravimetric analysis (TGA), solid state decomposition point measurements, and preparative sublimations were carried out. A summary of the sublimation and decomposition data for **12**, **13**, and **15** is found in Table 14. Complex **14** was not studied in detail, since it loses tetrahydrofuran at low temperatures and converts to **15**. Among the series, **13** sublimed at 190 °C/0.05 Torr with the highest recovery (80.9%) and lowest residue (3.6%). Complexes **12** and **15** sublimed at 185 and 205 °C/0.05 Torr with recoveries of 70.6% and 66.0%, respectively. Complexes **12** and **15** had nonvolatile residues of 8.1 and 10.2 %, respectively. The solid state decomposition temperatures of **12**, **13**, and **15** were 300, 325, and 280 °C, respectively.

Table 14. Sublimation temperature, percent recovery, percent nonvolatile residue, and decomposition temperatures for **12**, **13**, and **15**.

Complex	Sublimation Temperature (°C/0.05 torr)	% Recovery	% Nonvolatile Residue	Solid State Decomposition Temperature (°C)
12	185	70.6	8.1	300
13	190	80.9	3.6	325
15	205	66.0	10.2	280

Thermogravimetric analyses were performed on **12**-**15** to understand their thermal stabilities and volatilities (Figure 17). Complexes **12** and **13** have similar TGA traces with one step sublimations occurring between 115-320 °C and 115-290 °C, respectively. The residues for **12** and **13** were 20 and 25% upon reaching 350 °C, which indicates some self-decomposition during the analyses. The TGA trace for **15** has two weight loss events that are not clearly separated. The first event occurs from 115 to 227 °C and the second occurs from 230 to 308 °C, resulting in a final residue of 29%. The TGA trace for **14** shows three weight loss regimes. The first event occurs from 78 to 126 °C and likely corresponds to loss of THF (observed loss = 9% at 150 °C; calculated for THF loss = 8%). Two additional weight loss events were observed from 188 to 292 °C and 398 to 482 °C. A final residue of 26% was observed at 500 °C. The TGA traces for **14** and **15** differ significantly, which suggests that the tetrahydrofuran ligand in **14** has a large impact on its decomposition. Flame tests on the TGA residues of **13** and **15** after reaching 550 ºC revealed bright red and yellow-green emissions, respectively, which were identical to the emission colors observed with $SrTp_2$ (**1**), $SrCl_2•(H_2O)_2$, $[BaTp_2]_2$ (**2**), and $Ba(OH)_2•(H_2O)_8$. Hence, the TGA residues of **12** and **15** contain metal ions. A similar flame test on the TGA residue of **12** showed a blue-green emission, which was identical to the flame test for $CaTp_2$. A flame test using $CaCl_2•(H_2O)_2$ showed red-orange emission. It is likely that the green emission of boron is more intense than the calcium emission, and thus the presence of calcium in the TGA residue of **12** is likely but not conclusively established.

Figure 17. Thermogravimetric analysis traces of **12-15** at 10 °C/min.

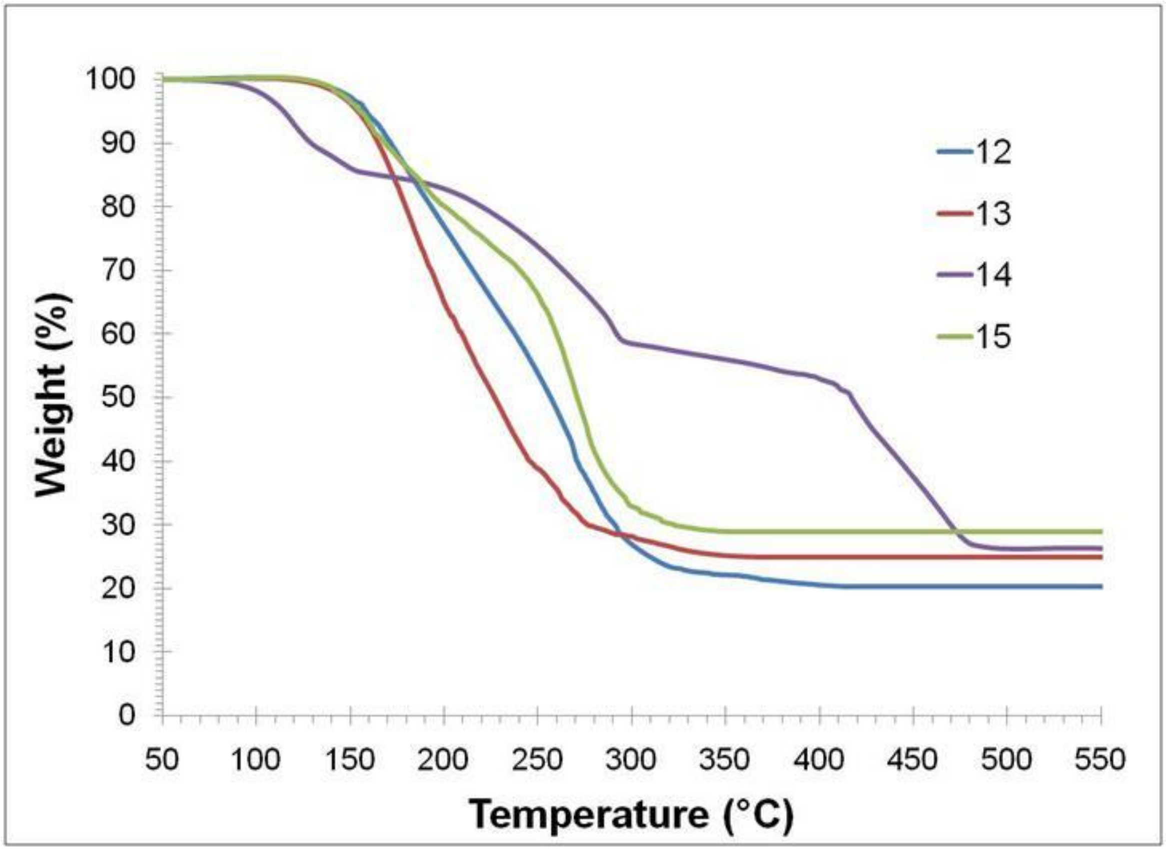

Among **12-15**, **12** and **13** exhibit the highest thermal stabilities and highest volatilities. Complex **14** loses tetrahydrofuran at <100 ºC, which corresponds to a decomposition reaction and makes it less useful as a film growth precursor. Previous work with group 2 precursors showed that the use of neutral donors to saturate the metal coordination spheres usually affords complexes with low thermal stability, due to facile neutral ligand loss facilitated by the low Lewis acidities of group 2 ions.[86] However, the relatively high residues observed in the TGA traces and preparative sublimations, as well as the moderate solid state decomposition temperatures, imply some decomposition with **12-15** and limit their potential as group 2 ALD precursors. For comparison, the solid state decomposition temperatures of $SrTp_2$ (**1**) (363 °C), $SrTp^{Et2}_2$ (**6**) (>400 °C), and $BaTp^{Et2}_2$ (**7**)

(~380 °C) are considerably higher than those of **12**, **13**, and **15**. The boron-hydrogen bonds in 1**2-15** are probably the most reactive sites, and are not shielded from electrophilic attack as well as those in **1**, **6**, and **7**. Additionally, **12-15** contain two potentially reactive boron-hydrogen bonds per ligand, compared to one such bond per Tp-based ligand. Finally, while **12**, **13**, and **15** pose little advantage over **1**, **6**, **7**, and related Tp species as ALD precursors, their thermal stabilities are considerably higher than many group 2 CVD precursors and they may find applications in this area.[1]

3.3 Conclusions

Complexes of calcium, strontium, and barium containing κ^3-N,N,H-Bp^{tBu2} ligands have been synthesized and structurally characterized. While these complexes are not as thermally stable as **1**, **6**, and **7**, they still may find use in CVD, since they are more thermally stable than many existing CVD precursors. Additionally, the κ^3-N,N,H-Bp^{tBu2} ligands are highly distorted upon complexation to strontium and barium due to intraligand and interligand *tert*-butyl interactions. Distortions to this degree have not been previously observed for existing metal complexes containing Bp-based ligands and suggest that the Bp^{tBu2} ligand may be able to accommodate a variety of metal sizes to form stable complexes.

3.4 Experimental Section

General Considerations. All reactions were performed under argon using standard glovebox or Schlenk line techniques. Tetrahydrofuran was distilled from sodium benzophenone ketyl. Hexane was distilled from P_2O_5. Anhydrous pentane was purchased from Alfa Aesar. tBu_2pzH was synthesized by a literature procedure.[87] $TlBp^{tBu2}$ was prepared by salt metathesis with $LiBp^{tBu2}(THF)$, otherwise following a previously reported procedure that employed $LiBp^{tBu2}$.[75] All other starting materials and solvents were purchased from Acros or Aldrich Chemical Company.

^{1}H and $^{13}C\{^{1}H\}$ NMR spectra were obtained at 400 and 125 MHz in benzene-d_6, respectively. Infrared spectra were obtained using Nujol as the medium. Elemental analyses were performed by Midwest Microlab, Indianapolis, Indiana. Melting points were obtained on an Electrothermal Model 9200 melting point apparatus and are uncorrected. TGA analyses were conducted on a Perkin Elmer Pyris 1 TGA system between 50 and 550 °C, using nitrogen as the flow gas with a heating rate of 10 °C/min. The carbon microanalysis values for **3** were consistently low, in spite of five separate analyses with and without the addition of V_2O_5 as a combustion enhancer. Preparative sublimations and thermal decomposition points were conducted as previously described in chapter 2.

Preparation of $LiBp^{tBu2}$(THF) (11). A 100-mL Schlenk flask was charged with tBu_2pzH (4.450 g, 24.68 mmol), toluene (20 mL), and a stir bar. To the clear solution, 6.18 mL of a 2 M $LiBH_4$ solution in tetrahydrofuran (0.269 g, 12.4 mmol) was added by syringe. The mixture was stirred at ambient temperature for 0.25 h, at which point the volatile components were removed under reduced pressure. Toluene (20 mL) was added to the resultant white residue, and the mixture was refluxed for 18 h. Hydrogen evolution slowly occurred during the reflux period. The mixture was cooled to room temperature, and then the volatile components were removed under reduced pressure to afford a colorless gel-like residue. Tetrahydrofuran (15 mL) was added to the residue slowly, which resulted in a clear solution. The solution was stored in a -23 °C freezer for 18 h, during which time colorless crystals of **11** formed (2.700 g, 49%): mp 200 °C (dec.); IR (Nujol, cm^{-1}) $\nu_{B\text{-}H}$ = 2088-2479, $\nu_{C\text{-}N}$ = 1522; ^{1}H NMR (C_6D_6, 23 °C, δ) 6.11 (s, 2H, 4-C*H*), 4.50 (broad s, 2H, BH_2), 3.48 (t, J

= 6.8 Hz, 4H, $CH_2C\mathit{H}_2O$), 1.62 (s, 18H, $C(C\mathit{H}_3)_3$), 1.36 (s, 18H, $C(C\mathit{H}'_3)_3$), 1.29 (multiplet, 4H, $C\mathit{H}_2CH_2O$); $^{13}C\{^1H\}$ NMR (C_6D_6, 23 °C, ppm) 159.44 (s, C_q), 157.81 (s, C'_q), 99.10 (s, 4-*C*H), 68.42 (s, $CH_2\mathit{CH}_2O$), 32.58 (s, $\mathit{C}(CH_3)_3$), 32.03 (s, $\mathit{C}'(CH_3)_3$), 31.45 (s, $C(\mathit{C}H_3)_3$), 31.14 (s, $C(\mathit{C}'H_3)_3$), 25.35 (s, $CH_2\mathit{CH}_2O$).

Anal. Calcd for $C_{26}H_{48}BN_4Li$: C, 69.33; H, 10.74; N, 12.44. Found: C, 69.39; H, 10.67; N, 12.53.

Preparation of $CaBp^{tBu2}_2$ (12). A 100-mL Schlenk flask was charged with CaI_2 (0.200 g, 0.680 mmol), $TlBp^{tBu2}$ (0.253 g, 1.360 mmol), and a stir bar. Tetrahydrofuran (30 mL) was added, resulting in the immediate formation of a bright yellow precipitate of thallous iodide. The reaction mixture was stirred for 18 h at ambient temperature, at which time the volatile components were removed under reduced pressure to afford a yellow residue. Hexane (30 mL) was added to this solid, and the resulting mixture was filtered through a 3-cm pad of Celite on a medium glass frit to yield a clear filtrate. Removal of the volatile components and vacuum drying for 1 h at 0.05 Torr afforded **12** as a white powder (0.180 g, 67%). An analytical sample and X-ray quality crystals were obtained by crystallization from hexane at -23 °C: mp 209-210 °C; IR (Nujol, cm^{-1}) $\nu_{B\text{-}H}$ = 2066-2564, $\nu_{C\text{-}N}$ = 1524; ^1H NMR (C_6D_6, 23 °C, δ) 5.98 (s, 4H, 4-C*H*), 4.58 (broad s, 4H, $B\mathit{H}_2$), 1.50 (s, 36H, $C(C\mathit{H}_3)_3$), 1.17 (s, 36H, $C(C\mathit{H}'_3)_3$); $^{13}C\{^1H\}$ NMR (C_6D_6, 23 °C, ppm) 161.45 (s, C_q), 158.99 (s, C'_q), 100.96 (s, 4-*C*H), 32.65 (s, $\mathit{C}(CH_3)_3$), 32.03 (s, $\mathit{C}'(CH_3)_3$), 31.73 (s, $C(\mathit{C}H_3)_3$), 31.16 (s, $C(\mathit{C}'H_3)_3$).

Anal. Calcd for $C_{44}H_{80}B_2CaN_8$: C, 67.51; H, 10.30; N, 14.31. Found: C, 67.47; H, 10.17; N, 14.36.

Preparation of SrBp$^{tBu2}{}_2$ (13). In a fashion similar to the preparation of **2**, treatment of SrI_2 (0.292 g, 0.855 mmol) with TlBp^{tBu2} (0.971 g, 1.69 mmol) afforded **13** as a white solid (0.550 g, 79%). The analytical sample and single crystals for the X-ray crystallographic analysis were obtained by sublimation at 190 °C/0.05 Torr (0.243 g, 35%): mp 202-204 °C; IR (Nujol, cm^{-1}) $\nu_{B\text{-}H}$ = 2081-2537, $\nu_{C\text{-}N}$ = 1523; ^{1}H NMR (C_6D_6, 23 °C, δ) 5.96 (s, 4H, 4-C*H*), 4.50 (broad s, 4H, BH_2), 1.48 (s, 36H, C(CH_3)$_3$), 1.16 (s, 36H, C(CH'_3)$_3$); ^{13}C{^{1}H} NMR (C_6D_6, 23 °C, ppm) 161.03 (s, C_q), 158.80 (s, C'_q), 100.33 (s, 4-*C*H), 32.53 (s, *C*(CH_3)$_3$), 32.18 (s, C'(CH_3)$_3$), 31.31 (s, C(CH$_3$)$_3$), 31.18 (s, C(C'H$_3$)$_3$).

Anal. Calcd for $C_{44}H_{80}B_2N_8Sr$: C, 63.64; H, 9.71; N, 13.49. Found: C, 61.52; H, 9.37; N, 13.97.

Preparation of BaBp$^{tBu2}{}_2$(THF) (14). In a fashion similar to the preparation of **12**, treatment of BaI_2 (0.227 g, 0.580 mmol) with TlBp^{tBu2} (0.669 g, 1.162 mmol) afforded **14** as a white solid (0.553 g, 63%). The analytical sample and single crystals for the X-ray crystallographic analysis were obtained by crystallization from pentane at -23 °C: mp 155 °C (dec.); IR (Nujol, cm^{-1}) $\nu_{B\text{-}H}$ = 2079-2493, $\nu_{C\text{-}N}$ = 1519; ^{1}H NMR (C_6D_6, 23 °C, δ) 6.00 (s, 4H, 4-C*H*), 4.52 (broad s, 4H, BH_2), 3.55 (t, J = 6.2 Hz, 4H, CH$_2$CH_2O), 1.45 (s, 36H, C(CH_3)$_3$) 1.35 (m, 4H, CH_2CH$_2$O), 1.21 (s, 36H, C(CH'_3)$_3$); ^{13}C{^{1}H} NMR (C_6D_6, 23 °C, ppm) 160.57 (s, C_q), 158.42 (s, C'_q), 100.57 (s, 4-*C*H), 68.45 (s, CH$_2$$CH_2$O), 32.45 (s, *C*(C$H_3$)$_3$), 32.29 (s, C'(CH_3)$_3$), 31.09 (s, C(CH$_3$)$_3$), 30.66 (s, C(C'H$_3$)$_3$), 25.43 (s, CH$_2CH_2$O).

Anal. Calcd for $C_{48}H_{88}B_2BaN_8O$: C, 60.54; H, 9.31; N, 11.77. Found: C, 60.89; H, 9.03; N, 11.70.

Preparation of $BaBp^{tBu2}{}_2$ (15). Sublimation of **14** at 205 °C/0.05 Torr afforded colorless microcrystals of **15** (0.130 g, 37 %). The analytical sample and single crystals for the X-ray crystallographic analysis were obtained by crystallization from hexane at -23 °C: mp 183-185 °C; IR (Nujol, cm^{-1}) $\nu_{B\text{-}H}$ = 2091-2512, $\nu_{C\text{-}N}$ = 1523; ^1H NMR (C_6D_6, 23 °C, δ) 5.96 (s, 4H, 4-C*H*), 4.56 (broad s, 4H, BH_2), 1.45 (s, 36H, C(CH_3)$_3$), 1.17 (s, 36H, C(CH'_3)$_3$); $^{13}C\{^1H\}$ NMR (C_6D_6, 23 °C, ppm) 160.40 (s, C_q), 158.40 (s, C'_q), 100.27 (s, 4-*C*H), 32.39 (s, *C*(CH_3)$_3$), 32.32 (s, *C'*(CH_3)$_3$), 31.35 (s, C(*C*H_3)$_3$), 30.65 (s, C(*C*'H_3)$_3$).

Anal. Calcd for $C_{44}H_{80}B_2BaN_8$: C, 60.05; H, 9.16; N, 12.73. Found: C, 59.80; H, 9.05; N, 12.61.

Preparation of $BH_2(tBu_2pz)(tBu_2pzH)$ (16). A 100-mL Schlenk flask was charged with **1** (0.365 g, 0.810 mmol), diethyl ether (30 mL), and a stir bar. A second flask was charged with pivalic acid (0.083 g, 0.813 mmol), diethyl ether (10 mL), and a stir bar. The pivalic acid solution was slowly added by cannula to the flask containing **11**, resulting in the formation of a white precipitate. After 3 h, the reaction mixture was filtered through a 3-cm pad of Celite on a medium glass frit to yield a colorless filtrate. Removal of the volatile components under reduced pressure afforded **6** as a white powder (0.235 g, 78%). The analytical sample and crystals for the X-ray crystallographic analysis were obtained crystallization from hexane at -23 °C (0.120 g, 40%): mp 178-179 °C (dec.); IR (Nujol, cm^{-1}) $\nu_{B\text{-}H}$ = 2200-2527, $\nu_{C\text{-}N}$ = 1562; ^1H NMR (C_6D_6, 23 °C, δ) 6.02 (s, 2H, 4-C*H*), 4.50 (broad s, 2H, BH_2), 1.54 (s, 18H, C(CH_3)$_3$), 1.26 (s, 18H, C(CH'_3)$_3$); $^{13}C\{^1H\}$ NMR (C_6D_6, 23 °C, ppm) 158.15 (s, C_q), 156.97 (s, C'_q), 99.97 (s, 4-*C*H), 32.44 (s, *C*(CH_3)$_3$), 31.66 (s, *C'*(CH_3)$_3$), 30.63 (s, CH(*C*H_3)$_3$), 30.36 (s, C(*C*'H_3)$_3$).

Anal. Calcd for $C_{22}H_{41}BN_4$: C, 70.95; H, 11.10; N, 15.04. Found: C, 71.12; H, 11.31; N, 15.17.

X-Ray Crystallographic Structure Determinations of 13-16. Diffraction data were measured on a Bruker X8 APEX-II kappa geometry diffractometer with Mo radiation and a graphite monochromator. Frames were collected at 100 K with the detector at 40 mm, 0.3° between each frame, and were recorded for 5 or 10 s. APEX-II[73] and SHELX[74] software were used in the collection and refinement of the models. Crystals of 3 were colorless and irregular. 132194 total data were measured, averaging to 19520 unique data (Rint = 0.033). Hydrogen atoms were placed in observed or calculated positions. The asymmetric unit contains one complex with all atoms on general positions. Complex 4 was obtained as irregular colorless crystals. 74326 hkl data points were harvested which averaged to 13138 data (Rint = 0.090). Hydrogen atoms were placed in calculated positions. The complexes are discrete and mononuclear. Crystals of 5 appeared as colorless irregular fragments. 85889 reflections were counted, which averaged to 18027 independent data (Rint = 0.042). Hydrogen atoms were placed at calculated or observed positions. Crystals of 6 were obtained as colorless fragments. 72640 reflections were measured, yielding 6350 unique data (Rint = 0.054). Hydrogen atoms were placed in observed or calculated positions. The asymmetric unit contains one neutral molecule with an internal hydrogen bond between N(1) and N(3).

CHAPTER 4

Synthesis, Structural Characterization, and Properties of Heavier Alkaline Earth Complexes Containing Bis(pyrazolyl)borate or Bis(3,5-diisopropylpyrazolyl)borate Ligands

4.1 Introduction

Chapter 3 described the synthesis, structure, and properties of a series of calcium, strontium and barium complexes containing Bp^{tBu2} ligands. Complexes **12**, **13**, and **15** had sublimation temperatures between 185-205 °C/0.05 Torr. In this chapter, the synthesis and thermal stabilities of group 2 complexes containing the bis(pyrazolyl)borate (Bp) and the bis(3,5-diisopropylpyrazolyl)borate (Bp^{iPr2}) ligands were explored in an effort to reduce molecular weight, increase volatility, and hopefully retain high thermal stability.

In this chapter, the synthesis, structure, and properties of a series of calcium, strontium, and barium complexes containing Bp and Bp^{iPr2} ligands are described. These complexes also incorporate tetrahydrofuran ligands. In addition, attempted synthesis of the key starting material KBp^{iPr2} (**17**) by a literature method instead afforded the structurally novel complex $KTp^{iPr2}(iPr_2pzH)_3$ (**18**) (Tp^{iPr2} = tris(3,5-diisopropylpyrazolyl)borate; iPr_2pzH = 3,5-diiso-propylpyrazole). An alternate procedure for the synthesis of KBp^{iPr2} is described herein.

4.2 Results and Discussion

Synthetic Aspects. KBp was prepared in 72% yield using a literature procedure, which entailed thermolysis of a 1:2 molar ratio mixture of solid KBH_4 and pyrazole at 120

°C.[62] A previously reported synthesis of KBp^{iPr2} (**17**) relied upon heating a solid mixture of KBH_4 and iPr_2PzH in a 1:2 stoichiometry at 120 °C, followed by crystallization from hexane.[81] However, multiple attempts to reproduce this synthesis instead afforded KTp^{iPr2}(iPr_2PzH)$_3$ (**18**). Optimization involved conducting the thermolysis at 180 °C with a 1:6 stoichiometry of KBH_4 and iPr_2PzH, which afforded colorless crystals of **18** in 53% yield (eq 12). For comparison, KTp^{iPr2} was previously synthesized by heating a 1:3 molar ratio of solid KBH_4 and iPr_2PzH at 260 °C, followed by crystallization from pentane.[88] In the present work, **17** was synthesized in 56% yield by treatment of a 1:2 molar ratio of KBH_4 and iPr_2PzH in refluxing dimethylacetamide (DMAC), as described in the experimental section (eq 13). Complexes **17** and **18** are very soluble in tetrahydrofuran and toluene.

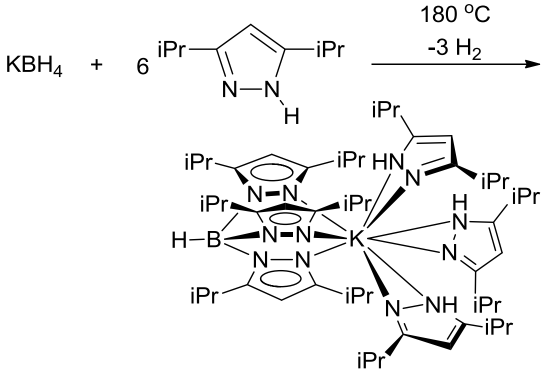

18, 53%

(12)

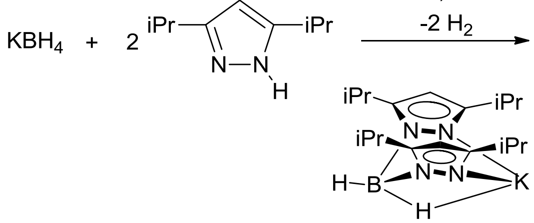

(13)

17, 56%

Treatment of MI_2 (M = Ca, Sr, Ba) with two equivalents of KBp or **17** yielded **19-24** as colorless crystalline solids upon workup (eq 14). Complexes **19** and **20** are very soluble in tetrahydrofuran and diethyl ether and are moderately soluble in hexane. By contrast, **21** is insoluble in hexane and diethyl ether, but is soluble in tetrahydrofuran. Complexes **22-24** are soluble in hexane, and their solubilities increase in the order **22** < **23** < **24**.

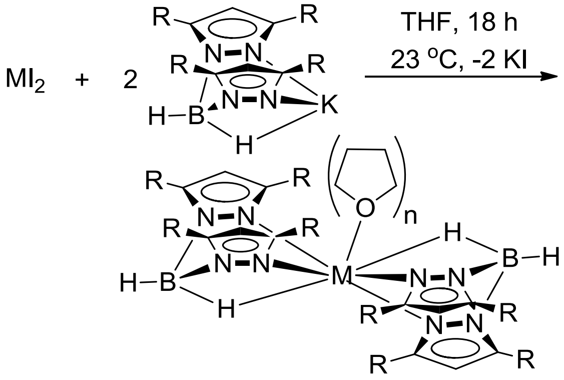

(14)

19, M = Ca, R = H, x = 2, 64%
20, M = Sr, R = H, x = 2, 81%
21, M = Ba, R = H, x = 4, 32%
22, M = Ca, R = iPr, x = 2, 63%
23, M = Sr, R = iPr, x = 2, 61%
24, M = Ba, R = iPr, x = 2, 48%

The compositions of **17-24** were assessed by spectral and analytical data, and by X-ray crystal structure determinations. In the ^1H NMR spectra of **17** and **22-24**, the 4-H atoms of the iPr_2pz groups were observed at δ 5.78 and 5.76, respectively. Additional resonances belonging to the magnetically inequivalent isopropyl groups were observed. The ^1H NMR spectra for **22-24** also contained resonances corresponding to two tetrahyrofuran ligands centered at δ 3.61 and 1.79, respectively. Similar to **17** and **22-24,** the ^1H NMR spectra for **18** showed the 4-H atom resonance of the Tp^{iPr2} ligand at δ 5.70, as well as the resonances from the magnetically inequivalent isopropyl groups. The three iPr_2pzH ligands in **18** showed the 4-H atom resonance at δ 5.84 and the methine and methyl resonances of the isopropyl groups at δ 2.60 and 1.21, respectively. A broad N-bound H resonance appeared at δ 9.98. Broad B-bound H atom resonances for **17** and **18** were centered at δ 3.45 and 4.90, respectively. The B-bound H atom resonances were not clearly observed in the ^1H NMR spectra of **22-24**, because the signals were too broad and overlapped with the downfield isopropyl methine and tetrahydrofuran 2-H atom resonances. The ^1H NMR spectra for **19-21** contained three resonances belonging to the three different protons from the pyrazolyl ring of the Bp ligand, with the 4-H resonance observed at about δ 6.0. All of the expected C atom resonances were observed in the $^{13}C\{^1H\}$ NMR spectra for **17-21**, **23**, and **24**. However, the $^{13}C\{^1H\}$ NMR spectrum for **22** only showed one C atom resonance at 25.79 ppm corresponding to the isopropyl methyl groups, instead of the expected two resonances. The methyl C atom resonances appear to overlap, which is supported by the inequivalent methyl proton resonances observed in the ^1H NMR spectrum of **22**. In the infrared spectra of **17** and **19-24**, the B-H stretches were observed in the range of 2248-2448 cm^{-1}. The C-N stretching frequencies were observed between 1492-1502 cm^{-1} and 1527-1532 cm^{-1} for **19-21** and **17** and **22-24**, respectively. The shift to higher wavenumbers for the C-N stretches in **17** and **22-24** appears to arise from the isopropyl substituents on the pyrazolyl groups, compared to H atoms in **19-21**. The infrared spectrum of **18** showed a B-H stretch at 2469 cm^{-1}, which is consistent with one B-H bond. Two C-N stretches in **18** were observed at 1529 and 1565 cm^{-1}, and correspond to the B-bound iPr_2pz moieities and the iPr_2pzH ligands in **18**. Furthermore, two N-H stretches at 3261 and 3358 cm^{-1} were observed, which arise from the iPr_2pzH ligands.

Evaluation of Thermal Stability and Volatility. Complexes **19-24** were studied by preparative sublimations, solid state decomposition temperature determinations, and thermogravimetric analysis (TGA) to assess their volatilities and thermal stabilities. Preparative sublimations of **19-24** between 160 and 220 °C at 0.05 Torr led to the vapor transport of complex mixtures of compounds, among which pyrazole (from **19-21**) or 3,5-diisopropylpyrazole (from **22-24**) were identified by ^{1}H NMR spectroscopy. The yields of sublimed materials were low, suggesting extensive decomposition prior to sublimation upon heating in the sublimation tube. The melting points for **19**, **20**, and **22-24** are 116, 121, 113, 168, and 167 °C, respectively. Upon melting, the liquid compounds exhibited gas evolution, which most likely corresponds to loss of the tetrahydrofuran ligands. After melting, **19**, **20**, and **22-24** remained colorless liquids until reaching temperatures between 330 and 360 °C, over which range the clear melts underwent rapid darkening (**19**, 360 ºC; **20**, 330 ºC; **22**, 340 ºC; **23**, 350 ºC; **24**, 348 ºC). Complex **21** melts at a higher temperature than the others (281 °C), and likewise shows gas evolution upon reaching the liquid state. The clear, colorless melt of **5** turned black rapidly at 330 °C, indicating thermal decomposition.

The TGA traces for **19-21** (Figure 18) show multiple weight loss regimes with final residues of 13, 42, and 67%, respectively, upon reaching 550 °C. After the initial weight losses for **4** (80-290 °C) and **5** (80-330 °C), the observed residual weights were 72 % and 91% , respectively. These weight residues likely correspond to tetrahydrofuran ligand loss, which would afford theoretical residues of 73 and 90%, respectively. In the TGA trace of **19**, two weight loss events occur between 70 and 250 °C, leading to a residual weight of 62% at 250 °C. This observed value is lower than the expected residue upon loss of two tetrahydrofuran ligands (70%). It is possible that the formation of $CaTp_2$ is occurring concurrently with tetrahydrofuran ligand loss. The TGA traces for **22-24** (Figure 19) show three major weight loss regimes, with final residues of 12, 25, and 26%, respectively, upon reaching 550 °C. The final residues for **22-24** are lower than those of **19-21**, perhaps because **22-24**, “MBp$^{iPr2}{}_2$”, or decomposition products thereof have more volatility than those of **19-21**. The first weight loss event in the TGA traces of **22-24** (**22**, 50-153 °C; **23**, 100-156 °C; **24**, 100-170 °C) show weight residues of 86, 85, and 85 %, respectively. These values correspond closely to the residues expected upon loss of the tetrahydrofuran ligands (**22**, 82%; **23**, 83%; **24**, 84 %). The TGA data for the strontium and barium complexes **20**, **21**, **23**, and **24** are consistent with tetrahydrofuran ligand loss at lower temperatures, followed by multiple decomposition steps that afford high weight residues at higher temperatures. For the calcium complexes **19** and **22**, the TGA indicates similar sequence. However, unlike the high weight residues for **20**, **21**, **23**, and **24**, **19** and **22** have lower final residual weights, consistent with the formation of volatile species during the TGA analyses.

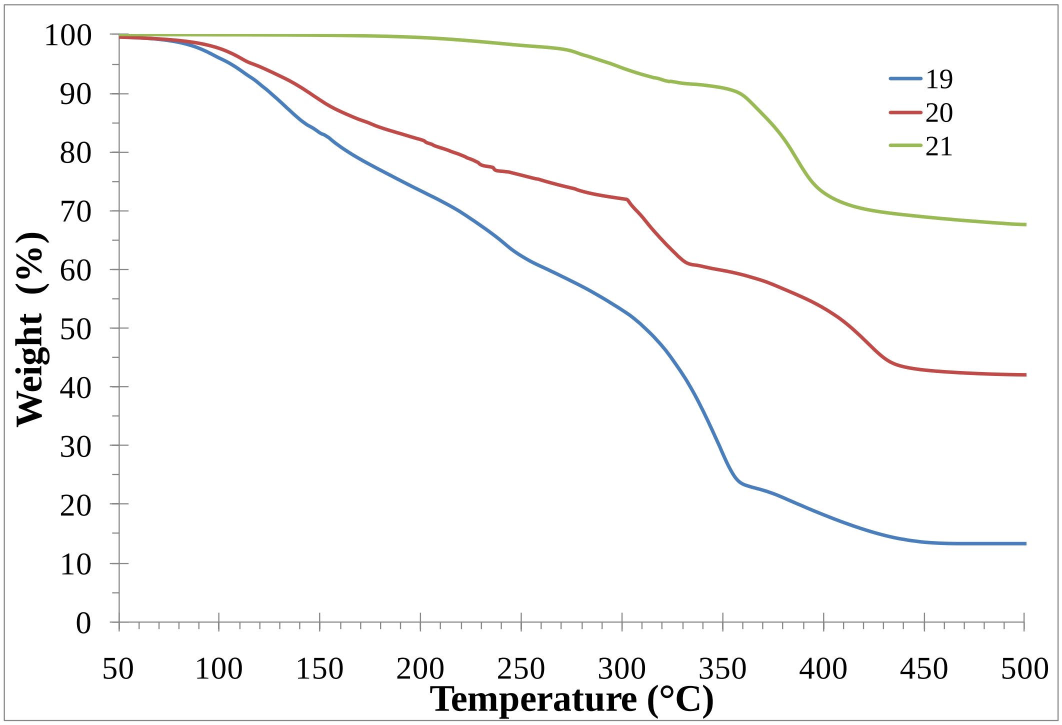

Figure 18. TGA traces of **19-21** from 50 to 550 °C at 10 °C/min under a flow of nitrogen.

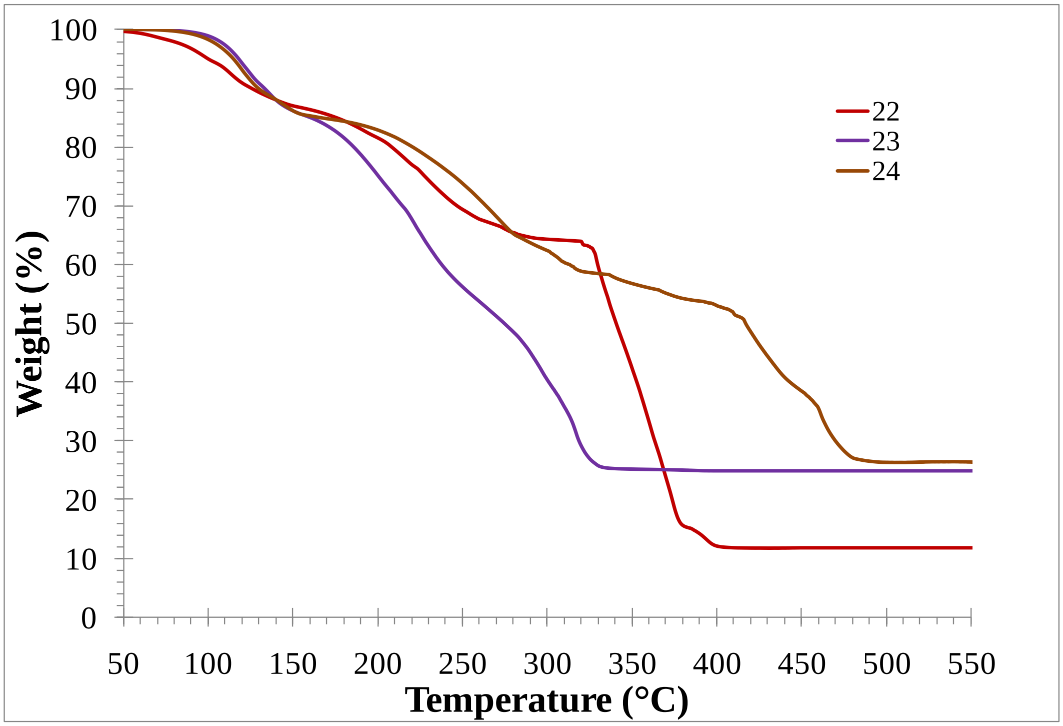

Figure 19. TGA traces of **22-24** from 50 to 550 °C at 10 °C/min under a flow of nitrogen.

Structural Aspects. The X-ray crystal structures of **18-24** were determined to establish the geometry about the metal centers and the bonding modes of the Bp and Bp^{iPr2} ligands. Experimental crystallographic data are summarized in Table 15, selected bond lengths and angles are given in Tables 16-20, and perspective views are presented in Figures 20-24. Complexes **23** and **24** are isostructural with **22**, and are not discussed specifically herein.

A perspective view of **18** is shown in Figure 20. The complex contains one κ^3-N,N,N Tp^{iPr2} ligand and three η^1-iPr_2pzH ligands, with overall distorted octahedral geometry about the K ion. The K-N bond distances associated with the Tp^{iPr2} ligand are 2.795(2), 2.822(2), and 2.912(2) Å, compared to very similar values of 2.782(3), 2.784(3), and 2.832(3) Å for the iPr_2pzH ligands. The average K-N bond distance found in **18** (2.82(4) Å) is similar to the related values in KTp^{tBu2} ($K\text{-}N_{avg}$ = 2.73(2) Å)),[80] $KTp^{Pic,Me}(H_2O)_2$ (Pic = 5-α-picolyl, $K\text{-}N_{avg}$ = 2.9(1) Å),[89] $KTp^{3Py,Me}(H_2O)$ (3Py = 3-pyridyl, $K\text{-}N_{avg}$ = 2.90(8) Å),[89] and $KTp^{R,H}$ (R = 2-methoxy-1,1-dimethylethyl, $K\text{-}N_{avg}$ = 2.692(2) Å).[65,90] The N-bound H atom of each iPr_2pzH ligand is directed toward the 2-N atoms of the Tp^{iPr2} ligand, suggesting the presence of weak intramolecular N-H···N hydrogen bonds. The pyrazolyl 2-N···H distances are 2.48(3) (to N(1)), 2.17(4) (to N(3)), and 2.26(3) Å (to N(5)). The sum of the van der Waals radii for N and H atoms is 2.75 Å,[82] so these interactions are consistent with hydrogen bonds. Further evidence of hydrogen bonding comes from broad N-H bond stretches in the infrared spectrum of **18** at 3261 and 3358 cm^{-1}. A sharp band at 3374 cm^{-1} was previously reported to arise from a non-hydrogen bonded N-H stretch in a iPr_2pzH adduct.[89] Accommodation of the isopropyl groups leads to significant steric congestion within the coordination sphere of **18**. B-N-N-M torsion angles have been proposed as a measure of the sterically-induced twisting of the pyrazoyl moieties in Tp-based ligands.[80] The B-N-N-K torsion angles in **18** range from 40.7(3) to 44.5(3)° (avg = 42(2)°), which are nearly double the corresponding torsion angles found in KTp^{tBu2}(C_6H_6) (avg = 23.4°), TlBp^{tBu2} (avg = 22.8°), and CsTp^{tBu2} (avg = 24.4°).[80] The larger torsion angles in **18**, compared to complexes containing the Tp^{tBu2} ligand, are caused by the extreme steric crowding that arises upon coordinating one Tp^{iPr2} and three iPr$_2$pzH ligands to the K ion. The structure of **18** is similar to that of [PbTp^{Me2}(Me$_2$pzH)$_3$]Cl, which contains one κ^3-Tp^{Me2} ligand and three Me$_2$pzH ligands arrayed with distorted octahedral geometry.[91] Unlike the hydrogen bonding in **18**, the three N-bound H atoms of the Me$_2$pzH ligands in [PbTp^{Me2}(Me$_2$pzH)$_3$]Cl form hydrogen bonds to the chloride counterion, apparently due to its higher basicity compared to the Tp^{Me2} N atoms that are bonded to the Pb^{2+} ion. In **18**, the 2-N atoms of the Tp^{iPr2} ligand are the most basic within the molecule, and it is not surprising that these N atoms act as hydrogen bond acceptors.

The molecular structures of **19-21** are similar and their perspective views are shown in Figures 21-23. Complexes **19** and **20** crystallize as monomeric complexes containing two Bp and two tetrahydrofuran ligands, with a coordination number of eight. By contrast, **21** contains two Bp and four tetrahydrofuran ligands, affording a coordination number of ten. In **19-21**, the Bp ligands adopt the κ^3-N,N,H coordination mode, through M-N bond formation to the 2-N atoms of the pyrazolyl fragments and M-H bond formation to one B-bound H atom per Bp ligand. κ^3-N,N,H coordination of Bp ligands is commonly observed in many metal complexes.[59b] Complexes **19-21** have M···H-B distances of 2.77(2) and 3.01(3) Å, 2.59(6) and 2.73(4) Å, and 3.23(3) and 3.33(2) Å, respectively. The sum of van der Waals radii for Ca + H, Sr + H, and Ba + H are 3.51, 3.69, and 3.88 Å, respectively.[82] As such, strong M-H interactions are present in **19-21**. The average Ca-N bond distance in **19** is

2.47(2) Å, which is similar to those in $CaTp_2$ (avg = 2.44(2) Å),[61b] $CaTp^{Me2}_2$ (avg = 2.454(2) Å),[61d] and $CaTp^{Et2}_2$ (**5**) (avg = 2.459(6) Å). The average Sr-N distance in **20** (2.64(2) Å) is slightly longer than those in $SrTp_2$ (**1**) (avg = 2.593(19) Å) and $SrTp^{Et2}_2$ (**6**) (avg = 2.606(9) Å). The average Ba-N distance in **21** is 2.88(2) Å, which again is longer than those in Tp-based complexes such as $BaTp^{Me2}_2$ (avg = 2.754(3) Å, 2.760(1) Å)[61a,d] and $BaTp^{Et2}_2$ (**7**) (avg = 2.78(2) Å). The slightly longer M-N distances in **19-21**, compared to related Tp complexes, is likely related to the higher coordination numbers in the former, which arise through tetrahydrofuran coordination and M-H bond formation. The M-O distances in **19** and **20** are 2.387(7) and 2.564(4) Å, respectively. The Ba-O bond lengths in **21** range from 2.788(1)-2.919(1) Å, with an average of 2.88(2) Å. The average N-B-N bond angles in **19-21** are 109.2(2), 109.2(3), and 110.3(4)°, respectively, indicating tetrahedral geometry about the boron atoms. The B-N-N-M torsion angles in **19** (0.72-8.62°) and **20** (2.39-7.37°) imply low steric congestion about the metal ions. The corresponding values in **21** are larger (0.20-20.02°) and suggest more steric congestion, consistent with the higher coordination number in **21** compared to **19** and **20**.

A perspective view of **22** is shown in Figure 24. Complex **22** is eight coordinate, and contains two κ^3-N,N,H-Bp^{iPr2} and two tetrahydrofuran ligands. The Ca-H distance in **22** (2.95(2) Å) is similar to the values in **19** (2.77(2), 3.01(3) Å), but is considerably longer than the related distances in $CaTp^{tBu}_2$ (2.47(2) Å)[84] and $Ca(C_5H_2(SiMe_3)_3)(HBEt_3)(THF)_2$ (2.21(4) Å).[92] The Ca-H interactions in **19**, **22**, and previously reported borohydride complexes are electrostatic, and the Ca-H distances appear to be determined by steric interactions about the Ca ion. In **19** and **22**, the coordination spheres are crowded with tetrahydrofuran ligands, which do not permit enough space for shorter Ca-H bonds. The Ca-N distances in **22** are

2.478(2) and 2.562(2) Å, respectively, with a Ca-O distance of 2.431(2) Å and a N-B-N bond angle of 110.9(2)°. The longer Ca-N distances in **22** versus **19** are likely related to the larger steric profile of the Bp^{iPr2} ligand compared to the Bp ligand. The B-N-N-Ca torsion angles in **22** are 4.4(2) (B-N(2)-N(1)-Ca) and 31.8(2)º (B-N(4)-N(3)-Ca), which are larger than those of **19** due to the higher steric congestion about the Ca ion arising from the isopropyl groups in **22**.

In **19** and **21,** the two M-H interactions are *anti* with respect to each other within each molecule, whereas **20** contains *syn* Sr-H units within each molecule. Such an arrangement in **20** also requires *cis*-coordination of the tetrahydrofuran ligands. A Cambridge Crystallographic Database search of compounds containing Bp-based ligands revealed no previous examples of *syn* M-H units such as those found in **20**. The most common orientation for Bp-based ligands is where the M···H-B and pyrazolyl moieties are *anti* to each other.[78,93-96] Divalent transition metal Bp complexes of the formula MBp_2 contain κ^3-N,N,H Bp ligands where the coordinated H atoms are 90° from one another in the equatorial plane.[97,98] Complexes **19**, **21-24**, $MgBp_2(THF)$,[78] $Y(Bp)_3$,[94] and $U(Bp^{Me2})_3$[95] all contain *syn* Bp and Bp^{Me2} ligand conformations within the metal coordination spheres, further illustrating the structural novelty of **20**.

Table 21 contains structural data for **19-21** and $MgBp_2(THF)$[78] associated with the M···H-B interactions. To allow direct comparison of the the M···H-B interactions, the M-H bond lengths were normalized to the ionic size of Ca^{2+} by subtracting or adding the difference between the M^{2+} and Ca^{2+} ionic radii to the M···H-B distance of the other group 2 ions. The data reveal that the Sr···H-B interactions in **20** are the strongest among the group, with Sr···H'-B distances of 2.59(6) and 2.73(4) Å. Stabilization of the *syn* conformation of

20 is probably a result of the ionic size, tetrahydrofuran ligand arrangement, and formation of stronger Sr···H-B interactions offsetting the slight increase in energy upon eclipsing the pyrazolyl moieties. The six membered B-$(NN)_2$-M chelate rings in **19-24** form boat conformations, due to the M-H bond formation. Depending on the strength of the M···H-B interaction, the boat can be shallow or deep. A plot of the M···H'-B distances versus the average B-N-N and M-N-N angles is shown in Figure 25. The plot indicates that the B-N-N angles vary little as a function of the M···H'-B distances (slope = 0.92), whereas the M-N-N bond angles change significantly with respect to the M···H'-B distance (slope = 16.09). Hence, the M-N bonds act as hinges for the M-H interactions, and thus the extent of the M-H interactions and depth of the boat are directly related to the M-N-N angles. Such flexibility of the M-N-N angles is facilitated by the non-directional, ionic M-N bonds.

Table 15. Crystal data and data collection parameters for **18**-**24**.

	18	**19**	**20**	**21**	**22**	**23**	**24**
Formula	$C_{54}H_{94}BKN_{12}$	$C_{20}H_{32}B_{2}$-$CaN_{8}O_{2}$	$C_{20}H_{32}B_{2}$-$N_{8}O_{2}Sr$	$C_{28}H_{48}B_{2}$-$BaN_{8}O_{4}$	$C_{44}H_{80}B_{2}$-$CaN_{8}O_{2}$	C_{44}H80B2-$N_{8}O_{2}Sr$	$C_{44}H_{80}BaB_{2}$-$N_{8}O_{2}$
FW	961.32	478.24	525.78	719.70	814.86	862.40	912.12
Space Group	P1bar	P21/c	P21/n	P21/c	P2/c	P2/c	P2/c
a (Å)	13.4823(4)	8.1820(3)	11.5239(11)	10.0475(3)	9.0091(6)	9.0253(4)	8.9791(5)
b (Å)	14.4362(4)	32.1359(13)	14.3932(14)	18.4400(5)	12.5037(7)	12.5252(6)	12.5148(7)
c (Å)	15.0315(4)	9.6550(4)	16.1877(17)	18.6347(5)	22.2896(14)	22.6409(10)	22.8178(13)
α	89.916(2)						
β	88.740(2)	97.639(2)	108.581(7)	99.0340(10)	99.030(4)	99.414(3)	97.585(3)
γ	88.405(2)						
V ($Å^3$)	2923.79(14)	2516.42(17)	2545.0(4)	3409.73(17)	2479.7(3)	2524.9(2)	2541.6(2)
Z	2	4	4	4	2	2	2
T (K)	100(2)	100(2)	100(2)	100(2)	100(2)	100(2)	100(2)
λ (Å)	0.71073	0.71073	0.71073	0.71073	0.71073	0.71073	0.71073
ρ_{calcd} (g,cm^{-3})	1.092	1.262	1.372	1.402	1.091	1.134	1.192
μ (mm-1)	0.135	0.282	2.151	1.209	0.168	1.108	0.822
R(F)(%)	9.02	5.89	9.02	2.85	6.64	6.94	4.83
Rw(F)(%)	20.36	13.22	14.86	6.85	12.22	13.15	11.55

$R(F) = \sum \| Fo | - | Fc \| / \sum | Fo |$; $Rw(F) = [\sum w(Fo^2 - Fc^2)^2 / \sum w(Fo^2)^2]^{1/2}$

Table 16. Selected bond lengths (Å) and angles (deg) for **18**.

K-N(1)	2.795(2)	N(5)-H(N11)	2.26(3)
K-N(3)	2.823(2)	K-N(1)-N(2)	115.89(16)
K-N(5)	2.913(2)	K-N(3)-N(4)	114.80(15)
K-N(7)	3.466(3)	K-N(5)-N(6)	111.51(15)
K-N(8)	2.780(3)	B-N(2)-N(1)	121.1(2)
K-N(9)	2.833(2)	B-N(4)-N(3)	121.7(2)
K-N(10)	3.396(2)	B-N(6)-N(5)	121.5(2)
K-N(11)	3.453(3)	N(2)-B-N(4)	111.0(2)
K-N(12)	2.781(3)	N(2)-B-N(6)	110.3(2)
N(1)-H(N7)	2.48(3)	N(4)-B-N(6)	109.2(2)
N(3)-H(N10)	2.17(4)		

Table 17. Selected bond lengths (Å) and angles (deg) for **19**.

Ca-O(1)	2.381(2)	Ca-N(7)-N(8)	117.47(15)
Ca-O(2)	2.394(2)	B(1)-N(2)-N(1)	119.26(19)
Ca-N(1)	2.451(2)	B(1)-N(4)-N(3)	118.82(19)
Ca-N(3)	2.491(2)	B(2)-N(6)-N(5)	119.3(2)
Ca-N(5)	2.443(2)	B(2)-N(8)-N(7)	119.4(2)
Ca-N(7)	2.477(2)	N(2)-B(1)-N(4)	109.2(2)
Ca-N(1)-N(2)	114.76(14)	N(5)-B(2)-N(7)	109.2(2)
Ca-N(3)-N(4)	114.38(15)	O(1)-Ca-O(2)	79.34(6)
Ca-N(5)-N(6)	118.64(15)		

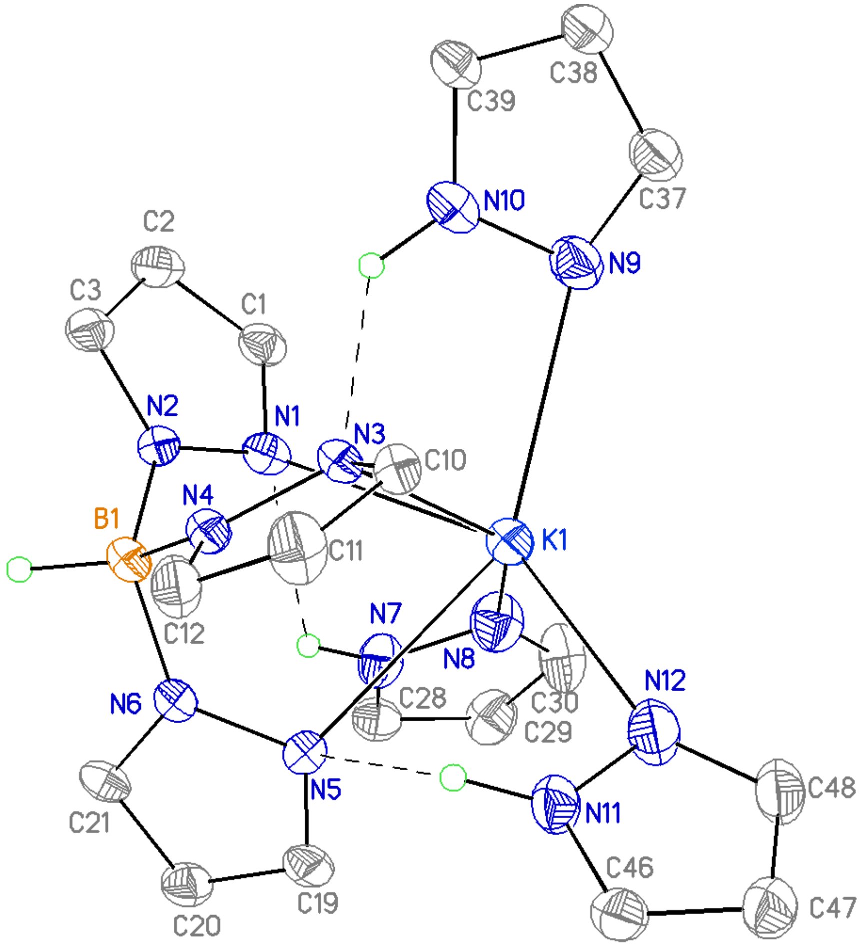

Figure 20. Perspective view of **18** with thermal ellipsoids at the 50% probability level. The isopropyl groups have been removed for clarity.

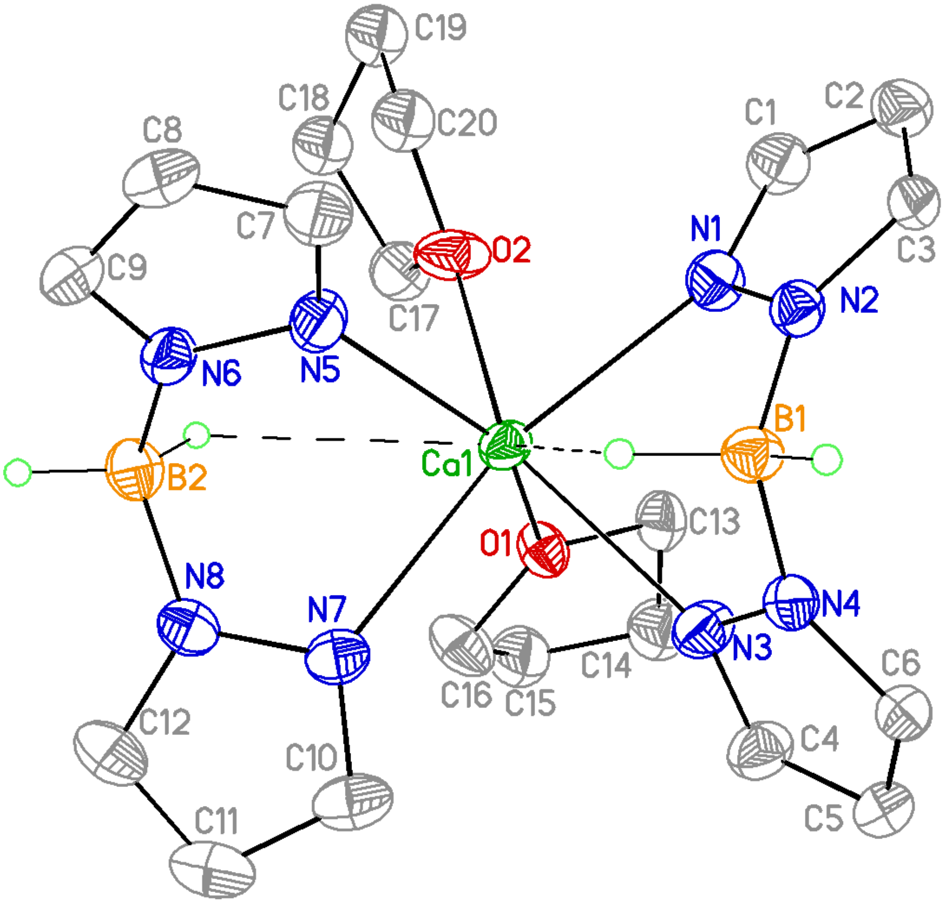

Figure 21. Perspective view of **19** with thermal ellipsoids at the 50% probability level.

Table 18. Selected bond lengths (Å) and angles (deg) for **20**.

Sr-O(1)	2.567(4)	Sr-N(7)-N(8)	108.7(4)
Sr-O(2)	2.560(4)	B(1)-N(2)-N(1)	120.2(5)
Sr-N(1)	2.624(5)	B(1)-N(4)-N(3)	120.2(5)
Sr-N(3)	2.641(5)	B(2)-N(6)-N(5)	119.8(5)
Sr-N(5)	2.634(5)	B(2)-N(8)-N(7)	120.1(6)
Sr-N(7)	2.676(5)	N(2)-B(1)-N(4)	108.9(5)
Sr-N(1)-N(2)	111.7(4)	N(5)-B(2)-N(7)	109.4(6)
Sr-N(3)-N(4)	110.8(4)	O(1)-Sr-O(2)	81.51(14)
Sr-N(5)-N(6)	109.6(4)		

Table 19. Selected bond lengths (Å) and angles (deg) for **21**.

Ba-O(1)	2.791(1)	B(1)-N(2)-N(1)	121.16(15)
Ba-O(2)	2.788(1)	B(1)-N(4)-N(3)	120.66(15)
Ba-O(3)	2.824(1)	B(2)-N(6)-N(5)	121.77(15)
Ba-O(4)	2.919(1)	B(2)-N(8)-N(7)	121.45(16)
Ba-N(1)	2.902(2)	N(2)-B(1)-N(4)	109.91(15)
Ba-N(3)	2.852(2)	N(6)-B(2)-N(8)	110.68(16)
Ba-N(5)	2.886(2)	O(1)-Ba-O(2)	139.28(4)
Ba-N(7)	2.862(2)	O(1)-Ba-O(3)	142.61(4)
Ba-N(1)-N(2)	118.34(11)	O(1)-Ba-O(4)	72.77(4)
Ba-N(3)-N(4)	120.82(11)	O(2)-Ba-O(3)	72.94(4)
Ba-N(5)-N(6)	115.86(11)	O(2)-Ba-O(4)	147.42(4)
Ba-N(7)-N(8)	115.64(11)	O(3)-Ba-O(4)	80.34(4)

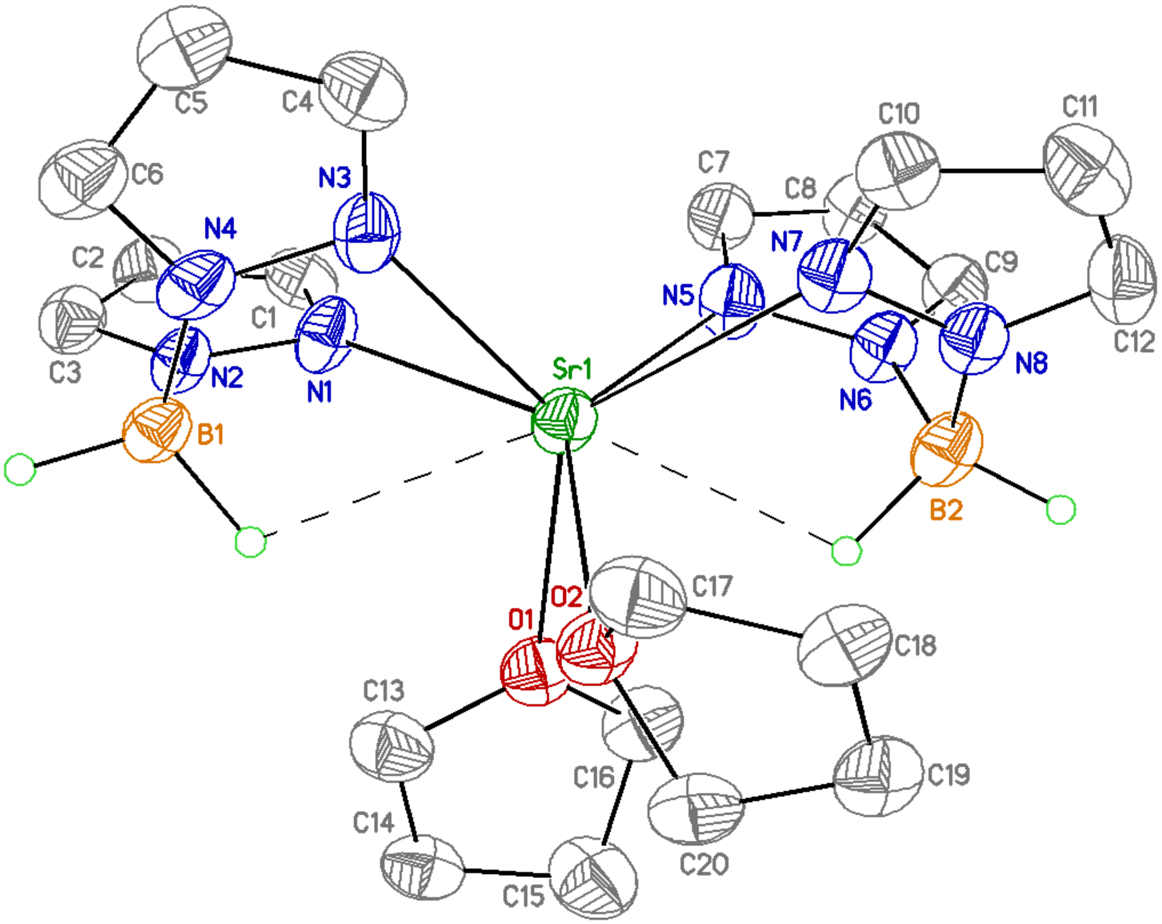

Figure 22. Perspective view of **20** with thermal ellipsoids at the 50% probability level.

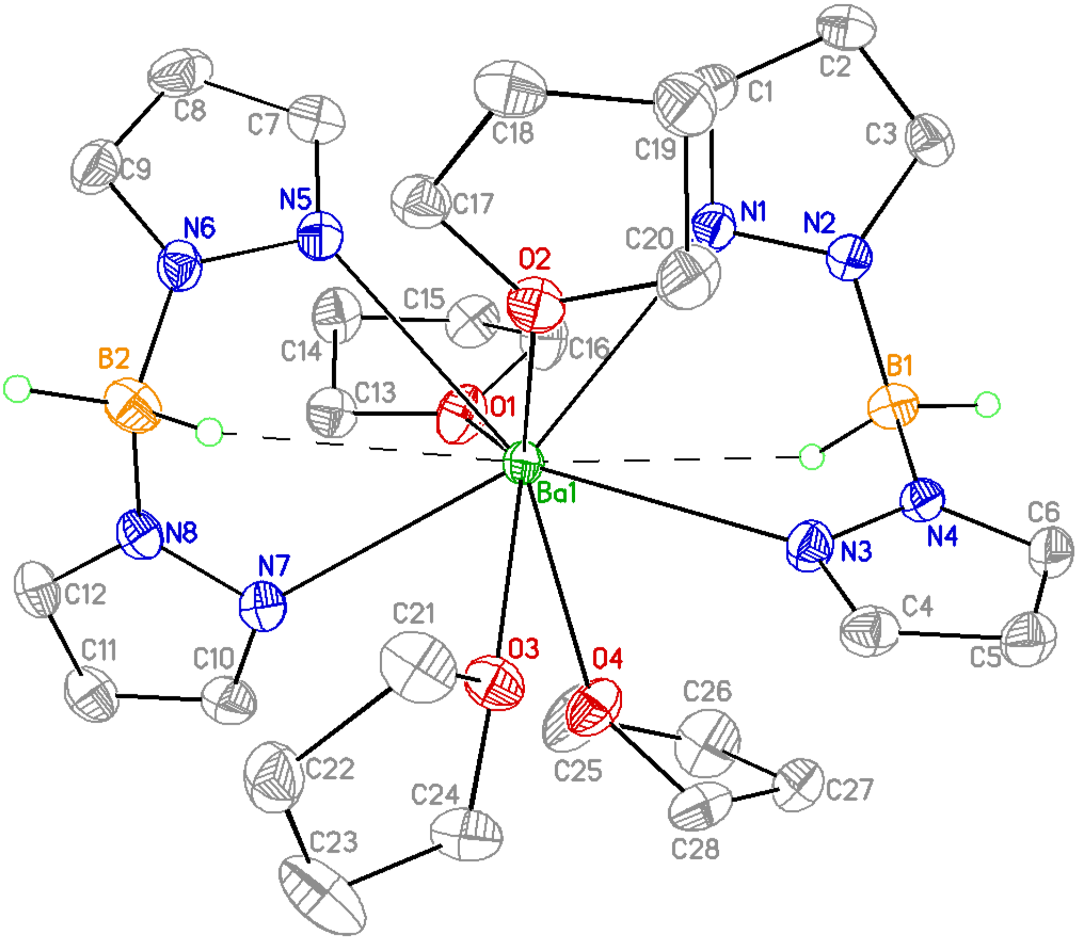

Figure 23. Perspective view of **21** with thermal ellipsoids at the 50% probability level.

Table 20. Selected bond lengths (Å) and angles (deg) for **22**.

Ca-O(1)	2.431(2)
Ca-N(1)	2.478(2)
Ca-N(3)	2.562(2)
Ca-N(1)-N(2)	118.22(13)
Ca-N(3)-N(4)	110.48(12)
B-N(2)-N(1)	117.55(18)
B-N(4)-N(3)	119.25(17)
N(2)-B-N(4)	110.9(2)
O(1)-Ca-O(1)’	149.28(8)

Table 21. Selected metrical data for **19-21** and $MgBp_2(THF)$.

Complex	M···H-B	M···H’-B[a]	$B-N-N_{avg}$	$M-N-N_{avg}$
$MgBp_2(THF)$[6]	2.69	2.97	118.6(3)	114.91
3	2.77(2) 3.01(3)	2.77(2) 3.01(3)	119.0(2) 119.35(5)	114.6(2) 118.1(6)
4	2.73(4) 2.59(6)	2.55(4) 2.41(6)	120.2(0) 120.0(2)	111.3(5) 109.2(5)
5	3.33(2) 3.23(3)	2.98(2) 2.88(3)	120.9(3) 121.6(2)	120(1) 115.8(1)

[a] Values are normalized to the ionic size of Ca^{2+} by subtracting or adding the difference between the M^{2+} and Ca^{2+} ionic radii to the M···H-B distance

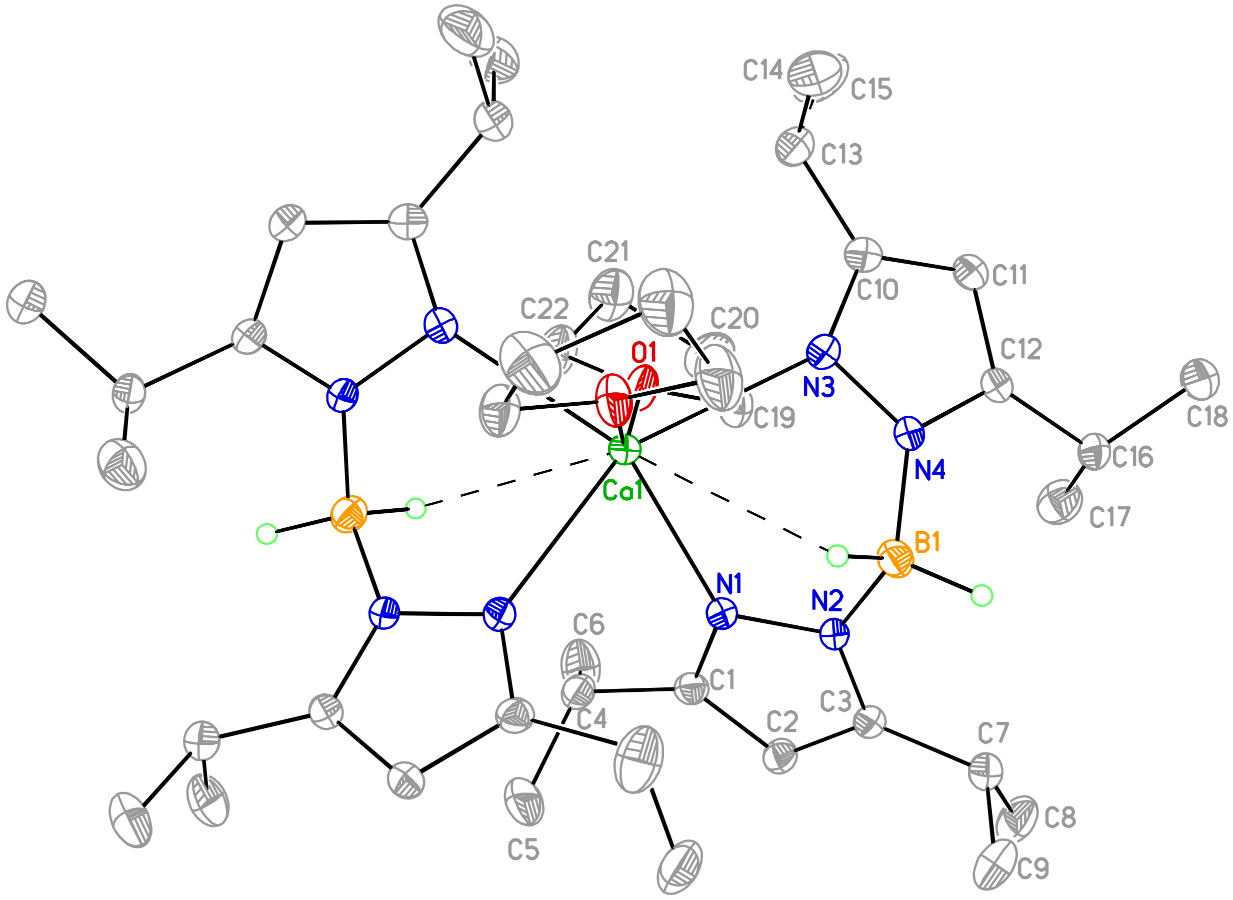

Figure 24. Perspective view of **22** with thermal ellipsoids at the 50% probability level.

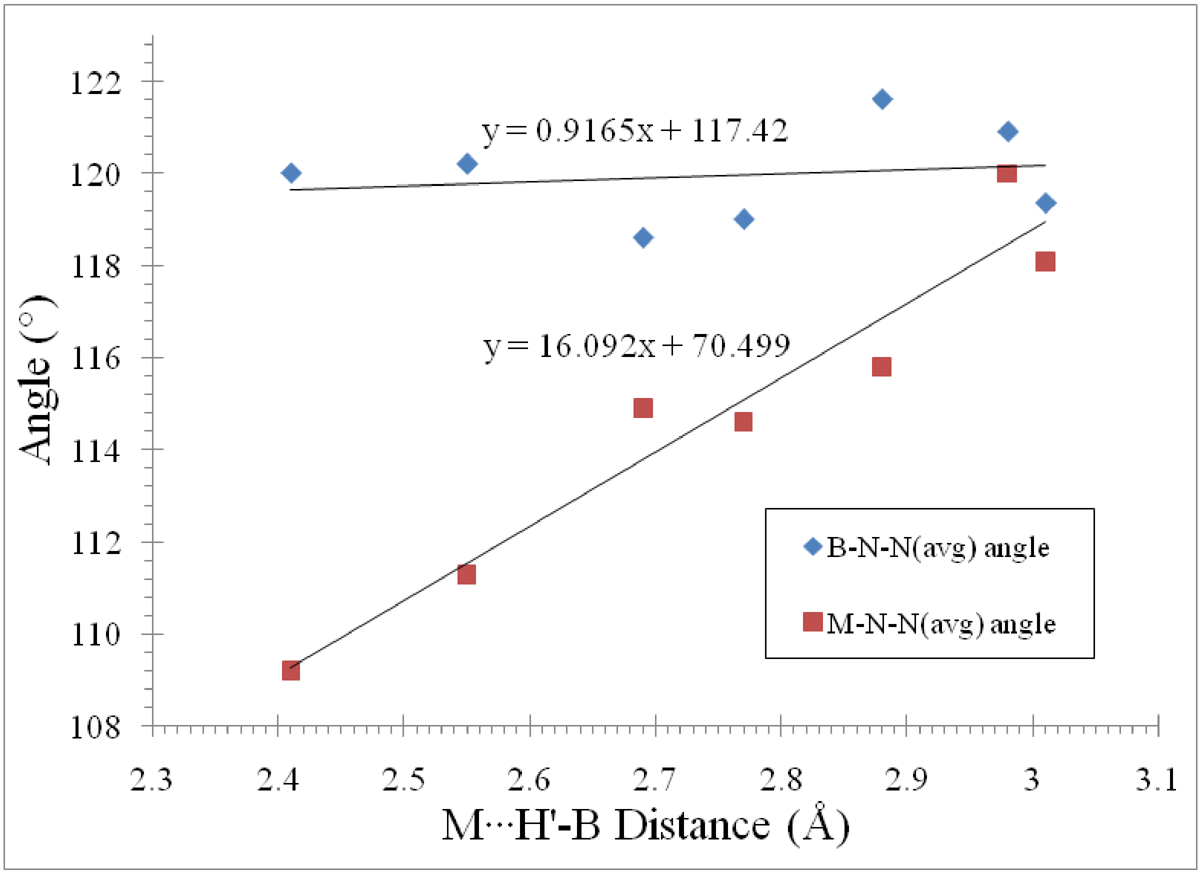

Figure 25. Plot of M···H'-B distances (Å) versus average B-N-N and M-N-N angles (°).

4.3 Conclusions

A series of complexes containing Bp and Bp^{iPr2} has been synthesized and structurally characterized. Unfortunatly, all of the complexes decomposed before volatilization, which implies that these complexes are not suitable for ALD or CVD applications. The sources of decomposition is likely related to the electron rich boron-hydrogen bond in Bp^{R2}-based ligands and the inability of the Bp and Bp^{iPr2} ligands to saturate the metal coordination spheres to avoid the formation of neutral donor adducts. The work presented herein demonstates that the strength of the M-H interaction in **19-21** is a function of the M-N-N angle and not the B-N-N angle, which is a consequence of the non-directional, ionic bonding between the metal and the Bp ligand. Although these complexes may not find applications in CVD or ALD, they represent rare structural examples of group 2 Bp^{R2}-based complexes.

4.4 Experimental Section

General Considerations. All reactions were performed under argon using either standard glovebox or Schlenk line techniques. Tetrahydrofuran was distilled from sodium benzophenone ketyl. Hexane was distilled from P_2O_5. KBp[7] and iPr_2pzH[9] were synthesized according to literature procedures. All other starting materials were purchased from Acros or Aldrich Chemical Company and were used as received.

^1H and $^{13}C\{^1H\}$ NMR spectra were obtained at 400, 300, 125, or 75 MHz in methylene chloride-d_2, benzene-d_6, or acetone-d_6. Infrared spectra were obtained using Nujol as the medium. Elemental analyses were performed by Midwest Microlab, Indianapolis, Indiana. Melting points were obtained on an Electrothermal Model 9200 melting point apparatus and are uncorrected. TGA was conducted on a Perkin Elmer Pyris 1 TGA system between 50 and 550 °C, using nitrogen as the flow gas with a hearting rate of 10 ºC/min.

Preparation of KBp^{iPr2} (17). A 100-mL round-bottomed flask was charged with KBH_4 (0.794 g, 14.72 mmol), iPr_2pzH (5.000 g, 32.42 mmol), anhydrous DMAC (50 mL), and a stir bar. The mixture was slowly heated in an oil bath to 120 °C, while carefully monitoring hydrogen evolution. Once gas evolution ceased (~670 mL), the oil bath was removed and the reaction mixture was allowed to cool to ambient temperature. The DMAC was then removed under reduced pressure. The resulting crude mixture was then heated to ~130 °C and the excess iPr_2pzH was distilled at 0.05 Torr. The product was washed with cold hexane (30 mL) and was isolated by vacuum filtration. To remove any unreacted

KBH_4, the solid was further dissolved in methylene chloride (25 mL) and the solution was filtered through a medium glass filter frit. The methylene chloride was removed under reduced pressure to afford **17** as a white powder (2.913 g, 56%). The analytical sample was obtained by crystallization of 0.25 g of **17** from toluene (20 mL) at -23 ºC: mp 168-169 °C; IR (Nujol, cm^{-1}) $\nu_{B\text{-}H}$ = 2248-2438, $\nu_{C\text{-}N}$ = 1526; ^1H NMR (CD_2Cl_2, 23 ºC, δ) 5.78 (s, 2H, 4-C*H*), 3.45 (broad s, 2H, BH_2,), 3.21 (septet, J = 6.8 Hz, 2H, C*H*$(CH_3)_2$), 2.80 (septet, J = 6.8 Hz, 2H, C*H*$(CH_3)_2$), 1.11 (d, J = 6.6 Hz, 12H, CH(CH_3)$_2$), 1.07 (d, J = 6.9 Hz, 12H, CH(CH_3)$_2$); $^{13}C\{^1H\}$ NMR (CD_2Cl_2, 23 ºC, ppm) 158.95 (s, C_q), 155.97 (s, C_q), 96.96 (s, 4-*C*H), 28.32 (s, *C*H$(CH_3)_2$), 26.42 (s, *C*H$(CH_3)_2$), 23.61 (s, CH(*C*H_3)$_2$), 23.48 (s, CH(*C*H_3)$_2$).

Anal. Cald for $C_{18}H_{32}BKN_4$: C, 61.01; H, 9.10; N, 15.81. Found: C, 61.02; H, 8.97; N, 15.53.

Preparation of $KTp^{iPr2}(HPz^{iPr2})_3$ (18). A 50-mL round-bottomed flask was charged with KBH_4 (0.112 g, 2.080 mmol), iPr_2pzH (2.000g, 13.137 mmol), and a stir bar. The flask was then heated at 180 ºC in an oil bath for 18 h, at which point gas evolution had ceased and the melt was a clear viscous liquid. The reaction mixture was cooled to room temperature, the resultant solid was dissolved in hexane (20 mL), and the solution was filtered through a 2-cm pad of Celite on a medium glass frit. The clear filtrate was set aside in an Erlenmeyer flask and slow evaporation at room temperature afforded colorless crystals of **18** (1.068 g, 53%): mp 147-149 °C; IR (Nujol, cm^{-1}) $\nu_{N\text{-}H}$ = 3261, 3358, $\nu_{B\text{-}H}$ = 2469, $\nu_{C\text{-}N}$ = 1565, 1529; ^1H NMR (CD_2Cl_2, 23 ºC, δ) 9.98 (b, 3H, N*H*), 5.84 (s, 3H, C*H*), 5.79 (s, 3H, 4-C*H*), 4.90 (broad s, 1H, B*H*), 3.19 (septet, J = 6.9 Hz, 3H, C*H*$(CH_3)_2$), 2.87 (septet, J = 6.9 Hz, 6H, C*H*$(CH_3)_2$), 2.60 (septet, J = 6.8 Hz, 3H, C*H*$(CH_3)_2$), 1.21 (d, J = 6.4 Hz, 36H, CH(CH_3)$_2$), 1.03 (d, J = 6.4 Hz, 18H, CH(CH_3)$_2$), 0.99 (d, J = 7.2 Hz, 18H, CH(CH_3)$_2$); $^{13}C\{^1H\}$ NMR (toluene-d_8, 23 °C, ppm) 159.33 (s, C_q), 155.66 (s, C_q), 154.40 (broad s, 2 C_q), 97.87 (s, 4-*C*H), 97.02 (s, 4-*C*H), 27.93 (s, $\mathit{C}H(CH_3)_2$), 27.30 (broad s, $\mathit{C}H(CH_3)_2$), 26.71 (s, $\mathit{C}H(CH_3)_2$), 23.67 (s, $CH(\mathit{C}H_3)_2$), 23.43 (s, $CH(\mathit{C}H_3)_2$), 23.02 (s, $CH(\mathit{C}H_3)_2$).

Anal. Cald for $C_{54}H_{94}B_2KN_{12}$: C, 67.46; H, 9.78; N, 17.49. Found: C, 67.64; H, 9.81; N, 17.76.

Preparation of $CaBp_2(THF)_2$ (19). A 100-mL Schlenk flask was charged with CaI_2 (0.200 g, 0.680 mmol), KBp (0.253 g, 1.360 mmol), and a stir bar. Tetrahydrofuran (30 mL) was added, resulting in the immediate formation of a white precipitate of KI. The reaction mixture was stirred for 18 h, at which point the volatile components were removed under reduced pressure to afford a white residue. Hexane (30 mL) was added to extract the product. The resulting solution was filtered through a 3-cm pad of Celite on a medium glass frit to yield a clear filtrate, which was placed in a -23 °C freezer for 24 h. Decanting of the solvent with a fine cannula, followed by vacuum drying at ambient temperature for 1 h, afforded colorless crystals of **19** (0.804 g, 64%): mp 115-116 °C; IR (Nujol, cm^{-1}) $\nu_{B\text{-}H}$ = 2263-2415, $\nu_{C\text{-}N}$ = 1500; ^1H NMR (CD_2Cl_2, 23 °C, δ) 7.59 (d, J = 1.8 Hz, 4H, C*H*), 7.41 (d, J = 1.8 Hz, 4H, C*H*), 6.13 (t, J = 1.8 Hz, 4H, C*H*), 3.71 (b, 4H, $B\mathit{H}_2$), 3.69 (m, 8H, $CH_2C\mathit{H}_2O$), 1.80 (m, 8H, $C\mathit{H}_2CH_2O$); $^{13}C\{^1H\}$ NMR (CD_2Cl_2, 23 °C, ppm) 139.82 (s, *C*H), 135.54 (s, *C*H), 104.29 (s, 4-*C*H), 69.03 (s, $CH_2\mathit{C}H_2O$), 25.69 (s, $\mathit{C}H_2CH_2O$).

Anal. Cald for $C_{20}H_{32}B_2CaN_8O_2$: C, 50.23; H, 6.74; N, 23.43. Found: C, 50.58; H, 6.69; N, 23.67.

Preparation of $SrBp_2(THF)_2$ (20). In a fashion similar to the preparation of **19**, treatment of SrI_2 (0.207 g, 0.606 mmol) with KBp (0.218 g, 1.172 mmol) afforded **20** as a white powder (0.250 g, 81%). The analytical sample and single crystals for the X-ray crystallographic analysis were obtained by crystallization from hexane at -23 ºC: mp 118-121 °C; IR (Nujol, cm^{-1}) $\nu_{B\text{-}H}$ = 2264-2416, $\nu_{C\text{-}N}$ = 1502; ^{1}H NMR (CD_2Cl_2, 23 ºC, δ) 7.57 (d, J = 2.4 Hz, 4H, C*H*), 7.46 (d, J = 1.8 Hz, 4H, C*H*), 6.14 (t, J = 1.8 Hz, 4H, 4-C*H*), 3.69 (m, 8H, CH_2CH_2O), 3.61 (broad s, 2H, BH_2), 1.78 (m, 8H, CH_2CH_2O); $^{13}C\{^1H\}$ NMR (CD_2Cl_2, 23 ºC, ppm) 139.62 (s, *C*H), 135.44 (s, *C*H), 104.30 (s, 4-*C*H), 68.83 (s, CH_2CH_2O), 25.66 (s, CH_2CH_2O).

Anal. Calcd for $C_{20}H_{32}B_2N_8O_2Sr$: C, 45.68; H, 6.13; N, 21.32. Found: C, 45.84; H, 6.09; N, 21.49.

Preparation of $BaBp_2(THF)_4$ (21). A 100-mL Schlenk flask was charged with BaI_2 (0.257 g, 0.657 mmol), KBp (0.245 g, 1.317 mmol), and a stir bar. Tetrahydrofuran (30 mL) was added, resulting in the immediate formation of a white precipitate of KI. The reaction mixture was stirred for 18 h, then the resulting mixture was filtered through a 3-cm pad of Celite on a medium glass frit to yield a clear filtrate. The filtrate was reduced in volume to about 10 mL, and the solution was place in a -23 ºC freezer for 24 h. Decanting of the solvent with a fine cannula, followed by vacuum drying at ambient temperature for 1 h, afforded colorless crystals of **21** (0.150 g, 32%) : mp 280-282 °C; IR (Nujol, cm^{-1}) $\nu_{B\text{-}H}$ = 2253-2448, $\nu_{C\text{-}N}$ = 1492; ^{1}H NMR (acetone-d_6, 23 ºC, δ) 7.44 (d, J = 1.6 Hz, 8H, C*H*), 7.28 (d, J = 1.6 Hz, 8H, C*H*), 5.95 (t, J = 2.0 Hz, 4H, 4-C*H*), 4.07 (broad s, J = 4H, BH_2), 3.61 (m, 16H, CH_2CH_2O), 1.78 (m, 16H, CH_2CH_2O); $^{13}C\{^1H\}$ NMR (acetone-d_6, 23 ºC, ppm) 139.24 (s, *C*H), 134.82 (s, *C*H), 103.36 (s, 4-*C*H), 68.03 (s, CH_2CH_2-O), 26.12 (s, CH_2CH_2-O); (0.5 equivalents of tetrahydrofuran was lost due to its lability at room temperature.

Anal. Calcd for $C_{26}H_{44}B_2BaN_8O_{3.5}$: C, 45.65; H, 6.49; N, 16.40. Found: C, 45.73; H, 6.39; N, 16.58.

Preparation of $CaBp^{iPr2}{}_2(THF)_2$ (22). In a fashion similar to the preparation of **19**, treatment of CaI_2 (0.205 g, 0.698 mmol) with KBp^{iPr2} (0.483 g, 1.362 mmol) afforded **22** as a white solid (0.352 g, 63%). The analytical sample and single crystals for the X-ray crystallographic analysis were obtained by crystallization from hexane at -23 ºC: mp 112-113 ºC; IR (Nujol, cm^{-1}) $\nu_{B\text{-}H}$ = 2285-2432, $\nu_{C\text{-}N}$ = 1527; ^1H NMR (CD_2Cl_2, 23 °C, δ), 5.76 (s, 4H, 4-C*H*), 3.63 (m, 8H, CH_2CH_2O), 3.38 (septet, J = 6.8 Hz, 8H, C*H*$(CH_3)_2$), 2.42 (septet, J = 6.8 Hz, 8H, C*H*$(CH_3)_2$), 1.79 (m, 8H, CH_2CH_2O), 1.18 (d, J = 6.6 Hz, 24H, $CH(CH_3)_2$), 0.94 (d, J = 7.5 Hz, 24H, $CH(CH_3)_2$); $^{13}C\{^1H\}$ NMR (CD_2Cl_2, 23 °C, ppm) 159.76 (s, C_q), 155.99 (s, C_q), 96.68 (s, 4-*C*H), 68.62 (s, CH_2CH_2O) 27.62 (s, *C*H$(CH_3)_2$), 26.42 (s, *C*H$(CH_3)_2$), 25.79 (s, CH_2CH_2O), 23.54 (s, 2 overlapping $CH(CH_3)_2$).

Anal. Calcd for $C_{44}H_{80}B_2CaN_8O_2$: C, 64.85; H, 9.90; N, 13.75. Found: C, 64.46; H, 9.93; N, 13.96.

Preparation of $SrBp^{iPr2}{}_2(THF)_2$ (23). In a fashion similar to the preparation of **20**, treatment of SrI_2 (0.201 g, 0.589 mmol) with KBp^{iPr2} (0.415 g, 1.17 mmol) afforded **23** as a white solid (0.310 g, 61%). The analytical sample and single crystals for the X-ray crystallographic analysis were obtained by crystallization from hexane at -23 ºC: mp 167-168 ºC; IR (Nujol, cm^{-1}) $\nu_{B\text{-}H}$ = 2279-2429, $\nu_{C\text{-}N}$ = 1532; ^1H NMR (CD_2Cl_2, 23 °C, δ), 5.76 (s, 4H, 4-C*H*), 3.57 (m, 8H, CH_2CH_2O), 3.38 (septet, J = 6.9 Hz, 8H, C*H*$(CH_3)_2$), 3.38 (septet, J = 7.0 Hz, 8H, C*H*$(CH_3)_2$), 1.78 (m, 8H, CH_2CH_2O), 1.16 (d, J = 6.4 Hz, 24H, $CH(CH_3)_2$), 1.03 (d, J = 7.2 Hz, 24H, $CH(CH_3)_2$); $^{13}C\{^1H\}$ NMR (CD_2Cl_2, 23 °C, ppm) 159.44 (s, C_q), 156.02 (s, C_q), 96.33 (s, 4-*C*H), 68.51 (s, CH_2CH_2O), 28.15 (s, *C*H$(CH_3)_2$), 26.40 (s, *C*H$(CH_3)_2$), 25.75 (s, CH_2CH_2O), 23.75 (s, $CH(CH_3)_2$), 23.57 (s, $CH(CH_3)_2$).

Anal. Cald for $C_{44}H_{80}B_2N_8O_2Sr$: C, 61.28; H, 9.35; N, 12.99. Found: C, 61.30; H, 9.36; N, 12.95.

Preparation of BaBp^{iPr2}$_2$(THF)$_2$ (24). In a fashion similar to the preparation of **20**, treatment of BaI_2 (0.204 g, 0.522 mmol) with KBp^{iPr2} (0.363 g, 1.02 mmol) afforded **24** as a white solid (0.205 g, 48%). The analytical sample and single crystals for the X-ray crystallographic analysis were obtained by crystallization from hexane at -23 °C: mp 165-167 °C; IR (Nujol, cm^{-1}) $\nu_{B\text{-}H}$ = 2274-2426, $\nu_{C\text{-}N}$ = 1530; ^{1}H NMR (CD_2Cl_2, 23 °C, δ) 5.76 (s, 4H, 4-C*H*), 3.61 (m, 8H, $CH_2C\mathit{H}_2O$), 3.36 (septet, J = 6.6 Hz, 8H, C*H*(CH_3)$_2$), 2.66 (septet, J = 6.6 Hz, 8H, C*H*(CH_3)$_2$), 1.79 (m, 8H, $C\mathit{H}_2CH_2O$), 1.15 (d, J = 6.6 Hz, 24H, CH(C*H*$_3$)$_2$), 1.03 (d, J = 6.6 Hz, 24H, CH(C*H*$_3$)$_2$); ^{13}C{^{1}H} NMR (CD_2Cl_2, 23 °C, ppm) 159.28 (s, *C*$_q$), 156.12 (s, *C*$_q$), 96.48 (s, 4-*C*H), 68.32 (s, $CH_2\mathit{C}H_2O$), 28.14 (s, *C*H(CH_3)$_2$), 26.31 (s, *C*H(CH_3)$_2$), 25.78 (s, $\mathit{C}H_2CH_2O$), 23.83 (s, CH(*C*H$_3$)$_2$), 23.58 (s, CH(*C*H$_3$)$_2$).

Anal. Calcd for $C_{44}H_{80}B_2BaN_8O_2$: C, 57.94; H, 8.84; N, 12.29. Found: C, 58.09; H, 8.61; N, 12.40.

X-Ray Crystallographic Structure Determinations of 18-24. Diffraction data were measured on a Bruker *X8 APEX-II* kappa geometry diffractometer with Mo radiation and a graphite monochromator. Frames were collected at 100 K with the detector at 40 mm and 0.3° between each frame, and were recorded for 10 s unless otherwise noted. *APEX-II*[73] and *SHELX*[74] software were used in the collection and refinement of the models. Crystals of **18** appeared as colorless thin fragments. 97116 reflections were measured, yielding 17717 unique data (Rint = 0.121). Hydrogen atoms were placed in observed or calculated positions. Three sets of pendant isopropyl groups were described with positional disorder at C35, C36, C41, C42, and C54 and were refined using partial occupancy sites and held isotropic.

Complex **19** crystallized as colorless rods. 48358 hkl data points were harvested, which averaged to 6392 data (Rint = 0.079). Hydrogen atoms were calculated or observed. The C-C bonds in the two disordered tetrahydrofuran ligands were held fixed at 1.54 Å and partial occupancies were assigned for C14, C15, C18, C19, and C20, which were kept isotropic during refinement. Crystals of **20** were obtained as colorless plates. 68843 reflections were counted, which averaged to 12155 independent data (Rint = 0.22). Hydrogen atoms were placed at calculated or observed positions. Statistically, this is a poor structure due to crystal quality, but certainly the overall connectivity of the complex is correct. Crystals of **21** were colorless fragments. 89094 total data were measured, averaging to 9799 unique data (Rint = 0.043). Hydrogen atoms were placed in observed or calculated positions. One of the tetrahydrofuran ligands was disordered in a 55/45 ratio at one carbon (C22). Complex **22** crystallized as colorless plates and yielded 72788 total data, of which 6198 were independent (Rint = 0.064). Hydrogen atom positions were either calculated or observed. The central Ca ion occupies a 2-fold rotation axis. Complex **23** produced crystalline colorless triangular plates. 56905 data were recorded to merge into 6299 data (Rint = 0.134). Hydrogen atoms were placed in calculated or observed positions. The crystal diffracted poorly, which required a 48 hour collection time (30 s frames). There are typical large thermal parameters for parts of the isopropyl groups and the tetrahydrofuran ligands. The Sr ion occupies a crystallographic 2-fold rotation axis. Complex **24** is isostructural with **22** (vide supra). Crystals were colorless flat rods. 88165 data were integrated to net 9664 independent data. Hydrogen atoms were placed in calculated and observed positions. There was significant disorder and partial occupancies were assigned for atoms C4, C5, C6, C13, C14, C15, C19, C22, and O1. These atoms were held isotropic during refinement. The Ba ion occupies a crystallographic 2-fold rotation axis. Lowering the space group symmetry did not resolve the disorder.

CHAPTER 5

A Solid State Thermolysis Route to the Formation of the Heteroleptic Complex $TpCaBH_4$

5.1 Introduction

Hydrogen fuel cell technology continues to gain interest because of the negative environmental effects of hydrocarbon-based fuels.[100-102] A major challenge in the implementation of hydrogen as a next generation fuel is the ability to store it safely and efficiently.[100-102] Compounds containing borohydride ligands are prime candidates for hydrogen storage materials because they exhibit the highest weight capacity for hydrogen.[100,101] In particular, $NaBH_4$, $Ca(BH_4)_2$, and $Mg(BH_4)_2$ have high hydrogen content with percent weights of 10.57, 11.47, and 14.82 %, respectively.[101] When metal borohydrides are heated, the decomposition reaction involves formation of metal hydride, metal boride, and hydrogen gas.[100a,c,d] Calcium and strontium amidoboranes have been investigated for potential use in hydrogen storage.[102] When $Ca(NH_2BH_3)_2\cdot 2NH_3$ was heated to 300 °C, 8.8 % by weight of hydrogen gas evolved.[102a] The evolution of H_2, NH_3, and B_2H_6 occurred upon the decomposition of $Sr(NH_2BH_3)_2$ at 80 °C, and therefore is not useful as a hydrogen storage material.[102b]

In Chapter 4, a series of group 2 complexes containing Bp and Bp^{iPr2} ligands for potential use as ALD precursors was described. Unfortunatly, all of these complexes decomposed into multiple products as indicated by the TGA traces and preparative sublimations. In order to gain insight into the possible decomposition pathways, a careful preparative sublimation of **19** was carried out. Surprisingly, one of the decomposition products was $TpCaBH_4$ (**25**), as determined by spectral methods. This chapter discusses the thermolysis of **19** at reduced pressures to generate **25** and $CaTp_2$. Further treatment of **25** with tetrahydrofuran afforded $[TpCaBH_4(THF)]_4$ (**26**) and $TpCaBH_4(THF)$ (**27**). Addition of either methanol or ethanol to **27** resulted in the formation of oligomeric complexes (**28** and **29**). Since **25-27** contain borohydride ligands, these complexes could find practical use as hydrogen storage materials.

5.2 Results and Discussion

Synthetic Aspects. In Chapter 4, the preparative sublimation of **19** at 190-200 °C/0.05 Torr led to the formation of multiple decomposition products. Analysis of the sublimate and residue with NMR and infrared spectroscopy indicated that the major decomposition products were $CaTp_2$ and **25**. Since only two major products were isolated, it is proposed that three equivalents of **19** decomposed to form three equivalents of **25** and one equivalent of $CaTp_2$ (eq 15). Careful optimization of equation 15 led to isolated yields of 84 and 90 % for **25** and $CaTp_2$, respectively, further supporting the proposed reaction. Dissolving **25** in tetrahydrofuran, followed by the appropriate work up as described in the experimental section, afforded colorless crystals of **26** and **27** (eq 16). Alternatively, salt metathesis routes involving the treatment of KTp with $Ca(BH_4)_2(THF)_2$ in tetrahydrofuran, also afforded colorless crystals of **26** and **27** (eq 17). Further treatment of **27** with methanol or ethanol afforded the oligomeric complexes, **28** and **29**. The source of the BO_3 unit in **29** is likely a result of trace amounts of water in the ethanol. Complex **25** was soluble in tetrahydrafuran, with no solubility in toluene or diethyl ether. Compounds **26** and **27** were soluble in tetrahydrofuran and toluene but not soluble in hexane. By contrast, **28** and **29** were only soluble in polar solvents such as acetone, ethanol, and methanol. Single crystals suitable for X-ray structural analysis were obtained for **26-29** and will be discussed in detail below.

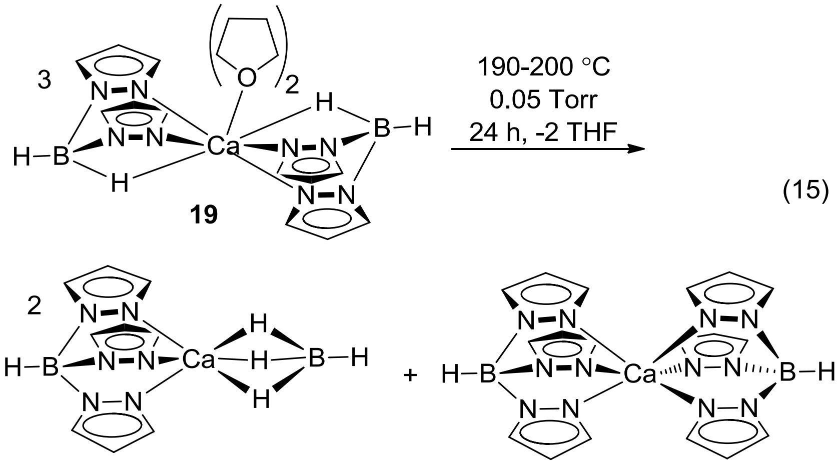

25, 84%   90%

(15)

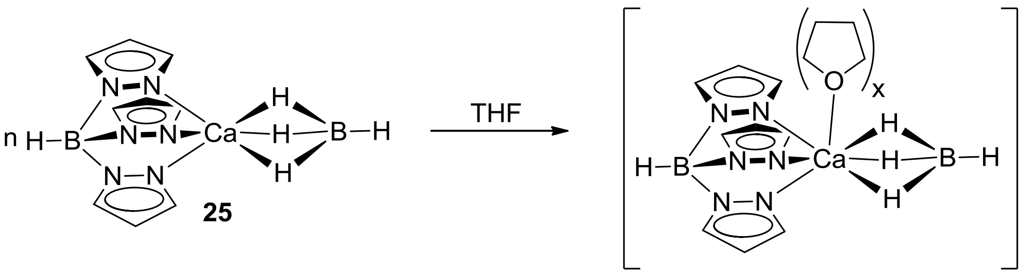

26, x = 1, n = 4, 73%
27, x = 2, n = 1, 43%

(16)

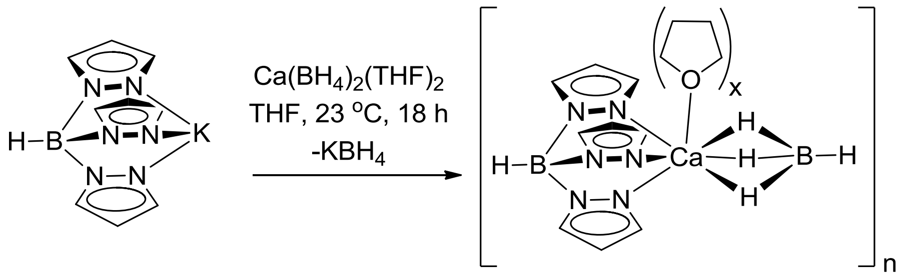

26, x = 1, n = 4, 52%
27, x = 2, n = 1, 55%

(17)

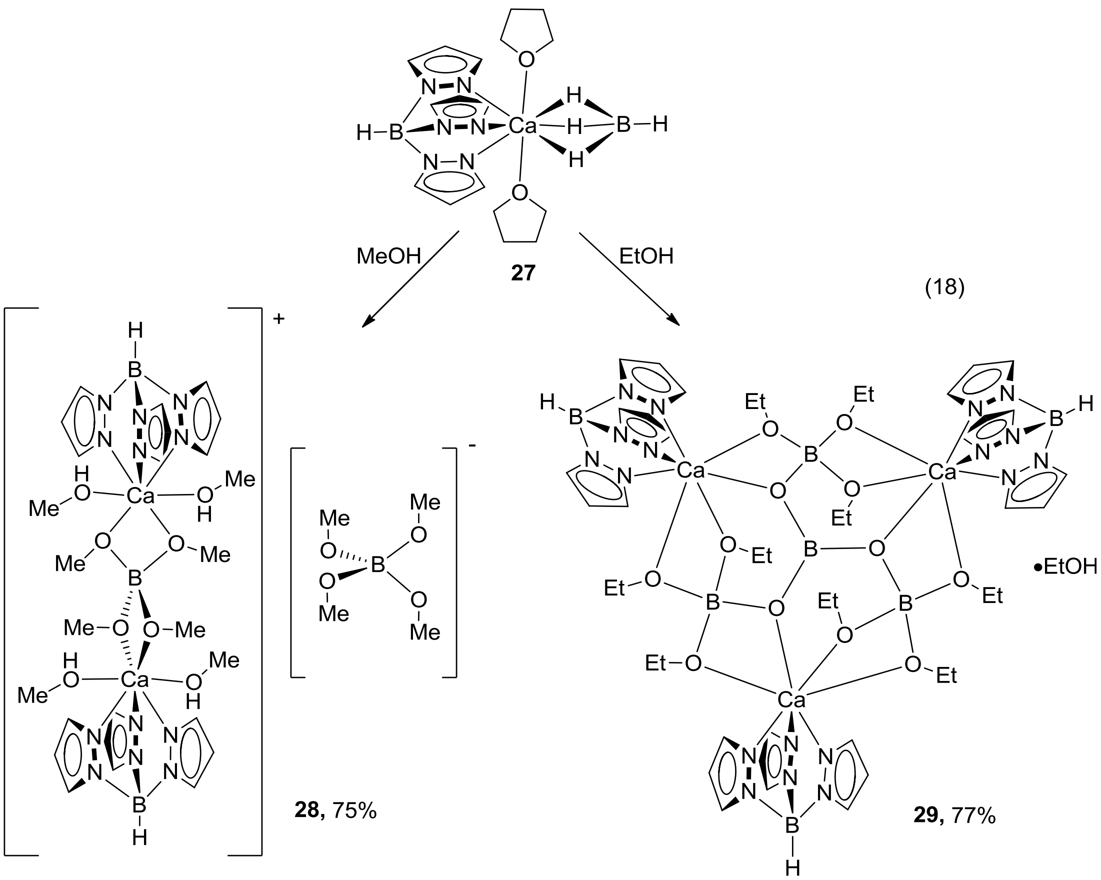

27

(18)

28, 75%

29, 77%

The compositions of **25-29** were assessed using spectral and analytical data, and X-ray crystal structure analysis. Despite many purification attempts, C, H, N microanalyses for **25-27** could not be obtained within ± 0.4% of the calculated values. In the ^{1}H NMR spectra of **25**, **28**, and **29**, resonances belonging to the magnetically inequivalent 3- and 5-H atoms on the pyrazolyl ring were observed at δ ~7.64 and 7.62, and the respective H atoms of **26** and **27** were observed at about δ 7.90 and 7.62. The 4-H resonances of **25-29** were observed between δ 5.96 and 6.12. The B-bound H resonances from the Tp ligand were only observed in the ^{1}H NMR spectra of **25-27** and were very broad at about δ 4.75. Proton resonances of the ^{11}B-bound H atoms from the BH_4 moeity in **25-27** were observed at δ -0.13, 1.16, and 1.14, respectively, and consisted of a quartet (J = 81 Hz). The 1-H and 2-H atom resonances of the THF ligand were observed at about δ 3.5 and 1.2. There was only one set of resonances corresponding to the methyl H atoms from the methoxy groups in **28** even though there are several inequivalent methoxy groups in the molecule. This is likely because of dynamic exchange between the two $B(OMe)_4$ moieties, as well as proton exchange between CD_3OD, methanol adducts, and methoxy groups. Complex **29** has D_{3h} symmetry, and thus only one set of methyl and methine proton resonances from the ethoxy groups were observed. Resonances corresponding to the methyl and methine protons from the ethanol were not observed. It is likely that the ethanol is undergoing site exchange with the ethoxy groups. In the infrared spectra of **25-27**, the B-H stretches from the BH_4 moiety were observed over the range of 2157-2224 cm^{-1}. The B-H stretches from the Tp ligands of **25-29** were observed over the range of 2441-2466 cm^{-1} and the C-N stretches were observed at about 1503 cm^{-1}, which are similar to the analogous stretches for $CaTp^{Me2}{}_2$ ($\nu_{B\text{-}H}$ = 2526 cm^{-1}, $\nu_{C\text{-}N}$ = 1538 cm^{-1}).[61d]

Structural Aspects (26-29). The X-ray crystal structures of **26-29** were determined to establish the geometry about the metal centers and the bonding modes of the Bp and Bp^{iPr2} ligands. Experimental crystallographic data are summarized in Table 22, selected bond lengths and angles are given in Tables 23-26, and perspective views are presented in Figures 26-29.

Perspective views of **26** and **27** are shown in Figures 26 and 27, respectively. Complex **26** crystallizes as a tetrameric complex consisting of four $[TpCa(THF)]^+$ units bridged by four $[BH_4]^-$ units with a center of inversion. The molecular structure of **27** exists as a monomeric complex containing a κ^3-bound Tp ligand, a κ^3-bound $[BH_4]^-$ ligand, and two tetrahydrofuran ligands. The average Ca-N bond lengths in **20** and **21** are 2.455(13) and 2.471(7) Å, respectively, which are similar to the average C-N bond lengths in other calcium

Tp-based complexes ($CaTp_2$, 2.44(2) Å;[61b] $CaTp^{Me2}{}_2$, 2.454(2) Å;[61d] $CaTp^{Et2}{}_2$ (**5**), 2.459(6) Å). The average Ca-O bond distances in **26** and **27** are 2.373(4) and 2.384(11) Å, respectively, which are within experimental error of the average Ca-O bond length in **19** (2.388(7) Å). The Ca-O bond length in **22** is 2.431(2) Å and is slightly longer than **26** and **27**, which is likely related to the steric congestion within the coordination sphere of **22** versus **26** and **27**. The Ca-H bond distances for **26** and **27** range from 2.38(5) to 2.58(4) Å and 2.409(18) to 2.420(19) Å, respectively. Comparison structures containing relevant Ca-H interactions include $Ca(BH_4)_2(CH_3OCH_2CH_2OCH_3)$,[99] $Ca(C_5H_2(SiMe_3)_3)(HBEt_3)(THF)_2$,[92] and $CaTp^{tBu}{}_2$,[84] with Ca-H bond lengths of 2.46(7) (average), 2.47(2), and 2.21(4) Å,[84] respectively. The large range of Ca-H bond distances observed thoughout the literature demonstrates the ionic nature of calcium-hydride interactions, and thus the strength of the Ca-H interaction is highly dependent on the ligand arrangement around the calcium ion. The average N-B-N bond angles for **26** and **27** are 110.3(8)° and 109.9(8)°, respectively, and indicate that the boron atoms from the Tp ligands are in tetrahedral geometry.

A perspective view of **28** is shown in Figure 28. The $[B(OMe)_4]^-$ counter ion is omitted from the X-ray crystal structure since it is not involved in any significant metal interactions. Complex **28** consists of two $[TpCa(MeOH)_2]^+$ units bridged together by a $[B(OMe)_4]^-$ unit, for a coordination number of seven per calcium ion. The average Ca-N distance in **28** is 2.49(3) Å and is similar to the Ca-N distances found in $CaTp_2$ (2.44(2) Å),[61b] $CaTp^{Me2}{}_2$ (2.454(2) Å),[61d] and **5** (2.459(6) Å). The average Ca-O bond distances for the calcium-methanol interactions and calcium-$B(OMe_4)$ interactions were 2.381(13) and 2.39(3) Å, respectively, which are similar to the average Ca-O bond distances in **26** (2.373(4) Å) and **27** (2.384(11) Å). The O(3)-B(2)-O(4) and O(5)-B(2)-O(6) bond angles in **28** are

98.9(3)° and 99.3(3)°, respectively, whereas the remaining O-B(2)-O angles are larger with an average of 114.9(4)°, and indicates that the boron atom is in a distorted tetrahedral geometry.

A perspective view of **29** is shown in Figure 29. Complex **29** contains three [TpCaB(EtO)$_3$] units held together by a [BO$_3$] core and has D_{3h} symmetry. There is one equivalent of ethanol per trimeric unit in the crystal lattice that is not shown in Figure 29. Each calcium metal center is engaged in κ^3-coordination with a Tp ligand, and κ^4-coordination with the [(B(EtO)$_3$O)$_3$B] moiety for a total coordination number of seven per calcium ion. The average Ca-N bond length is 2.462(4) Å and is slightly longer than the average Ca-N bond lengths in CaTp$_2$ (2.44(2) Å),[61b] CaTp$^{Me2}{}_2$ (2.454(2) Å),[61d] and **5** (2.459(6) Å). The average Ca-O bond length is 2.45(7) Å and is similar to the related values in **26**-**28**. The average B(2)-O distance is 1.468(14) Å and the the B(3)-O(2) bond length is 1.3530(15) Å. The shorter distance in the B(3)-O(2) bond length is related to B(3) having a higher degree of Lewis acidity compared to B(2), which has four substituents. The average N-B(1)-N bond distance is 110.3(7) ° which is within experimental error of 109.5° and thus the geometry about the boron bound Tp ligand is tetrahedral.

Table 22. Crystal data and data collection parameters for **26-29.**

	26	**27**	**28**	**29**
Formula	$C_{26}H_{44}B_4CaN_{12}O_2$	$C_{17}H_{30}B_2CaN_6O$	$C_{30}H_{56}B_4Ca_2N_{12}O_{12}$	$C_{47}H_{81}B_7Ca_3N_{18}$-$O_{13}$
FW	680.13	412.17	900.27	1302.21
Space group	P1bar	P21/n	P1	P63/m
a (Å)	11.1854(6)	9.4290(4)	14.7469(6)	16.9880(4)
b (Å)	12.8190(6)	14.4707(6)	16.0986(6)	16.9880(4)
c (Å)	13.8733(7)	16.7495(7)	21.3320(8)	13.5711(4)
α (°)	92.260(2)	90	73.8910(10)	90
β (°)	102.222(2)	104.5230(10)	80.4230(10)	90
γ (°)	105.636(2)	90	85.9690(10)	120
V ($Å^3$)	1862.33(16)	2212.35(16)	4796.1(3)	3391.80(15)
Z	2	4	4	2
T (K)	250(2)	100(2)	100(2)	100(2)
λ (Å)	0.71073	0.71073	0.71073	0.71073
ρ_{calc} g cm^{-3}	1.213	1.237	1.247	1.275
μ mm^{-1}	0.347	0.307	0.301	0.311
R(F) (%)	6.94	3.67	8.12	4.05
Rw(F) (%)	17.45	8.82	22.00	10.35

$R(F) = \sum \| Fo | - | Fc \| / \sum | Fo |$; $Rw(F) = [\sum w(Fo^2 - Fc^2)^2 / \sum w(Fo^2)^2]^{1/2}$

Table 23. Selected bond lengths (Å) and angles (deg) for **26**.

Ca(1)-N(1)	2.432(3)	Ca(2)-N(7)	2.462(3)
Ca(1)-N(3)	2.465(3)	Ca(2)-N(9)	2.444(3)
Ca(1)-N(5)	2.464(3)	Ca(2)-N(11)	2.464(3)
Ca(1)-O(1)	2.369(2)	Ca(2)-O(2)	2.376(3)
Ca(1)-H(4)B(2)	2.50(5)	Ca(2)-H(1)B(2)	2.44(6)
Ca(1)-H(2)B(2)	2.52(4)	Ca(2)-H(3)B(2)	2.55(4)
Ca(1)-H(3)B(2)	2.58(4)	Ca(2)-H(1)B(#3)	2.38(5)
Ca(1)-H(4)B(3)	2.50(5)	Ca(2)-H(4)B(#3)	2.50(5)
Ca(1)-H(2)B(3)	2.44(5)	N(7)-Ca(2)-N(9)	79.03(10)
N(1)-Ca(1)-N(3)	77.27(11)	N(9)-Ca(2)-N(11)	76.57(10)
N(3)-Ca(1)-N(5)	74.72(10)	N(7)-Ca(2)-N(11)	76.23(10)
N(1)-Ca(1)-N(5)	78.64(10)	B(4)-N(8)-N(7)	122.5(3)
B(1)-N(6)-N(5)	121.7(3)	B(4)-N(10)-N(9)	121.7(3)
B(1)-N(4)-N(3)	121.5(3)	B(4)-N(12)-N(11)	121.5(3)
B(1)-N(2)-N(1)	122.6(3)	N(8)-B(4)-N(10)	110.4(3)
N(2)-B(1)-N(4)	111.3(3)	N(10)-B(4)-N(12)	110.4(3)
N(4)-B(1)-N(6)	108.8(3)	N(8)-B(4)-N(12)	110.6(3)
N(2)-B(1)-N(6)	110.5(3)		

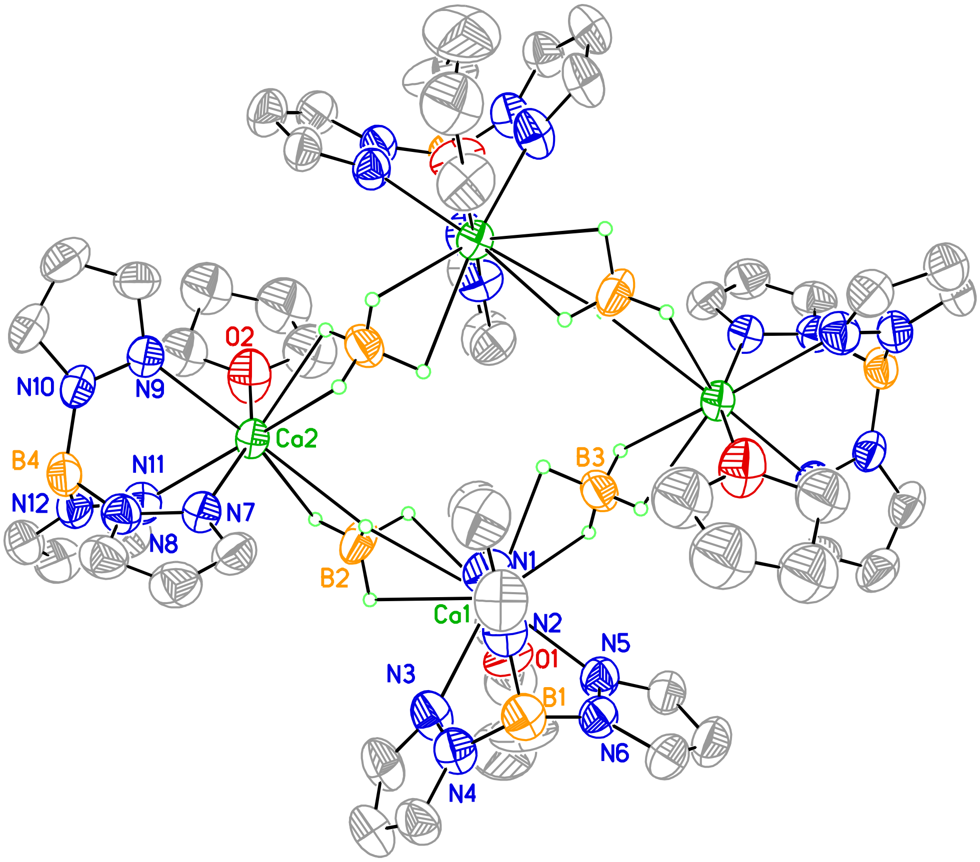

Figure 26. Perspective view of **26** with thermal ellipsoids at the 50% probability level.

Table 24. Selected bond lengths (Å) and angles (deg) for **27**.

Ca(1)-N(1)	2.4653(11)	Ca(1)-H(1)B(2)	2.420(19)
Ca(1)-N(3)	2.4652(10)	Ca(1)-H(2)B(2)	2.409(18)
Ca(1)-N(5)	2.4813(10)	Ca(1)-H(3)B(2)	2.417(19)
Ca(1)-O(1)	2.3950(9)	Ca(1)-O(2)	2.3725(9)
N(1)-Ca(1)-N(3)	79.62(4)	N(2)-B(1)-N(4)	110.00(10)
N(3)-Ca(1)-N(5)	75.77(3)	N(4)-B(1)-N(6)	108.90(10)
N(1)-Ca(1)-N(5)	75.67(3)	N(2)-B(1)-N(6)	110.85(10)
B(1)-N(6)-N(5)	121.94(9)	B(1)-N(2)-N(1)	122.91(10)
B(1)-N(4)-N(3)	122.65(9)		

Table 25. Selected bond lengths (Å) and angles (deg) for **29**

Ca(1)-N(1)	2.4653(15)	Ca(1)-O(1)	2.5365(16)
Ca(1)-N(3)	2.4580(19)	Ca(1)-O(2)	2.3719(16)
Ca(1)-O(3)	2.4313(12)	B(2)-O(1)	1.450(3)
B(2)-O(2)	1.485(3)	B(2)-O(3)	1.468(2)
B(3)-O(2)	1.3530(15)	O(2)-B(3)-O(2A)	120.0
N(1)-Ca(1)-N(3)	74.97(5)	N(2)-B(1)-N(2A)	111.0(2)
N(1)-Ca(1)-N(1A)	83.41(7)	N(2)-B(1)-N(4)	109.61(13)
B(1)-N(2)-N(1)	123.19(15)	B(1)-N(4)-N(3)	121.12(19)

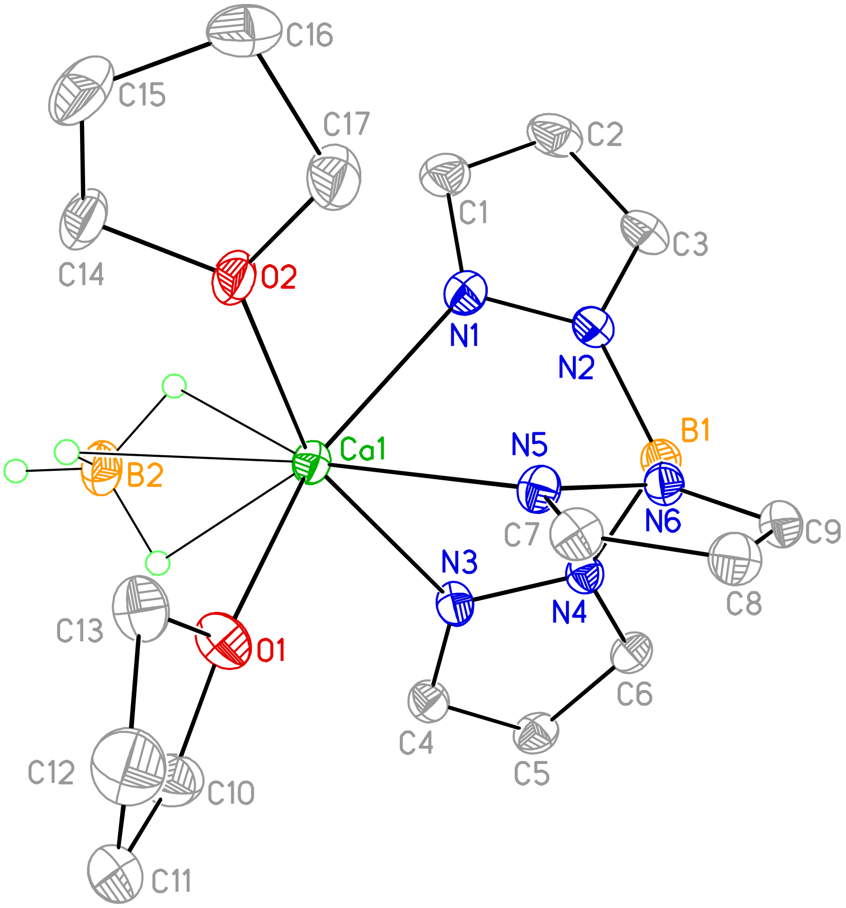

Figure 27. Perspective view of **27** with thermal ellipsoids at the 50% probability level.

Table 26. Selected bond lengths (Å) and angles (deg) for **28.**

Ca(1)-N(1)	2.466(4)	Ca(2)-N(7)	2.445(4)
Ca(1)-N(3)	2.504(4)	Ca(2)-N(9)	2.491(4)
Ca(1)-N(5)	2.535(3)	Ca(2)-N(11)	2.521(4)
Ca(1)-O(1)	2.361(3)	Ca(2)-O(7)	2.397(3)
Ca(1)-O(2)	2.379(3)	Ca(2)-O(8)	2.386(3)
Ca(1)-O(3)	2.404(3)	Ca(2)-O(5)	2.372(3)
Ca(1)-O(4)	2.352(3)	Ca(2)-O(6)	2.423(3)
N(2)-B(1)-N(4)	110.9(4)	N(8)-B(3)-N(10)	111.7(4)
N(4)-B(1)-N(6)	108.2(4)	N(10)-B(3)-N(12)	107.8(5)
N(2)-B(1)-N(6)	111.0(4)	N(8)-B(3)-N(12)	110.7(4)
B(1)-N(2)-N(1)	122.9(4)	B(3)-N(8)-N(7)	122.9(4)
B(1)-N(4)-N(3)	123.0(3)	B(3)-N(10)-N(9)	122.0(4)
B(1)-N(6)-N(5)	121.5(3)	B(3)-N(12)-N(11)	120.0(4)
N(1)-Ca(1)-N(3)	76.89(12)	N(7)-Ca(2)-N(9)	77.83(14)
N(3)-Ca(1)-N(5)	74.74(12)	N(9)-Ca(2)-N(11)	74.06(12)
N(1)-Ca(1)-N(5)	76.61(12)	N(7)-Ca(2)-N(11)	76.09(14)
O(3)-B(2)-O(4)	98.9(3)	O(3)-B(2)-O(6)	115.5(4)
O(3)-B(2)-O(5)	114.9(4)	O(4)-B(2)-O(5)	114.3(4)
O(4)-B(2)-O(6)	114.8(4)	O(5)-B(2)-O(6)	99.3(3)

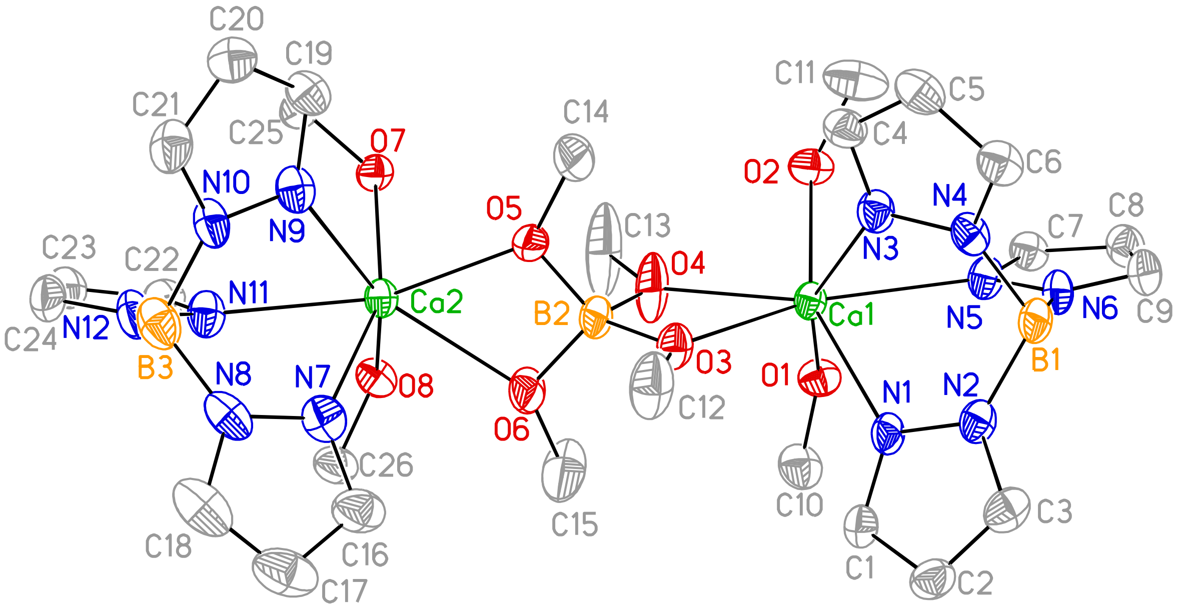

Figure 28. Perspective view of **28** with thermal ellipsoids at the 50% probability level. The $[B(OMe)_4]^-$ counter ion is removed for clarity.

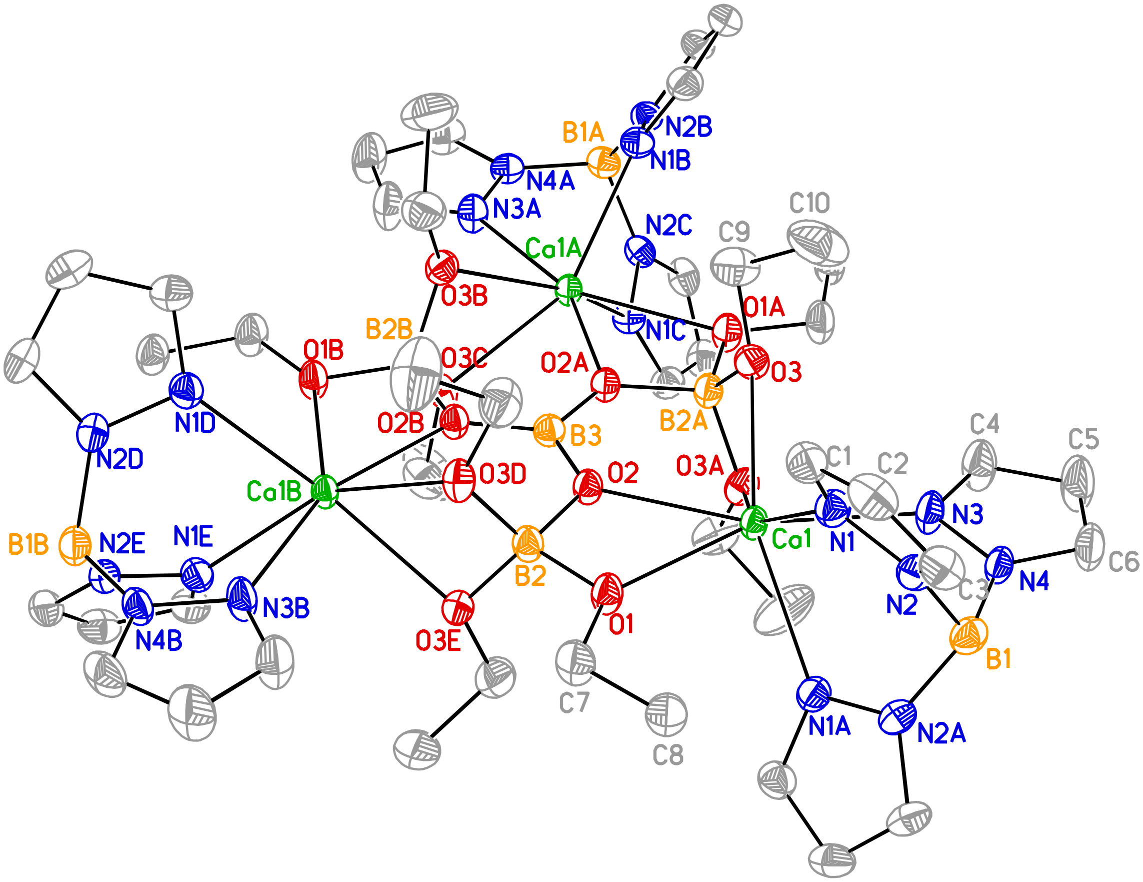

Figure 29. Perspective view of **29** with thermal ellipsoids at the 50% probability level.

5.3 Conclusions

Heteroleptic calcium complexes composed of a Tp ligand and either a BH_4 ligand or alkoxyborate-based ligand have been synthesized and structurally characterized. Significantly, a new solid state thermolysis route to the formation of **25** has been described. Crystal structures of **26** and **27** reveal that **26** exists as a tetrameric complex, whereas **27** exists as a monomer. The molecular structure of **28** was composed of a dimeric complex consisting of two $[TpCa(MeOH)_2]^+$ units bridged by a $[B(OMe)_4]^-$ moiety and a $[B(OMe)_4]^-$ counter ion not engaged in any interactions with the calcium ion. The cystral structure of **29** reveals a trimeric complex containing three $[TpCaB(OEt)_3]$ units connected by a BO_3. Complexes **25-27** all contain BH_4 ligands, and therefore could find pontial use as hydrogen storage materials.

5.4 Experimental

Preparation of TpCaBH$_4$ (25). A vial was charged with **19** (1.642 g, 3.433 mmol) and then heated in a sublimation tube at 190-200 °C/0.05 Torr for 24 hours. Crystalline solids of $CaTp_2$ volatilized and condensed at the cold end leaving a white powder in the vial. Isolation of the white powder afforded **1** (0.513 g, 84 %). mp 298-300 °C; IR (Nujol, cm^{-1}) $\nu_{B\text{-}H}$ = 2441 (B-H), $\nu_{B\text{-}H}$ = 2404-2171 (BH_4), $\nu_{C\text{-}N}$ = 1505; ^1H NMR (CD_3OD, 23 ºC, δ) 7.65 (d, J = 2.4 Hz, 3H, C*H*), 7.62 (d, J = 1.6 Hz, 3H, C*H*), 6.12 (t, J = 2.2 Hz, 3H, 4-C*H*), 4.65 (broad, 1H, ^{11}B*H*), -0.13 (quartet, J = 80.8 Hz, 4H, BH_4); $^{13}C\{^1H\}$ NMR (CD_3OD, 23 ºC, ppm) 141.27 (s, *C*H), 136.16 (s, *C*H), 104.48 (s, 4-*C*H).

Anal. Calcd for $C_9H_{14}B_2CaN_6$: C, 40.34; H, 5.27; N, 31.36. Found: C, 31.08; H, 5.07; N, 23.44.

Preparation of [TpCaBH$_4$(THF)]$_4$ (26). A 100 mL Schlenk flask was charged with **1** (0.200 g, 0.746 mmol) and 20 mL of toluene. The resulting cloudy solution was filtered through 3cm of Celite on a medium glass frit. To the clear filtrate, 50mL of hexane was carefully layered on top of the filtrate and left at room temperature. After a week, the solution afforded colorless crystals of **2** (0.185 g, 73 %).

Alternative preparation of 26. A 100 ml Schlenk flask was charged with Ca(BH$_4$)$_2$(THF)$_2$ (0.200 g, 0.935 mmol), KTp (0.236 g, 0.936 mmol), and a stir bar. Tetrahydrofuran (30 mL) was added, resulting in the slow formation of a white precipitate, KBH$_4$. The reaction mixture was stirred for 18 h, after which the volatiles were removed under reduced pressure to leave a white residue. Toluene (20 mL) was added to extract the product. The resulting mixture was filtered through a 3-cm pad of Celite on a medium glass frit to yield a clear filtrate. Hexane (50 mL) was layered on top of the filtrate and set aside at room temperature. After about one week the solution afforded colorless crystals of **2** (0.165 g, 52 %): mp 192-194 °C; IR (Nujol, cm^{-1}) $\nu_{B\text{-}H}$ = 2442 (B-H), $\nu_{B\text{-}H}$ = 2403-2224 (BH$_4$), $\nu_{C\text{-}N}$ = 1504; ^{1}H NMR (C$_6$D$_6$, 23 °C, δ) 7.96 (s, 12H, C*H*), 7.62 (s, 12H, C*H*), 5.96 (s, 12H, 4-C*H*), 4.75 (broad, 4H, B*H*), 3.53 (s, 16H, OC*H*$_2$CH$_2$) 1.16 (quartet, J = 81.6 Hz, 16H, B*H*$_4$) 1.16 (s, 16H, C*H*$_2$CH$_2$O); ^{13}C{^{1}H} NMR (CD$_6$D$_6$, 23 °C, ppm) 141.40 (s, *C*H), 135.34 (s, *C*H), 103.98 (s, 4-*C*H) 69.03 (s, O*C*H$_2$CH$_2$), 25.18 (s, *C*H$_2$CH$_2$O).

Anal. Calcd for $C_{52}H_{88}B_8Ca_4N_{24}O_4$: C, 45.92; H, 6.52; N, 24.71. Found: C, 46.32; H, 6.52; N, 21.17.

Preparation of TpCaBH$_4$(THF)$_2$ (27). Similar to the preparation of **26,** A 100 mL Schlenk flask was charged with **1** (0.200 g, 0.746 mmol) and tetrahydrofuran (20 mL), followed by layering with hexane (50 mL). After a week, the solution afforded colorless crystals of **3** (0.132 g, 43 %).

Alternative preparation of 27. Similar to the alternative preparation of **26,** The reaction between $Ca(BH_4)_2(THF)_2$ (0.200 g, 0.935 mmol) and KTp (0.236 g, 0.936 mmol), followed by layering with tetrahydrofuran (20 mL)/ hexane (50 mL) afforded colorless crystals of **3** (0.210 g, 55 %): mp 190-192 °C; IR (Nujol, cm^{-1}) ν_{B-H} = 2459 (B-H), ν_{B-H} = 2399-2157 (BH_4) , ν_{C-N} = 1502; ^1H NMR (C_6D_6, 23 ºC, δ) 7.90 (s, 3H, C*H*), 7.60 (d, J = 2.4 Hz, 3H, C*H*), 5.97 (s, 3H, 4-C*H*), 4.90 (broad, 4H, B*H*), 3.54 (s, 8H, OCH_2CH_2), 1.26 (s, 16H, CH_2CH_2O)1.14 (quartet, J = 81.3 Hz, 4H, BH_4); $^{13}C\{^1H\}$ NMR (C_6D_6, 23 ºC, ppm) 141.26 (s, *C*H), 135.34 (s, *C*H), 104.01 (s, 4-*C*H) 68.65 (s, OCH_2CH_2), 25.40 (s, CH_2CH_2O).

Anal. Calcd for $C_{17}H_{30}B_2CaN_6O_2$: C, 49.54; H, 7.34; N, 20.39. Found: C, 47.16; H, 6.99; N, 19.07.

Preparation of [(TpCa(MeOH))$_2$(μ-(B(OMe)$_4$)][B(OMe)$_4$] (28). A 100 mL Schlenk flask was charged with **27** (0.200 g, 0.746 mmol) and 20 mL of methanol. The resulting clear solution was placed next to a hot oven. After one week, colorless crystals began to deposit on the flask affording **28 (**0.254 g, 75 %): mp 268-270 °C; IR (Nujol, cm^{-1}) ν_{B-H} = 2453, ν_{C-N} = 1503; ^1H NMR (CD_3OD, 23 ºC, δ) 7.64 (d, J = 2 Hz, 6H, C*H*), 7.62 (d, J = 1.6 Hz, 6H, C*H*), 6.12 (t, J = 2.2, 6H, 4-C*H*), 3.54 (s, 36H, OCH_3) ; $^{13}C\{^1H\}$ NMR (CD_3OD, 23 ºC, ppm) 140.91 (s, *C*H), 135.86 (s, *C*H), 104.32 (s, 4-*C*H) 49.84 (s, OCH_3).

Anal. Calcd for $C_{30}H_{60}B_4Ca_2N_{12}O_{12}$: C, 39.85; H, 6.69; N, 18.59. Found: C, 39.55; H, 6.55; N, 17.97.

Preparation of [(TpCaB(OEt)$_3$O)$_3$B]·EtOH (29). A 100 mL Schlenk flask was charged with **27** (0.200 g, 0.746 mmol) and 20 mL of ethanol. The resulting clear solution was layered with hexane (50 mL) and within two days colorless crystals of **29** (0.250 g, 77 %) deposited on the flask: mp 268-270 °C; IR (Nujol, cm^{-1}) $\nu_{B\text{-}H}$ = 2466, $\nu_{C\text{-}N}$ = 1502; ^{1}H NMR (CD_3OD, 23 ºC, δ) 7.63 (d, J = 2.4 Hz, 9H, C*H*), 7.62 (d, J = 1.6 Hz, 9H, C*H*), 6.12 (t, J = 2.2, 9H, 4-C*H*), 3.60 (quartet, J = 6.9 Hz, 20H, OCH_2CH_3), 1.17 (triplet, J = 7.0 Hz, 30H); ^{13}C{^{1}H} NMR (CD_3OD, 23 ºC, ppm) 140.92 (s, *C*H), 135.87 (s, *C*H), 104.34 (s, 4-*C*H), 58.324 (s, OCH_2CH_3), 18.36 (s, OCH_2CH_3).

Anal. Calcd for $C_{47}H_{81}B_7Ca_3N_{18}O_{13}$: C, 43.35; H, 6.27; N, 19.36. Found: C, 43.68; H, 6.26; N, 18.99.

CHAPTER 6

Atomic Layer Deposition of BaB_2O_4 Thin Films from an Exceptionally Thermally Stable Tris(pyrazolyl)borate-Based Precursor

6.1 Introduction

In Chapter 2, the synthesis and chacterization of a series of volatile and thermally stable group 2 complexes containing alkyl substituted Tp^{R2} (R = H, Et, nPr) ligands was described. $BaTp^{Et2}_2$ (**7**) has optimum precursor characteristics with a sublimation temperature of 210 °C/0.05 Torr and only 0.1% residue and a solid state decomposition temperature of ~380 °C. The present chapter describes the ALD growth of BaB_2O_4 films from $BaTp^{Et2}_2$ and water. This process exhibits self-limited ALD growth up to 375 °C, which demonstrates the exceptional thermal stability of $BaTp^{Et2}_2$. ALD precursors with the highest thermal stability permit self-limited growth over the widest possible temperature range, may allow the growth of crystalline materials at higher temperatures, and also may deposit higher purity materials due to the absence of decomposition pathways that incorporate undesired elements such as carbon and hydrogen. $BaTp^{Et2}_2$ also contains a 2:1 B/Ba ratio, and this precursor stoichiometry is maintained in the BaB_2O_4 films. Use of heterobimetallic precursors to control the ratios of two different elements in thin films is rare in ALD, and generally affords poor stoichiometry control.[103] Group 2 metal borates are important thin film materials,[13] and there are only a few reports of their growth by CVD.[14,46] This is the first report of a metal borate film growth by ALD.

6.2 Results and Discussion

ALD growth of BaB_2O_4 on silicon substrates was studied using $BaTp^{Et2}_2$ and water vapor. The growth behavior was assessed by varying precursor pulse lengths, substrate temperatures, and the number of deposition cycles. Investigation of growth rate as a function of $BaTp^{Et2}_2$ pulse length was performed at 325 °C (Figure 30). The number of deposition cycles, the water pulse length, and the length of the purge after the water pulse were held constant at 2000, 0.5 s, and 5.0 s, respectively. The $BaTp^{Et2}_2$ reservoir was maintained at 205 °C and the purge length after the $BaTp^{Et2}_2$ pulse was 10.0 s. The growth rate was 0.23 Å/cycle with $BaTp^{Et2}_2$ pulses of $\geq$ 1 s, which demonstrates self-limited ALD growth.

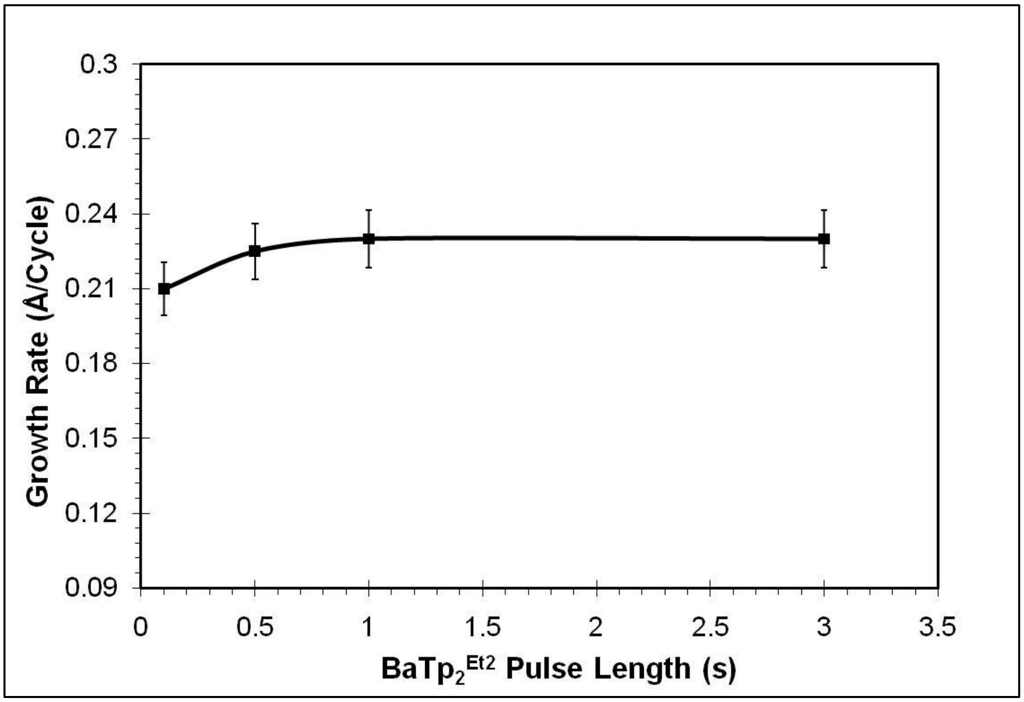

Figure 30. Plot of pulse length of $BaTp^{Et2}_2$ versus growth rate at 325 °C.

The dependence of growth rate on substrate temperature was also investigated (Figure 31). Depositions were carried out using $BaTp^{Et2}_2$ and water pulse lengths of 3.0 s and 0.5 s, respectively, and 2000 deposition cycles. Nitrogen purge lengths of 10.0 s and 5.0 s were used after the $BaTp^{Et2}{}_2$ and water pulses, respectively. A growth rate of 0.23 Å/cycle was observed between 250 and 375 °C. An area of constant growth rate within a specific temperature range is termed the "ALD window," and is characteristic of a robust ALD process.[22a-c] Growth rates of 0.17 and 0.34 Å/cycle were observed at substrate temperatures of 240 and 400 °C, respectively, which are outside of the ALD window. The thickness varies linearly with the number of cycles as indicated in Figure 32, and passes through zero, which indicates that there is no significant delay in nucleation at the beginning cycles of the ALD run.

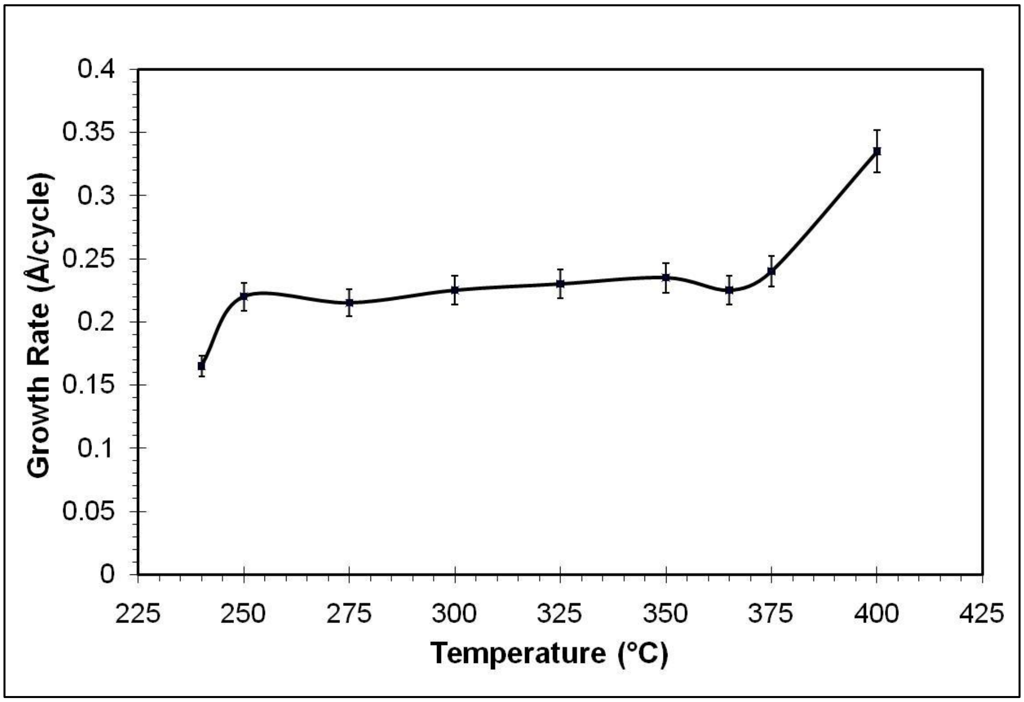

Figure 31. Plot of substrate temperature versus growth rate BaB_2O_4.

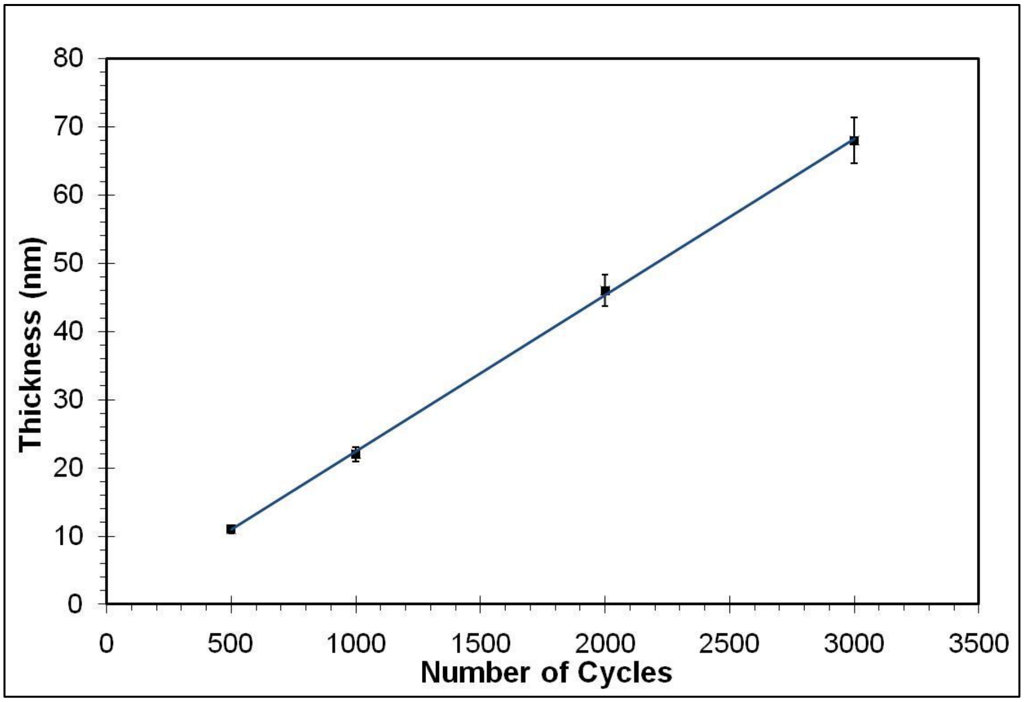

Figure 32. Plot of number of cycles versus thickness of BaB_2O_4 films.

ERDA was performed on 45-47 nm thick BaB_2O_4 films deposited at 325 and 350 °C to determine the elemental compositions (Table 27). The B/Ba ratios were close to the expected ratio for BaB_2O_4. Hydrogen concentrations for films grown at 325 and 350 °C were 1.2 ± 0.2 and 0.84 ± 0.1 at %, respectively, and the carbon concentrations were 0.3 ± 0.3 and <0.2 at %, respectively. For both samples, the nitrogen concentration was below the detection limit of 0.2 at %.

Table 27. Elemental composition of thin films deposited from $BaTp^{Et2}_2$ and water, as determined by ERDA.

T(°C)	B:Ba Ratio	O:Ba Ratio	%H	%C
325	2.1(3)	3.8(4)	1.2(2)	0.3(3)
350	2.2(3)	4.7(4)	0.84(10)	<0.2

XPS on a film deposited at 325 °C revealed Ba $3d_{5/2}$ and Ba $3d_{3/2}$ binding energies of 775.5 and 790.9 eV, respectively, with an O 1s ionization at 530.8 eV (Figure 33). The B 1s and Ba $4p_{1/2}$ ionizations were superimposed at 190.7 eV, and thus reliable B concentration data could not be obtained. After argon ion sputtering for 1 min, the carbon and nitrogen ionizations were below the detection limits (Figure 34). All films were amorphous as determined by X-ray diffraction. Annealing of an amorphous film grown at 325 °C at 550 °C in an oxygen atmosphere afforded crystalline β-BaB_2O_4 (Figure 35).

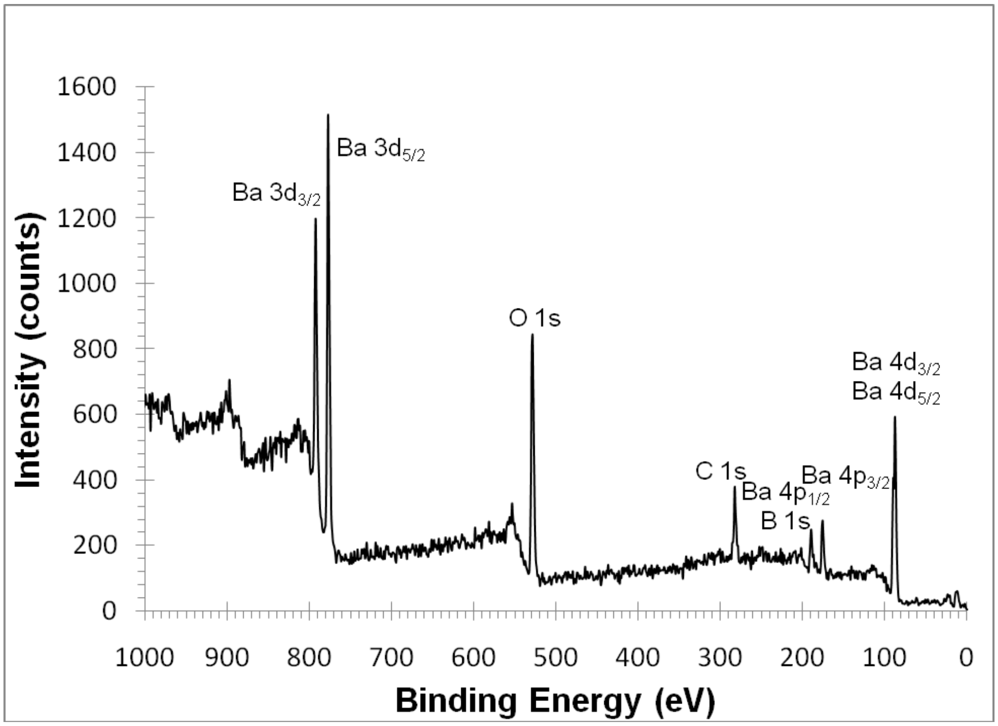

Figure 33. XPS of a film grown at 325 °C, with no argon ion sputtering.

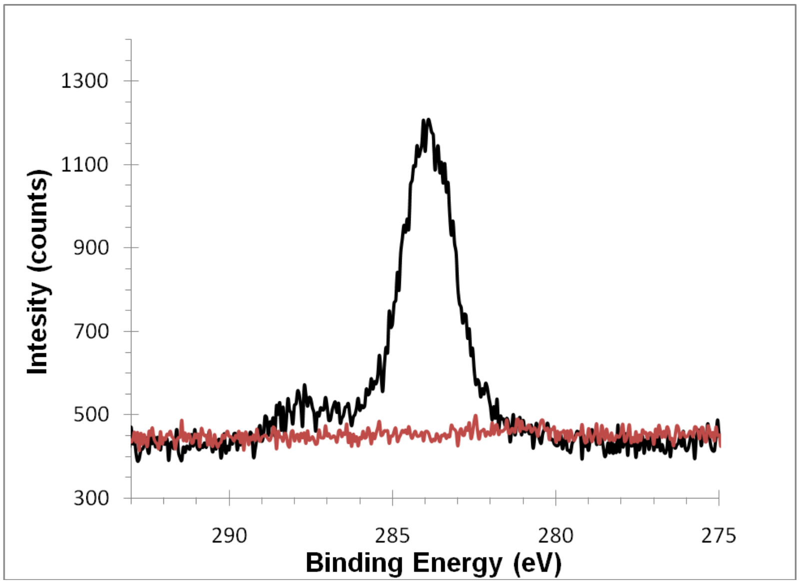

Figure 34. XPS of a film grown at 325 °C, showing the C 1s ionizations. The black trace shows the spectrum of the as-deposited film, while the red trace shows the spectra after one minute of argon sputtering to remove surface contaminants.

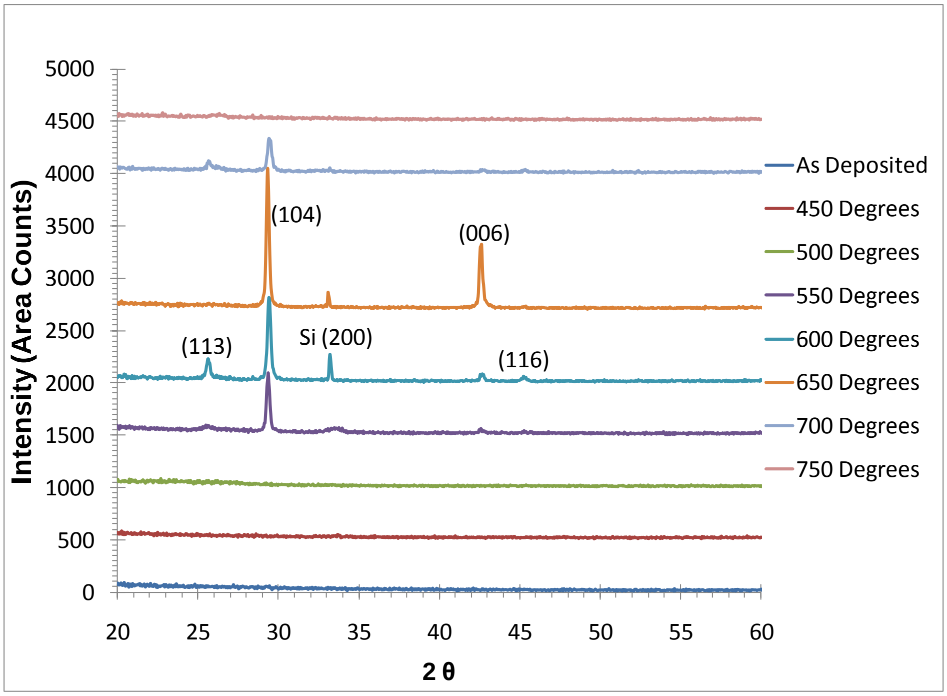

Figure 35. XRD patterns of a film deposited at 350 °C and annealed under O_2 at various temperatures.

AFM and SEM were used to probe the surface morphology of the as-deposited films. Micrographs of characteristic film surface features were collected for films deposited at 325 and 350 °C, with thicknesses of 68 and 47 nm, respectively. Films deposited at both temperatures were smooth and featureless. The AFM rms surface roughnesses of typical 2 x 2 μm^2 areas in both films were 0.53 nm (Figure 36). SEM micrographs revealed smooth, pinhole-free films at all magnifications (Figures 37 and 38).

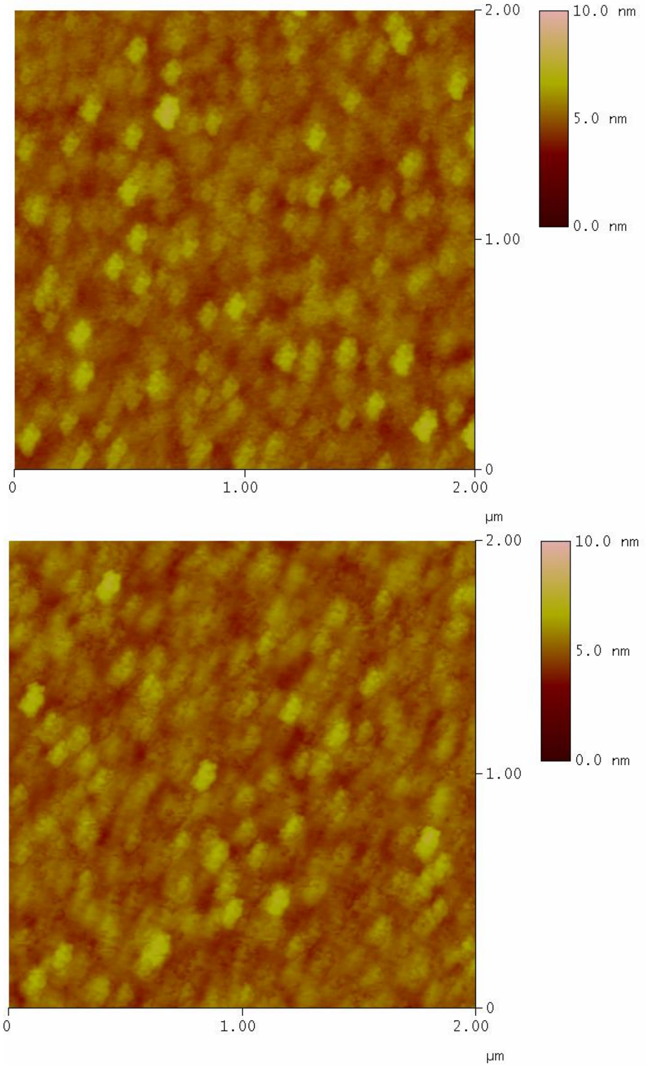

Figure 36. Representative AFM images of films grown at 325 (top) and 350 °C (bottom). The film thicknesses were 67 nm and 47 nm.

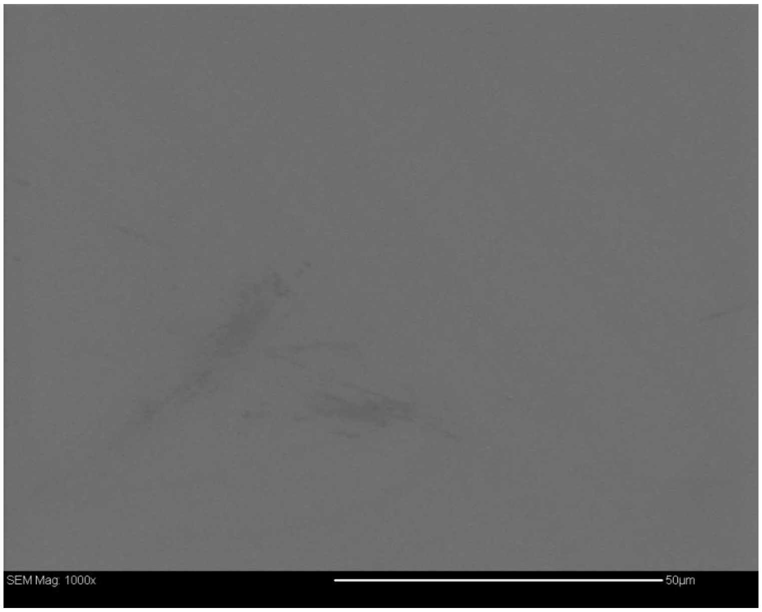

Figure 37. A SEM image of a 68 nm thick BaB_2O_4 film grown at 325 °C on a silicon substrate.

Figure 38. A SEM image of a 47 nm thick BaB_2O_4 film grown at 350 °C on a silicon substrate.

The results described herein are significant from several perspectives. Foremost, $BaTp^{Et2}_2$ has high thermal stability, which allows self-limited ALD film growth to occur up to 375 °C. The decomposition temperature of $BaTp^{Et2}_2$ (~380 °C in the solid state) is much higher than those of widely used CVD precursors.[1] The most thermally stable Ba ALD precursor reported to date is $Ba(C_5H_2tBu_3)_2$, which may be thermally stable up to 350 °C as a solid.[57] The upper temperature limit of BaB_2O_4 ALD growth described herein exceeds that of $BaTiO_3$ ALD growth from $Ba(C_5H_2tBu_3)_2$, $Ti(OiPr)_4$, and water by 50 °C.[57] Tris(pyrazolyl)borate ligands have been coordinated to most metals in the periodic table.[59] Ba is one of the most difficult elements in the periodic table for which to prepare volatile and thermally stable compounds, so the present success with $BaTp^{Et2}_2$ suggests that many other metal complexes containing tris(pyrazolyl)borate ligands should also combine volatility and high thermal stability. Precursor thermal decomposition destroys self-limited ALD growth and low decomposition temperatures represent a drawback of most existing ALD precursors.[22a-c] Hence, complexes containing tris(pyrazolyl)borate ligands may constitute a general class of thermally stable ALD precursors. Dimeric $[BaTp_2]_2$ (**1**) (Tp = tris(pyrazolyl)borate) has been used as a CVD precursor for BaB_2O_4 films,[46a] but it undergoes thermal decomposition at 330 °C and does not offer enhanced thermal stability compared to $Ba(C_5H_2tBu_3)_2$.[57] The higher thermal stability of $BaTp^{Et2}_2$ (**7**), relative to $[BaTp_2]_2$ (**1**), highlights the importance of careful ALD precursor optimization.

Bimetallic precursors with 1:2 Sr/Ta ratios have been used for the ALD growth of Sr-Ta-O films.[103a,b] Variable Sr/Ta ratios (0.5-1.5) were observed depending upon the deposition conditions, possibly due to loss of volatile tantalum species from the growing film.[103b] ALD growth of $PrAlO_x$ and $NdAlO_x$ films was demonstrated using bimetallic isopropoxide precursors with 1:1 metal ratios, but substoichiometric Pr/Al and Nd/Al ratios (0.30-0.71) were obtained.[103c] $Bi(CH_2SiMe_3)_3$ was employed with ozone for the ALD growth of Bi-Si-O films.[103d] The Si/Bi ratio increased from about 1.5 at 200 °C to about 5 at 450 °C. In the present work, the 2:1 B/Ba stoichiometry of $BaTp^{Et2}_2$ is maintained in the BaB_2O_4 thin films, within the uncertainty of the ERDA measurements. Such stoichiometry control implies that two Tp^{Et2} ligands remain coordinated to the surface-bound Ba species, and that hydrolysis of $BaTp^{Et2}_2$ is rapid and very efficient. $[BaTp_2]_2$[46a] and $MgTp_2$[46b] have been employed with dioxygen as precursors for the CVD growth of BaB_2O_4 and $Mg_2B_2O_5$ films, respectively, at 750-900 °C. While the 2:1 B/Ba ratio of $[BaTp_2]_2$ was retained in BaB_2O_4, $Mg_2B_2O_5$ has a 1:1 B/Mg ratio, which differs from the 2:1 ratio in $MgTp_2$. The high CVD growth temperatures probably afford decomposition products that can lead to variable B/metal ratios in the thin films. ALD growth of B_2O_3 and BN films has been reported,[104] as has boron phosphate on silica surfaces.[105,22d]

β-BaB_2O_4 is an important thin film material, and has many applications due to its nonlinear optical properties.[13,14,46a] Thin films of BaB_2O_4 have not been previously grown by ALD, presumably due to the difficulty in controlling the B/Ba ratio with separate precursors. CVD growth of BaB_2O_4 films required a 2.5:1 ratio of B to Ba precursors for optimum depositions.[14a] BaB_2O_4 must possess the crystalline β-phase to exhibit nonlinear optical properties. The present work provides a solution to controlling the B/Ba stoichiometry in BaB_2O_4, but films grown at 375 °C (the upper limit of the ALD window) on silicon remain amorphous. $SrTiO_3$ and $BaTiO_3$ are also important thin film materials that must be crystalline to exhibit the desired ferroelectric properties.[48,49,56,57] The ALD growth of $BaTiO_3$ films from $Ba(C_5H_2tBu_3)_2$, $Ti(OiPr)_4$, and water has an upper limit of 325 °C,[57] but affords amorphous material. It is not clear if $BaTp^{Et2}_2$ is an appropriate precursor for $BaTiO_3$ growth, due to the facile B incorporation described herein. An oxygen precursor other than water may avoid B incorporation, and experiments are in progress to probe this issue. Hwang and coworkers showed that use of a 3-nm thick crystalline $SrTiO_3$ seed layer led to the subsequent growth of a crystalline $SrTiO_3$ layer at 370 °C with the desired perovskite structure using an ALD process with $[Sr(thd)_2]_3$, $Ti(OiPr)_2(thd)_2$, and water.[49b] This process may not proceed by a true ALD mechanism, since $[Sr(thd)_2]_3$ lacks sufficient reactivity toward water to form SrO films below its decomposition temperature,[48f,57] and $Ti(OiPr)_2(thd)_2$ undergoes thermal decomposition at ~230 °C.[106] It is possible that other crystalline substrates may lead to growth of β-BaB_2O_4 at temperatures as low as 375 °C, without having to resort to post-deposition annealing.

6.3 Conclusion

The present work describes a significant enhancement of thermal stability in a Ba ALD precursor, relative to existing Ba ALD and CVD precursors, through use of a tris(pyrazolyl)borate-based ligand. $BaTp^{Et2}_2$ also confers a precise 2:1 B/Ba ratio in the BaB_2O_4 films. Precursors containing tris(pyrazolyl)borate ligands should allow the ALD growth of a variety of metal borate films, and similar B/metal stoichiometry control should be possible. Precursor-based composition control, as documented herein, is largely unprecedented in the ALD growth of ternary materials.

6.4 Experimental

BaB_2O_4 Film Deposition. A SUNALE R-75 ALD reactor manufactured by Picosun Oy was used for thin film deposition experiments. The reactor was operated under a flow of nitrogen at a pressure of 1-2 mbar. The deposition of BaB_2O_4 thin films by ALD was studied employing barium bis(tris(diethylpyrazolyl)borate), $BaTp^{Et2}_2$, as the barium and boron source and water as the oxygen source. $BaTp^{Et2}_2$ was prepared according to a previously published procedure. In initial growth trials, the sublimation temperature for $BaTp^{Et2}_2$ was found to be optimum at 205 °C at the reactor pressure. The substrate temperatures were between 240 and 400 °C. Nitrogen was used as both the carrier and purge gas and was obtained from air using a Texol GeniSys nitroGenerator. Deposition experiments were performed using a range of $BaTp^{Et2}_2$ pulse lengths, water pulse lengths, and nitrogen purge lengths to determine the extent of surface saturation. Films were deposited on Si(100) substrates obtained from Silicon Quest International. One substrate, one fourth of a 4 inch wafer, was used in each deposition experiment. The native oxide was not removed prior to deposition.

Film Characterization Methods. Film thicknesses were determined by the fitting of reflectance spectra collected between 1100-190 nm, using the method of Ylilammi and Ranta-aho.[107] Reflectance spectra were measured using a Jasco V-570 UV/Vis/NIR double beam spectrophotometer. The film growth rate was determined by dividing the measured film thickness by the number of deposition cycles performed. X-ray diffraction spectra were collected with a Philips MPD 1880 diffractometer using Cu Kα radiation. Atomic force micrographs were obtained using a Park Autoprobe atomic force microscope, and were performed in the contact mode. Surface roughness was calculated as root-mean-square (rms) values. X-ray photoelectron spectroscopy was done using a Perkin-Elmer 5500 XPS system using monochromatized Al Kα radiation. Surface contaminants were sputtered away using 0.5 kV Ar ions. Elemental concentrations of BaB_2O_4 thin films were determined by ERDA at Forshchungszentrum Dresden-Rossendorf

CHAPTER 7

The Atomic Layer Deposition of SrB_2O_4 Thin Films using the Thermally Stable Precursor bis(tris(pyrazolyl)borate)strontium

7.1 Introduction

In Chapter 6, $BaTp^{Et2}_2$ (**7**) and water were used to deposit thin films of BaB_2O_4 by ALD growth. Self-limited film growth was observed up to 375 °C, demonstrating that $BaTp^{Et2}_2$ is the most thermally stable barium precursor to date. $SrTp_2$ also has high thermal stability in the solid state up to ~363 °C, with a recovery of 99 % and residue of 0.1 % upon sublimation at 200 °C/0.05 Torr (Chapter 2). In this chapter, the ALD growth of SrB_2O_4 from the thermally stable precursor $SrTp_2$ and water is described. This process exhibits an ALD window between 300-375 °C and affords high quality SrB_2O_4 thin films with low impurity incorporation throughout this temperature range.

7.2 Results and Discussion

SrB_2O_4 Film Growth Studies. Thin film deposition of SrB_2O_4 by ALD was carried out using $SrTp_2$ as the strontium and boron source and water as the oxygen source. In order to assess the growth behavior, precursor pulse lengths, substrate temperatures, and the number of cycles were varied. Thin film growth rate was investigated as a function of $SrTp_2$ pulse length at 350 °C (Figure 39). The number of deposition cycles, length of water pulse, and length of purge after the water pulse were kept constant at 1500, 0.3 s, and 5.0 s, respectively. The purge length after the $SrTp_2$ pulse was held constant at 5.0 s. $SrTp_2$ pulse lengths of ≥ 2 s showed a constant growth rate of about 0.47 Å/cycle, with a slightly lower growth rate of 0.45 Å/cycle at $SrTp_2$ pulse lengths of 0.1 and 0.5 s, respectively. A key element of ALD growth is the saturation of surface sites on the substrate with each precursor pulse. When this condition is met, precursor doses beyond the minimal amount for saturation results in a consistent growth rate. Inspection of Figure 39 indicates that self-limited film growth occurred at $SrTp_2$ pulse lengths of ≥ 2.0 s, and pulse times below this point resulted in sub-saturative growth.

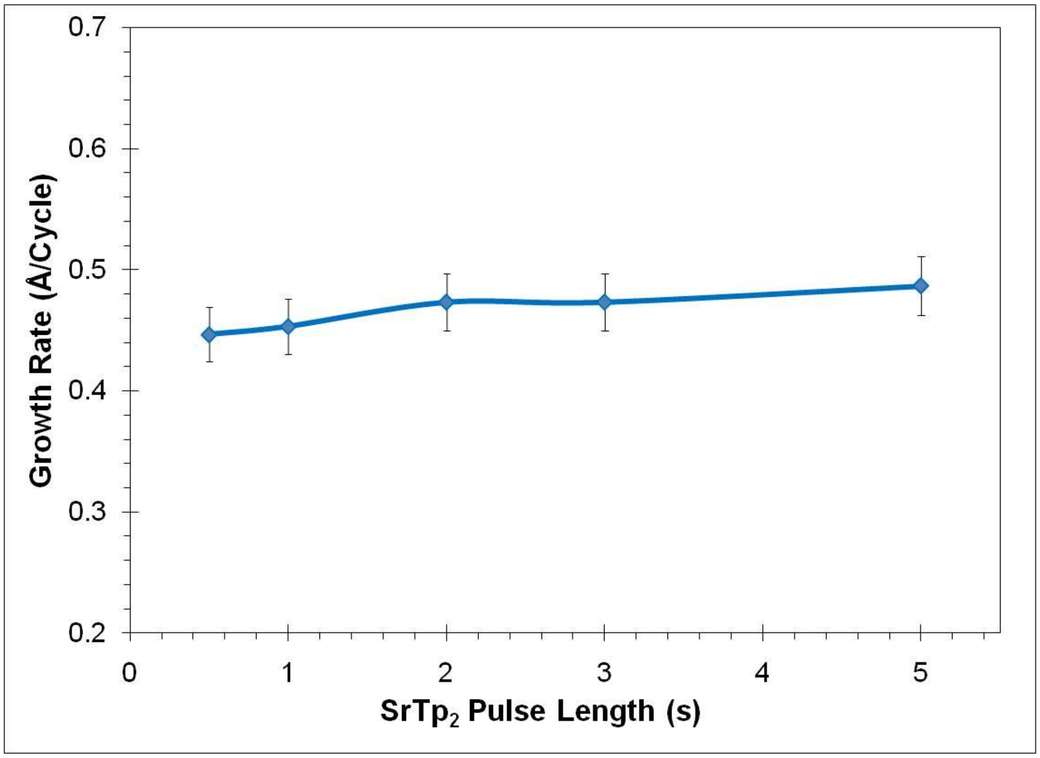

Figure 39. Growth rate as a function of $SrTp_2$ pulse length.

Thin film growth was also investigated as a function of the water pulse at 350 °C (Figure 40). In these experiments, the number of deposition cycles, $SrTp_2$ pulse length, and length after the $SrTp_2$ and water pulses were kept constant at 1500, 3.0 s, and 5.0 s, respectively. Water pulse lengths of ≥ 0.3 s showed a constant growth rate of 0.47 Å/cycle, with lower growth rates of 0.43 and 0.45 Å/cycle at water pulse lengths of 0.1 and 0.2 s, respectively. Figure 40 indicates that self-limited film growth occurred at water pulse lengths of ≥ 0.3 s.

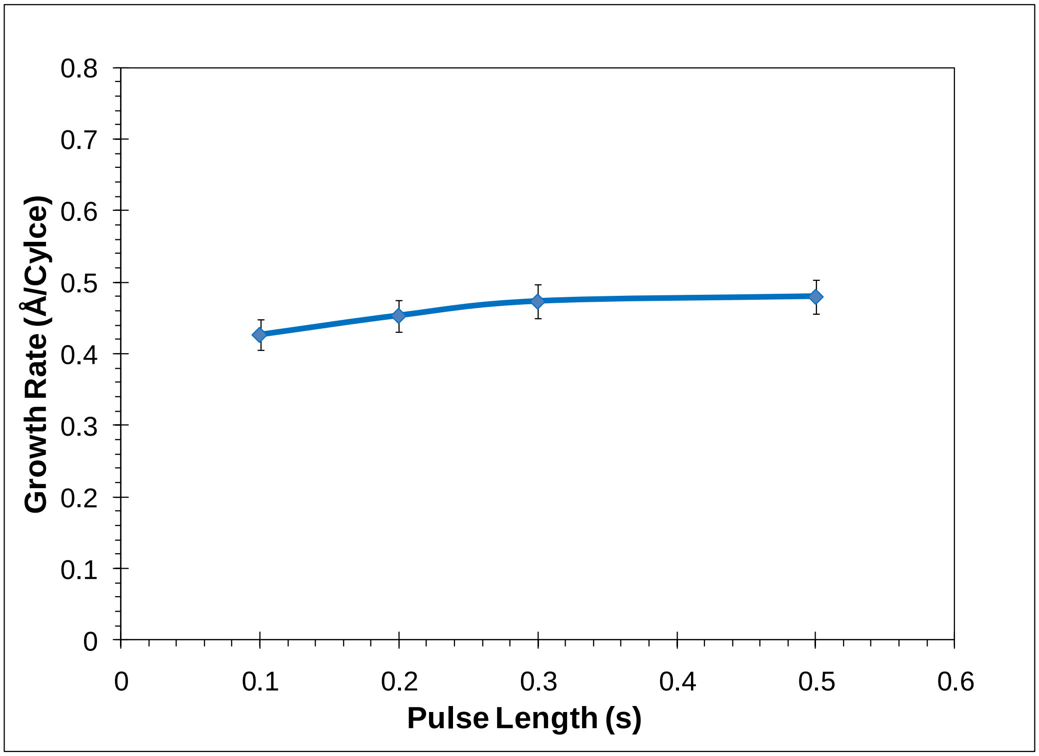

Figure 40. Growth rate as a function of water pulse length.

The growth rate as a function of deposition temperature was also investigated (Figure 41). The conditions in these depositions consisted of $SrTp_2$ and water pulse lengths of 3.0 and 0.3 s, respectively, purge lengths between pulses of 5.0 s, and 1500 deposition cycles. A consistent growth rate of approximately 0.47 Å/cycle was observed over the temperature range of 300-375 °C. Observation of constant growth rate over a certain temperature range is referred to as the "ALD Window", and is observed in many ALD processes.[22a-c] Growth rates of 0.41 and 0.55 Å/cycle were observed for substrate temperatures of 275 and 400 °C, respectively, thus, these temperatures are outside of the ALD window.

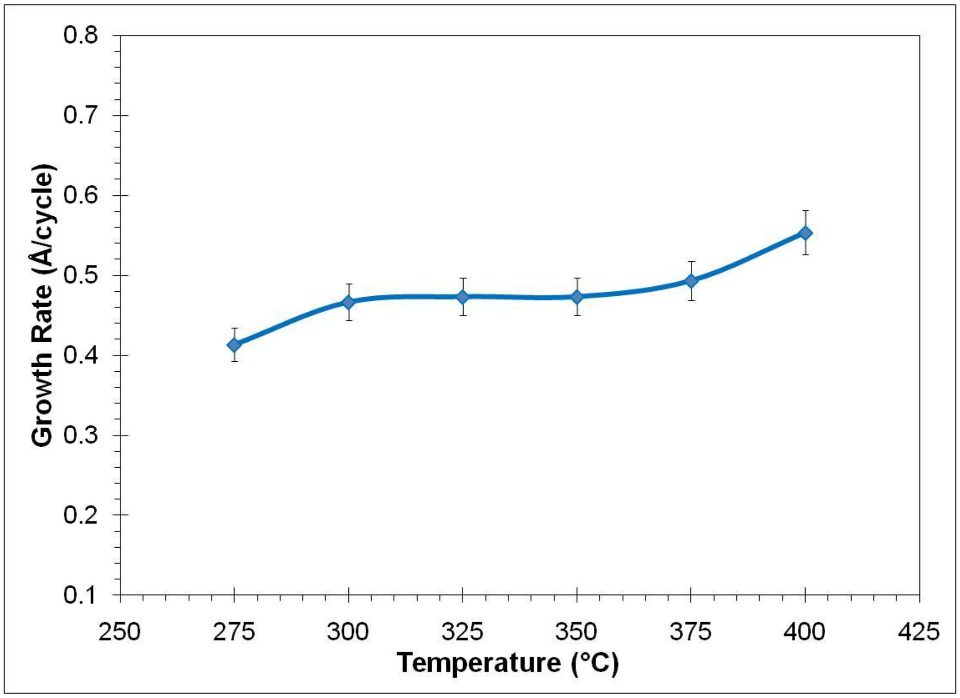

Figure 41. Growth rate as a function of deposition temperature. An ALD window is observed between 300 to 375 °C.

A plot of thickness versus the number of deposition cycles is shown in Figure 42. In this set of experiments the $SrTp_2$ and water pulse lengths were 3.0 and 0.3 s, respectively, with a substrate temperature of 350 °C. As shown in Figure 42, the thickness of the film varied linearly with the number of cycles, indicating that the number of saturation sites per cycle remain constant. The line of best fit shows a y-intercept of 1.5 nm, which is within experimental error of zero and suggests that there is no initiation period during the first few deposition cycles.

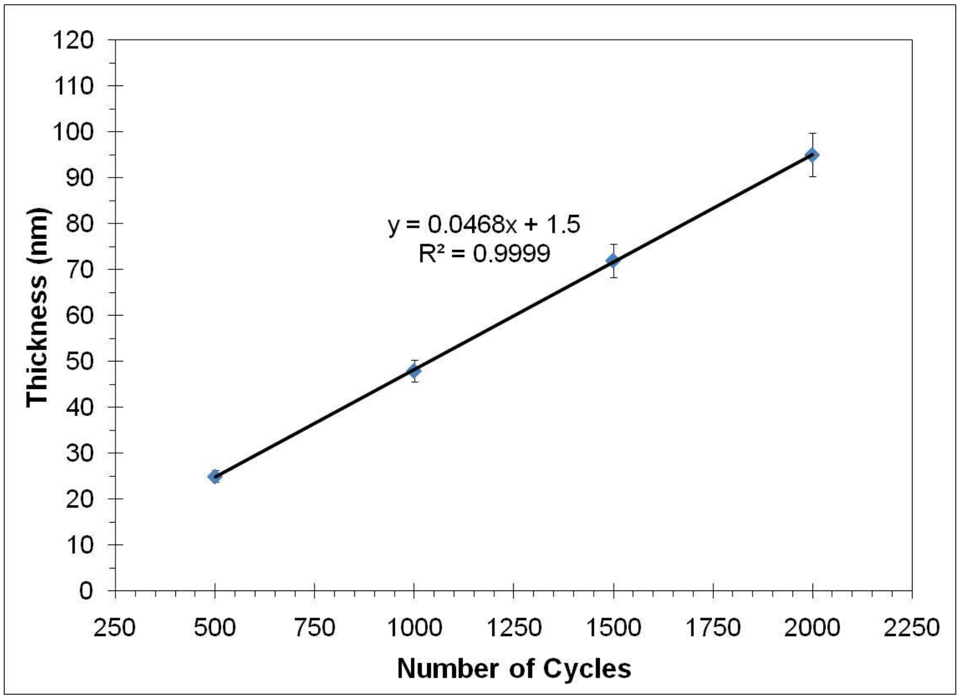

Figure 42. Film thickness as a function of the number of deposition cycles. The data were collected at 350 °C using 3.0 s pulse lengths $SrTp_2$ and 0.3 s pulse lengths for water.

SrB_2O_4 Film Characterization. ERDA was performed on representative SrB_2O_4 samples to probe the elemental compositions (Table 27). For samples deposited at 275 and 325 °C the B/Sr ratios were 1.85(20) and 1.81(20), respectively, and are within experimental error of the expected ratio for SrB_2O_4. By contrast, samples deposited at 350 and 400 °C have B/Sr ratios of 1.65(10) and 1.32(10) atom %, respectively, and are not within experimental error of a 2:1 B/Sr ratio. The O/Sr ratios for films deposited at 275, 325, 375, and 400 °C are 3.99(20), 3.56(2), 3.29(1), and 2.92(10) atom %, respectively. The decrease in the B/Sr and O/Sr ratios with respect to temperature is likely related to boron oxide loss at increased temperatures. The carbon and nitrogen concentrations are below the detection limit (< 0.1 at. %) for samples deposited at temperatures $\leq$ 350 °C and suggest efficient elimination reactions during depositions. The hydrogen, carbon, and nitrogen concentrations were 1.55(8), 1.0(2), and 0.8(2) atom %, respectively, at 400 °C. The increase in hydrogen, carbon, and nitrogen concentrations in samples deposited at 400 °C suggests precursor decomposition, since 400 °C is outside the ALD window and above the solid state decomposition temperature of $SrTp_2$.

Table 27. Elemental composition of SrB_2O_4 films as determined by ERDA.

T(°C)	B/Sr	O/Sr	%H	%C	%N
275	1.85(20)	3.99(20)	0.49(6)	<0.1	<0.1
325	1.81(20)	3.56(20)	0.37(4)	<0.1	<0.1
350	1.65(10)	3.29(10)	0.87(7)	<0.1	<0.1
400	1.32(10)	2.92(10)	1.55(8)	1.0(2)	0.8(2)

XPS was performed on 71 nm thick films deposited at 325 and 350 °C to give insight into the composition of the films. The XPS analysis for both thin films were very similar, thus only the film deposited at 325 °C will be discussed. Figure 43 shows two survey scans of a film deposited at 325 °C, before and after argon ion sputtering for two minutes. After two minutes of argon ion sputtering, the O 1s, Sr 3s, Sr $3p_{1/2}$, Sr $3p_{3/2}$, B 1s, Sr $3d^5$, and O 2s ionizations were observed at binding energies of 534, 359, 282, 272, 194, 135, and 21 eV, respectively. The C 1s, S 2s, and S $2p^3$ ionizations were observed at 287, 234, and 171 eV, respectively and disappeared after 2 minutes of argon ion sputtering, which indicates that the origins of carbon and sulfur are due to surface contaminants. The N 1s ionization was below the detection limit for both the sputtered and non-sputtered samples.

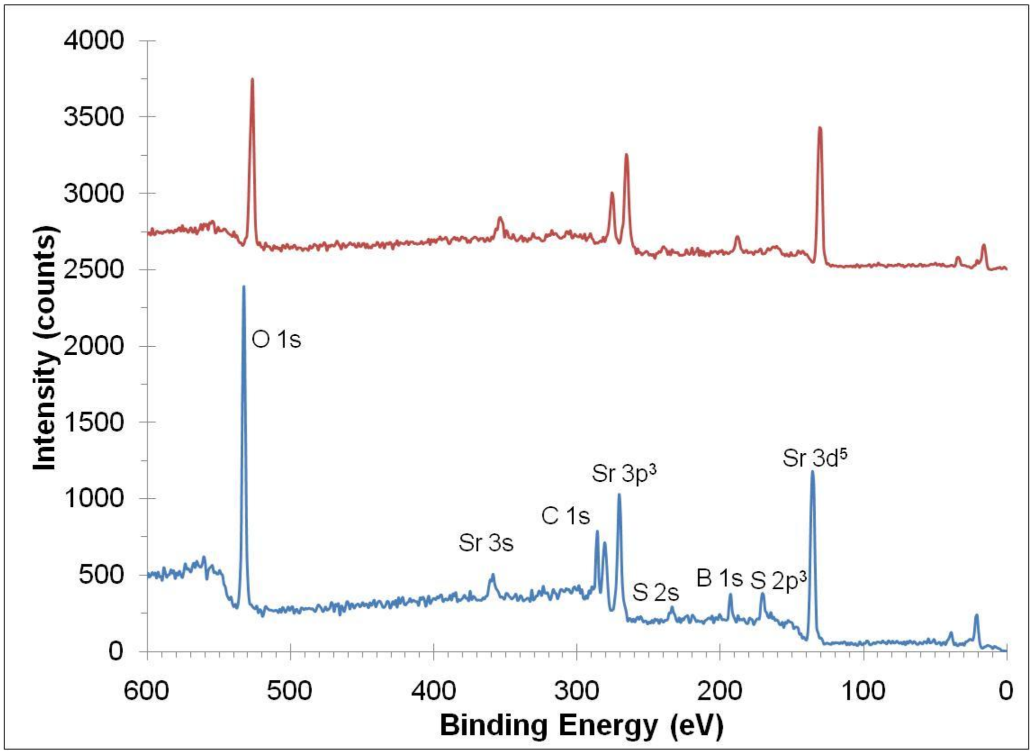

Figure 43. XPS of a 71 nm film deposited at 325 °C before (blue) and after 2 minute argon ion sputtering (red).

Powder XRD experiments were performed on a thin film deposited at 350 °C with a film thickness of 71 nm to understand the crystallization behavior upon annealing under oxygen (Figure 44). The as-deposited film was amorphous, only showing the (310) diffraction peak from the Si(310) plane, PDF=39-0973. The Si(310) reflection remained pronounced throughout all annealing temperatures. A reflection at 2θ = 30.1° appeared after annealing the thin film at 600 °C. Further annealing the film at 650 °C caused the reflection at 2θ = 30.1° to intensify, with the appearance of an additional reflection at 2θ = 44.3°. Both reflections disappeared upon annealing at 750° C. The reflections at 650 °C were not easily matched to any specific crystalline strontium borate phase, since there are many strontium borate phases that matched at least one of the reflections. Additionally, there are only two reflections observed in the XRD spectra and strontium borate phases have many more reflections. The absence of reflections in the XRD spectra could be related to preferential orientation in the thin film. XPS of a thin film annealed at 650 °C showed ionizations corresponding to strontium, boron, and oxygen, which suggests that the reflections are related to a crystalline strontium borate phase (Figure 45). Films annealed at 1100 °C under oxygen showed many reflections, however, none matched any specific strontium borate phases. XPS on films annealed at 1100 °C only showed ionizations corresponding to Si, O, and Sr with respective percent concentrations of 32.6, 64.2, and 3.3 atom % (Figure 46). The reflections observed in the XRD spectra of films annealed at 1100 °C are likely related to multiple forms of SiO_2, since none of the reflections matched any crystalline strontium silicate phases.

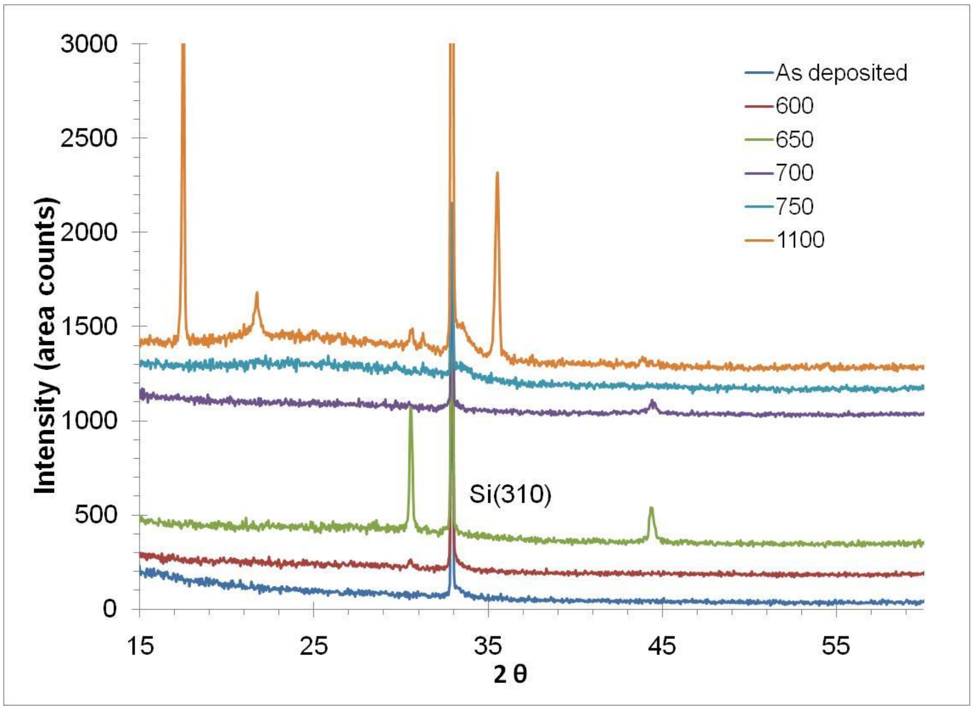

Figure 44. XRD annealing study on a thin film deposited at 325 °C under oxygen.

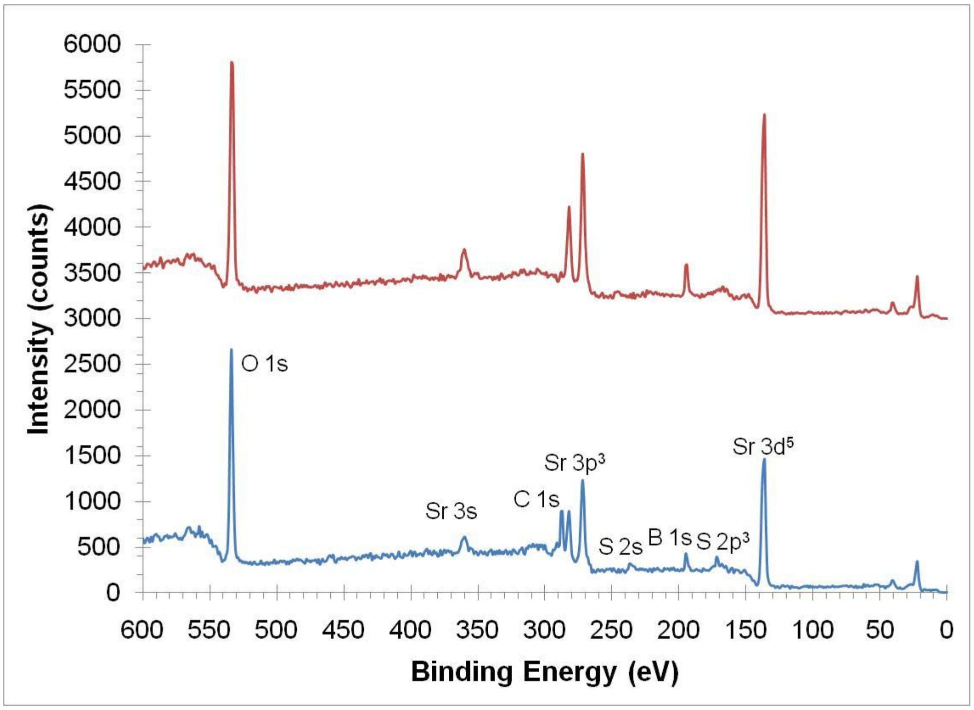

Figure 45. XPS of a 71 nm film deposited at 350 °C annealed under O_2 at 650 °C for one hour before (blue) and after (red) sputtering with argon ions for two minutes.

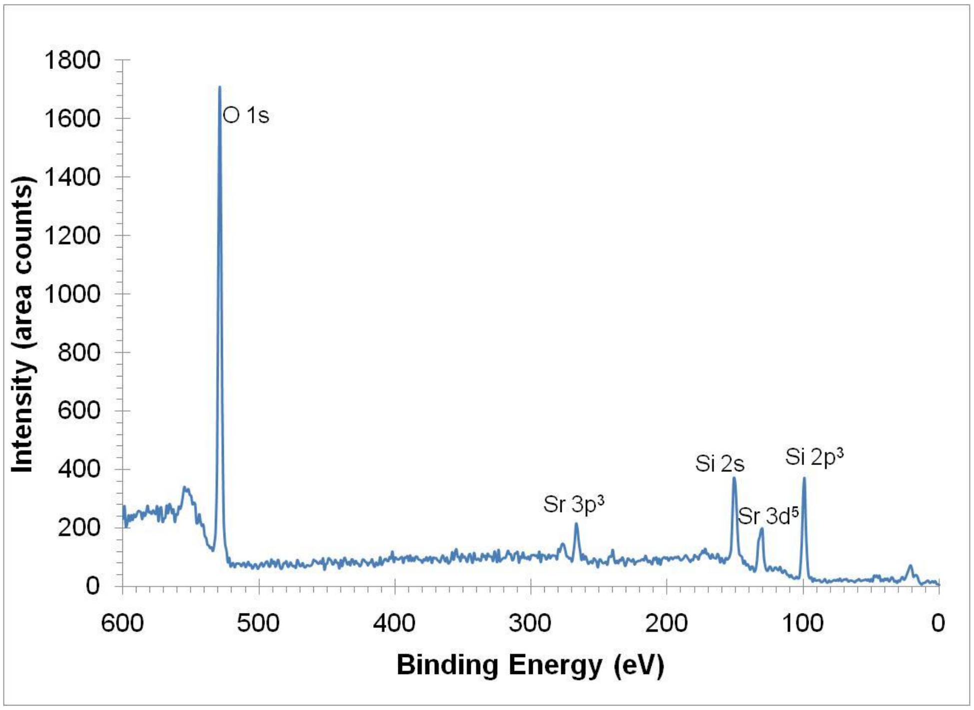

Figure 46. XPS of a 71 nm film deposited at 350 °C annealed under O_2 at 1100 °C for one hour and sputtered with argon ions for 4 minutes.

The surface morphology was investigated by AFM and SEM. The AFM micrographs of 71 nm thick films deposited at 325 and 350 °C are shown in Figure 47. The rms surface roughnesses of a typical 2 µm x 2µm areas were 0.3 and 0.2 nm for films deposited at 325 and 350 °C, respectively. The SEM micrographs of films deposited in the same conditions show films free of cracks and pinholes, with very uniform surfaces (Figure 48 and 49). AFM and SEM micrographs indicated that thin films deposited at 325 and 350 °C were smooth and featureless.

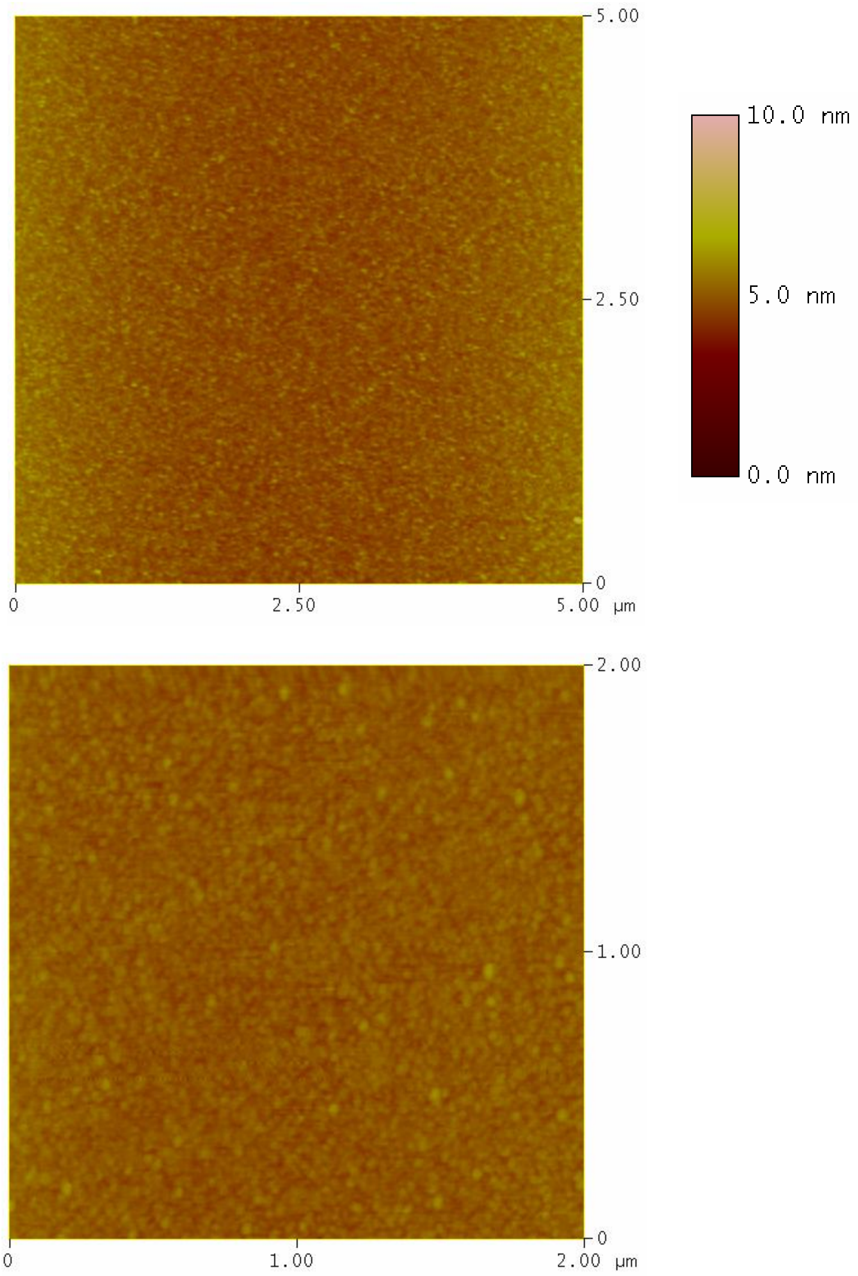

Figure 47. AFM images of SrB_2O_4 thin film surfaces grown at 325 (top, rms roughness = 0.3 nm) and 350 °C (bottom, rms roughness = 0.2 nm).

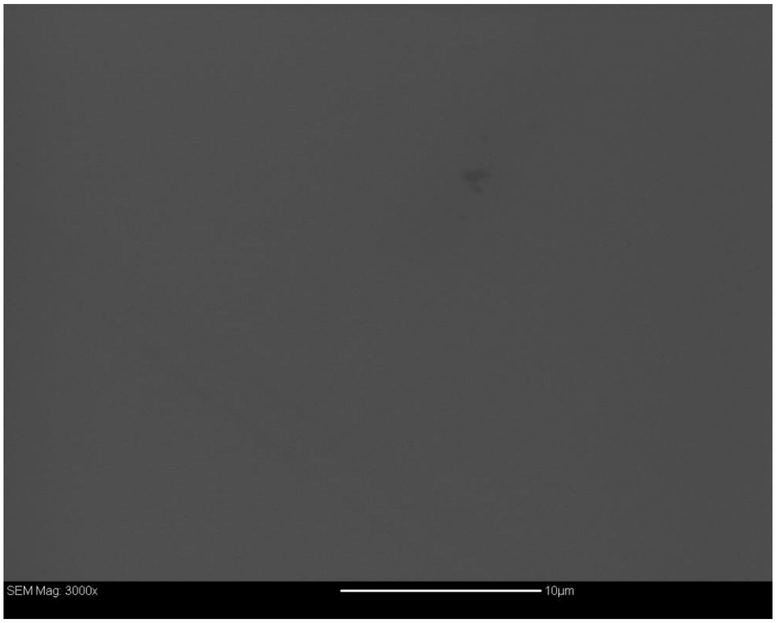

Figure 48. SEM images of a 71 nm thick SrB_2O_4 film deposited at 325 °C on a silicon substrate.

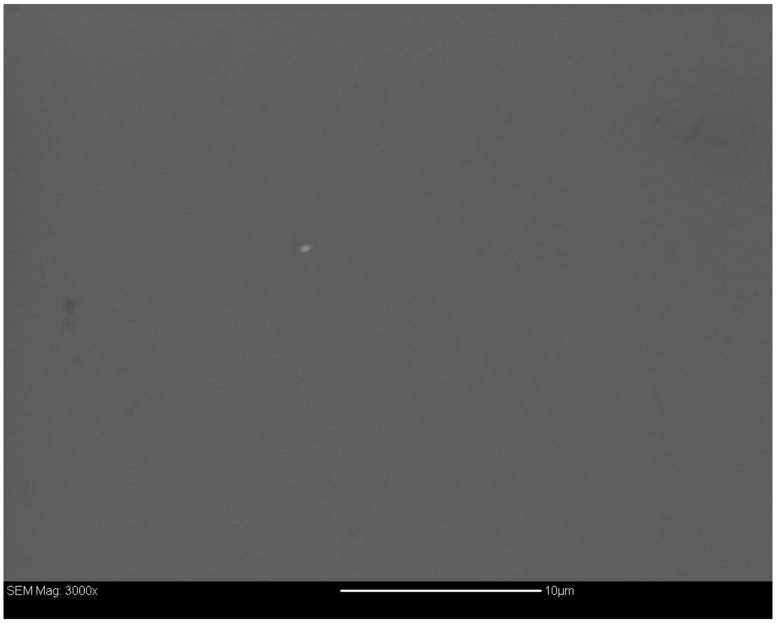

Figure 49. SEM images of a 71 nm thick SrB_2O_4 film deposited at 350 °C on a silicon substrate.

The work documented herein demonstrates the first example of the deposition of SrB_2O_4 by ALD film growth. An ALD window was observed between 300 and 375 °C, demonstrating the exceptional thermal stability of $SrTp_2$. The upper limit of the ALD window usually corresponds well to the decomposition temperature of the precursor.[60] In the deposition of BaB_2O_4 (Chapter 6) it was shown that $BaTp^{Et2}{}_2$ is the most thermally barium precursor reported, with an ALD window upper limit of 375 °C. Similarly, the ALD of SrB_2O_4 also has an ALD window upper limit of 375 °C, and is comparable to the most thermally stable strontium ALD precursors. Precursor thermal decomposition destroys self-limited ALD growth and low decompositions temperatures represent a drawback of most existing precursors.[22a-c] In the ALD of SrS using $Sr(C_5H_2iPr_3)_2$and H_2S, self-limited film growth was observed up to 400 °C.[56b] However, these films contained high carbon levels of 2 atom %, for which the authors claim was a result of precursor thermal decomposition.[56b] Kwon and co-workers were able to deposit crystalline $SrTiO_3$ up to 370 °C using $Ti(OiPr)_2(thd)_2$, plasma enhanced H_2O, and $[Sr(thd)_2]_3$ in combination with a 3 nm $SrTiO_3$ crystalline seed layer.[49b] It is highly likely that more than just an ALD mechanism was at work during these depositions, since the $Ti(OiPr)_2(thd)_2$ precursor undergoes thermal decomposition at ~230 °C.[106] $Sr(C_5H_2iPr_3)_2(THF)$, $Ti(OiPr)_4$, and water were used to deposit $SrTiO_3$ at substrate temperatures of 250-325 °C.[58b] Significant decomposition of $Sr(C_5H_2iPr_3)_2(THF)$ began to occur by 300 °C, as evidenced by the variability of growth rate as a function of strontium precursor pulse length.[58b] $Sr(C_5H_2tBu_3)_2$ has been synthesized, structurally characterized, and is reported to have a decomposition temperature of 370 °C.[58a] Reports of ALD growth using $Sr(C_5H_2tBu_3)_2$ are limited to the deposition of $SrTiO_3$ and were only performed at a substrate temperature of 250 °C.[108] Clearly, the thermal stability of

$SrTp_2$ is comparable to existing group 2 ALD precursors, and therefore Tp-based strontium complexes represent an important new class of ALD precursors.

In Chapter 6, it was proposed that a precise 2:1 boron/barium ratio found in the films was a consequence of the 2:1 ratio observed in the precursor, $BaTp^{Et2}_2$. In this work, the boron/strontium ratio is within experimental error of 2 throughout the ALD window. Although it seems logical that a 2:1 boron/strontium ratio might be observed with $SrTp_2$, Malandrino and coworkers demonstrated the CVD growth of $Mg_2B_2O_5$ using $MgTp_2$ and oxygen at a temperature of 750 °C .[46b] Additionally, other strontium borate phases such as SrB_4O_7, $Sr_2B_2O_5$, and $Sr_3B_2O_6$ are common phases reported.[19f] The ALD of ternary materials is dependent on the thermal stability of each precursor involved in the deposition, hence, the precursor that has the lowest thermal stability should dictate the upper limit of self-limited film growth.[22a-c] Thus, ALD precursors that can deliver multiple elements are advantageous, since the film growth is only dependent on the properties of one precursor. As discussed in Chapter 6, there are few examples in the literature of bimetallic ALD precursors.[100]

Strontium borates doped with lanthanides are useful phosphors with applications as LEDs and FEDs.[18,19] There has been recent effort in the design of oxide-based phosphors over traditional sulfide-based phosphors because of their reduced degradation under applied voltages, lack of hazardous constituents, and acceptable atmospheric stability.[109] There are advantages to using thin film phosphors compared to powder based phosphors. Phosphors as thin films make it possible to achieve smaller pixel spot sizes to obtain higher resolution.[110a] Also, there is lower outgassing from thin film oxide-based phosphors during FED operation.[110] In the present work, the deposition of SrB_2O_4 thin films displayed a relatively large ALD window between 300 and 375 °C. There are many lanthanide ALD processes which show ALD windows over similar temperature ranges,[111] thus facile incorporation of lanthanide ions should be achievable by ALD processes.

7.3 Conclusions

The ALD of SrB_2O_4 has been demonstrated with $SrTp_2$ and water. A wide ALD window was observed from 300-375 °C, which indicates that $SrTp_2$ is one of the most thermally stable strontium ALD precursors reported to date. $SrTp_2$ acts as a single source ALD precursor and is able to transfer a 2:1 B/Sr ratio at deposition temperatures of 350 °C and below, which is similar to previous results involving the deposition of BaB_2O_4 using $BaTp^{Et2}_2$. Because of the high thermal stability and wide ALD window, the deposition of lanthanide containing strontium borate thin films by ALD should be feasible and could have a large impact on current borate-based phosphor technology.

7.4 Experimental

SrB_2O_4 Film Deposition. An SUNALE R-75BE ALD reactor manufactured by Picosun Oy was used for thin film deposition experiments. The reactor was operated under a flow of nitrogen at a pressure of 1-2 mbar. The deposition of SrB_2O_4 thin films by ALD was studied employing bis(tris(pyrazolyl)borate)strontium, $SrTp_2$, as the strontium and boron source and water as the oxygen source. $SrTp_2$ was prepared according to a previously published procedure.[62] In initial growth trials, the sublimation temperature for $SrTp_2$ was found to be optimum at 202 °C at the reactor pressure. The substrate temperatures were between 250 and 400 °C. Nitrogen was used as both the carrier and purge gas and was obtained from air using a Texol GeniSys nitroGenerator. Deposition experiments were performed using a range of $SrTp_2$ pulse lengths, water pulse lengths, and nitrogen purge lengths to determine the extent of surface saturation. Films were deposited on Si(100) substrates obtained from Silicon Quest International. One substrate, one fourth of a 4 inch wafer, was used in each deposition experiment. The native oxide was not removed prior to deposition.

Film Characterization Methods. Film thicknesses were determined by the fitting of reflectance spectra collected between 1100-190 nm, using the method of Ylilammi and Ranta-aho.[107] Reflectance spectra were measured using a Jasco V-570 UV/Vis/NIR double beam spectrophotometer. The film growth rate was determined by dividing the measured film thickness by the number of deposition cycles. Powder X-ray diffraction experiments were performed on a Rigaku R200B 12 kW rotating anode diffractometer, using Cu Kα radiation (1.54056 Å) at 40 kV and 190 mA. Atomic force micrographs were obtained using a MultiMode nanoscope IIIa (Digital Instruments, VEECO). The samples were measured using the tapping mode in air with an E scanner with a maximum scanning size of 12 µm at a frequency of 1 or 2 Hz. The tip employed was a Tap150AI-G with a resoncance frequency of 150 kHz and a force constant of 5 N/m. Surface roughness was calculated as root-mean-square (rms) values. Scanning electron micrographs were obtained with a Hitachi S-2400 instrument operating at 25 kV. X-ray photoelectron spectroscopy was done using a Perkin-Elmer 5500 XPS system using monochromatized Al Kα radiation. Surface contaminants were sputtered away using 0.5 kV Ar ions. Elemental concentrations of SrB_2O_4 thin films were determined by ERDA at Forshchungszentrum Dresden-Rossendorf.

CHAPTER 8

Atomic Layer Deposition of CaB_2O_4 using a Bis(Tris(pyrazolyl)borate)calcium as a Highly Thermally Stable Boron and Calcium Source

8.1 Introduction

There are several reports of group 2 metal borate thin film depositions by chemical vapor deposition (CVD).[14,46] Marks and coworkers grew crystalline β-barium borate films by CVD using direct liquid injection of $Ba(thd)_2$(tetraglyme) (thd = 2,2,6,6-tetramethylheptanedionate) and $B(O^iPr)_3$ solutions, with oxygen and nitrous oxide as the oxidizer gases.[14a] These films were deposited between 640 and 840 °C, and a Ba:B precursor stoichiometry of 1:2.5 was required to achieve stoichiometric BaB_2O_4 films.[14a] Malandrino and coworkers deposited $Mg_2B_2O_5$ and BaB_2O_4 films by CVD using the single source precursors $MgTp_2$ and $[BaTp_2]_2$ (**2**), respectively, at temperatures between 750-900 °C with oxygen as the co-reactant.[46] The CVD growth of group 2 borate films using $MgTp_2$ and (**2**) motivated us to investigate the properties of a series of calcium, strontium, and barium complexes containing Tp-based ligand systems for use as potential ALD precursors (Chapter 2). Significantly, many of these Tp-based precursors combined solid state thermal decomposition temperatures of > 400 °C with sublimation temperatures of ≤ 200 °C at 0.05 Torr. In ALD, the precursor must be volatile, thermally stable at the substrate temperature, and highly reactive towards a secondary precursor.[22a-c] If the precursor undergoes thermal decomposition at the substrate temperature, the self-limited growth mechanism will be lost, which leads to non-uniform films with poor thickness control.[22a-c] In Chapter 6 the ALD growth of BaB_2O_4 using the optimized precursor $BaTp^{Et2}{}_2$ (**7**) and water was discussed. The upper limit of self-limited ALD growth was 375 °C, which demonstrates the exceptional thermal stability of $BaTp^{Et2}_2$. The B/Ba ratios in BaB_2O_4 thin films deposited within the ALD window were 2:1, suggesting that Tp-based group 2 complexes are able to confer a precise 2:1 boron to metal ratio in metal borate thin films. As discussed in Chapter 6 and 7, there are few reports of single source ALD precursors that deliver two elements simultaneously,[103] and control of the element stoichiometries with such precursors is difficult.

Herein the ALD growth of CaB_2O_4 films using $CaTp_2$ and water is described. The thermal stability and volatility of $CaTp_2$ has been evaluated using TGA, solid state decomposition temperatures, and preparative sublimations. Film growth parameters were investigated by varying the precursor pulse lengths, substrate temperatures, and number of deposition cycles. The films were characterized by ERDA, XPS, XRD, and AFM, and SEM.

8.2 Results and Discussion

Thermal Stability and Volatility of $CaTp_2$. $CaTp_2$ was prepared according to a literature procedure.[61e] Its suitability as an ALD precursor was assessed by melting point and solid state decomposition temperature determinations, preparative sublimations, and TGA. The melting point of $CaTp_2$ was 278-280 °C, which is similar to a previously reported value of 275-276 °C.[61e] The solid state decomposition temperature was 385 °C. For comparison, the decomposition temperatures for $CaTp^{Et2}_2$ (**5**) and $CaTp^{nPr2}_2$ (**8**) were > 400 °C. Sublimation at 180 °C /0.05 Torr for three hours afforded a 99.7% sublimed recovery of $CaTp_2$ and a nonvolatile residue of 0.2%. $CaTp_2$ sublimes at a lower temperature than $CaTp^{Et2}_2$ (210 °C/0.05 Torr) and $CaTp^{nPr2}_2$ (240 °C/0.05 Torr), due to its lower molecular weight. The TGA trace for $CaTp_2$ is shown in Figure 50. A one step weight loss indicates sublimation from 240-370 °C, with a final weight residue of 2.2%. The high thermal stability and low sublimation temperature suggested that $CaTp_2$ would be a good ALD precursor.

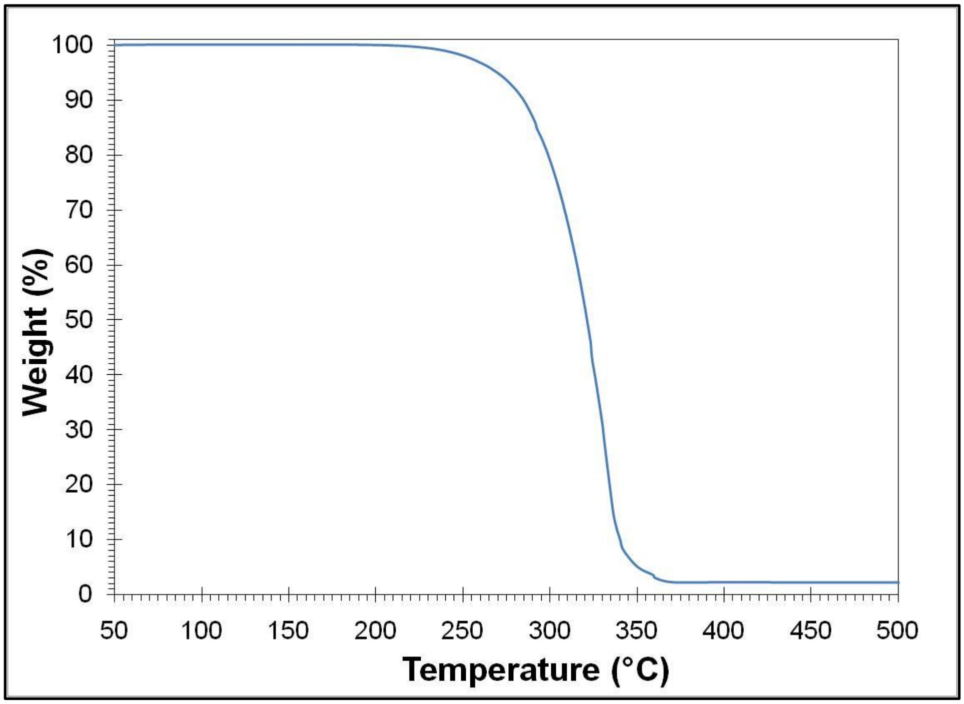

Figure 50. TGA trace for $CaTp_2$ from 50-500 °C at 10 °C.

CaB_2O_4 Film Growth Studies. In initial deposition trials, $CaTp^{Et2}{}_2$ and water were examined as precursors. However, no film deposition occurred, despite many attempts with various substrates and reactor parameters. The lack of film growth with $CaTp^{Et2}{}_2$ probably arises from its slow hydrolysis rate due to the steric protection of the boron-hydrogen bonds and calcium ion by the encapsulating ethyl substituents. Accordingly, ALD growth studies were carried out using $CaTp_2$ as the calcium and boron source and water as the oxygen source. The growth behavior was investigated by varying the precursor pulse lengths, substrate temperatures, and the number of deposition cycles. A plot of growth rate versus

$CaTp_2$ pulse length at 350 °C is shown in Figure 51. The number of deposition cycles, length of the water pulse, and length of the purges after the water and $CaTp_2$ pulses were kept constant at 2000 cycles, 0.3 s, and 5.0 s, respectively. $CaTp_2$ pulse lengths of $\geq$ 2.0 s showed a growth rate of 0.36 Å/cycle, with lower growth rates of 0.34 and 0.33 Å/cycle observed for 1.0 and 0.5 s, respectively. In ALD, it is important to saturate all of the surface reactive sites with each precursor pulse. When this condition is met, precursor doses beyond the minimal amount for saturation result in a consistent growth rate. In Figure 51, it is apparent that self-limited film growth occurred at $CaTp_2$ pulse lengths of $\geq$ 2.0 s and shorter pulse lengths may result in sub-saturative growth. A similar plot of growth rate versus water pulse length showed saturative behavior with $\geq$ 0.3 s pulses. For the deposition studies below, $CaTp_2$ pulses of 3.0 s were used to assure delivery of a saturative precursor dose. The $CaTp_2$ consumption rate varied between 0.13 and 0.16 mg/cycle with 2.0 and 3.0 s pulse lengths, so the longer pulse length used only slightly more precursor. With a 5.0 s pulse length of $CaTp_2$, the consumption rate was 0.19 mg/cycle.

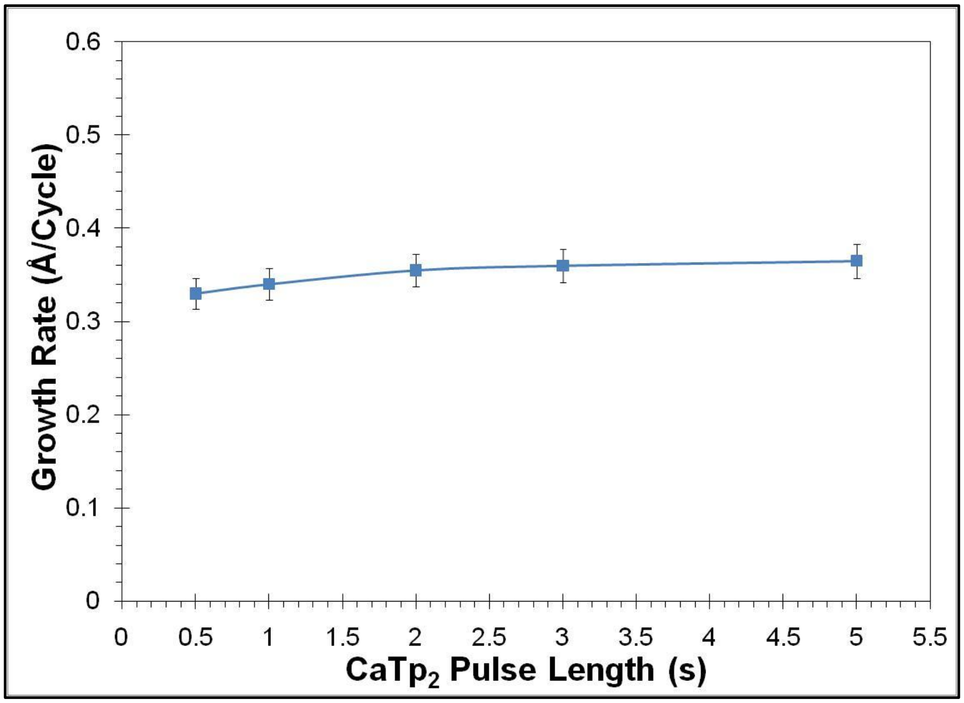

Figure 51. Growth rate as a function of $CaTp_2$ pulse length.

The dependence of the growth rate on substrate temperature is shown in Figure 52. In these depositions, the $CaTp_2$ and water pulse lengths were 3.0 and 0.3 s, respectively. The number of cycles and purge lengths after the $CaTp_2$ and water pulses were kept constant at 2000 cycles and 5.0 s, respectively. A constant growth rate of 0.34-0.36 Å/cycle was observed over the temperature range of 300-375 °C. A temperature region of constant growth rate is referred to as the "ALD Window", which is commonly observed in robust ALD processes.[22a-c] For comparison, an ALD window in the growth of BaB_2O_4 films using $BaTp^{Et2}_2$ and water was observed from 250-375 °C, with a growth rate of 0.23 Å/cycle within this range. The present growth rate of 0.36 Å/cycle is higher than the BaB_2O_4 growth rate. The higher growth rate is likely related to the smaller molecular volume of $CaTp_2$, which allows a higher area density of $CaTp_2$ in the surface monolayer, compared to $BaTp^{Et2}_2$. In addition, $CaTp_2$ should be more reactive than $BaTp^{Et2}{}_2$ toward hydrolysis, since it has less steric protection around the metal ion and boron-hydrogen bond. Growth rates of 0.31 and 0.38 Å/cycle were observed at temperatures of 275 and 400 °C, respectively, which are clearly outside the ALD window. The slight increase in growth rate at 400 °C suggests minor precursor self-decomposition, and is consistent with the $CaTp_2$ solid state decomposition temperature of 385 °C.

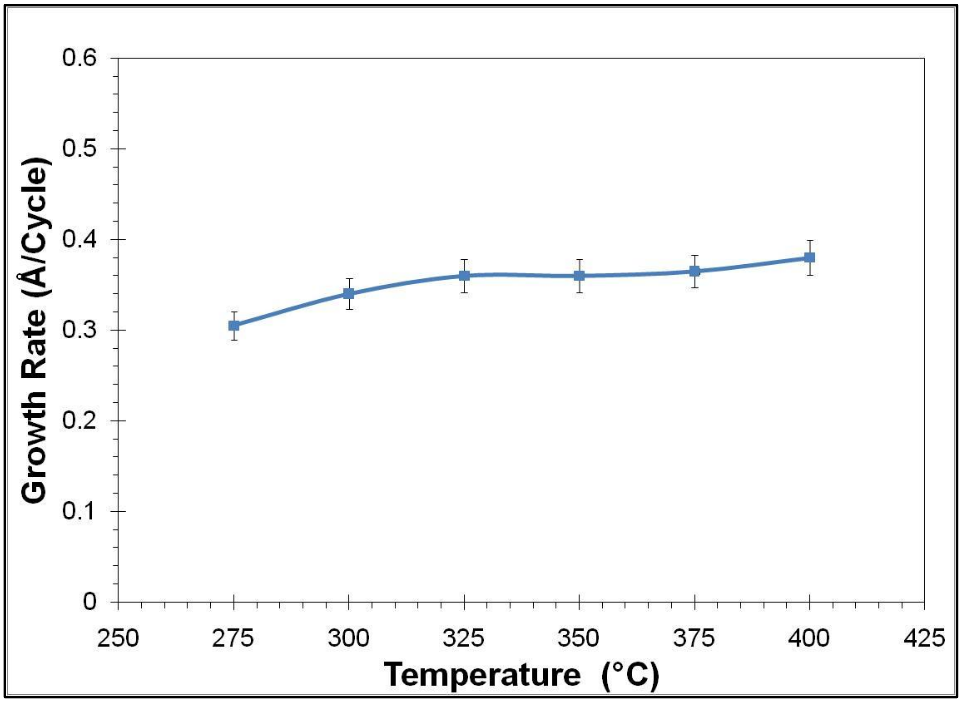

Figure 52. Growth rate as a function of deposition temperature. An ALD window is observed between 315 to 387 °C.

Figure 53 shows a plot of film thickness versus the number of deposition cycles. The $CaTp_2$ pulse lengths, water pulse lengths, purge lengths after the source pulses, and substrate temperature were kept constant at 3.0 s, 0.3 s, 5.0 s, and 350 °C, respectively. The film thicknesses vary linearly with the number of cycles. Additionally, the line of best fit shows a y-intercept of zero and thus suggests that there is no initiation period during the first few deposition cycles.

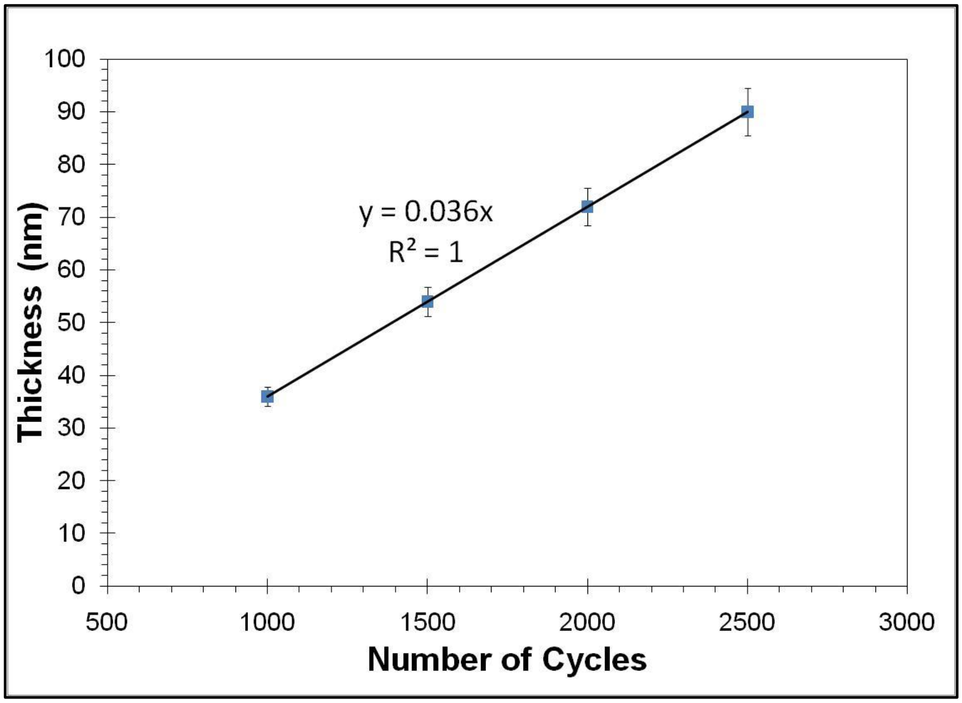

Figure 53. Film thickness as a function of the number of deposition cycles.

There are very few ALD processes in the literature involving the deposition of materials containing calcium ions, because of the lack of thermally stable calcium precursors. β-Diketonate and cyclopentadienyl complexes are the only precursors that have been used in the ALD growth of calcium-containing materials.[10,12c,50,52,112] The ALD growth of CaS using $[Ca(thd)_2]_3$ and hydrogen sulfide gas was reported and uniform films were obtained within the ALD window (325-400 °C) with a growth rate of about 0.50 Å/cycle.[12c] At temperatures of > 400 °C, the growth rate increased significantly and the films were no longer uniform, probably due to $[Ca(thd)_2]_3$ self-decomposition.[12c] Leskelä and coworkers employed the alternate precursor $Ca(thd)_2$(tetraen) (tetraen = tetraethylenepentamine) along with hydrogen sulfide for the ALD growth of CaS films.[50] However, the growth rate (0.43 Å/cycle) and ALD window (300-350 °C) were decreased compared to $[Ca(thd)_2]_3$.[50] $[Ca(thd)_2]_3$ has also been used for the ALD growth of calcium fluoride films with either HF[10a] or TiF_4[10b] as the co-reactant. With HF, a low growth rate of about 0.25 Å/cycle resulted between 320 to 400 °C.[10a] For CaF_2 films deposited using TiF_4 as the fluorine source, the growth rate increased substantially to 1.6 Å/cycle and remained constant between 300-350 °C.[10b] The only report of a cyclopentadienyl-based calcium precursor described $Ca(C_5H_2iPr_3)_2$ in the ALD growth of calcium oxide and calcium hafnium oxide thin films.[112] However, the film growth rates increased with increasing $Ca(C_5H_2iPr_3)_2$ pulse lengths, implying that self-limited growth was not occurring.[112] In the present work, a growth rate of 0.34-0.36 Å/cycle was observed over a temperature range of 300-375 °C. This temperature range is similar to the other ALD processes involving the use of $[Ca(thd)_2]_3$ and $Ca(thd)_2$(tetraen). Hence, Tp-based calcium complexes represent an important new class of ALD precursors that are comparable to the widely employed thd-based complexes of calcium.

CaB_2O_4 Film Characterization. To assess the composition of the films, ERDA was performed on representative samples (Table 29). The B/Ca ratios for films deposited at 275, 325, and 350 °C were 1.84(11), 1.85(11), and 1.89(13), respectively. The O/Ca ratios at 275, 325, and 350 °C were 4.08(18), 4.03(15), and 3.73(18), respectively. These values are within experimental error of those expected for CaB_2O_4. By contrast, the B/Ca and O/Ca ratios for films deposited at 400 °C were 1.42(10) and 2.99(14), respectively. These ratios are significantly lower than those of the CaB_2O_4 films, and suggest loss of boron oxide at this deposition temperature. The hydrogen concentration for films deposited at 275, 325, and 350 °C were 0.22(2), 0.48(4), and 0.35(4) atom %. The carbon and nitrogen concentrations were below the detection limits of 0.1 and 0.3 atom %, respectively. The low hydrogen, carbon, and nitrogen concentrations in films deposited at ≤ 350 °C are indicative of efficient ligand elimination reactions at the surface during film growth. Such low impurity levels are also derived from the high thermal stability of $CaTp_2$ and highlight the importance of careful ALD precursor design. A film deposited at 400 °C showed hydrogen and carbon concentrations of 1.13(6) and 0.66(15) atom %, respectively, which are higher than the corresponding concentrations observed within the ALD window. Precursor decomposition may contribute to these higher concentrations. The nitrogen concentration in the 400 °C film was below the detection limit.

Table 29. Elemental composition of CaB_2O_4 films as determined by ERDA.

T(°C)	B/Ca	O/Ca	%H	%C	%N
275	1.84(11)	4.08(18)	0.22(2)	<0.1	<0.3
325	1.85(11)	4.03(15)	0.48(4)	<0.1	<0.3
350	1.89(13)	3.73(18)	0.35(4)	<0.1	<0.3
400	1.42(10)	2.99(14)	1.13(6)	0.66(15)	<0.3

Films deposited at 325 and 350 °C with thicknesses of 72 nm were analyzed by XPS. XPS analyses of both samples afforded similar results, so only the film deposited at 325 °C is discussed herein. The survey scans for the film deposited at 325 °C, before and after argon ion sputtering, are shown in Figure 54. After two minutes of argon ion sputtering, the O 1s, Ca 2s, Ca $2p_{1/2}$, Ca $2p_{3/2}$, B 1s, and O 2s ionizations were observed at binding energies of 530, 437, 349, 345, 190, and 23 eV. A C 1s ionization for the non-sputtered sample was observed at 286 eV, which disappeared after sputtering with argon ions for two minutes, indicating that the origin of carbon is due to surface contamination. The N 1s ionization was below the detection limit for both the sputtered and non-sputtered samples.

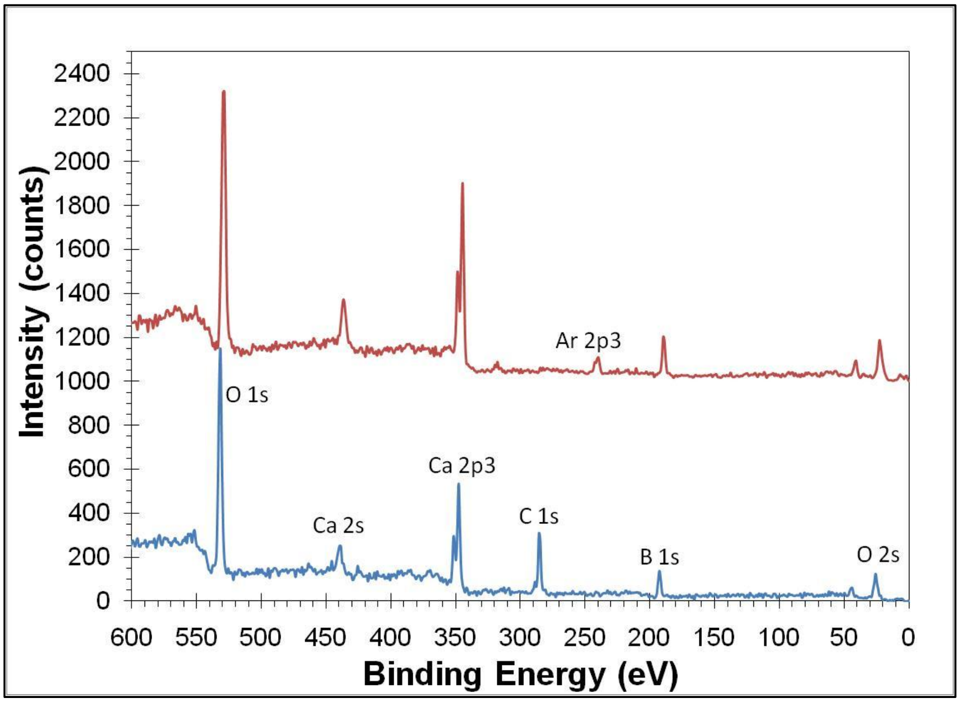

Figure 54. XPS of a 72 nm film deposited at 325 °C. Survey scan of the as is sample (blue) and 2 minute argon ion sputtered (red).

Powder XRD experiments on samples grown at 350 and 400 °C indicated that both films were amorphous. Annealing of the amorphous CaB_2O_4 films under oxygen or nitrogen atmospheres at temperatures between 500 and 1000 °C did not afford crystalline calcium borate thin films, presumably because loss of boron oxide at temperatures above 400 °C prevents the formation of a stable crystalline phase.

The surface morphologies of representative samples were investigated using AFM and SEM. AFM images for films deposited at 325 and 350 °C are shown in Figure 55. The rms surface roughnesses for films deposited at 325 and 350 °C on typical 2 μm x 2 μm areas were 0.3 nm. SEM images for films deposited under the same conditions showed surfaces that were free of pinholes and cracks (Figures 56 and 57). The AFM and SEM images on films deposited at 325 and 350 °C indicate that these films are smooth and featureless.

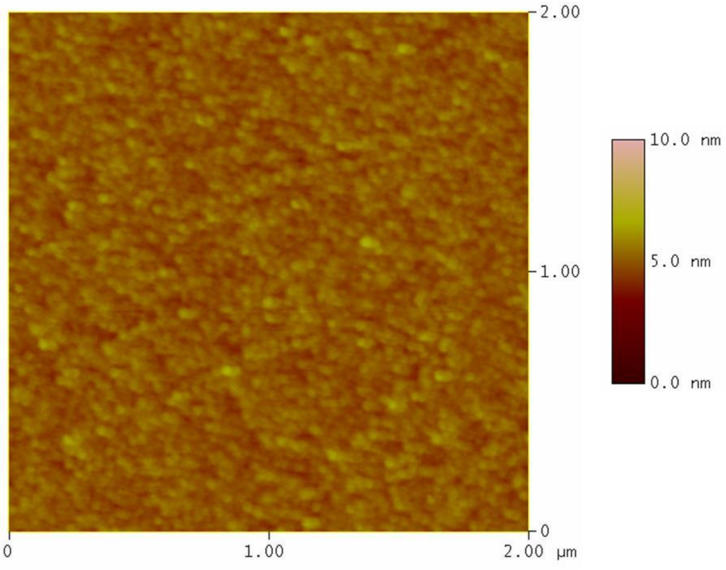

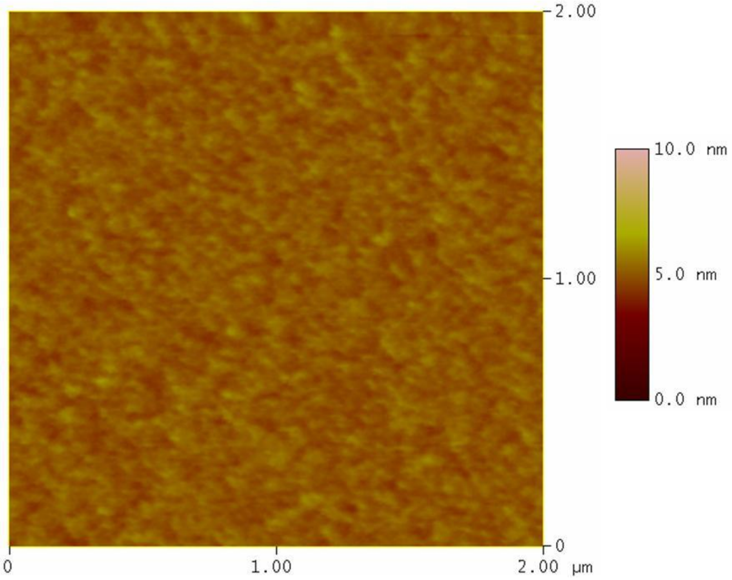

Figure 55. AFM images of CaB_2O_4 thin film surfaces grown at 325 °C (top, rms roughness = 0.3 nm) and 350 °C (bottom), rms roughness = 0.3 nm).

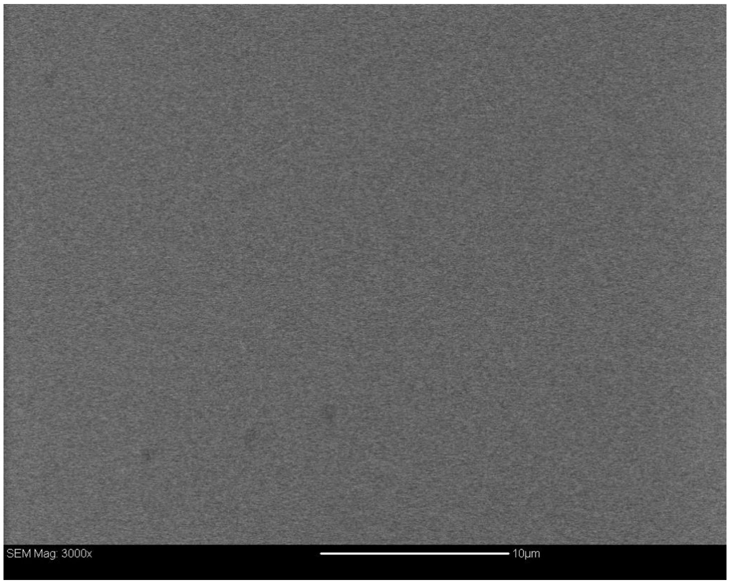

Figure 56. SEM images of a 72 nm thick CaB_2O_4 deposited at 325 °C on a silicon substrate.

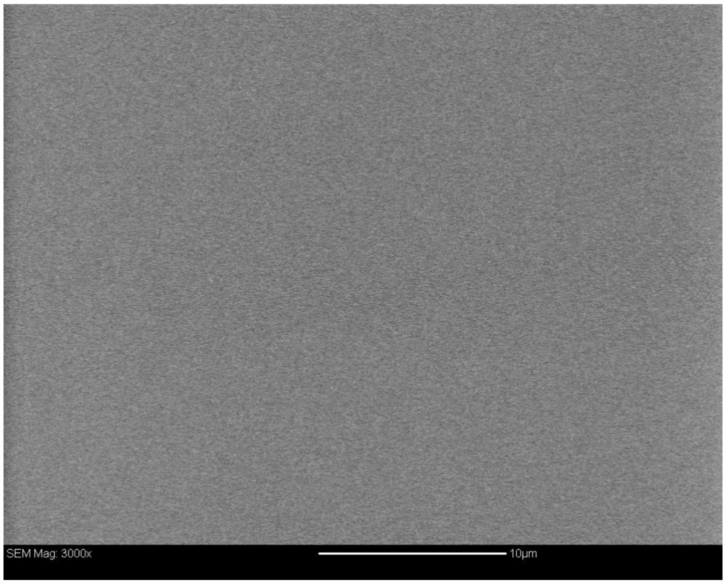

Figure 57. SEM images of a 72 nm thick CaB_2O_4 deposited at 350 °C on a silicon substrate.

An important finding on the ALD of BaB_2O_4 was that $BaTp^{Et2}_2$ acts as a single source precursor for boron and barium and confers a precise 2:1 boron to barium ratio within the experimental uncertainty of ERDA. For CaB_2O_4 films deposited at temperatures of $\leq$ 350 °C, the boron to calcium ratios were also 2:1 within the experimental error of the ERDA analyses. Hence, $CaTp_2$ also acts as a single source precursor for boron and calcium. Such stoichiometry control implies that two Tp ligands remain coordinated to the surface-bound calcium species, and that hydrolysis of $CaTp_2$ is rapid and very efficient. Precursors that deliver two or more elements simultaneously in ALD growth are advantageous, since stoichiometric control of the material is possible, ALD processing times are decreased, and the development of ternary or quaternary materials by ALD should be greatly simplified. However, as described in Chapter 6, the performance of the few bimetallic ALD precursors in the literature has been mixed.[103]

High temperature solid state methods involving $CaCO_3$ and boric acid are typically employed for the synthesis of bulk calcium borate phases.[15,16,17] Boric acid has a melting point of 450 °C and is volatile at high temperatures, and hence stoichiometric control of boron in film growth procedures is difficult.[113] The work documented herein offers a new low temperature route for the formation of CaB_2O_4 thin films. Based upon the present work and the work described in Chapter 6 involving the ALD growth of BaB_2O_4 films from $CaTp^{Et2}_2$ and water, metal(II) precursors of the formula MTp_2 should serve as general ALD precursors to MB_2O_4 films. In the current study, CaB_2O_4 films were obtained at growth temperatures of $\leq$ 350 °C, but lower B/Ca and O/Ca ratios were observed at 400 °C apparently due to boron oxide volatilization. Hence, use of a deposition temperature of $\leq$ 350 °C affords metastable CaB_2O_4 films. Malandrino and coworkers reported that CVD growth $[BaTp_2]_2$ with oxygen at 750 °C afforded BaB_2O_4 films, where the 2:1 B/Ba stoichiometry in $[BaTp_2]_2$ and the BaB_2O_4 films coincided.[46a] By contrast, the CVD growth of $Mg_2B_2O_5$ films from $MgTp_2$ with oxygen at 750 °C afforded a B/Mg ratio in the film (1/1) that differed from that of $MgTp_2$ (2/1).[46b] Such a difference in stoichiometry suggests that precursor decomposition plays a role in the film growth at these high growth temperatures, and that the thermodynamically most stable borate composition is deposited at 750 °C. The ALD growth from Tp-based precursors at growth temperatures lower than the temperature at which boron oxide volatilizes (~400 °C) should lead to thin films where the boron to metal ratios are the same as in the precursors. Such a prediction implies that ALD precursors containing boron to metal ratios that are different from the 2:1 values in the present work should lead to thin films containing different boron to metal ratios.

7.3 Conclusions

The ALD growth of CaB_2O_4 films was demonstrated using $CaTp_2$ and water. Self-limited growth was demonstrated at 350 ºC with $CaTp_2$ pulse lengths of ≥ 2.0 s. An ALD window was observed between 300 and 375 °C, which is comparable to the related ranges in previously reported ALD processes employing thd-based precursors. The film thicknesses varied linearly with the number of growth cycles, suggesting the absence of an initiation period in the beginning of the film growth. ERDA and XPS on samples deposited below 350 °C showed low hydrogen, nitrogen, and carbon concentrations. Within the ALD window, precise 2:1 boron to calcium ratios were observed in the CaB_2O_4 thin films. ERDA on films deposited at 400 °C indicated loss of boron and oxygen, presumably originating through volatilization of B_2O_3. The present work implies that Tp-based precursors constitute a general class of ALD precursors to metal borate films, and that the boron to metal ratio in the precursor should be maintained in the thin film as long as the deposition temperature is below the volatilization point of boron oxide.

8.4 Experimental

General Considerations. $CaTp_2$ was synthesized by a literature procedure.[61e] The melting point of $CaTp_2$ was determined on an Electrothermal Model 9200 melting point apparatus and is uncorrected. TGA was conducted on a Perkin-Elmer Pyris 1 TGA system between 50-500 °C, using nitrogen as the flow gas with a heating rate of 10 °C/min. Preparative sublimations and solid state decomposition studies of $CaTp_2$ were performed according to the procedure described in Chapter 2.

CaB_2O_4 Film Deposition. A SUNALE R-75BE ALD reactor manufactured by Picosun Oy was used for thin film deposition experiments. The reactor was operated under a flow of nitrogen at a pressure of 1-2 mbar. The deposition of CaB_2O_4 thin films by ALD was studied with $CaTp_2$ as the calcium and boron source and water as the oxygen source. In initial growth trials, the sublimation temperature for $CaTp_2$ was found to be optimum at 198 °C at the reactor pressure. The substrate temperatures were varied between 275 and 400 °C. Nitrogen (99.9995%) was used as both the carrier and purge gas and was obtained from air using a Texol GeniSys nitroGenerator. Deposition experiments were performed using a range of $CaTp_2$ pulse lengths, water pulse lengths, and nitrogen purge lengths to determine the extent of surface saturation. Films were deposited on Si(100) substrates obtained from Silicon Quest International. One substrate (one quarter of a 4-inch wafer) was used in each deposition experiment. The native oxide was not removed prior to deposition.

Film Characterization Methods. Film thicknesses were determined by the fitting of reflectance spectra collected between 1100-190 nm, using the method of Ylilammi and Ranta-aho.[107] Reflectance spectra were measured using a Jasco V-570 UV/VIS/NIR double beam spectrophotometer. The film growth rate was determined by dividing the measured film thickness by the number of deposition cycles. Powder X-ray diffraction experiments were performed on a Rigaku R200B 12 kW rotating anode diffractometer, using Cu Kα radiation (1.54056 Å) at 40 kV and 190 mA. Atomic force micrographs were obtained using a MultiMode nanoscope IIIa (Digital Instruments, VEECO). The samples were measured using the tapping mode in air with an E scanner with a maximum scanning size of 12 µm at a frequency of 1 or 2 Hz. The tip employed was a Tap150AI-G with a resonance frequency of 150 kHz and a force constant of 5 N/m. Surface roughness was calculated as root-mean-square (rms) values. Scanning electron micrographs were obtained with a Hitachi S-2400 instrument operating at 25 kV. X-ray photoelectron spectroscopy was performed with a Perkin-Elmer 5500 XPS system using monochromatized Al Kα radiation. Surface contaminants were sputtered using 0.5 kV Ar ions. Elemental concentrations of CaB_2O_4 thin films were determined by ERDA at Forshchungszentrum Dresden-Rossendorf.

CHAPTER 9

Conclusions

A series of heavy alkaline earth complexes containing various poly(pyrazolyl)borate ligands has been synthesized, characterized, and their properties investigated. The new Tp-based group 2 complexes are volatile (sublimation temperatures of 200-240 °C/0.05 Torr), exceptionally thermally stable (decomposition temperatures of > 380 °C), and some even melt prior to evaporation, and thus could find use as viable ALD precursors. A series of group 2 Bp^{R2} (R=H, iPr, tBu) complexes represent the first structurally characterized calcium, strontium, and barium Bp-based complexes in the literature. The structures show strong metal-hydrogen interactions, and therefore are coordinated in a κ^3-N,N,H fashion. The Bp^{tBu2} ligands are highly distorted in order to avoid interligand and intraligand steric interactions, which illustrates the flexibility of this ligand to accommodate metals with large ionic radii. In addition, $CaBp^{tBu2}{}_2$ (**12**) and $SrBp_2{}^{tBu2}$ (**13**) sublime at temperatures between 185-190 °C/0.05 Torr and show a one step weight loss in the TGA traces, indicative of sublimation. Although **12** and **13** may not be useful for ALD applications, they are as volatile and thermally stable as many currently used CVD precursors and could find use in this area. The group 2 complexes containing Bp^{R2} (R = H, iPr) are not suitable precursors for ALD or CVD, because they decompose, as evidenced in the TGA traces. Heating $CaBp_2(THF)_2$ (**19**) at 190-200°C/0.05 Torr afforded the heteroleptic complex $TpCaBH_4$ (**25**). Reaction of **25** with methanol or ethanol led to the formation of structurally diverse oligomers (**28** and **29**).

The ALD growth of BaB_2O_4 with $BaTp^{Et2}_2$ and water was described. This represents the most thermally stable barium ALD precursor to date. Furthermore, it was demonstrated that $BaTp^{Et2}_2$ acts as a bimetallic precursor and confers a precise 2:1 boron/metal ratio. Similarily, $CaTp_2$ and $SrTp_2$ were used with water for the ALD growth of CaB_2O_4 and SrB_2O_4. In both cases, self-limited film growth occurred up to 375 °C. Within the ALD window, a 2:1 boron/metal ratio was also transferred to the thin film.

The work documented herein represents the synthetic development of a new class of group 2 ALD precursors that have unprecedented thermal stability and allow for precise stoichiometric control of group 2 borates. Most solid state metal borate syntheses involve high temperature methods, which can be a problem because the volatilization of B_2O_3 occurs at relatively low temperatures (~400 °C), thus leading to either thermodynamically stable phases or metal borate phases that are deficient in boron and oxygen. The group 2 Tp-based precursors described in this thesis offer new low temperature routes to the formation of group 2 borates with excellent boron to metal stoichiometric control. In addition, this work suggests the possibility of attaining metastable group 2 borate phases not accessible through high temperature synthetic methods. The development of group 2 ALD precursors still remains a significant problem because of the technological importance of materials such as $BaTiO_3$ and $(Sr,Ba)TiO_3$. The group 2 Tp-based precursors developed in this thesis may not be useful as a generic class of group 2 ALD precursors, as they are limited by boron incorporation; however, the present work should help to guide future studies in this area and offers a useful model for ALD precursor selection.

REFERENCES

1. (a) Wojtczak, W. A.; Fleig, P.F.; Hampden-Smith, M. J. *Adv. Organomet. Chem.* **1996**, *40*, 215-340. (b) Guglielmo, G. G.; Malandrino, G.; Ignazio, F. L. *Coord. Chem. Rev.* **2007**, *251*, 1931-1948. (c) Wessels, B. W. *Annu. Rev. Mater. Sci.* **1995**, *25*, 525-546. (d) Matthews, J. S.; Rees, W. S. Jr. *Adv. Inorg. Chem.* **2000**, *50*, 173-192.
2. (a) Yamamichi, S.; Sakuma, T.; Takemura, K.; Miyasaka, Y. *Jpn. J. Appl. Phys.* **1991**, *30*, 2193-2196. (b) Abe, K.; Komatsu, S. *Jpn. J. Appl. Phys.* **1992**, *31*, 2985-2988. (c) Dietz, G. W.; Antpöhler, W.; Klee, M.; Waser, R. *J. Appl. Phys.* **1995**, *78*, 6113-6121. (d) Fukuda, Y.; Aoki, K.; Numata, K.; Nishimura, A. *Jpn. J. Appl. Phys.* **1994**, *33*, 5255-5258.
3. (a) Choi, K. J.; Biegalski, M.; Li, Y. L.; Sharan, A.; Schubert, J.; Uecker, R.; Reiche, P.; Chen, Y. B.; Pan, X. Q.; Gopalan, V.; Chen, L. –Q.; Schlom, D. G.; Eom, C. B. *Science* **2004**, *306*, 1005-1009. (b) Nakano, H.; Suzuki, K.; Kizima, K. *J. Am. Ceram. Soc.* **2006**, *89*, 1461-1464. (c) Shin, J.; Nascimento, V. B.; Borisevich, A. Y.; Plummer, E. W.; Kalinin, S. V.; Baddorf, A. P. *Phys. Rev. B* **2008**, *77*, 245237. (d) Shin, J.; Goyal, A.; Jesse, S.; Kim, D. H. *Appl. Phys. Lett.* **2009**, *94*, 252903.
4. (a) Kawano, H.; Morii, K.; Nakayama, Y. *J. Appl. Phys.* **1993**, *73*, 5141-5146. (b) Horikawa, T.; Mikami, N.; Makita, t.; Tanimura, J.; Kataoka, M.; Sato, K.; Nunoshita, M. *Jpn. J. App. Phys.* **1993**, *32*, 4126-4130. (c) Ezhilvalavan, S.; Tseng, T. –Y. *Mater. Chem. Phys.* **2000**, *65*, 227-248. (d) Jeong, D. S.; Ahn, K. H.; Woo, Y. P.; Hwang, C. S. *Appl. Phys. Lett.* **2004**, *84*, 94-96. (e) Saravanan K. V.; Raju, K. C. J.; Krishna, M. G.; Bhatnagar, A. K. *J. Mater. Sci.* **2007**, *42*, 1149-1155.

5. (a) Yu. T.; Chen, C. H.; Chen, X. F.; Zhu, W.; Krishnan, R. G. *Ceram. Int.* **2004**, *30*, 1279-1282. (b) Yu. T.; Zhu, W. G.; Chen, C. H.; Chen, X. F.; Krishnan, R. G. *Physica B* **2004**, *348*, 440-445. (c) Yaginuma, S.; Yamaguchi, J.; Itaka, K.; Koinuma, H. *Thin Solid Films* **2005**, *486*, 218-221.
6. (a) Scott, J. F.; Paz De Araujo, C. A. *Science* **1989**, *246*, 1400-1405. (b) Haertling, G. H. *J. Vac. Sci. Technol. A* **1991**, *9*, 414-420. (c) Haertling, G. H. *J. Am. Ceram. Soc.* **1999**, *82*, 797-818. (d) Kittl, J. A.; Knaepen, W.; Afanas'ev, V. V.; Pierreux, D.; Manger, D.; and coworkers. *ESC Transactions* **2009**, *19*, 29-40.
7. (a) Sun, D. –L.; Wu, A. –Y.; Yin, S. –T. *J. Am. Ceram. Soc.* **2008**, *91*, 169-173. (b) Luo, L.; Kuzminykh, Y.; Catalano, M.; R.; Malandrino, G.; Hoffman, P. *ECS Transactions* **2009**, *25*, 173-179. (c) Amaral, F.; Valente, M. A.; Costa, L. C. *J. Non-Cryst. Solids* **2010**, *356*, 822-827.
8. (a) Amanuma, K.; Hase, T.; Miyasaka, Y. *Appl. Phys. Lett.* **1995**, *66*, 221-223. (b) Lee, J. J.; Thio, C. L.; Desu, S. B. *J. Appl. Phys.* **1995**, *78*, 5073-5077.
9. (a) Sheng, Z. Z.; Hermann, A. M. *Nature* **1988**, *332*, 138-139. (b) Geballe, T. H.; Hulm, J. K. *Science* **1988**, *239*, 367-375. (c) Horowitz, H. S.; McLain, S. J.; Sleight, A. W.; Druliner, J. D.; Gai, P. L.; Van Kavelaar, M. J.; Wagner, J. L.; Biggs, B. D.; Poon, S. J. *Science* **1989**, *243*, 66-69. (d) Chang, K. –W.; Wessels, B. W.; Qian, W.; Dravid, V. P.; Schindler, J. L.; Kannewurf, C. R.; Studebaker, D. B.; Marks, T. J.; Feenstra, R. *Physica C* **1998**, *303*, 11-20. (e) Hubert-Pfalzgraf, L. G.; Guillon, H. *Appl. Organometal. Chem.* **1998**, *12*, 221-236.
10. (a) Yilammi, M.; Ranta-aho, T. *J. Electrochem. Soc.* **1994**, *141*, 1278-1284. (b) Pilvi, T.; Arstila, K.; Leskelä, M.; Ritala, M. *Chem. Mater.* **2007**, *19*, 3387-3392. (c) Pilvi,

T.; Ritala, M.; Leskelä, M; Bischoff, M.; Kaiser, U.; Kaiser, N. *Appl. Optics* **2008**, *47*, C271-C274.

11. Ihanus, J.; Hänninen, T.; Hatanpää, T.; Ritala, M.; Leskelä, M. *J. Electrochem. Soc.* **2004**, *151*, H221-H225.
12. (a) Li, W.-M.; Ritala, M.; Leskelä, M.; Lappalainen, R.; Jokinen, J.; Soininen, E.; Hüttl, B.; Nykänen, E.; Niinistö, L. *J. Appl. Phys.* **1998**, *84*, 1029-1035. (b) Soininen, P.; Niinistö, L.; Nykänen, E.; Leskelä, M. *Appl. Surf. Sci.* **1994**, *75*, 99-105. (c) Rautanen, J.; Leskelä, M.; Niinistö, L.; Nykänen, E.; Soininen, P.; Utriainen, M. *Appl. Surf. Sci.* **1994**, *82*, 553-558. (d) Tammenmaa, M.; Anstson, H.; Asplund, M.; Hiltunen, L.; Leskelä, M.; Niinistö, L. *J. Cryst. Growth* **1987**, *84*, 151-154. (e) Saanila, V.; Ihanus, J.; Ritala, M.; Leskelä, M. *Chem. Vap. Deposition* **1998**, *4*, 227-233. (f) Soininen, P.; Nykänen, E.; Niinistö, L.; Leskelä, M. *Chem. Vap. Deposition* **1996**, *2*, 69-74.
13. (a) Nikogosyan, D. N. *Nonlinear Optical Crystals: A Complete Survey*; Springer: New York; 2005. (b) Chen, C.; Lin, Z.; Wang, Z. *Appl. Phys. B* **2005**, *80*, 1-25. (c) Keszler, D. A. *Curr. Opin. Sol. State Mater. Sci.* **1996**, *1*, 204-208. (d) Becker, P. *Adv. Mater.* **1998**, *10*, 979-992. (e) Nikogosyan, D. N. *Appl. Phys. A* **1991**, *52*, 359-368.
14. (a) Studebaker, D. B.; Stauf, G. T.; Baum, T. H.; Marks, T. J.; Zhou, H.; Wong, G. K. *Appl. Phys. Lett.* **1997**, *70*, 565-567. (b) Wersand-Quell, S.; Orsal, G.; Thévenin, P.; Bath, A. *Thin Solid Films* **2007**, *515*, 6507-6511
15. (a) Norrestam, R.; Nygren, M.; Bovin, J. –O. *Chem. Mater.* **1992**, *4*, 737-743. (b) Chety R.; Millon, E.; Boudrioua, A.; Loulergue, J. C.; Dahoun, A.; Perrière, J. *J. Mater. Chem.* **2001**, *11*, 657-659. (c) Kubota, H.; Takahashi, R.; Kim, T. –W.; Kawazoe, T.; Ohtsu, M.; Arai, N.; Yoshimura, M.; Nakao, H.; Furuya, H.; Mori, Y.;

Sasaki, T.; Matsumoto, Y. ; Koinuma, H. **2004**, *223*, 241-244. (d) Reshak, A.; H.; Auluck, S.; Kityk, I. V.; Majchrowski, A.; Kasprowicz, D.; Drozdowski, M.; Kisielewski, J.; Lukasiewicz, T.; Michalski, E. *J. Mater. Sci*. **2006**, *41*, 1927-1932. (e)Barros, G.; Guedes, I.; Misoguti, L.; Zilio, S. C.; Loong, C. –K.; Wang, J.; Hu, X.; Zhang, H. *Applied Physics B: Lasers and Optics*, **2009**, *94*, 221-225. (f) Shimizu, H.; Nishida, T.; Takeda, H.; Shiosaki, T. *J. Cryst. Growth* **2009**, *311*, 916-920. (g) Kumar, R. A.; Dhanasekaran, R. *J. Cryst. Growth* **2009**, *311*, 41-543.

16. (a) Lu, X.; You, Z.; Li, J.; Zhu, Z.; Jia, G.; Wang, Y.; Wu, B.; Tu, C. *J. Cryst. Growth* **2005**, *281*, 416-425. (b) Lu, X.; You, Z.; Li, J.; Zhu, Z.; Jia, G.; Wu, B.; Tu, C. *J. Appl. Phys.* **2006**, *100*, 033103. (c) Lu, X.; You, Z.; Li, J.; Zhu, Z.; Jia, G.; Wu, B.; Tu, C. *Phys. Stat. Sol. A* **2006**, *203*, 551-553.
17. (a) Xu, K.; Loiseau, P.; Aka, G.; Lejay, J. *Crystal Growth and Design* **2009**, *9*, 2235-2239. (b) Xu, K.; Loiseau, P.; Aka, G.; Maillard, R.; Maillard, A.; Taira, T. *Opt. Express* **2008**, *16*, 17735-17744.
18. (a) Hao, J. H.; Gao, J. *Appl. Phys. Lett*. **2004**, *85*, 3720-3722. (b) Berezovskaya, I. V.; Efryushina, N. P.; Voloshinovskii, A. S.; Stryganyuk, G. B.; Pir, P. V.; Dotsenko, V. P. *Radiat. Mes.* **2007**, *42*, 878-881. (c) Huang, J.; Zhou, L.; Pang, Q.; Gong, F.; Sun, J.; Wang, W. *Luminescence* **2009**, *24*, 363-452. (d) Guo, C.; Luan, L.; Shi, F. G.; Ding, X. *J. Electrochem. Soc.* **2009**, *156*, J125-J128. (e) Zhang, Q.; Wang, J.; Zhang, G.; Su, Q. *J. Mater. Chem.* **2009**, *19*, 7088-7092. (f) Hao, J. H.; He, G. G. *J. Lumin.* **2007**, *122-123*, 577-579.
19. (a) Yen, W. M.; Weber, M. J. *Inorganic Phosphors: Compositions, Preparation, and Optical Properties*, CRC Press **2004**. (b) Leskelä, M.; Koskentalo,T.; Blasse, G. *J.*

Solid State Chem. **1985**, *89*, 272-279. (c) Schipper, W. J.; van der Voort, D.; van der Berg, P.; Vroon, Z. A. E. P.; Blasse, G. *Mater. Chem. Phys.* **1993**, *33*, 311-317. (d) Peterson, J. R.; Xu, W.; Dai, S. *Chem. Mater.* **1995**, *7*, 1686-1689. (e) Seo, H. J.; Moon, B. K.; Kim, B. J.; Kim, J. B.; Tsuboi, T. *J. Phys. Condens. Mater.* **1999**, *11*, 7635-7644. (f) Pir, P. V.; Dotsenko, V. P.; Efryushina, N. P.; Berezovskaya, I. V. *Inorg. Mater.* **2006**, *42*, 901-907. (g) Chang, C. –K.; Chen, T. –M. *Appl. Phys. Lett.* **2007**, *91*, 081902. (h) Song, W. –S.; Kim, Y. –S.; Yang, H. *Mater. Chem. Phys.* **2009**, *117*, 500-503. (i) Pekgözlü, İ.; Karabulut, H. *Inorg. Mater.* **2009**, *45*, 61-64.

20. (a) Mahan, J. E. *Physical Vapor Depositoin of Thin Films*; John Wiley & Sons, Inc.: New York, New York, 2000. (b) Rossnagel, S. M. *J. Vac. Sci. and Technol. A* **2003**, *21*, S74-S87.

21. (a) Pierson, H. O. *Handbook of Chemical Vapor Depostion (CVD)*; Noyes Publications/William Andrew Publishing: Norwich, New York, 1999. (b) Hitchman, M. L.; Jenson, K. F. *Chemical Vapor Deposition: Principles and Applications*; Academic Press: London, 1993. (c) Dobkin, D. M.; Zuraw, M. K. *Principles of Chemical Vapor Deposition*; Kluwer Academic Publishers: The Dordrecht, The Netherlands, 2003.

22. (a) Leskelä, M.; Ritala, M. *Angew. Chem. Int. Ed.* **2003,** *42*, 5548-5554. (b) Niinistö, L.; Päiväsaari, J.; Niinistö, J.; Putkonen, M.; Nieminen, M. *Phys. Stat. Sol. A* **2004**, *201*, 1443-1452. (c) Putkonen, M.; Niinistö, L. *Top. Organomet. Chem.* **2005**, *9*, 125-145. (d) Puurunen, R. L. *J . Appl. Phys.* **2005**, *97*, 121301. (e) George, S. M. *Chem. Rev.* **2010**, *110*, 111-131. (f) Knez, M.; Nielsch, K.; Niinistö, L. *Adv. Mater.* **2007**, *19*, 3425-3438.

23. (a) Otway, D. J.; Rees Jr.; W. S. *Coord. Chem. Rev.* **2000**, *210*, 279-328. (b) Sievers, R. E.; Turnipseed, S. B.; Huan, L.; Lagalante, A. F. *Coord. Chem. Rev.* **1993**, *128*, 285-291.

24. Drake, S. R.; Hursthouse, M. B.; Malik, K. M. A.; Otway, D. J. *Dalton. Trans.* **1993**, 2883-2890.

25. Arunasalam, V. C.; Drake, S. R.; Hursthouse, M. B.; Malik, K. M. A.; Miller, S. A. S.; Mingos, D. M. P. *Dalton. Trans.* **1996**, 2435-2442.

26. Brooks, J.; Davies, H. O.; Leedham, T. J.; Jones, A. C.; Steiner, A. *Chem. Vap. Deposition* **2000**, *6*, 66-69.

27. Drozdov, A. A.; Trojanov, S. I. *Polyhedron* **1992**, *11*, 2877-2882.

28. Rees, W. S.; Carris, M. W.; Hesse, W. *Inorg. Chem.* **1991**, *30*, 4479-4481.

29. Paw, W.; Baum, T. H.; Lam, K. -C.; Rheingold, A. L. *Inorg. Chem.* **2000**, *39*, 2011-2014.

30. Drake, S. R.; Miller, S. A. S.; Williams, D. J. *Inorg. Chem.* **1993**, *32*, 3227-3235.

31. Gardiner, R. A.; Gordon, D. C.; Stauf, G. T.; Vaartstra, B. A.; Ostrander, R. L.; Rheingold, A. L. *Chem. Mater.* **1994**, *6*, 1967-1970.

32. Purdy, A. P.; Berry, A. D.; Holm, R. T.; Fatemi, M.; Gaskill, D. K. *Inorg. Chem.* **1989**, *28*2, 2799-2803.

33. Malandrino, G.; Richeson, D.; Marks, T. J.; DeGroot, D. C.; Schindler, J. L.; Kannewurf, C. R. *Appl. Phys. Lett.* **1991**, *58*, 182-184.

34. (a) Timmer, K.; Meinenma, H. A. *Inorg. Chim. Acta* **1991**, *187*, 99-106. (b) Norman, J. A.; Pez, G. P. *Chem. Commun.* **1991**, 971-972. (c) Polyanskaya, T. M.; Gatilov, Y. V.; Martynova, T. N.; Nikulina, L. D. *Zhurnal Strukturnoi Khimii*, **1992**, *33*, 190-194.

(d) Polyanskaya, T. M.; Furmanova, N. G.; Martynova, T. N. *J. Struct. Chem.* **1993**, *34*, 879-887. (e) Polyanskaya, T. M.; Chistyakov, M. A.; Simonenko, E. P.; Sevast'anov, V. G.; Kuznetsov, N. T. *Inorg. Chim. Acta* **2009**, *362*, 5133-5138.

35. Motevalli, M.; O'Brian, P.; Watson, I. M. *Polyhedron* **1996**, *15*, 1865-1875.
36. (a)Timmer, K.; Spee, K. I. M. A.; Mackor, A.; Meinema, H. A. *Inorg. Chim. Acta* **1991**, *190*, 109-117. (b) Marks, T. J.; Belot, J. A.; Reedy, C. J.; McNeely, R.; J.; Studebaker, D. B.; Neumayer, D. A.; Stern, C. L. *J. Alloy Compd.* **1997**, *251*, 243-248. (c) Belot, J. A.; Neumayer, D. A.; Reedy, C. J.; Studebaker, D. B.; Hinds, B. J.; Stern, C. L. Marks, T. J. *Chem. Mater.* **1997**, *9*, 1638-1648.
37. Thompsom, S. C.; Cole-Hamilton, D. J.; Gilliland, D. D.; Hitchman, M. L.; Barnes, J. C. *Adv. Mater. Opt. Electr.* **1992**, *1*, 81-97.
38. (a) Schulz, D. L.; Hinds, B. J.; Stern, C. L.; Marks, T. J. *Inorg. Chem.* **1993**, *32*, 249-250. (b) Schulz, D. L.; Hinds, B. J.; Neumayer, D. A.; Stern, C. L.; Marks, T. J. *Chem. Mater.* **1993**, *5*, 1605-1617. (c) Studebaker, D.B.; Neumayer, D. A.; Hinds, B. J.; Stern, C. L.; Marks, T. J. *Inorg. Chem.* **2000,** *39*, 3148-3157.
39. Neumayer, D. A.; Belot, J. A.; Feezel, R. L.; Reedy, C.; Stern, C. L.; Marks, T. J. *Inorg. Chem.* **1998**, *37*, 5625-5633.
40. Pasko, S.; Hubert-Pfalzgraf, L. G.; Richard, P.; Abrutis, A. *Inorg. Chem. Comm.* **2005**, *8*, 483-487.
41. (a) El-Kaderi, H. M.; Heeg, M. J.; Winter, C. H. *Organometallics* **2004**, *23*, 4995-5002. (b)Sedai, B.; Heeg, M. J.; Winter, C. H. *Organometallics* **2009**, *28*, 1032-1038.
42. (a) Caulton, K.; Chisholm, M. H.; Drake, S. R.; Huffman, J. C. *Chem. Commun.* **1990**, 1498-1499. (b) Rees, W. S. Jr.; Moreno, D. A. *Chem. Commun.* **1991**, *24*, 1759-1760.

(c) Purdy, A. P.; George, C. F.; Callahan, J. H. *Inorg. Chem.* **1991**, *30,* 2812-2819. (d) Hermann, W. A.; Huber, N. W.; Priermeier, T. *Angew. Chem. Int. Ed. Engl.* **1994**, *33*, 105-107. (e) Chi, Y.; Ranjan, S.; Chou, T.; Liu, C.; Peng, S.; Lee, G. *Dalton Trans.* **2001**, 2462-2466.

43. (a) Hitzbleck, J.; O'Brien, A. Y.; Forsyth, C. M.; Deacon, G. B.; Ruhlandt-Senge, K. *Chem. Eur. J.* 2004, *10,* 3315-3323. (b) El-Kaderi, H. M.; Heeg, M. J.; Winter, C. H. *Polyhedron* 2005, 645-653. (c) El-Kaderi, H. M.; Heeg, M. J.; Winter, C. H. *Eur. J. Inorg. Chem.* 2005, 2081-2088. (d) Hitzbleck, J.; O'Brien, A. Y.; Forsyth, C. M.; Deacon, G. B.; Ruhlandt-Senge, K. *Inorg. Chem.* 2006, *45*, 10329-10337. (e) Hitzbleck, J.; Deacon, G. B.; Ruhlandt-Senge, K. *Angew. Chem. Int. Ed.* 2004, *43,* 5218-5220.

44. Kunze, K.; Bihyr, L.; Atanasova, P.; Hampden-Smith, M. J.; Duesler, E. N. *Chem. Vap. Deposition* **1996**, *2*, 105-108.

45. Vargas, W.; Ruhlandt-Senge, K. *Eur. J. Inorg. Chem.* **2003,** 3472-3479.

46. (a) Malandrino, G.; Nigro, R. L.; Fragalà, I. L. *Chem. Vap. Deposition* **2007,** *13,* 651-655. (b)) Malandrino, G.; Nigro, R. L.; Fragalà, I. L. *Inorg. Chim. Acta* **2007,** *360*, 1138-1142.

47. (a)Lee, S. W.; Kwon, O. S.; Hwang, C. S. *Microelectron. Eng.* **2005**, *80*, 158-161. (b) Kwon, O. S.; Kim, S. K.; Cho, M.; Hwang, C. S.; Jeong, J. *J. Electrochem. Soc.* **2005**, *152,* C229-C236. (c) Kil, D. -S.; Lee, J.-M.; Roh, J.-S. *Chem. Vap. Deposition* **2002**, *8,* 195-197.

48. (a) Lee, J. H.; Cho, Y. J.; Min, Y. S.; Kim, D. *J. Vac. Sci, Technol. A* **2002**, *20,* 1828-1830. (b) Kil, D. –S.; Lee, J. –M.; Roh, J. S. *Chem. Vap. Deposition* **2002**, *8,* 195-197.

(c) Kwon, O. S.; Kim, S. K.; Cho, M.; Hwang, C. S.; Jeong, J. *J. Electrochem. Soc.* **2005**, *4*, C229-C236. (d) Lee, S. W.; Kwon, O. S.; Hwang, C. S. **2005**, *80*, 158-161. (e) Lee, S. W.; Kwon, O. S.; Han, J. H.; Hwang, C. S. *ECS Transactions* **2007**, *6*, 87-89. (f) Kwon, O. S.; Lee, S. W.; Han, J. H.; Hwang, C. S. *J. Electrochem. Soc.* **2007**, *154*, G127-G133.

49. (a) Ahn, J. –H.; Kim, J. –Y.; Kang, S. –W.; Kim, J. –H.; Roh, J. –S. *Appl. Phys. Lett.* **2007**, *91*, 062910. (b) Lee, S. W.; Kwon, O. S.; Han, J. H.; Hwang, C. S. *Appl. Phys. Lett.* **2008**, *92*, 222903. (c) Lee. S. W.; Han, J. H.; Kwon, O. S.; Hwang, C. S. *J. Electrochem. Soc.* **2008**, *155*, G253-G257. (d) Lee, S. W.; Han, J. H.; Hwang, C. S. *ECS Transactions* **2009**, *19*, 685-698. (e) Lee, S. W.; Han, J. H.; Hwang, C. S. *Electrochem. Solid St.* **2009**, *12*, G69-G71. (f) Ahn, J. –H.; Kim, J. –Y.; Kim, J. –S.; Roh, J. –S.; Kang, S. –W. *Electrochem. Solid St.* **2009**, *12*, G5-G8.

50. Hänninen, T.; Mutikainen, I.; Saanila, V.; Ritala, M.; Leskelä, M. *Chem. Mater.*, **1997**, *9*, 1234–1240.

51. Kosola, A.; Putkonen, M.; Johansson, L. –S.; Niinisto, L. *Appl. Surf. Sci.* **2003**, *211*, 102-112.

52. Nilson, O.; Fjellvåg, H.; Kjekshus, A. *Thin Solid Films* **2004**, *450*, 240-247.

53. Nilson, O.; Rauwel; E.; Fjellvåg, H.; Kjekshus, A. *J. Mater. Chem.* **2007**, *17*, 1466-1475.

54. Lie, M.; Nilsen, O.; Fjellvåg, H.; Kjekshus, A. *Dalton Trans.* **2009**, 481-489.

55. (a) Hanusa, T. P. *Chem. Rev.* **1993**, *93*, 1023-1036. (b) Hanusa, T.P. *Organometallics* **2002**, *21*, 2559-2571.

56. (a) Vehkamäki, M.; Hatanpää, T.; Hänninen, T.; Ritala, M.; Leskelä, M. *Electrochem. Solid St.* **1999**, *2*, 504-506. (b) Ihanus, J.; Hänninen, T.; Hatanpää, T.; Aaltonen, T.; Mutikainen, I.; Sajavaara, T.; Keinonen, J.; Ritala, M.; Leskelä, M. *Chem. Mater.* **2002**, *14*, 1937-1944.
57. Hatanpää, T.; Vehkamäki, M.; Mutikainen, I.; Kansikas, J.; Ritala, M.; Leskelä, M. *Dalton Trans.* **2004**, 1181-1188.
58. (a) Hatanpää, T.; Ritala, M.; Leskelä, M. *J. Organomet. Chem.* **2007**, *692*, 5256-5262. (b) Vehkamäki, M.; Hatanpää, T.; Hänninen, T.; Ritala, M.; Leskelä, M. *Chem. Vap. Deposition* **2001**, *7*, 75-80.
59. (a) Trofimenko, S. *Chem. Rev.* **1993**, *93*, 943-980. (b) Trofimenko, S. *Scorpionates-The Coordination Chemistry of Polypyrazolylborate Ligands*; Imperial College Press: London, 1999.
60. Dezelah IV, C. L.; Wiedmann, M. K.; Mizohata, K.; Baird, R. J.; Niinistö, L.; Winter, C. H. *J. Am. Chem. Soc.* **2007**, *129*, 12370-12371.
61. (a) Dutremez, S. G.; Leslie, D. B.; Streib, W. E.; Chisholm, M. H.; Caulton, K. G. *J. Organomet. Chem.* **1993**, *462*, C1-C2. (b) Sohrin, Y.; Matsui, M.; Hata, Y.; Hasegawa, H.; Kokusen, H. *Inorg. Chem.* **1994**, *33*, 4376-4383. (c) Belderraín, T. R.; Contreras, L.; Paneque, M.; Carmona, E. *J. Organomet. Chem.* **1994**, *474*, C5-C7. (d) Belderraín, T. R.; Contreras, L.; Paneque, M.; Carmona, E.; Monge, A.; Ruiz, C. *Polyhedron* **1996**, *15*, 3453-3463. (e) Sohrin, Y.; Kokusen, H.; Kihara, S.; Matsui, M.; Kushi, Y.; Shiro, M. *J. Am. Chem. Soc.* **1993**, *115*, 4128-4136.
62. Trofimenko, S. *J. Am. Chem. Soc.* **1967**, *89*, 3170-3177.

63. (a) Dezelah, C. L., IV; El-Kadri, O. M.; Szilágyi, I.; Campbell, J. M.; Arstila, K.; Niinistö, L.; Winter, C. H. *J. Am. Chem. Soc.* **2006**, *128*, 9638-9639. (b) Dezelah, C. L., IV; El-Kadri, O. M.; Kukli, K.; Arstila, K.; Baird, R. J.; Lu, J.; Niinistö, L.; Winter, C. H. *J. Mater. Chem.* **2007**, *17*, 1109-1116.

64. Hu, Z.; Gorun, M. *Inorg. Chem.* **2001**, *40*, 667-671.

65. Chisholm, M. H.; Gallucci, J. C.; Yaman, G. *Chem. Commun.* **2006**, 1872-1874.

66. Steiner, A.; Stalke, D. *Inorg. Chem.* **1995**, *34*, 4846-4853.

67. Williams, R. A.; Hanusa, T. P.; Huffman, J. C. *Organometallics* **1990**, *9*, 1128-1134.

68. Williams, R. A.; Tesh, R. F.; Hanusa, T. P. *J. Am. Chem. Soc.* **1991**, *113*, 4843-4851.

69. Harvey, M. J.; Quisenberry, K. T.; Hanusa, T. P.; Young, V. G. Jr. *Eur. J. Inorg. Chem.* **2003**, 3383-3390.

70. Trofimenko, S. *J. Am. Chem. Soc.* **1967**, *89*, 6288-6294.

71. Noyce, D. S.; Ryder, E. Jr.; Walker, B. H. *J. Am. Chem. Soc.* **1955**, *20*, 1681-1686.

72. Swamer, F. W.; Hauser, C. R. *J. Am. Chem. Soc.* **1950**, *72*, 1352-1356.

73. *APEX II* collection and processing programs are distributed by the manufacturer. Bruker AXS Inc., Madison WI, USA, 2005

74. Sheldrick, G.M. *Acta Crystallogr.* **2008**, *A64*, 112-122.

75. Dowling, C.; Ghosh, P.; Parkin, G. *Polyhedron,* **1997**, *16*, 3469-3473.

76. (a) Ghosh, P.; Hascall, T.; Dowling, C.; Parkin, G. *J. Chem. Soc., Dalton Trans.* **1998**, 2255-2257. (b) Dowling, C. M.; Parkin, G. *Polyhedron* **2001**, *20*, 285-289.

77. (a) Kokusen, H.; Sohrin, Y.; Kihara, S.; Matsui, M. *Anal. Sci.* **1991**, *7*, 7-10. (b) Yasuda, N.; Kokusen, H.; Sohrin, Y.; Kihara, S.; Matsui, M. *Bull. Chem. Soc. Jpn.* **1992**, *65*, 781-785.

78. Loroño-Gonzalez, D. J.; *Acta Crystallogr. C* **2008**, *C64*, m229-m232.

79. Jung, O.-S.; Jeong, J. H.; Sohn, Y. S. *Organometallics* **1991**, *10*, 2217-2221.

80. Dowling, C. M.; Leslie, D.; Chisholm, M. H.; Parkin, G. *Main Group Chem.* **1995**, *1*, 29-52.

81. Maria, L. Domingo, A.; Santos, I. *Inorg. Chem. Commun.* **2003**, *6*, 58-60.

82. (a) Bondi, A. *J. Phys. Chem.* **1964**, *68*, 441-451. (b) Mantina, M.; Chamberlin, A. C.; Valero, S.; Cramer, C. J.; Truhlar, D. G. *J. Phys. Chem. A* **2009**, *113*, 5806-5812.

83. Bremer, M.; Nöth, H.; Thomann, M.; Schmidt, M. *Chem. Ber.* **1995**, *128*, 455-460.

84. Harder, S.; Brettar, J. *Angew. Chem. Int. Ed.* **2006**, *45*, 3474-3478.

85. Arrowsmith, M.; Hill, M. S.; Kociok-Köhn, G. *Organometallics* **2009**, *28*, 1730-1738.

86. Pfeiffer, D.; Heeg, M. J.; Winter, C. H. *Inorg. Chem.* **2000**, *39*, 2377-2384.

87. Elguero, J.; Gonzalez, E.; Jacquier, R. *Bull. Soc. Chim. Fr.* **1968**, 707-713.

88. Kitajima, N.; Fujisawa, K.; Fujimoto, C.; Moro-oka, Y.; Hashimoto, S.; Kitagawa, T.; Toriumi, K.; Tatsumi, K.; Nakamura, A. *J. Am. Chem. Soc.*, **1992**, *114*, 1277-1291.

89. Weis, K.; Vahrenkamp, H. *Inorg. Chem.*, **1997**, *36*, 5589-5591.

90. Chisholm, M. H.; Gallucci, J. C.; Yaman, G. *Inorg. Chem.* **2007**, *46*, 8676-8683.

91. Reger, D. L.; Ding, Y.; Rheingold, A. L.; Ostrander, R. L. *Inorg. Chem.* **1994**, *33*, 4226-4230.

92. Harvey, M. J.; Hanusa, T. P.; Pink, M. *Chem. Commun.* **2000**, 489-490.

93. Capporto, P.; Mani, F.; Mealli, C. *Inorg. Chem.* **1978**, *17*, 1232-1329.

94. Reger, D. L.; Lindeman, J. A.; Lebioda, L. *Inorg. Chem.* **1988**, *27*, 1890-1896.

95. Carvalho, Â.; Domingos, P.; Gaspar, P.; Marques, N.; Pires De Matos, A.; Santos, I., *Polyhedron,* **1992**, *11*, 1481-1488.

96. Maria, L.; Domingos, Â.; Santos, I. *Inorg. Chem.* **2003**, *42*, 3323-3330.

97. Dias, H. V. R.; Gordan, J. D. *Inorg. Chem.* **1996**, *35*, 318-324.

98. (a) Guggenberger, L. J.; Prewitt, C. T.; Meakin. P.; Trofimenko, S.; Jesson, J. P. *Inorg. Chem.* **1973**, *12*, 508-515. (b) Reger, T. D.; Wright, T. D.; Smith, M. D.; Rheingold, A. L.; Rhagitan, B. *J. Chem. Crystallogr.* **2000**, *30*, 665-670.

99. Hanecker, E.; Moll, J.; Nöth, H. *Z. Naturforsch.* **1984**, *39b*, 424-430.

100. (a) Frankcombe, T. J. *J. Phys. Chem. C* **2010**, *114*, 9503-9509. (b) Kim, J. –H.; Jin, S. –A.; Shim, J. –H.; Cho, Y. –W. *J. Alloy. Compd.* **2010**, *114*, 9503-9509. (c) Wang, L. –L.; Graham, G. D.; Robertson, I. M.; Johnson, D. D. *113*, 20088-20096. (d) Riktor, M. D.; Sørby, M. H.; Chłopek, K.; Fichtner, M.; Hauback, B. C. *J. Chem. Mater.* **2009**, *19*, 2754-2759.

101. Orimo, S. –i.; Nakamori, Y.; Eliseo, J. R.; Züttel, A.; Jensen, C. M. *Chem. Rev.* **2007**, *107*, 4111-4132.

102. (a) Chua, Y. S.; Wu, G.; Xiong, Z.; He, T.; Chen, P. *Chem. Mater.* **2009**, *21*, 4899-4904. (b) Zhang, Q.; Tan, C.; Fang, C.; Fang, F.; Sun, D.; Ouyang, L; Zhu, M. *J. Phys. Chem. C* **2010**, *114*, 1709-1714.

103. (a) Likosius, M.; Wenger, C.; Pasko, S.; Costina, I.; Dabrowski, J.; Sorge, R.; Müssig, H.-J.; Lohe, C. *IEEE Trans. Elecron Dev.* **2008**, *55*, 2273-2377. (b) Vehkamäki, M.; Ritala, M.; Leskelä, M.; Jones, A. C.; Davies, H. O.; Sajavaara, T.; Rauhala, E. *J. Electrochem. Soc.* **2004**, *151*, F69-F72. (c) Gaskell, J. M.; Przybylak, S.; Jones, A. C.; Aspinall, H. C.; Chalker, P. R.; Black, K.; Potter, R. J.; Taechakumput, P.; Taylor, S. *Chem. Mater.* **2007**, *19*, 4796-4803. (d) Harjuoja, J.; Hatanpää, T.; Vehkamäki, M.;

Väyrynen, S.; Putkonen, M.; Niinistö, L.; Ritala, M.; Leskelä, M.; Rauhala, E. *Chem. Vap. Deposition* **2005**, *11*, 362-367.

104. (a) Putkonen, M.; Niinistö, L. *Thin Solid Films* **2006**, *514*, 145-149. (b) Ferguson, J. D.; Weimer, A. W.; George, S. M. *Thin Solid Films* **2002**, *413*, 16-25. (c) Mårlid, B.; Ottosson, M.; Pettersson, U.; Larsson, K.; Carlsson, J.-O. *Thin Solid Films* **2002**, *402*, 167-171.

105. (a) Brei, V. V.; Kaspersky, V. A.; Gulyanitskaya, N. U. *React. Kinet. Catal. Lett.* **1993**, *50*, 415-421. (b) Gun'ko, V. M. *Kinet. Catal.* **1993**, *34*, 463-466.

106. Turgambaeva, A. E.; Krisyuk, V. V.; Sysoev, S. V.; Igumenov, I. K. *Chem. Vap. Deposition* **2001**, *7*, 121-124

107. Ylilammi, M; Ranta-aho, T. *Thin Solid Films,* **1993**, *232*, 56-62.

108. Popovici, M.; Van Elshocht, S.; Menou, N.; Swerts, J.; Pierreux, D.; Dlabie, A.; Brijs, B.; Conard, T.; Opsomer, K.; Maes, J. W.; Wouters, D. J.; Kittle, J. A. *J. Electrochem. Soc.* **2010**, *157*, G1-G4.

109. (a) Lee, R. Y.; Zhang, F. L.; Penczek, J.; Wagner, B. K.; Yocom, P. N.; Summers, C. J. *J. Vac. Sci. Technol. B* **1998**, *16*, 855-857. (b) Park, J. C.; Moon, H. K.; Kim, D. K.; Byeon, S. H.; Kim B. C.; Suh, K. S. *Appl. Phys. Lett.* **2000**, *77*, 2162. (c) Kumar, D.; Sankar, J.; Cho, K. G.; Craciun, V.; Singh, R. K. *Appl. Phys. Lett.* **2000**, *77*, 2518-2520.

110. (a) Hao, J.; Cocivera, M. *J. Phys. Condens. Matter* **2002**, *14*, 925-933. (b) Hao, J.; Cocivera, M. *Appl. Phys. Lett.* **2001**, *79*, 740-742.

111. (a) Putkonen, M.; Nieminen, M.; Niinistö, J.; Niinistö, L. *Chem. Mater.* **2001**, *13*, 4701-4707. (b) Päiväsaari, J.; Putkonen, M.; Niinistö, L. *Thin Solid Films* **2005**, *472*,

275-281. (c) Päiväsaari, J.; Dezelah, C. L.; Back, D.; El-Kaderi, H. M.; Heeg, M. J.; Putkonen, M.; Niinistö, L.; Winter, C. H. *J. Mater. Chem.* **2005**, 4224-4233.

112. Kukli, K.; Ritala, M.; Sajavaara, T.; Hänninen, T.; Leskelä, M. *Thin Solid Films* **2006**, *500*, 322-329.
113. Lamoreaux, R. H.; Hildenbrand, D. L; Brewer, L. *J. Phys. Chem. Ref. Data* **1987**, *16*, 419-443.

ABSTRACT

THE SYNTHESIS, STRUCTURE, AND PROPERTIES OF GROUP 2 POLY(PYRAZOLYL)BORATES AND THEIR USE FOR THE ATOMIC LAYER DEPOSITION OF GROUP 2 BORATES

by

MARK JOSEPH SALY

December 2010

Advisor: Dr. Charles H. Winter

Major: Chemistry (Inorganic)

Degree: Doctor of Philosophy

A series of heavy alkaline earth complexes containing Tp^{R2}-based ligands has been synthesized, structurally characterized, and their properties investigated. Salt metathesis routes involving MI_2 (M = Ca, Sr, Ba) with either KTp^{Et2} or KTp^{nPr2} afforded $MTp^{Et2}{}_2$ or $MTp^{nPr2}{}_2$ in good to moderate yields. All of these complexes are volatile and exceptionally thermally stable, and have acceptable properties for use as group 2 atomic layer deposition (ALD) precursors.

In addition, a series of group 2 complexes containing Bp^{R2}-based ligand systems were synthesized. Treatment of MI_2 (M = Ca, Sr, Ba) with two equivalents of $TlBp^{tBu2}$, KBp, and KBp^{iPr2} in tetrahydrofuran at ambient temperature afforded $MBp^{tBu2}{}_2(THF)_n$, $MBp_2(THF)_n$, and $MBp^{iPr2}{}_2(THF)_2$, respectively. In the MBp^{tBu2} complexes, the Bp^{tBu2} ligands undergo deformation in order to avoid intraligand and interligand *tert*-butyl group steric repulsions. Some of the Bp^{tBu2} complexes have enough volatility and thermal stability to be used as ALD or CVD precursors; however, the Bp and Bp^{iPr2} complexes decompose prior to volatilization. The thermolysis of three equivalents of $CaBp_2(THF)_2$ at 190-200 °C/0.05 Torr afforded one

equivalent of $CaTp_2$ and two equivalents of $TpCaBH_4$ in good yields. Treatment of $TpCaBH_4$ with methanol and ethanol, followed by the appropriate work up procedure, led to the isolation of $[(TpCa(MeOH)_2)_2(\mu\text{-}B(OMe)_4)][B(OMe)_4]$ and $[(TpCaB(OEt)_3O)_3B]\cdot EtOH$, respectively.

The ALD film growth of MB_2O_4 (M = Ca, Sr, Ba) has been demonstrated using $CaTp_2$, $SrTp_2$, or $BaTp^{Et2}{}_2$ and water. For the ALD growth of BaB_2O_4, an ALD window was observed from 250-375 °C with a growth rate of 0.23 Å/cycle. In the ALD growth of CaB_2O_4 and SrB_2O_4, an ALD window was observed from 300-375 °C, respectively, with a consistent growth rate of approximately 0.36 and 0.47 Å/cycle, respectively. In the temperature versus growth rate plots for $CaTp_2$, $SrTp_2$, and $BaTp^{Et2}$, precursor saturation occurred at ≥ 3.0, ≥ 3.0, and ≥ 1.0 s, respectively. Elastic recoil detection analysis (ERDA) of representative samples prepared within the ALD windows indicated that the films were consistent with the composition of MB_2O_4, which demonstrates that Tp^{R2}-based ligands are able to act as a single source precursor for metal and boron, and confer a precise 2:1 boron/metal ratio.

AUTOBIOGRAPHICAL STATEMENT

MARK JOSEPH SALY

Education	Ph.D., Inorganic Chemistry, Wayne State University, Detroit, MI 2005-2010; GPA: 3.79/4.00 Advisor: Professor Charles H. Winter
	B.S., Chemistry, Saginaw Valley State University, Saginaw, MI 1999-2004; GPA: 3.30/4.00 Minor: Mathematics

Publications

"Volatility, High Thermal Stability, and Low Melting Points in Heavier Alkaline Earth Metal Complexes Containing Tris(pyrazolyl)borate Ligands," Mark J. Saly, Mary J. Heeg, and Charles H. Winter, *Inorg. Chem.* **2009**, *48*, 5303-5312.

"Atomic Layer Deposition Growth of BaB_2O_4 Thin Films from an Exceptionally Thermally Stable Tris(pyrazolyl)borate-Based Precursor" Mark J. Saly, Frans Munnik, Ronald J. Baird, Charles H. Winter, *Chem. Mater.* **2009**, *29*, 3742-3744.

"Highly Distorted κ^3-N,N,H Bonding of Bis(3,5-di-*tert*-butylpyrazolyl)borate Ligands to the Heavier Group 2 Elements" Mark J. Saly, Mary J. Heeg, Charles H. Winter, *Organometallics*, Publication date (Web): **July 1, 2010**, DOI: 10.1021/om100434e.

"Atomic Layer Deposition of CaB_2O_4 Films Using Bis(tris(pyrazolyl)borate)calcium as a Highly Thermally Stable Boron and Calcium Source," Mark J. Saly, Frans Munnik, Charles H. Winter, *J. Mater. Chem.* **July 2010**, accepted for publication 8/25/10.

"The Atomic Layer Deposition of SrB_2O_4 Thin Films using the Thermally Stable Precursor bis(tris(pyrazolyl)borate)strontium", Mark J. Saly, Frans Munnik, Charles H. Winter, *Manuscript in Preparation.*

Selected Presentations

"Volatile, Thermally Stable Tris(pyrazolyl)borate Complexes of the Heavy Alkaline Earth Metals with Optimized Properties for Use in Atomic Layer Deposition Film Growth" Mark J. Saly, Mary Jane Heeg, Charles H. Winter, 8th International Conference on Atomic Layer Deposition; Bruges, Belgium; July 2, 2008, (Oral Presentation).

"Atomic Layer Deposition Growth of BaB_2O_4 Thin Films from an Exceptionally Thermally Stable Tris-(pyrazolyl)borate-Based Precursor" Mark J. Saly, Frans Munnik, Ronald J. Baird, Charles H. Winter; Meeting of the Michigan Chapter of the AVS University of Michigan, Ann Arbor, MI; April 22, 2009, (Invited Oral Presentation)

"Atomic Layer Deposition Growth of BaB_2O_4 Thin Films from an Exceptionally Thermally Stable Tris-(pyrazolyl)borate-Based Precursor" Mark J. Saly, Frans Munnik, Ronald J. Baird, Charles H. Winter; 9th International Conference on Atomic Layer Deposition; Monterey, California; July 19-22, 2009, (Poster Presentation)

"Atomic Layer Deposition of Strontium Metaborate from a New Thermally Stable Precursor" Mark J. Saly, Frans Munnik, Charles H. Winter; 239th National ACS Meeting; San Francisco, California; March 21-25, 2010, (Poster Presentation)